Design of new sulfate-based positive electrode materials for Li- and Na-ion batteries

Marine Reynaud

Ph.D. Dissertation

Speciality: Materials Science

presented at the

Université de Picardie Jules Verne

by

Marine REYNAUD

for the degree of Doctor of Philosophy of the Université de Picardie Jules Verne

---

Design of new sulfate-based positive electrode materials
for Li- and Na-ion batteries

---

defended on 9 December 2013, post referees' approval, in front of the committee:

Dr. Robert DOMINKO	**Research Director**	**Referee**
Dr. M. Rosa PALACÍN	**Research Director CSIC**	**Referee**
Dr. Valérie PRALONG	**Research Director CNRS**	**Examiner**
Dr. Juan RODRÍGUEZ-CARVAJAL	**Research Scientist ILL**	**Examiner**
Pr. Christian MASQUELIER	**Professor**	**Examiner**
Dr. Gwenaëlle ROUSSE	**Assistant Professor – HDR**	**Examiner**
Dr. Jean-Noël CHOTARD	**Assistant Professor**	**Director**
Pr. Jean-Marie TARASCON	**Professor**	**Director**

Thèse de Doctorat

Spécialité: Sciences des Matériaux

présentée à l'

Université de Picardie Jules Verne

par

Marine REYNAUD

pour obtenir le grade de Docteur l'Université de Picardie Jules Verne

Elaboration de nouveaux matériaux à base de sulfates pour l'électrode positive des batteries à ions Li et Na

soutenue le 9 décembre 2013, après avis des rapporteurs, devant le jury d'examen :

Dr. Robert DOMINKO	**Directeur de Recherche**	**Rapporteur**
Dr. M. Rosa PALACÍN	**Directeur de Recherche CSIC**	**Rapporteur**
Dr. Valérie PRALONG	**Directeur de Recherche CNRS**	**Examinateur**
Dr. Juan RODRÍGUEZ-CARVAJAL	**Scientifique ILL**	**Examinateur**
Pr. Christian MASQUELIER	**Professeur**	**Examinateur**
Dr. Gwenaëlle ROUSSE	**Maître de Conférences – HDR**	**Examinateur**
Dr. Jean-Noël CHOTARD	**Maître de Conférences**	**Directeur**
Pr. Jean-Marie TARASCON	**Professeur**	**Directeur**

A mes parents, mes frère et soeur,
et mes grands-parents,
A Mikel.

Abstract

The next generations of Li- and Na-ion batteries will rely on the development of new sustainable, low-cost and safe positive electrode materials. To this end, we explored the world of minerals with an emphasis on spotting structures having the prerequisites for insertion and deinsertion of alkaline ions. From this survey, we embarked on the investigation of bimetallic sulfates derived from the *bloedite* mineral and having the general formula $A_xM(SO_4)_2 \cdot nH_2O$ (A = Li, Na, M = 3d transition metal and $n = 0, 4$). These systems present rich crystal chemistry, undergoing phase transitions upon heating and removal of water. The new structures were determined by combining X-ray, neutron and electron diffraction techniques. We have also shown that lithium-based compounds $Li_xM(SO_4)_2$ present interesting antiferromagnetic properties resulting from their peculiar structures, which solely enable super-super-exchange interactions. Finally, and more importantly, we identified among the isolated compounds three iron-based sulfates, namely $Na_2Fe(SO_4)_2 \cdot 4H_2O$, $Na_2Fe(SO_4)_2$ and $Li_2Fe(SO_4)_2$, which present attractive electrochemical properties against both lithium and sodium. With a potential of 3.83 V *vs.* Li^+/Li^0, the new *marinite* phase $Li_2Fe(SO_4)_2$ displays the highest potential ever observed for the Fe^{III+}/Fe^{II+} redox couple in a fluorine-free iron-based inorganic compound, only rivaled by the *triplite* form of $LiFeSO_4F$.

Résumé

Les prochaines générations de batteries à ions lithium et sodium seront basées sur le développement de nouveaux matériaux d'électrode positive durables, peu chers et sûrs. Dans ce but, nous avons exploré le monde des minéraux à la recherche de structures présentant les pré-requis pour l'insertion et la désinsertion d'ions alcalins. Nous avons alors entrepris l'étude de sulfates bimétalliques dérivés du minéral *bloedite*, ayant pour formule générale $A_x M(SO_4)_2 \cdot n H_2O$ (A = Li, Na, M = métal de transition 3d, et n = 0, 4). Ces systèmes présentent une cristallochimie riche, montrant des transitions structurales en fonction de la température ainsi qu'avec le départ des molécules d'eau. Les nouvelles structures ont été déterminées en combinant les techniques de diffraction des rayons X, neutrons et électrons. Nous avons également montré que les composés à base de lithium $Li_x M(SO_4)_2$ présentent des propriétés antiferromagnétiques intéressantes, du fait notamment de leurs structures particulières qui permettent seulement des interactions de super-super-échange. Enfin et surtout, nous avons, parmi les composés isolés, identifié trois sulfates à base de fer, à savoir $Na_2Fe(SO_4)_2 \cdot 4H_2O$, $Na_2Fe(SO_4)_2$ et $Li_2Fe(SO_4)_2$, qui présentent des propriétés électrochimiques intéressantes face au lithium et au sodium. Avec un potentiel de 3,83 V *vs.* Li^+/Li^0, la nouvelle phase *marinite* $Li_2Fe(SO_4)_2$ affiche le plus haut potentiel jamais observé pour le couple redox Fe^{III+}/Fe^{II+} dans un composé inorganique à base de fer et dépourvu de fluor, et est en fait seulement dépassé par celui de la forme *triplite* de $LiFeSO_4F$.

It was prepared at the laboratory:

Laboratoire de Réactivité et Chimie des Solides (LRCS)
Université de Picardie Jules Verne (UPJV)
Unité Mixte de Recherche CNRS (UMR 7314)
33, rue Saint Leu
80039 AMIENS cedex
FRANCE

under the supervision of:

Pr. Jean-Marie Tarascon
Dr. Jean-Noël Chotard

and in close collaboration with:

Dr. Gwenaëlle Rousse

Acknowledgements

Table of contents

General introduction

Since the harnessing of fire (*c.a.* -400 000 years ago), the history of the different energy sources used over the time has been intimately linked to technological, economical, social and political changes [1,2]. Muscular power and wood were the only sources of energy at the early ages. During the Antiquity, Greeks and Romans started using the wind force for transportation, and at the middle age, windmills and watermills were developed for grinding and sawing. Later, massive use of wood for constructions and industries (metallurgy, forge, glasswork, *etc.*) led to the rapid deforestation of Europe at the 17th and 18th centuries, which pushed forwards the exploitation of coal. Coal and steam engines, which were invented at the end of the 18th century, would then constitute a breakthrough couple, which marked the beginning of the Industrial Revolution in Occident. Finally, the end of the 19th century witnessed at its turn a considerable acceleration of the industrial development, with on one hand the development of oil refining techniques and the invention of the combustion engine, and on the other hand the beginning of large-scale electricity production and distribution and the design of electric motors. This led to the Second Industrial Revolution and the birth of a new individual mean of transport, the automobile.

Nowadays, we are certainly at our turn at the dawn of a new breakthrough in the field of energy. Most of the energy consumed worldwide is currently supplied by fossil fuels (*i.e.* petroleum, coal and gas) [3]. The massive use of these energy sources is now at the origin of growing economical and political concerns since the resources are limited and are on the way of depletion. Indeed, the world is facing a rapid increase of the energy demand (**Figure G.I.1**), mainly due to the boom of global exchanges, the rapid population growth (the world population has increased by ~13-22% every decade since 1950, and the United Nations projections show no slowdown of this trend for the 21st century [4]), as well as the fast growing of the developing countries, which yearn to have the same standards of living as the developed countries. Combining the growing energy demand with the fears about a possible supply run out has inevitably led to a gradual rise of the fossil fuels' prices since the first oil crisis at the beginning of the 1970s.

Besides, the massive use of these fossil fuels is also behind environmental issues, as their consumption generates high levels of greenhouse gases (**Figure G.I.1**). The scientific community has noticed since the 1950s an important impact of these gases on the climate system, with many changes being unprecedented over decades to millennia: the atmosphere and oceans have warmed, the amounts of snow and ice have diminished, sea level has risen, *etc.* [5]. The exact consequences of these climate changes are still debated, but they will undoubtedly affect the global ecosystem

(**Figure G.I.1**) and are likely to induce repeated extreme weather events (*e.g.* storms, floods, droughts), large population migrations (due to shoreline erosion, coastal flooding and agricultural disruption), *etc.* Limiting climate changes definitively require substantial reductions of greenhouse gas emissions.
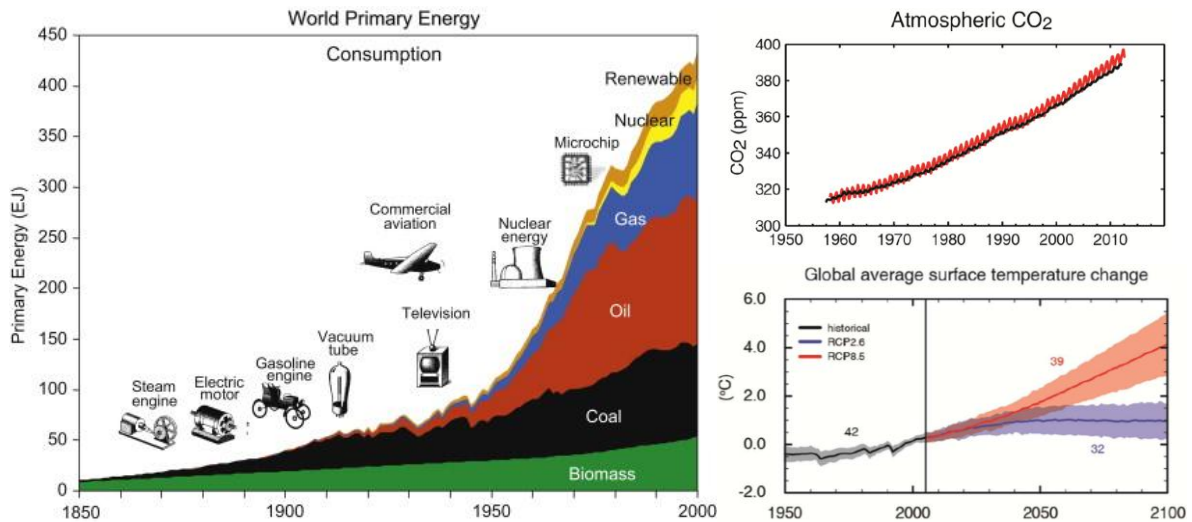
Figure G.I.1: On the left, world energy consumption by fuel type in the period 1850-2000, with indications of the major technological inventions over this period (from **[3]**). On the right, evolution of the global average temperature changes (with optimistic and pessimistic predictions shown in blue and red, respectively) and of the atmospheric CO_2 content since 1950 (from **[5]**).

There is therefore a urge for the development of more abundant, renewable and less contaminating energy sources, such as hydropower, wind and solar energies, biomass and geothermal energy. However, most of these sustainable energies are intermittent, and hence they have to be coupled with storage solutions in order to balance energy supply and demand. Among the various options available, which are discussed in detail in reference **[6]**, electrochemical storage devices (*e.g.* fuel cells, batteries, supercapacitors **[7]**), and in particular batteries, appear as one of the most promising strategies. Batteries convert electric energy into chemical energy when charged and reversibly provide electric energy when discharged with high conversion efficiency and no gas emission. Moreover, these devices can be adapted in shape and size (from few mm^3 to several dozen m^3), and can therefore be considered for both stationary storage applications (*e.g.* load levelling, uninterrupted power supply UPS) and mobile applications (*e.g.* portable electronics, electric and hybrid vehicles).

Several technologies of batteries do exist, the more common being the *lead-acid*, the *nickel-cadmium* (Ni-Cd), the *nickel-metal hydride* (Ni-MH), and the *lithium* batteries. Thanks to their high energy density as compared with other technologies, the lithium-ion batteries have rapidly flooded the market of portable electronics since the beginning of the 1990s, and they are now about to conquer

electric vehicles and mass storage. However, despite 30 years of intensive academic and industrial research and development focused on this technology, there is still place for improvement. Present challenges are two-fold. On one hand, the increasing demand for powering systems of portable electronic devices and zero-emission vehicles stimulates research towards higher energy and higher voltage Li-ion systems, and on the other hand, the development of mass storage required lower-cost batteries, for which expectations are presently placed in a sister-technology: the Na-ion batteries. In both cases, design and optimization of new battery materials are required.

The work presented herein is perfectly in line with this context, as it was aimed at designing new sustainable, low-cost and safe positive electrode materials displaying high voltages for Li- and Na-ion batteries. To achieve this goal, inspired by mineral species, we explored a new family of sulfate compounds having the general formula $A_2M(SO_4)_2 \cdot nH_2O$ (A = alkali, M = 3d transition metal, and n = 0, 4). The present manuscript describes the main results obtained through this study.

This thesis is divided in four chapters:

After giving a few historical elements on the development of the Li-ion and Na-ion batteries, the first chapter proposes an overview of the main families of positive electrode materials that were investigated for these two battery technologies. This will permit to highlight the different strategies explored to increase the energy density stored in the positive electrode, the main concepts brought out from these investigations, as well as to present the main achievements reached at the beginning of our work.

The second chapter describes how we took example from minerals, namely the *bloedite* $Na_2Mg(SO_4)_2 \cdot 4H_2O$ and the *eldfellite* $NaFe(SO_4)_2$, to design novel iron-based electrode materials. We prepared thus four compounds that could cycled *versus* both lithium and sodium and that display relatively high operating potentials of 3.6 V *vs.* Li^+/Li^0 and 3.3-3.4 V *vs.* Na^+/Na^0.

The third chapter focuses on a new series of compounds of general formula $Li_2M(SO_4)_2$ (M = Co, Fe, Mn, Ni, Zn, Mg), which present a rich crystal chemistry. Moreover the iron counterpart shows attractive electrochemical properties, with an elevated potential of 3.83 V *vs.* Li^+/Li^0, which is in fact the highest potential ever reported for the Fe^{III+}/Fe^{II+} redox couple in a fluorine-free inorganic compound. A detail characterization of the lithium extraction/insertion process in this new $Li_2Fe(SO_4)_2$ phase is presented therein.

Besides these attractive electrochemical results, the bimetallic sulfate compounds presented in this thesis can also constitute materials of interest for physical studies, as their structures present peculiar arrangements that solely enable super-super-exchange interactions. The fourth chapter is thus dedicated to a magnetic study of the $Li_2M(SO_4)_2$ phases (M = Co, Fe, Mn, Ni), which all display antiferromagnetic behavior. Moreover, models for their ground-state magnetic structures, determined from neutron powder diffraction, are proposed and confronted to the Goodenough-Kanamori-Anderson rules. The knowledge of these ground-state magnetic structures is indeed of high importance for the battery community, as they are involved in all theoretical calculations (in particular DFT calculations), which are aimed at simulating and understanding the properties of the current electrode materials and eventually establish models capable of predicting better materials for the next generations of batteries. Moreover, an attempt of correlation between the magnetic and electrochemical properties is proposed at the end of the chapter.

As part of conclusion, we summarize the main results achieved within this thesis work, and compare the electrochemical performances of the new sulfate compounds presented herein to other iron-based polyanionic electrode materials that have been studied up to now. Finally, we conclude with a discussion on the few indicators which have been proposed to rationalize the redox potential variations in these compounds with the hope that they help to design new high-performance electrode materials for the next generations of batteries.

Chapter I.   State of the art

This first chapter is aimed at giving an insight of the battery research landscape at the time we started this thesis work towards the search for new sustainable positive electrode materials for the next generations of Li-ion and Na-ion batteries. However, we should precise that we do not pretend to provide here an exhaustive review of the state of the art of this field, and therefore there will be inevitable shortages in this overview.

I.1   Brief overview of the main technologies of batteries

All batteries are based on a same, simple concept. An electrochemical cell consists of two *electrodes*, a *positive* and a *negative* one (often improperly called the *cathode* and the *anode*, respectively), which are separated by an ion-conductive electronic-insulating medium, called *electrolyte* (**Figure I.1**). The two electrodes have different chemical potentials, determined by their respective chemistries (*i.e.* their redox couples). When these electrodes are connected by means of an external circuit, the electrochemical reactions proceed concurrently at both sides, and electrons spontaneously flow from the more negative to the more positive potential. At the same time, electroneutrality is ensured by ion transport through the electrolyte. When one of the redox reactions is finished, the electron flow (the current) stops. If the process can be reversed by applying an external potential difference, then the battery[*] can be recharged. In principle, the two electrodes can be chosen from any favored redox reaction, although only a few dozen of them have been commercially exploited **[8]**.
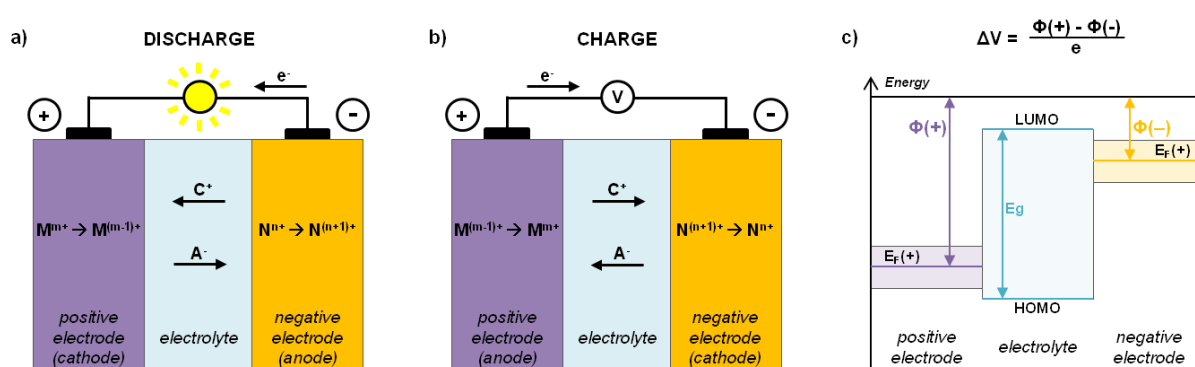
Figure I.1: (a) and (b) Schematic operation principle of an electrochemical cell on discharge and on charge, respectively. (c) Energy diagram of an electrochemical cell.

---

[*] The term "battery" was initially reserved to refer to a stack of cells, connected in series and/or in parallel to provide the required voltage and capacity, respectively; nowadays, it is commonly used to name a single electrochemical cell too.

The most commercialized rechargeable batteries are the *lead-acid*, the *nickel-cadmium* (Ni-Cd), the *nickel-metal hydride* (Ni-MH), and the *lithium* batteries. Selecting the proper technology depends on its intrinsic performances and on the aimed application. The major three criteria are the output voltage (expressed in V), the amount of energy (given in terms of specific capacity, in mAh/kg and mAh/L, or energy density, in Wh/kg or Wh/L)) and the electrical power density (expressed in W/kg or W/L) that the battery needs to provide to the electrical device (**Figure I.2**). Other characteristics have to be taken into account too, and include the size and mass of the battery, its reliability, durability, safety and its cost. In practice, the relative importance of each factor is rather application dependent. For instance, energy density would be the main criterion when choosing a battery for portable or transportation applications, while more importance would be attached to cost in the case of mass storage.
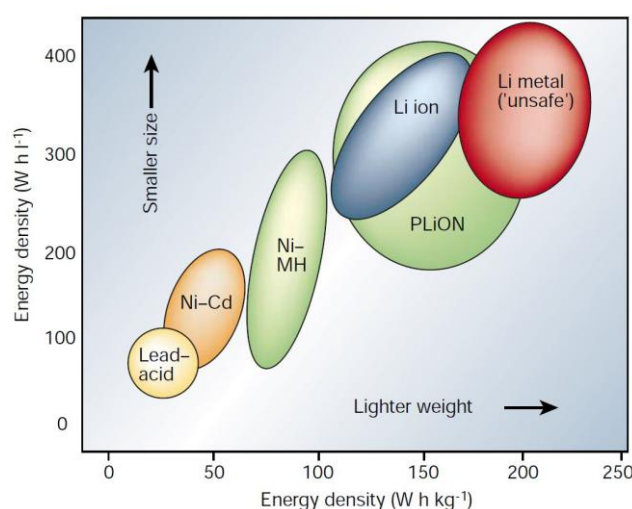
Figure I.2: Comparison of the different battery technologies in terms of volumetric and gravimetric energy density (from **[9]**).

I.1.1   Lead-acid batteries

Lead-acid batteries were the first rechargeable (secondary) batteries to be developed. They were proposed by Gaston Planté in 1860 **[10,11]**, that is sixty years after the very first primary battery, the "pile" of Alessandro Volta **[12]**. In these batteries, both electrodes involve lead redox couples, and the sulfuric-acid-based electrolyte directly takes part in the electrochemical reactions. Being cheap and reliable, they are still the most commonly used rechargeable batteries, in particular for automobile SLI systems (Starting, Lightning and Ignition).

I.1.2   Nickel-based technologies

Nickel-cadmium batteries, which have been developed from the turn of the 19th century **[13,14]**, present more power but are more expensive. They are mainly used in transportation (aeronautic), telecommunications and uninterrupted power supply (UPS) devices. The world's biggest battery,

installed in Fairbanks (Alaska, USA) is based on this technology and can provide 26 MW of standby power for 15 minutes, *i.e.* the time needed to start up a standard backup generator **[15]**. For smaller applications, the Ni-Cd batteries have been progressively replaced by Ni-MH batteries since the beginning of the 1990s **[16]**. These latter offer indeed higher performances and avoid the use of toxic cadmium. They are also employed to power hybrid electric vehicles (*e.g.* Toyota Prius).

I.1.3   High-temperature batteries

In the 1960s, the quest for higher energy density batteries turned the research focus to alkali metal negative electrodes. The motivation for employing lithium or sodium indeed relied on the fact that they are among the lightest elements (M_{Li} = 6.941 g/mol and M_{Na} = 22.990 g/mol) and the most electropositive ones (-3.045 V *vs.* SHE* for Li^+/Li^0 and -2.714 V *vs.* SHE for Na^+/Na^0). However, given their instability with water, the use of alkali metals required moving towards non-aqueous electrolytes, which would add some complexity since electrochemistry in these media were much less developed. Inspired by the recent progress made at that time on solid electrolytes for high temperature fuel cells **[17]**, the Ford Motor Company developed the first prototypes of sodium cells, which consisted of molten sulfur and molten sodium at the positive and the negative electrodes, respectively, separated by the so-called β''-alumina solid electrolyte, and were operated at around 300°C **[18,19]**. Large-size Na/S batteries have been produced and installed in particular in Japan, where there are still employed for large-scale stationary storage **[20]**. At the beginning of the 1980s, a derivative technology, a molten-salt battery (Na // β''-Al_2O_3 // $NiCl_2$) called ZEBRA, was proposed by Coetzer and Nolte **[21]**. It has been later developed and commercialized by a Swiss company MES-DEA for automotive and stationary storage applications **[22,23]**, but have remained a niche technology.

Following the same model, the first lithium rechargeable batteries were proposed at Argonne National Laboratory (ANL) in the late 1960s **[24]**. They used molten lithium and molten sulfur as the two electrodes with molten salts (LiCl-KCl) as the electrolyte and were operated at around 450°C. Because of difficulties with liquid electrode containment, the lithium and sulfur active materials were replaced by a solid lithium-aluminum alloy anode and a solid metal sulfide cathode (in particular the low cost FeS and FeS_2) **[25,26]**. However, development of this technology eventually ceased around 1990 due to corrosion, temperature and other insurmountable issues.

---

* SHE: Standard Hydrogen Electrode

I.1.4   The first room-temperature lithium batteries

The development of rechargeable lithium batteries operating at room temperature and using organic electrolytes was more successful. It was made possible by the discovery, at the beginning of the 1970s, of inorganic compounds which reacted reversibly with alkali cations according to intercalation reactions **[27,28]**. The feasibility of a lithium-based non-aqueous rechargeable cell was first demonstrated by Whittingham (Exxon Research and Engineering Co.), who employed titanium sulfide TiS_2 as the positive electrode and lithium metal as the negative one **[29–34]**. Consecutively to this first achievement, several other chalcogenides were investigated as positive electrode materials in lithium-based cells (*e.g.* FeS_2, MoS_2, $NiPS_3$) **[35–43]**, and soon researchers started considering also oxide compounds (*e.g.* V_2O_5, MoO_3, $LiCoO_2$), which displayed higher redox potentials **[31,44–51]**.

At the beginning of the 1980s, Moli Energy commercialized the first rechargeable lithium battery using *molybdenite* MoS_2 as a positive electrode and metallic lithium as the negative one **[39,40]**. However, these *lithium-metal batteries* had soon to be withdrawn from sale because of safety issues. Indeed, the combination of a lithium metal anode with a liquid electrolyte resulted in a non-uniform plating of the lithium upon cycling, and the growth of uneven dendrites could cause short-circuits and explosion hazards. To circumvent this issue, two strategies were pursued, in which either the negative electrode or the electrolyte was modified **[9]**. The first alternative would give birth to the so-called *lithium-ion batteries* while the second approach would led to the *lithium polymer batteries* (**Figure I.3**).
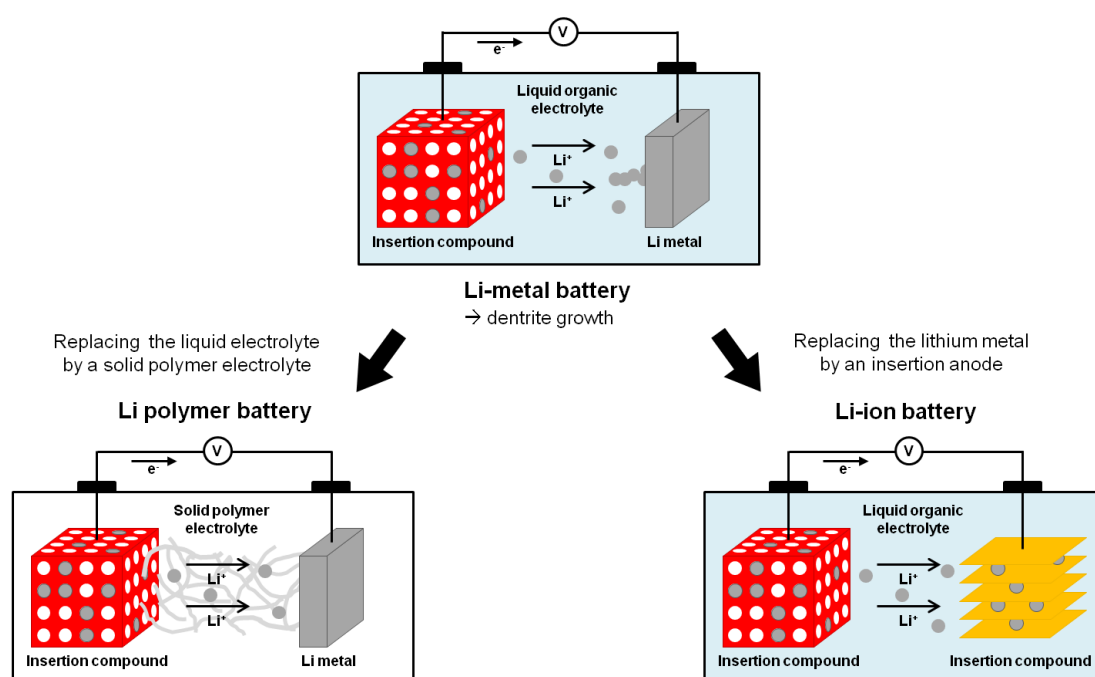
Figure I.3: Schematic representations of a lithium-metal battery, a lithium polymer battery and a lithium-ion battery.

I.1.5   Lithium-ion batteries

The first attempts to prevent the growth of dendrites consisted in replacing the metallic lithium anode by lithium alloys **[52–56]**. However, these electrodes survived only a limited number of cycles owing to extreme volume changes during operation. This option was put aside for a few decades prior the arrival of electrode nanostructuring, which enabled to bypass such volume issues.

Next, the use of a second insertion material for the negative electrode was envisaged **[57]**. In fact, the concept of *rocking-chair batteries* (in which cations "rock" between two host electrodes) had been previously used in nickel metal hydride (Ni-MH) cells; it was implemented for the first time in lithium cells by Murphy (rutile MO_2) **[58]** and by Scrosati (Li_xWO_2 // Li_xTiS_2 2V) **[59–61]**. Note that nowadays the term of *rocking-chair batteries* is barely used to refer to such lithium batteries having two-insertion materials at both electrode, since they are more commonly called *Li-ion batteries*.

At that time, graphite intercalation compounds (GIC), which had been used as negative electrode in batteries for several decades **[62–65]**, were also studied as possible lithium host materials **[66–69]**. However, their potential use as a replacement of the lithium metal in commercial cells was long disregarded, because a pre-lithiation of the anode was required before being assembled against the conventional TiS_2 or MoS_2 cathode materials. In the mid-1980s, Yoshino (Asahi Kasei Co.) eventually bypassed this additional step by employing the carbonaceous material against a lithium-containing cathode material **[70]**, namely $LiCoO_2$ (which had been previously discovered by Goodenough at the beginning of the decade **[48–51]**). Few years later, such a graphite // $LiCoO_2$ cell would become the first commercialized Li-ion batteries (SONY in 1991 **[71–74]**, followed by A&T battery – an Asahi Kasei and Toshiba joint-venture company – in 1992 **[75,76]**). This technology presents an average potential of 3.6 V (*i.e.* three times that of classical alkaline batteries) and reaches energy densities as high as 120-150 Wh/kg (*i.e.* two or three times those of the usual Ni-Cd batteries), and has now been used for more than 20 years to power high-performance portable electronic devices.

I.1.6   Lithium polymer batteries

The second alternative to prevent the formation of dendrites at the lithium-metal anode was proposed by Armand in 1979 and involved the replacement of the liquid electrolyte by a dry one: a solid solution of a lithium salt into polyethylene oxide **[77–79]**, which gave birth to the so-called *lithium solid-polymer electrolyte (Li-SPE) batteries*, or more simply *lithium-metal polymer batteries*. Such batteries (Li-metal anode // Li-salt in PEO // $LiFePO_4$ cathode) are presently produced at an industrial scale by Batscap **[80]** and power the Bluecar of Bolloré **[81]**, which has recently encountered a great success through the Paris Autolib car-sharing program. However, this technology is restricted to large systems (electric vehicles or stationary storage) and is hardly

transferable to portable devices, as it requires to be maintained at relatively high temperatures (60-90°C) for both operation and storage.

Concurrently to Armand, several groups tried to develop a *lithium hybrid polymer electrolyte (Li-HPE) battery* **[82–84]**, in which the electrolyte would be a polymer matrix swollen with liquid solvent and a lithium salt. Such batteries have been developed by the companies Valence Technologies and Danionics but were never materialized at industrial scale because lithium metal dendrites were still an issue.

Later, at the beginning of the 1990s, with the aim of combining the recent commercial success of liquid Li-ion batteries with the manufacturing advantages presented by the polymer technology, Bellcore researchers introduced a polymeric electrolyte in a Li-ion system (*i.e.* a battery with intercalation compounds at both electrodes, no lithium metal at the anode) **[85–88]**. These all-plastic, thin-film and flexible batteries, so-called *plastic Li-ion (PLiON) batteries*, have been commercialized by Valence Technology and others since 1999 **[89]**.
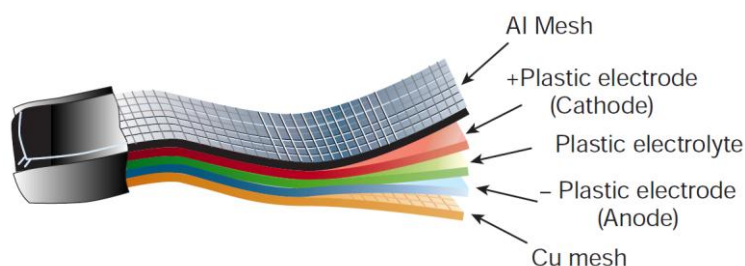
Figure I.4: Schematic drawing of a PLiON cell (adapted from **[9]**).

Finally, more recently, a new generation of bonded-liquid electrolyte Li-ion cells have been developed, in which the electrolyte is a gel-coated microporous poly-olefin separator bonded to the electrodes. Confusingly called *Li-ion polymer batteries* or even simply *lithium polymer batteries*, they are currently commercialized (*e.g.* by Danionics) and are integrated in small electronic devices (*e.g.* the new range of Apple portable products).

I.1.7   Sodium-ion batteries

After the success of the Li-ion batteries, new expectations have been placed since the turn of the 2010s in the development of a Na-ion technology, which is believed to provide more sustainable batteries at a lower cost.

In fact, the concept of Na-ion battery is far from being new, since sodium intercalation chemistry **[27,28]** was studied in tandem with the lithium one in the 1970s and 1980s **[36,90–94]**. However research on room-temperature sodium batteries has been almost abandoned after the boom of

Li-ion batteries in the 1990s-2000s, and published reports on the sodium technology during this period are therefore very limited as compared to those reporting on the lithium one [95–100].

Despite offering lower energy densities than the lithium-ion, there has been a resurgent interest in Na-ion batteries in recent years [8,101–105] after the emergence of some concerns about lithium supplies. Although current lithium main producers (Talison in Australia, SQM and Rockwood Lithium in Chile, FMC in Argentina, Tianqi Lithium in China) assure that they possess enough resources to provide the lithium needed for the launch of the electrical vehicle for the next 70 years [106,107], there are speculations about lithium prices in front of the increasing demand predicted for the next few years and because most of the untapped lithium is localized in remote or politically sensitive area (Bolivia in particular [108]). Sodium being far more abundant and well distributed on the Earth than lithium (**Table I.1**), it is much less prone to become a strategic resource and suffer from geopolitical issues than lithium does. Moreover, replacing lithium by sodium enables to use aluminum current collectors (instead of cupper ones) and thereby further reduce the battery cost.

Table I.1: Natural abundance and world production of lithium and sodium (from [109,110]), and some physicochemical properties of these alkali metals.

	Li	Na
Abundance in Earth crust	20 ppm	23000 ppm
Average world production	24 600 tons	281 800 000 tons
BGS Relative Supply Risk Index in 2012[*]	6.7	*n.a.*
Specific capacity	3.86 Ah/g	1.16 Ah/g
A^+/A^0 redox potential	-3.045 V *vs.* SHE	-2.714 V *vs.* SHE
Ionic radius [111]	0.76 Å	1.02 Å

---

[*] The Relative Supply Risk Index is given on a scale from 1 (very low risk) to 10 (very high risk). It results from an evaluation based on several factors that might affect the availability of a chemical element, which includes the natural abundance in the Earth's crust, the location of current production and reserves, the political stability of those locations, the recyclability and the substitutability [109].

I.2   Positive electrode materials for Li- and Na-ion batteries

Contrary to other battery technologies, lithium batteries rely on a rich and versatile chemistry, with a large range of materials suitable for the negative and positive electrodes (**Figure I.5**). However, as it can be noticed from this figure, the main factor limiting the energy density of these batteries has been the lack of high-capacity positive electrode materials [9]. Therefore, most of the work done for the last 30 years has been dedicated to the search for new cathode materials displaying better performances.
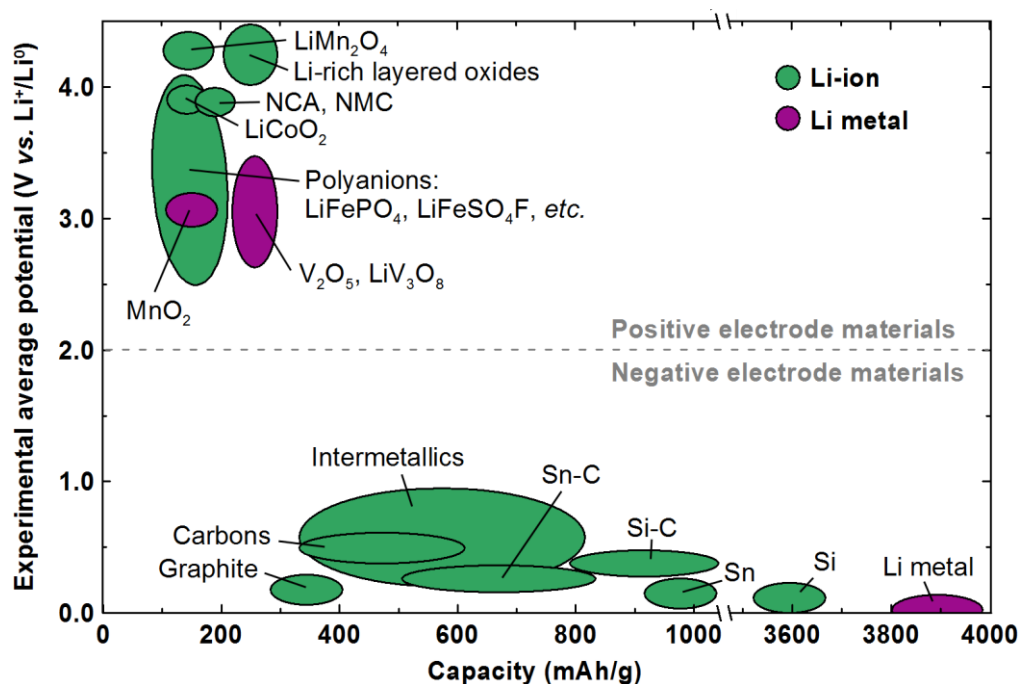
Figure I.5: Voltage *versus* capacity of some positive and negative electrode materials presently used or under considerations for the rechargeable lithium-based cells (adapted from [9]).

The ideal positive electrode material would be based on a redox couple having a high potential, but compatible with the stability window of current electrolytes (*i.e.* < 4.8 V *vs.* Li^+/Li^0; see **Figure I.1.c**), and it would present a high specific capacity, which is proportional to the number of electrons exchanged per formula unit and inversely proportional to the molar mass of the compound. However, these two points are not the only requirements that a positive electrode should comply with. It should also react with lithium according to a highly-reversible insertion/deinsertion mechanism, so that it can offer good capacity retention. This reversibility is mainly related to structural or morphological modifications when Li^+ ions are removed from and uptaken into the compound. The electrode material should also be both a good ionic and electronic conductor, since these two properties are the main limiting kinetic factors for the redox reaction (more than charge transfer) and thus determine the charge/discharge rate capabilities of the electrode. Finally, it should contain lithium to be easily implemented in Li-ion batteries, and other constituents should be

preferably chosen among abundant, low-cost and non-toxic elements for safety and sustainability reasons.

In fact, most of the current positive electrode are based on cobalt and/or nickel, and these metals are rather scarce, expensive, and not environmentally and health benign (**Table I.2**). Researchers are therefore appealed to design electrode materials based on more sustainable elements, with iron and manganese being the more attractive ones (**Table I.2**). We should mention here that in the last few years, several electrode materials based on vanadium have been studied and have shown very interesting properties, with in particular the possibility of working with several oxidation states and making symmetrical cells with the same material at both electrodes. However the feasibility of integrating them into commercial batteries is still uncertain due to relative low competitiveness as compared with cobalt-, nickel- or manganese-based materials, and also because of the toxicity of vanadium (in particular at the oxidation state +V).

Since the first lithium battery of Whittingham, who used TiS_2 at the cathode side **[29–34]**, numerous positive electrode materials have been explored. After the sulfides, the battery community has mainly focused on two types of compounds, namely the oxides and the polyanions. Giving an exhaustive review of all these compounds is beyond the scope of this thesis (for that purpose, many review papers are available **[9,105,112–117]**), but the next part of this chapter intends to provide a small overview of the main families of electrode materials that have been studied for the last 30 years, with a focus on the strategies drawn for the design of high-energy electrode materials as well as on the relations that can exist between the compositions and structures of these compounds and their electrochemical properties.

Table I.2: Natural abundance, world production and indicators of toxicity for cobalt, nickel, iron, manganese, and vanadium (figures are taken from **[109,110,118,119]**).

	Co	Ni	Fe	Mn	V
Abundance in Earth crust	20 ppm	80 ppm	41000 ppm	950 ppm	160 ppm
World production in 2011 (tons)	151 000	1 826 000	3 012 000 000	47 300 000	67 000
BGS Relative Supply Risk Index in 2012[*]	7.6	6.2	5.2	5.7	6.7
Indicative metal prices in Sept. 2013	20 k€/ton	10 k€/ton	0.1 k€/ton	1.6 k€/ton	19 k€/ton
Recommended exposure limit (REL) set by the U.S. National Institute for Occupational Satety and Health (NIOSH)	0.05 mg/m^3	0.015 mg/m^3	1 mg/m^3	1 mg/m^3	0.05 mg/m^3

---

[*] See note * page 11.

Positive electrode materials for Na-ion batteries are also discussed. Indeed, as Na-ion technology works in a similar way to the Li-ion one, the knowledge and experience acquired for the latter has been leveraged to facilitate a rapid development of the former. As a result, new battery materials have been almost systematically evaluated for both technologies for the last few years. Despite the larger ionic radius of Na^+ as compared to Li^+ (**Table I.1** page 11), sodium-based compounds frequently adopt similar structures to that of their lithium counterpart. However, fundamental differences have been observed between lithium and sodium insertion in several materials **[120]**. One of the most convincing example may be the fact that the amount of sodium intercalated into graphite does not exceed 40 mAh/g **[121]**, while graphite is the negative electrode of most commercial Li-ion batteries (with practical capacities of about 300 mAh/g of C); presently the most promising negative electrodes for Na-ion batteries are in fact hard carbons. We can also mention that, for a same host compound, differences between Li and Na have also been observed in insertion mechanisms (successive phase transitions are common in the case of sodium), ionic diffusion properties (Na^+ migration barriers may be lower than that for Li^+ in layered structures), *etc*. Finally, we should note that some sodium compounds have no stable lithium analogues, which offers the possibility of finding novel intercalation structures, which could not be explored for lithium technology. We attempt to illustrate the majority of these points within the examples presented hereafter.

I.2.1   The first electrode material for lithium batteries: titanium sulfide TiS_2

As discussed earlier, the very first lithium battery used titanium sulfide at the positive electrode **[29–34]**. This compound presents indeed a favorable layered structure for lithium insertion (**Figure I.6.a**), which allows the formation of a solid solution over the entire composition range Li_xTiS_2 ($0 \leq x \leq 1$).
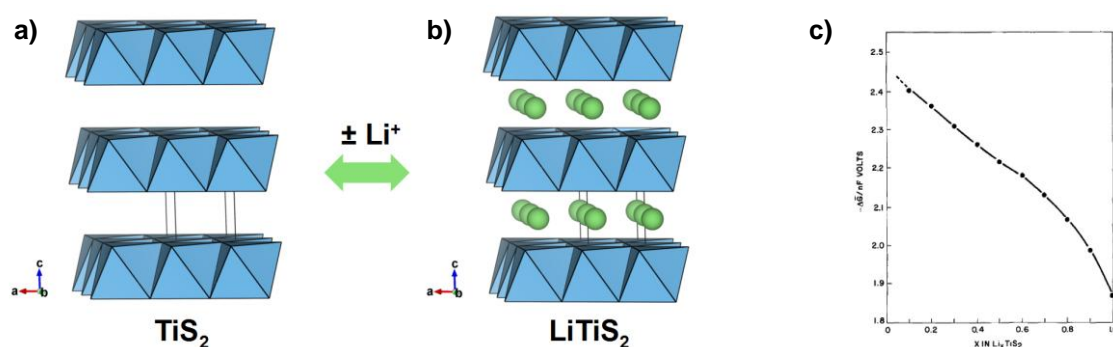
Figure I.6: (a) and (b) Representation of the structures of the end members of the solid-solution Li_xTiS_2 ($0 \leq x \leq 1$): TiS_2 and $LiTiS_2$, respectively. TiS_6 octahedra are displayed in blue and green ball represent the lithium cations. (c) Open circuit voltage (OCV) of the Li // TiS_2 cell as a function of the amount of lithium inserted into positive electrode material (*x*) (from **[31]**).

Its structure is built on a hexagonal close packing (*hcp*) array of sulfur ions, with half of the octahedral sites filled with titanium cations. These TiS_6 octahedra are arranged into layers parallel to the (001) plane, the $(TiS_2)_n$ sheets being maintained together through Van der Waals interactions. When discharging the Li // TiS_2 cell, lithium ions intercalate in between these layers (**Figure I.6.b**). The absence of phase transition upon this process favors its reversibility, as no extra energy expense is needed for the nucleation of new phases or for important structural rearrangement of the host material. The evolution of the potential of the electrode material *versus* the Li^+/Li^0 reference redox couple upon lithium insertion (*x*) is generally presented with an electrochemical curve as shown in **Figure I.6.c**.

Titanium disulfide was also tested against sodium **[27,122,123]**, but in this case Na^+ insertion is accompanied by several phase changes due to favored trigonal prismatic coordination for intermediate Na^+ content and octahedral coordination for Na/Ti ratios close to one.

I.2.2   Lithium transition-metal oxides

Following the studies on lithium intercalation into sulfides, researches rapidly turned towards oxides, which were expected to present higher redox potentials. Indeed, the replacement of sulfur by the more electronegative oxygen enhances the ionic character of the $M–X$ bond (M = transition metal and X = S, O, *etc.*), *i.e.* stabilizes the anti-bonding orbitals of the metal M, which translates to an increase of the potential of the redox couple $M^{n+}/M^{(n-1)+}$.

I.2.2.1   Layered oxides

As aforementioned, Goodenough demonstrated reversible lithium extraction/insertion in $LiCoO_2$ at the beginning of the 1980s **[48–51]**. This compound crystallizes in the same layered structure as α-$NaFeO_2$ (**Figure I.7.a**). It is built on a cubic close packing (*ccp*, or face-centered cubic packing, *fcc*) array of oxide ions, in which the transition metal (III+) and lithium (I+) cations occupy all octahedral sites in alternate sheets. Conversely to the layered structure of TiS_2, in which the TiS_6 octahedra are stacked directly one on the top of the other, in the α-$NaFeO_2$-type structure the $(MO_2)_n$ layers are slightly staggered to minimize ionic interactions.

Although the full removal of the lithium is feasible, Li_xCoO_2 undergoes a series of structural evolutions above 4.2 V *vs.* Li^+/Li^0 (*i.e.* ~ half delithiation) **[124–126]**. Some of these processes may be poorly reversible and some of the new phases are metastable. Therefore, for lifetime and safety motivations the delithiation is limited to 0.5 lithium (**Figure I.7.b**), thereby reducing the theoretical capacity to 137 mAh/g. Yet, $LiCoO_2$ has been the main material used as positive electrode in commercial Li-ion batteries for many years.
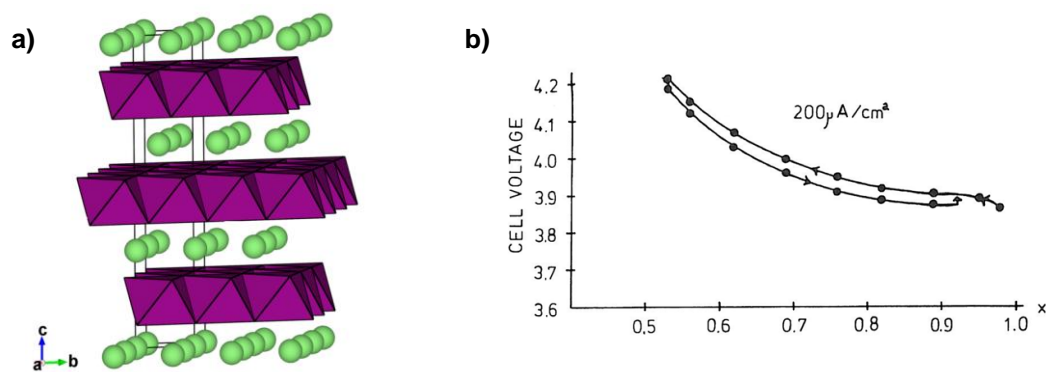
Figure I.7: (a) Representation of the layered structure of $LiCoO_2$. CoO_6 octahedra are displayed in purple and lithium are represented as green balls. (b) Typical charge/discharge curve obtained for a Li // Li_xCoO_2 cell (from **[48]**).

Following the discovery of $LiCoO_2$, extensive work was done in order to identify other layered oxides suitable as positive electrode materials. Being isostructural to $LiCoO_2$, $LiNiO_2$ was soon considered as a potential contender **[127–129]**. However, its electrochemical performances were poorer than expected because of the inevitable presence of nickel cations in the lithium layers. Moreover, the delithiated phases Li_xNiO_2 were found to be prone to oxygen release, which causes security issues when employed with organic solvents. From cost and sustainable points of view (*vide supra*, **Table I.2** page 13), cathodes based on elements such as manganese or iron were desirable. However, although numerous polymorphs of $LiFeO_2$ and diverse syntheses have been investigated, none of them was found to be successful **[130–138]**. Research on $LiMnO_2$ has been slightly more fruitful, but the layered lithium manganese oxides are not thermodynamically stable and convert easily upon cycling to the *spinel* structure (*cf.* § I.2.2.2 page 17) **[139–141]**.

Besides the studies of each individual $LiMO_2$ (M = Co, Ni, Mn) compound, a huge amount of papers and patents have been produced on metal substitutions in these layered phases. The approach consisted in stabilizing the layered structure, using either inert cations (*e.g.* Al, Ga, Mg) **[142–144]** or a combination of transition metals (*e.g.* Co, Ni, Mn, Ti). Noticeable progresses include the compounds $LiCo_{1-x}Ni_xO_2$ **[145–150]**, $LiNi_{1-x-y}Co_xAl_yO_2$ (in particular the composition x = 0.15 & y = 0.05, called NCA) **[151–156]**, or else $LiNi_{1-x-y}Mn_xCo_yO_2$ (in particular with x = y = ⅓, named NMC) **[157–162]**. In these compounds, the cobalt increases the electronic conductivity and the layerness of the structure, the small amount of nickel found in the lithium layer helps to stabilize the structure without being detrimental for the lithium diffusion, while electrochemically inactive cations (Al^{III+}, Mn^{IV+}) prevent full lithium removal and thus the collapsing of the structure. Metal substitution in layered compounds therefore lead to electrode material with good stability properties and high reversible capacities (up to 200 mAh/g).

Given that the large amount of work done on layered LiMO$_2$ compounds, it is no surprise that similar layered phases Na$_x$MO$_2$ (M = Co, Ni, Mn, Fe, V, Cr, *etc.*) have also been investigated for sodium intercalation electrodes **[163–173]**. In a general way, Na$_x$MO$_2$ systems form layered structures more easily than the lithium equivalents due to the larger ionic size difference between Na and transition metals **[174]**. These phases exist as several polytypes, which differ in the stacking of the oxygen layers (*e.g.* ABCABC, ABBA, ABBCCA). They are classified using a notation initially proposed by Delmas *et al.* **[163]**, in which "O*n"* and "P*n"* (*n* = 1, 2, 3, *etc.*) refer to structures having the alkali ions in octahedral and trigonal prismatic coordinations, respectively, while *n* indicates the number of sodium layers per unit cell. All Na$_x$MO$_2$ phases reversibly intercalate and deintercalate sodium upon electrochemical cycling, but the manganese and cobalt oxides have been the most studied. They generally show multistep voltage-composition curves with several very pronounced but reversible biphasic and single-phase domains **[171]**, due to Na-vacancy ordering and/or gliding of the oxygen planes. Finally, it is also interesting to note that half-desodiation of NaMnO$_2$ does not result in conversion to a *spinel* phase contrary to what happens with Li$_{0.5}$MnO$_2$.
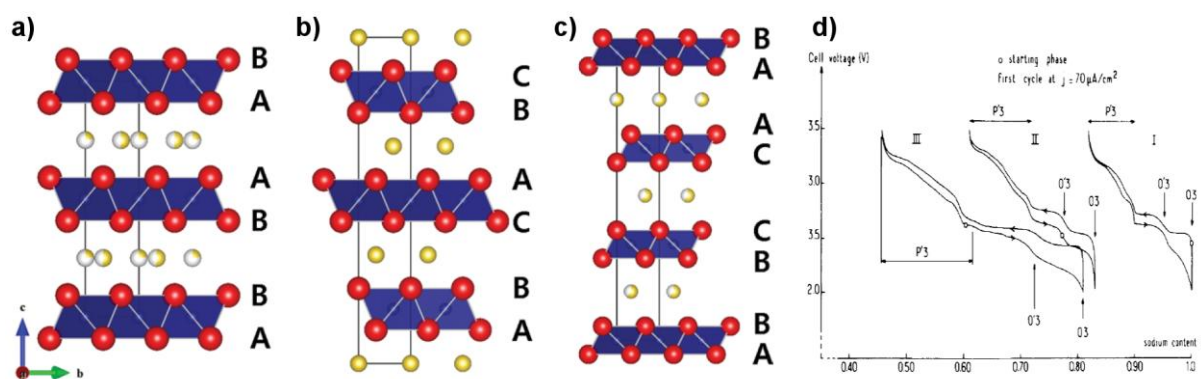
Figure I.8: Structures of P2-Na$_x$CoO$_2$, O3-Na$_x$CoO$_2$, P3-Na$_x$CoO$_2$ (from **[102]**) and electrochemical behavior of Na$_x$CoO$_2$ phases with P'3, O'3 and O3 packings (from **[91]**).

I.2.2.2   **Spinel *manganese oxide***

In parallel to layered oxides, Thackeray and Goodenough envisaged the use of tridimentional *spinel* structures, first with Fe$_3$O$_4$ **[175]** and then with LiMn$_2$O$_4$ **[176,177]**. The manganese compound would be then extensively developed by Bellcore labs in the 1980s and 1990s.

The LiMn$_2$O$_4$ *spinel* structure (named after the eponymous mineral MgAl$_2$O$_4$) is based on a *ccp* oxygen array, in which half of the octahedral sites are occupied by manganese and ⅛ of the tetrahedral sites by lithium atoms. The MnO$_6$ octahedra are connected to each other through their edges, while the LiO$_4$ tetrahedra share their four vertices with MnO$_6$ octahedra and their four faces with vacant octahedral sites, thus forming a three-dimensional network of conduction path for lithium diffusion (**Figure I.9.a**).

a)

b)
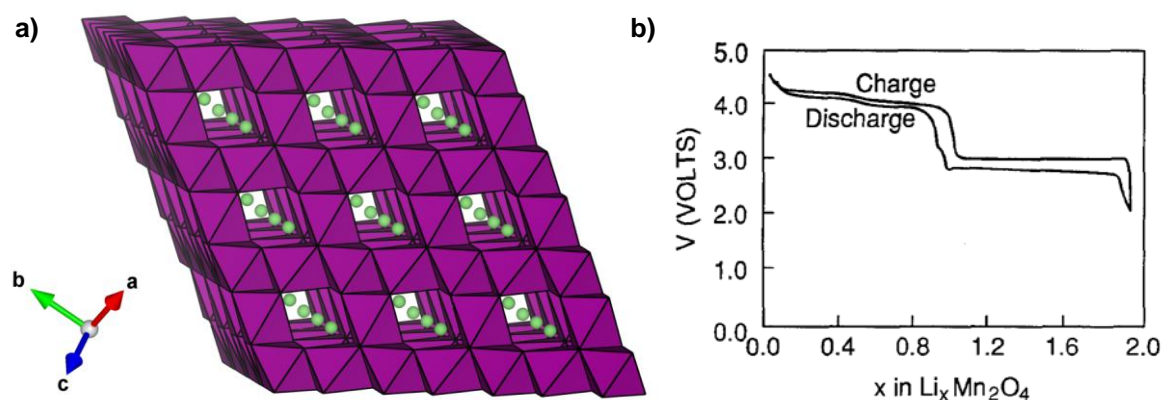
Figure I.9: (a) Structure of the *spinel* LiMn$_2$O$_4$. MnO$_6$ octahedra are displayed in purple and lithium atoms are represented as green balls. (b) Typical charge/discharge curve of a Li // Li$_x$Mn$_2$O$_4$ cell (from **[178]**).

Given that LiMn$_2$O$_4$ possesses one lithium per formula unit, with half of the manganese in the oxidation state +III and the other half in the oxidation state +IV, this amphoteric electrode material can be either oxidized to λ-MnO$_2$ with a potential centered around 4.1 V *vs.* Li$^+$/Li^0, or reduced to Li$_2$Mn$_2$O$_4$ with a plateau at ~3 V *vs.* Li$^+$/Li^0 (**Figure I.9.b**). However, in Li-ion batteries, in which the cathode is the sole source of lithium, only the upper plateau can be used, reducing to 148 mAh/g the useful capacity of the electrode material. One should note even so that *spinels* can be prepared with an excess of lithium (Li$_{1+x}$Mn$_2$O$_4$), so that the positive electrode acts as a reservoir to compensate irreversible lithium loss in the cell **[179]**.

Despite its specific capacity slightly lower than that of layered oxides, LiMn$_2$O$_4$ presents numerous advantages, including a high voltage, a good rate capability, and the non-toxicity and relative low cost of manganese, for which it has been long considered as a material of choice for high-power applications (*e.g.* electric vehicles). However, after more than 20 years of development, scientists still face stability issues when cycling at elevated temperatures (*i.e.* ~50°C). LiMn$_2$O$_4$ was indeed found to slowly dissolve in the organic electrolytes conventionally used in Li-ion batteries, and the resulting manganese contamination of the anode leads to severe capacity fade. Several reviews **[180–183]** describe in details these issues and the different solutions that have been proposed, which include improvement of the material stability *via* lithium excess **[179,184]** or metal substitution **[178,185–188]**, blending with layered materials **[189]**, or else chemical modification of the electrolyte (to prevent formation of HF, which favors the dissolution of the electrode material) **[190,191]**. Thanks to these efforts LiMn$_2$O$_4$ is, with LiFePO$_4$ (*cf.* § I.2.3.2 page 23), among the most used positive electrode materials for electric vehicles applications (*e.g.* Renault-Nissan).

I.2.2.3   *Li-rich layered oxides*

Pursuing the search for a layered lithium manganese oxide electrode material, interests were turned to Li_2MnO_3 at the turn of the 21st century. This compound presents a layered structure similar to the one of $LiCoO_2$, but with ¼ of the lithium atoms of Li_2MnO_3 lying in the transition metal sheet (Li_2MnO_3 can therefore be formulated as $Li[Li_{1/3}Mn_{2/3}]O_2$) **[192–194]** (**Figure I.10**). This compound is in fact nearly electrochemically inert since all the manganese is in the oxidation state +IV (*i.e.* the material cannot be oxidized) and all the octahedral sites are fully occupied in the lithium layer (*i.e.* it cannot be reduced). However, an electroactive $Li_{2-x}MnO_{3-x/2}$ could be prepared from Li_2O-leaching of Li_2MnO_3, which was induced either chemically by acid treatment **[195–197]** or electrochemically by charging the electrode up to 4.5 V *vs.* Li^+/Li^0 **[198,199]**.
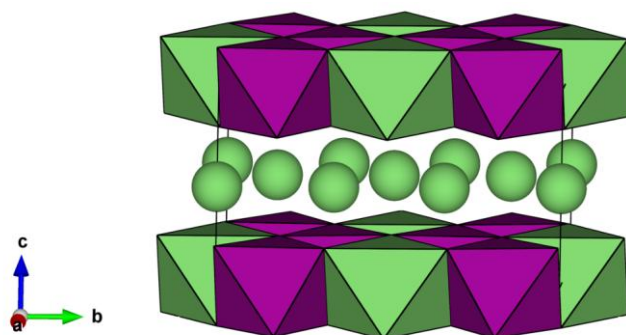
Figure I.10: Structure of Li_2MnO_3 (monoclinic, *C*2/*m*). MnO_6 and LiO_6 octahedra in the transition metal layer are displayed in purple and green, respectively. Li cations in the lithium layer are shown as green balls.

Besides, pioneering works involving partial metal substitution with cobalt, chromium and nickel in the Li/Mn layer of Li_2MnO_3 **[200–204]** led to the development of new composite cathode materials of the type $xLi_2MnO_3 \cdot (1-x)LiMO_2$, where $LiMO_2$ may refer to layered compounds such as $LiCo_{1/3}Ni_{1/3}Mn_{1/3}O_2$ **[205–210]** but also to *spinel* $LiMn_2O_4$ **[208,211]**. These compounds were reported to exhibit specific capacities greater than 250 mAh/g (*i.e.* exceeding the one of the classical layered electrodes), and are therefore currently receiving worldwide attention for the next generation of Li-ion batteries. Although many research groups can reproduce these outstanding performances, numerous ambiguities remain concerning the chemical nature of the compounds (*i.e.* whether they form short-range ordered domains**[206]** or homogeneous solid-solutions **[203,212]**), as well as the understanding of the exact oxidation/reduction mechanisms. However, our group recently demonstrated that this extra-capacity results from both cationic ($M^{n+} \leftrightarrow M^{(n+1)+}$) and anionic ($O^{2-} \leftrightarrow O_2^{2-}$) reversible redox processes **[213–217]**, hence opening a new road to the search of high capacity electrodes.

I.2.3   Polyanions

Beside oxides, compounds containing polyanion groups (with the general formula $(XO_z)^{n-}$, where X = Mo, W, S, P, Si, B, *etc*.) have been studied as positive electrode materials. The main advantage of these compounds resides in the fact that, for a given $M^{n+}/M^{(n-1)+}$ redox couple, they present higher redox potentials than oxides (due to the *inductive effect*, which will be discussed hereafter), and thereby, they give rise to attractive potentials for the Fe^{III+}/Fe^{II+} redox couple (between 2.8 and 4 V *vs.* Li^+/Li^0 as compared to ~2.5 V for iron oxides). Moreover, polyanionic compounds present strong and stable frameworks, which are essential for extensive cycling and safety issues, and exhibit a large variety of crystal structures, with great versatility towards cation and anion substitutions for a given structural type. Therefore, they are ideal compounds to understand the structure-properties relations and to design new electrode materials made up of cheap and abundant elements (with iron in particular). However, it should also be noticed that polyanionic compounds suffer from two main drawbacks: *(i)* limited gravimetric capacities because of the weight penalty arising from the presence of heavy polyanionic groups, and *(ii)* poor intrinsic electronic conductivities because of the lack of direct *M-M* or *M*-O-*M* interactions for electronic delocalization.

Once again, giving an exhaustive list of the various families of compounds studied as electrode materials is not the aim of this work. Numerous families of polyanions $(XO_z)^{n-}$ and several redox couples (*M* = Fe, Mn, Co, Ni, V, Ti, *etc.*) have been investigated for both lithium and sodium insertion electrode materials. The following pages will be mostly focused on iron-based compounds, as they are the materials showing the best compromise between performances, price and sustainability, as discussed earlier (*vide supra*, **Table I.2** page 13). The reader is invited to consult various review papers **[8,101–105,114–117]** for a wider outline of the different polyanionic compounds that have already been explored as electrode materials.

I.2.3.1   *The NASICON-type compounds* $A_xM_2(XO_4)_3$

In the middle of the 1980s, the groups of Torardi and Delmas were the first ones to demonstrate the feasibility of reversible alkali (Li and Na) insertion into the tridimensional frameworks of polyanionic compounds, with the NASICON phases $Fe_2(MoO_4)_3$ **[218,219]** and $(Li,Na)Ti_2(PO_4)_3$ **[95,220]**, respectively. Subsequently, Goodenough *et al.* extended this study to other NASICON-type compounds, namely $Fe_2(WO_4)_3$ and $Fe_2(SO_4)_3$ **[221–223]**. Whereas the Fe^{III+}/Fe^{II+} redox couple in a simple oxide like Fe_2O_3 was known to generally operate at a voltage around 2.5 V *vs.* Li^+/Li^0, they surprisingly found high potentials of 3.0 V for $Fe_2(MoO_4)_3$ and $Fe_2(WO_4)_3$ **[221]**, and even 3.6 V for both polymorphs of $Fe_2(SO_4)_3$ **[222–224]** (**Figure I.11**).
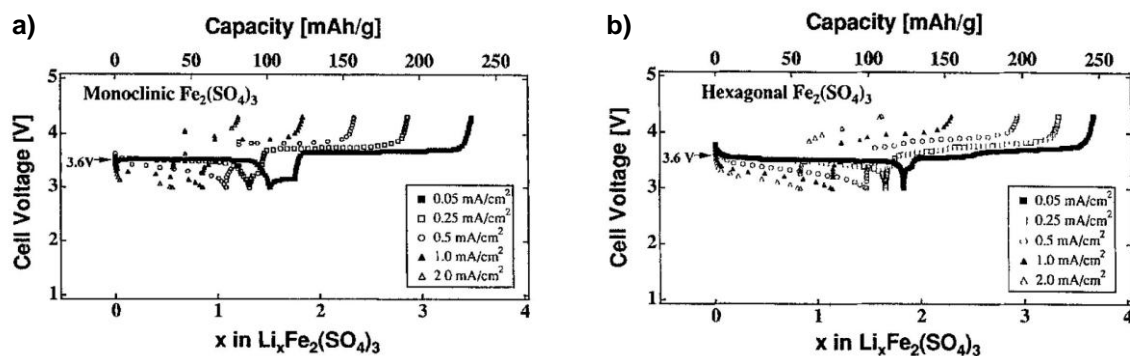
Figure I.11: Galvanostatic curves obtained for the (a) monoclinic and (b) rhombohedral polymorphs of $Fe_2(SO_4)_3$ cycled against a lithium anode (from **[224]**).

NASICON-type compounds were already well known at that time since they had been extensively studied in the 1970s as alternative solid electrolytes for Na/S batteries, after that Goodegough and Hong had found that $Na_{1+x}Zr_2Si_xP_{3-x}O_{12}$ ($0 \leq x \leq 3$) (which were baptized "NASICON", for NA SuperIonic CONductor, by Goodenough's colleagues **[225]**) presented high ionic conductivity properties comparable to the ones of β''-alumina **[226,227]**. These compounds have the general formula $A_aM_2(XO_4)_3$, where A = Li, Na, $a \leq 5$, M = transition metal and X = Mo, W, P, S, Si, *etc.*. They crystallize into two different structures, called NASICON and anti-NASICON, depending on the composition and/or the preparation procedure. They are both built on a three-dimensional framework of MO_6 octahedra and XO_4 tetrahedra, which are linked to each other by corners only. Each MO_6 octahedron shares its six corners with six SO_4 groups, while each SO_4 tetrahedron equally shares all its vertices with four different MO_6 octahedra. The basic $M_2(XO_4)_3$ repeating unit, made of two MO_6 octahedra bridged by three XO_4, has the shape of a lantern (**Figure I.12**). In the NASICON structure, these lantern units are stacked parallel to each other, while in the anti-NASICON framework they are alternatively oriented in two different directions, which are almost perpendicular one to another (**Figure I.12**). The latter anti-NASICON structure is thus less open than the NASICON one, and is therefore generally less favorable for alkali ion transport.
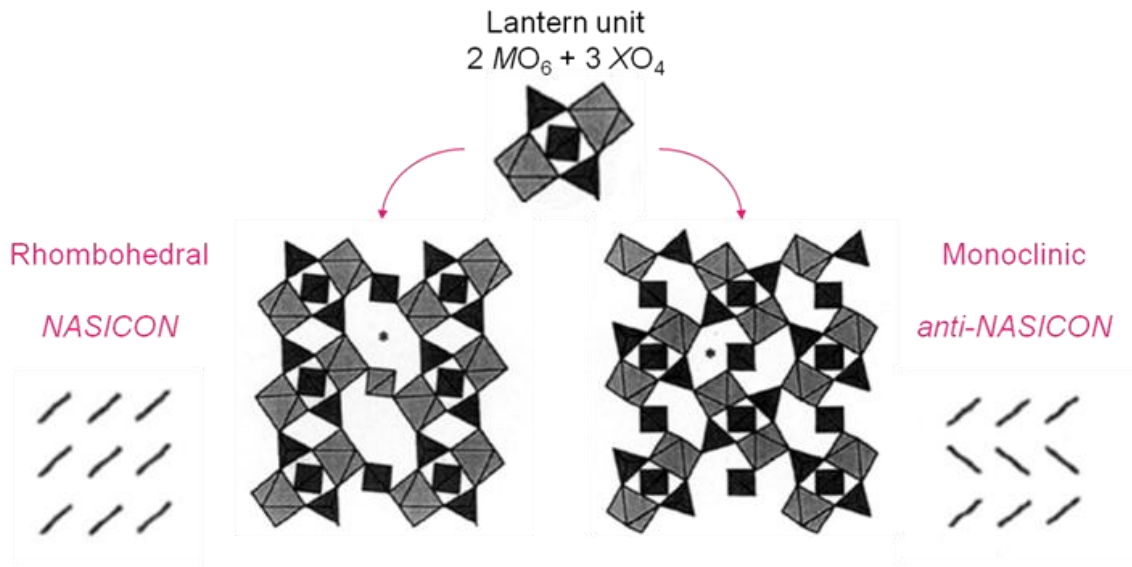
Figure I.12: Representation of the NASICON and anti-NASICON frameworks
(after the rhombohedral and the monoclinic structures of $Fe_2(SO_4)_3$, respectively [228,229]).

One important property of the NASICON-type structures is their ability to accommodate a large variety of atoms [230]. Playing on the $Li_xM_2(XO_4)_3$ composition, Goodenough *et al.* established the relative position of the redox couples of various transition metals (**Figure I.13.a**) [224,231], and they later found that the potential of a given redox couple could be tuned by changing the nature of the polyanion XO_4 (**Figure I.13.b**) [232]. For instance, they showed that varying X from phosphorous to sulfur increases the Fe^{3+}/Fe^{2+} and V^{3+}/V^{2+} redox potentials by 0.8 V. Moreover, the substitution of one sulfate group out of three by a phosphate group induces a change in the OCV of about 0.3 V (*i.e.* one third of the 0.8 V), suggesting that this effect is additive.
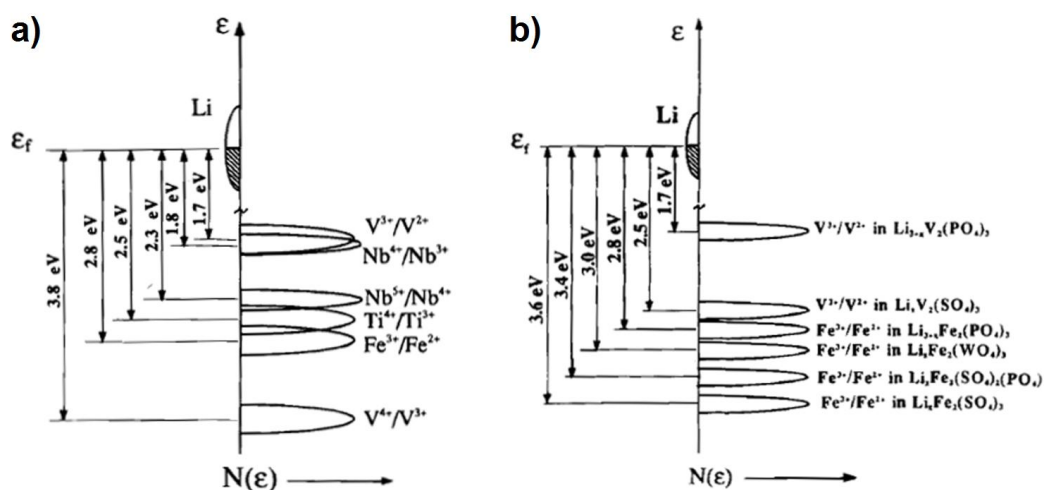
Figure I.13: (a) Relative energies of the redox couples of different transition metals in materials having a NASICON framework (from [231]). (b) Influence of the nature the polyanion on these redox energies (from [232]).

Goodenough explained these observations in terms of *inductive effect*: the strong covalent bonding within the polyanionic group XO_4 adjacent to the redox center M induces a polarization of the M–O bond (**Figure I.14**), which stabilizes the transition metal redox couple (*i.e.* it lowers the redox energy and raises the redox potential) **[222,232,233]**. Thus, the more electronegative is X, the stronger the covalent bonding X–O, the weaker the M–O bond, and the higher the potential of the $M^{n+}/M^{(n+1)+}$ redox couple.

$$PO_4^{3-} < MoO_4^{2-} \sim WO_4^{2-} < SO_4^{2-}$$
$$\longrightarrow E \nearrow$$
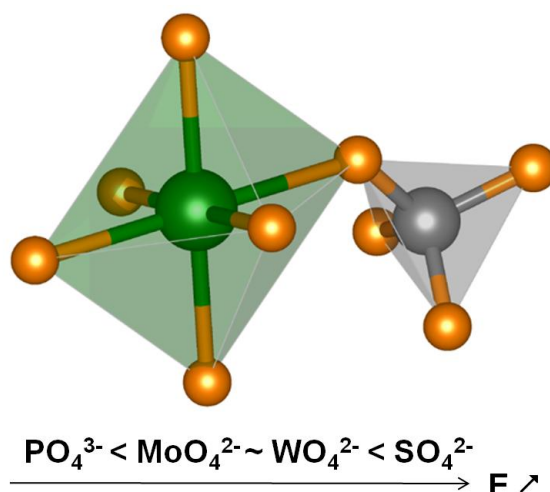
Figure I.14: Schematic representation of the inductive effect.

Consecutively, Goodenough *et al.* broadened their study by investigating lithium insertion into several different framework structures containing phosphate polyanions. Beside showing that even with the same polyanion the variation in structure could have an important effect on the position of a given redox couple **[234]**, they identified in the course of this study a new electrode material, namely $LiFePO_4$, which would have a major impact within the battery community in the following years **[233,235]**.

I.2.3.2   *Phospho-olivines AMPO₄ (A = Li, Na and M = Fe, Mn, Co, Ni)*

Goodenough rapidly identified $LiFePO_4$ as an attractive cathode material. With a theoretical capacity of 170 mAh/g (*i.e.* of the same order as with $LiNiO_2$), and despite an operating voltage lower than the ones of the layered oxides (3.45 V *vs.* Li^+/Li^0 compared to ~4 V for $LiCoO_2$), the so-called LFP become after $LiMn_2O_4$ the second low-cost Li-based material constituted of abundant and environmentally benign elements.

$LiFePO_4$, which is a mineral named *triphylite,* is isostructural to the *olivine* Mg_2SiO_4, which crystallizes in an orthorhombic unit cell (space group: *Pnma* or *Pmnb*, depending on the chosen description), but with the lithium and iron atoms being completely ordered between the octahedrally coordinated M1 and M2 sites, respectively **[236]**. Hence the *triphylite* $LiFePO_4$ structure (often confusingly refered to

as the *olivine* structure in the battery community) consists of edge-sharing FeO_6 octahedra, which give birth to layers parallel to the $(ac)_{Pmnb} \equiv (bc)_{Pnma}$ plane (**Figure I.15**). PO_4 tetrahedra brigde these octahedra sheets along the $b_{Pmnb} \equiv a_{Pnma}$-axis. Each phosphate group shares one of its edges with one FeO_6 octahedron, which is thus slightly distorted. The resulting electrostatic repulsions between the Fe and P cations weaken the Fe^{II}–O bond strength, which was explained to be at the origin the unusually high operating voltage observed for this electrode material (3.45 V vs. Li^+/Li^0) **[237]**. The lithium atoms sit at the intersection of tunnels, which run along the $a_{Pmnb} \equiv b_{Pnma}$ and the $c_{Pmnb} \equiv c_{Pnma}$ axes; conductivity studies have however shown that Li^+ diffusion was mostly 1D along the $[100]_{Pmnb} \equiv [010]_{Pnma}$ direction **[238]**.
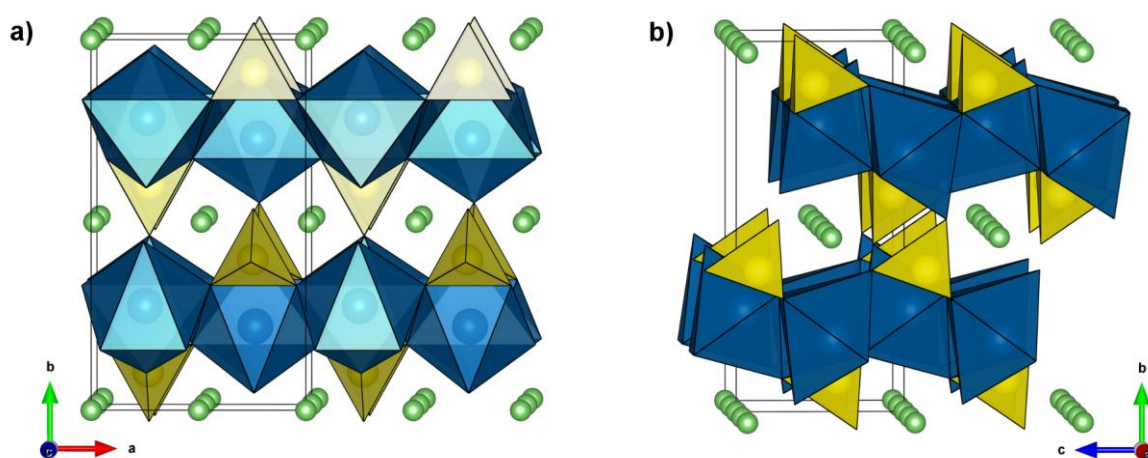
Figure I.15: Structure of $LiFePO_4$ described in the *Pmnb* unit cell, viewed along (a) the *c*- and (b) the *a*-axes. Blue octahedra and yellow tetrahedra represent the FeO_6 and PO_4 groups, respectively. Lithium atoms are displayed as green balls.

Lithium extraction occurs following a two-phase mechanism between the lithiated phase $LiFePO_4$ and the delithiated phase $FePO_4$, with a unit-cell volume change (ΔV/V) of 8.5 % **[237]**. This biphasic mechanism is conveyed in the plateau observed on the charge/discharge curve represented in **Figure I.16**. Initially, only ~0.7 lithium could be extracted at very low current densities, which corresponds to a reversible capacity of ~120 mAh/g **[233]**. Researchers identified rapidly that the limited reversible capacity and low rate capability was related to the poor electronic and ionic conductivity of the compound. Improving the electronic conductivity of the electrode materials was eventually achieved by coating the $LiFePO_4$ powder with conductive carbon **[239–241]**, while reducing the particle size of the active material enabled a better fueling of the ions **[242,243]**. The synthesis procedure of $LiFePO_4$ powders was also shown to be critical because some routes may favor the creation of defects into the structure: in case of Fe/Li mixing sites, the iron found in the lithium tunnel blocks the lithium diffusion, which results in poor electrochemical performances**[238,244,245]**.

Overall, in less than ten years, drastic improvements of the electrochemical performances of $LiFePO_4$ were achieved **[105,116,246–251]**, so that first LFP-based cell were commercialized in 2005 by the new A123 company. This technology is now envisaged for larger volume applications, such as transportation.
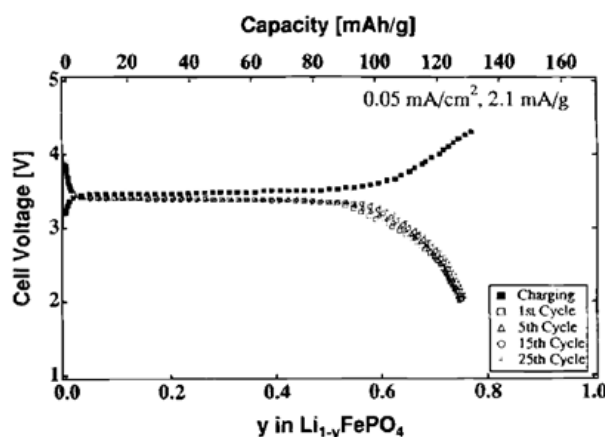
Figure I.16: Galvanostatic curve obtained for a Li // $LiFePO_4$ cell (from **[233]**).

Other *triphylite* phases $LiMPO_4$ (M = Mn, Co, Ni) were also envisaged as possible lithium hosts **[233,252–255]**. However, none of them has yet showed superior electrochemically properties than the iron compound, even if they have quite higher redox potentials. Given that the cobalt and nickel analogues should present operating voltages far from the stability windows of commonly used liquid electrolytes (4.8 V and 5.1 V *vs.* Li^+/Li^0, respectively), most of the expectations were focused on the manganese analogue, which displays a potential of 4.1 V *vs.* Li^+/Li^0. However, it suffers from very low intrinsic ionic and electronic conductivities ($\sigma \approx 10^{-16}$ S/cm at RT and $\Delta E \approx 1.1$ eV for $LiMnPO_4$ compared to $\sigma \approx 10^{-9}$ S/cm and $\Delta E \approx 0.6$ eV for $LiFePO_4$) **[256,257]** as well as large lattice distortions induced by the Jahn-Teller Mn^{III+} ions of the delithiated phase, which results in low capacity and poor rate capability.

Given that the success encountered by $LiFePO_4$ in Li-ion batteries, the search of a sodium equivalent was naturally investigated for Na-ion technology. However, the thermodynamically stable phase of $NaFePO_4$ does not crystallize in the *triphylite* structure but in another orthorhombic structure derived from *olivine*, namely the *maricite* structure, in which conversely to the *triphylite* the alkali atom (Na) and the transition metal (Fe) respectively occupy the M2 and the M1 sites **[236,258,259]**. Therefore, the *maricite* structure is characterized by the fact that the Na^+ cations are trapped into large cavities surrounded by the PO_4 groups and the $(FeO_6)_n$ chains running along the $[100]_{Pmnb} \equiv [010]_{Pnma}$ direction

(**Figure I.17**), which is likely the cause of the poor electrochemical behavior of this compound in sodium cells **[120,260]**.
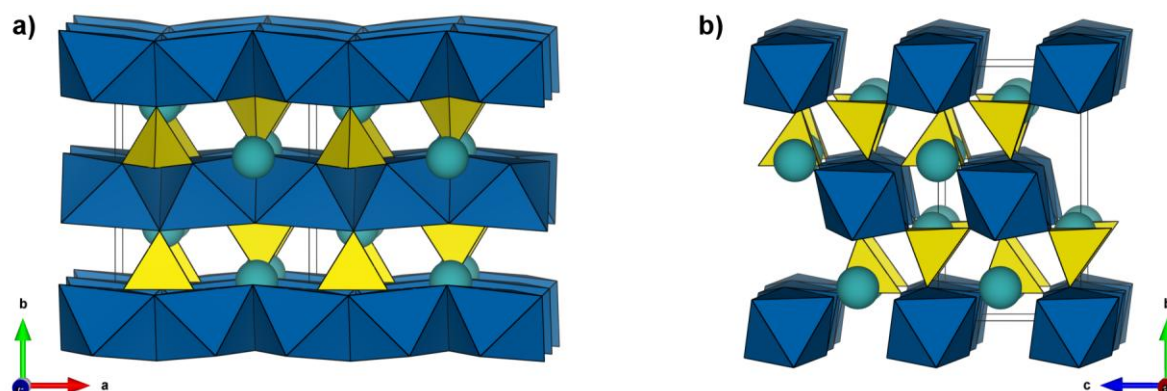
Figure I.17: Structure of NaFePO$_4$ described in the *Pmnb* unit cell, viewed along (a) the *c*- and (b) the *a*-axes. Blue octahedra and yellow tetrahedra represent the FeO$_6$ and PO$_4$ groups, respectively. Sodium atoms are displayed as cyan balls.

The direct synthesis of *triphylite* NaFePO$_4$ being unfavorable, this metastable phase could be obtained through cation exchange from LiFePO$_4$ **[261]**. The reversible uptake of ~0.9 Na$^+$ into the *triphylite* framework of FePO$_4$ (prepared by oxidation of LiFePO$_4$) occurs at an average voltage of 2.9 V *vs.* Na$^+$/Na^0, *i.e.* ~0.55 V lower than the potential observed for the lithiation process, which is significantly more than the 0.331 V difference usually expected from the comparison of the relative position of the Na$^+$/Na^0 and Li$^+$/Li^0 redox couples, as it is more widely commented by Ceder *et al.* in reference **[120]**. Another interesting feature is the fact that the sodium extraction/insertion process happens *via* the formation of an intermediate phase, as reflected in the charge curve by the presence of two distinct plateaus (**Figure I.18**) **[261]**. This intermediate phase, which has a Na$_{0.6/0.7}$FePO$_4$ stoichiometry, acts indeed as a buffer of the internal stresses in the structure due to the large dimensional mismatches between FePO$_4$ and NaFePO$_4$ (ΔV/V ≈ 18 %, as compared to ~ 8 % for the lithium system) **[262]**. Finally, the *triphylite* polymorph of NaFePO$_4$ has been shown to be sufficiently stable to maintain its structure for at least 50 cycles and up to 480°C **[261,263]**.
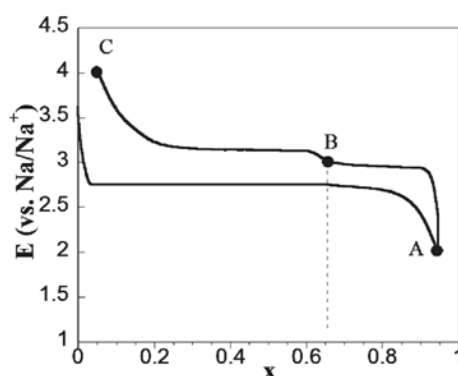
Figure I.18: Typical electrochemical curve obtained for a Na // *triphylite* NaFePO$_4$ cell in PITT mode (from **[261]**).

Besides the huge amount of work and the great hopes placed in the *triphylite* LiFePO$_4$ to stand as the material of choice for the next generation of positive electrode materials for Li-ion batteries, other polyanionic compounds with alternative compositions and structures were also investigated in search for higher energy electrode materials (*i.a.* other phosphates, pyrophosphates, silicates, borates, sulfates, *etc.*). Basically, there are two ways to increase the energy stored in a battery: *(i)* either by improving the specific capacity stored in the positive and the negative electrodes (*i.e.* the number of Li$^+$/e$^-$ accepted per gram of material), or *(ii)* by enhancing the difference of potential between both electrodes. Both directions were explored, as exemplified as follows by the silicates and the borates on the one hand, and by the fluorophosphates and fluorosulfates on the other hand.

I.2.3.3   Silicates Li$_2$MSiO$_4$ (M = Fe, Mn, Co)

In the quest for high specific capacity electrode materials, much hope has been placed into compounds that could afford more than one-electron reversible exchange per transition metal. Armand early identified the silicate Li$_2$FeSiO$_4$ as a possible candidate for such a challenge [264–267]. However, despite intensive research efforts having been devoted to Li$_2$*M*SiO$_4$ (*M* = Fe, Mn, Co) [268–280], limited achievements have been attained until now.

The Li$_2$*M*SiO$_4$ (*M* = Fe, Mn, Co) family presents a rich cristallochemistry, with all the polymorphs being derived from the β- and γ-Li$_3$PO$_4$ structures. These crystal structures consist of tetragonally packed oxygen ions (*i.e.* a distorted *hcp* array of oxygen ions), with half of the tetrahedral sites occupied by the three cations Li$^+$, M^{II+} and Si^{IV+}, so that face-sharing is avoided. In the β-type structures, all tetrahedra share corners and point in the same direction perpendicular to the close-packed planes, while in the γ-polymorphs, tetrahedra share both corners and edges and are oriented in opposite directions (**Figure I.19.a**). Several variants (named β$_I$, γ$_0$, γ$_{II}$, *etc.*) exist for both β and γ structures, involving either cation ordering or distortion of the parent structure. Recently, all polymorphs were shown to have very similar energies, which explains the difficulties encountered to control of synthesis of single-phase samples [281].
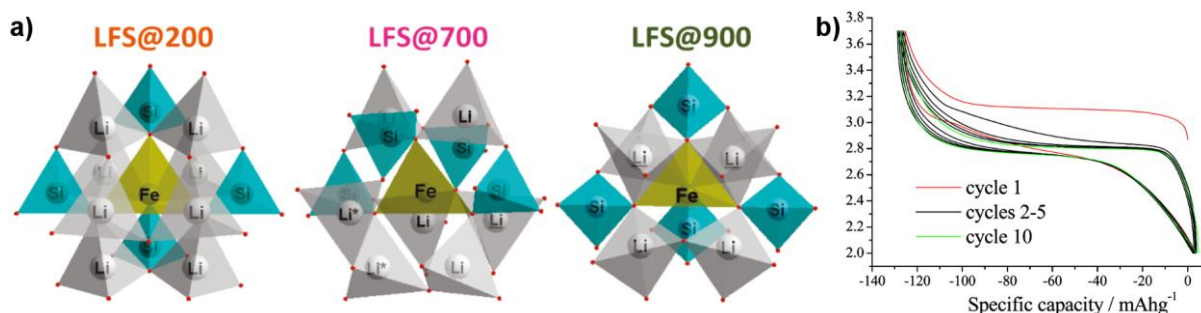
Figure I.19: (a) Structural representations of two polymorphs of Li$_2$FeSiO$_4$ (from [278]). (b) Cycling of Li$_2$FeSiO$_4$ (from [282]).

One of the peculiarities of this silicate family is its quite poor intrinsic conductivity ($\sigma \approx 5 \cdot 10^{-16}$ S/cm for Li_2MnSiO_4 and $6 \cdot 10^{-14}$ S/cm for Li_2FeSiO_4 at room temperature [283]), due to isolated MO_4 tetrahedra and tightly bounded Li^+ cations in tetrahedral sites. However this limitation could be overcome by combining carbon coating and particles nanosizing [274,284], as previously employed for $LiFePO_4$.

Similar electrochemical behavior was found for all Li_2FeSiO_4 polymorphs, as presented in **Figure I.19.b**. Almost one lithium (~160 mAh/g) can be removed from the structure during the first charge, which occurs around 3.1 V *vs.* Li^+/Li^0. Interestingly, Dominko and Masquelier showed that the exact value of this potential was closely related to the FeO_4 arrangements of the different polymorphs [278]. Subsequent charges and discharges, which offer reversible capacities of 120-140 mAh/g, experience a lowering of the voltage to 2.8 V *vs.* Li^+/Li^0, which results from a structural rearrangement to a more stable structure that minimizes repulsion between Fe^{III+} and Si^{IV+} cations in the charged phase [269,281,282]. The removal of the second lithium could not be achieved. In fact, recent theoretical calculations predicted that the Fe^{IV+}/Fe^{III+} redox couple would be located at a high voltage of 4.7 V *vs.* Li^+/Li^0 (*i.e.* close to the electrolyte stability limit) and would be accompanied by major structural rearrangement, both being detrimental to reversible cycling of the second lithium [281].

Unlike Li_2FeSiO_4, other members of the Li_2MSiO_4 family (M = Co, Mn) have not shown promising electrochemical properties so far. In addition to the poor ion and electron transport characteristics of Li_2MnSiO_4, Jahn-Teller Mn^{III+} (d^5) cations are unstable in their tetrahedral environment, thus leading to important loss of crystallinity during the first oxidation and poor reversibility during the subsequent cycle [283]. Stabilization of the manganese was investigated in mixed Fe/Mn silicates, but electrochemically cycling of such $Li_2Fe_{1-x}Mn_xSiO_4$ phases did not exceed 0.8 lithium ions [285,286].

I.2.3.4   *Borates Li*MBO_3 *(M = Fe, Mn, Co)*

$LiMBO_3$ (M = Fe, Mn, Co) borate phases were considered for the first time in 2001 as possible alternatives for positive electrode materials by Piffard *et* al. [287]. BO_3 groups are in fact the lightest polyanionic groups, so that the $LiMBO_3$ compounds have theoretical capacities as high as 220 mAh/g. Therefore, although the potential of the Fe^{III+}/Fe^{II+} redox couple is relatively low compared to other polyanionic compounds (2.8 V *vs.* Li^+/Li^0), an electrode material based on $LiFeBO_3$ could reach energy densities up to 617 Wh/kg, which is the highest theoretical energy density among the polyanionic compounds investigated up to now.

The crystal structure of LiMBO$_3$ (M = Fe, Mn, Co) is described in a monoclinic unit cell (space group: $C2/c$) [287,288]. It is built on edge-sharing FeO$_5$ trigonal bipyramids, which form chains along the <1 0 -1> directions (**Figure I.20**). Each planar BO$_3$ group links three of these chains *via* corner sharing. Within this 3D framework, lithium atoms lie in tetrahedral sites. However, there is still a controversy in the literature surrounding the exact structure of LiFeBO$_3$, in particular over the position of the lithium atoms [287,289–291].
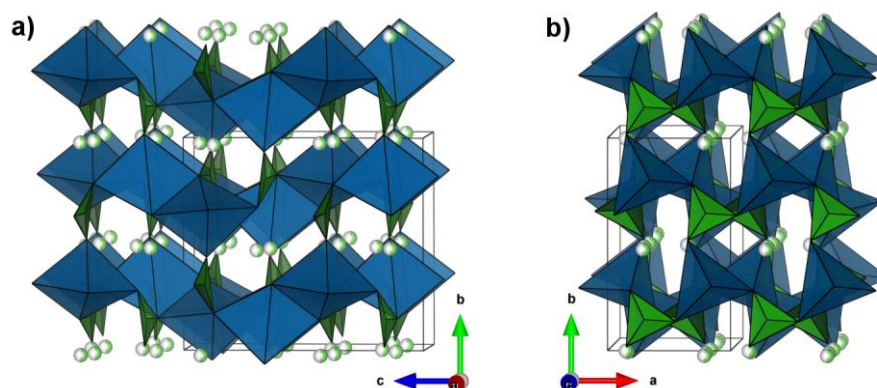
Figure I.20: Structure of LiMBO$_3$ viewed along (a) the a- and (b) the c-axes.
Blue bipyramids and green triangles represent the FeO$_6$ and BO$_3$ groups, respectively.
Lithium atoms are displayed as half-colored green balls.

Whereas Piffard's first results showed very limited reversible capacities for the three LiMBO$_3$ (M = Fe, Mn, Co) phases [287], a significant breakthrough was made by Yamada *et al.* in 2010 when they reported for LiFeBO$_3$ attractive reversible capacity of almost 1 lithium per iron atom (> 190 mAh/g at C/20) (**Figure I.21**) [289]. These impressive results were achieved by using nanosized particles and by paying special attention to prevent the samples from air exposure. Both experiments and *ab initio* calculations confirmed solid-solution behavior between isostructural end-members with a very small volume change (ΔV/V ≈ 2 %), which is favorable for reversible reaction and long-range cyclability [289,292].
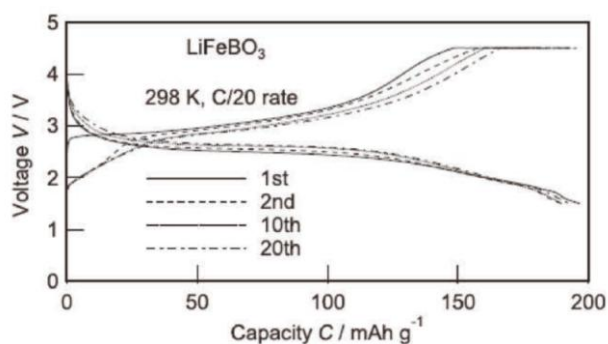
Figure I.21: Typical charge-discharge curves obtained for LiFeBO$_3$ (from [289]).

More recently, Ceder *et al.* compared the electrochemical performances of the monoclinic $LiMnBO_3$ with an hexagonal analogue. They showed that the former is the most interesting polymorph despite its lower redox potential (3.7 V *vs.* Li^+/Li^0 for the monoclinic form compared to 4.1 V for the hexagonal one). Consequently, Yamada *et al.* also studied the solid solution $LiFe_{1-x}Mn_xBO_3$ **[293]**. As expected, the potentials associated with the redox couples Fe^{III+}/Fe^{II+} and Mn^{III+}/Mn^{II+} were found to be at 3.0 V and 3.7 V *vs.* Li^+/Li^0, respectively. Thus, the introduction of manganese provides a higher potential, but in return, the practical capacity decreases and kinetic polarization increases. Finally, nanoscale $LiCoBO_3$ was also studied as electrode material **[294]**. First results showed that the electrochemical activity is centered around 4 V *vs.* Li^+/Li^0, but the reversible capacity was only of ~30 mAh/g at a moderate rate of C/20.

I.2.3.5   *Fluoro- and hydroxy-phosphates A_xMPO_4X (A = Li, Na, M = V, Fe, Mn and X = F, OH)*

In the early 2000s, Barker and co-workers proposed for the first time to use fluorophosphate compounds $AMPO_4F$ (with *A* an alkaline and *M* a 3d transition metal) as positive electrode materials **[295]**. Such compounds benefit from both the inductive effect of the phosphate groups and the high electronegativity of the fluorine anions, which should further stabilize the $M^{n+}/M^{(n-1)+}$ redox couple.

Most of the lithium-based $LiM^{III+}PO_4F$ compounds are isostructural to the naturally-occuring minerals *tavorite* $LiFePO_4OH$ **[296]** and *amblygonite-montebrasite* $LiAlPO_4(OH),F$ **[297]**, which both crystallize in the same triclinic structure (space group: *P*-1). This structure is characterized by one-dimensional chains of corner-sharing FeO_4X_2 (X = F, OH) octahedra, where two adjacent octahedra are linked through the fluorine atoms or the oxygen of the hydroxyl group (**Figure I.22**). These chains are interconnected by corner-sharing PO_4 tetrahedra. The resulting 3D framework delimitates different types of tunnels, at the rim of which lithium ions sit. Depending on the composition (*e.g.* F or OH, nature of the transition metal), the lithium occupies either two partially-occupied independent sites or a single site, although its exact position in some phases may still be the subject of controversy in the literature. Hence, this structure offers intersecting channels in which the Li^+ ions are able to diffuse in the three dimensions, while the $(FeO_4X_2)_n$ chains ensure 1D electronic diffusion.
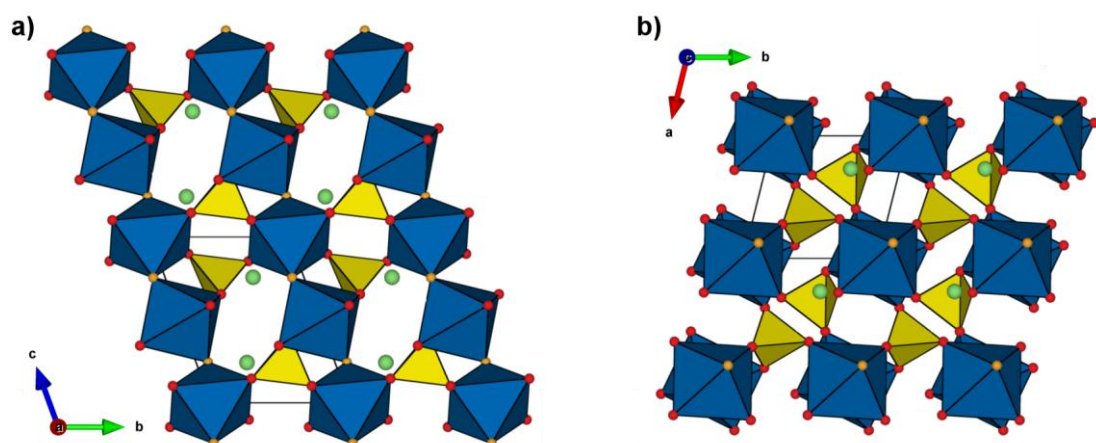
Figure I.22: Representation of the *tavorite* structure, viewed along (a) the *a*- and (b) the *c*-axes. Blue octahedra and yellow tetrahedra represent the FeO_6 and PO_4 groups, respectively. Lithium atoms are displayed as green balls. Oxygen and fluorine atoms are shown as red and orange balls, respectively.

I.2.3.5.1 <u>Lithium-based fluorophosphates</u>

From 2000 to 2007, Barker mainly studied the vanadium-based fluorophosphate $LiVPO_4F$ **[295,298– 305]**. This compound shows highly reversible lithium extraction/insertion in two potential ranges, around 1.8 V and 4.2 V *vs.* Li^+/Li^0, which are associated to the V^{III+}/V^{II+} and V^{IV+}/V^{III+} redox couples, respectively. The presence of these two plateaus offers the possibility of making a symmetrical 2.4V full cell by employing $LiVPO_4F$ at both the positive and the negative electrodes **[302]**. Moreover, long-range cyclability of graphite // LiVPO₄F cells has been demonstrated at a C/2 cycling rate, with more than 120 mAh/g after 200 cycles **[305]**. However, the low-availability and the high-toxicity of vanadium (as discussed earlier, **Table I.2** page 13) constitute the main obstacles for the commercialization of cells employing $LiVPO_4F$.

First reports on the synthesis and the electrochemical properties of the iron equivalent $LiFePO_4F$ were published in 2010 by the group of Armand and Tarascon **[306–308]** and by the one of Nazar **[309,310]**. Contrary to $LiVPO_4F$, lithium extraction from $LiFePO_4F$ is not feasible, because the oxidation of Fe^{III+} into Fe^{IV+} is located at too high a voltage (above 4.7 V *vs.* Li^+/Li^0, *i.e.* beyond the electrochemical stability window of the electrolyte). Conversely, high reversible lithium intercalation (up to 0.96 Li, that is 145 mAh/g) into $LiFePO_4F$ was observed at a moderate C/10 rate, with an operating voltage located close to 2.8 V *vs.* Li^+/Li^0 corresponding to the Fe^{III+}/Fe^{II+} couple (**Figure I.23.a**). The discharge process was described as a two-phase mechanism, leading to the phase Li_2FePO_4F, which conserves the *tavorite* framework with a volume expansion of about 8 %.

Here, it is interesting to note that the Fe^{III+}/Fe^{II+} redox potential observed for $LiFePO_4F$ corresponds to the one recorded for the NASICON $Li_3Fe(PO_4)_3$ (2.8 V *vs.* Li^+/Li^0 **[234,311]**), and is even lower than the one of the *olivine* $LiFePO_4$ (3.45 V *vs.* Li^+/Li^0 **[233,234]**), which both contain no fluorine. Therefore,

this observation illustrates well that the incorporation of fluorine into a given composition does not systematically enhance the potential of the redox center. In fact, besides the nature of the neighboring atoms of the redox center, many other structural factors (*e.g.* the connectivity between atoms, the nature of the bonding) experimentally affect the position of redox potential.
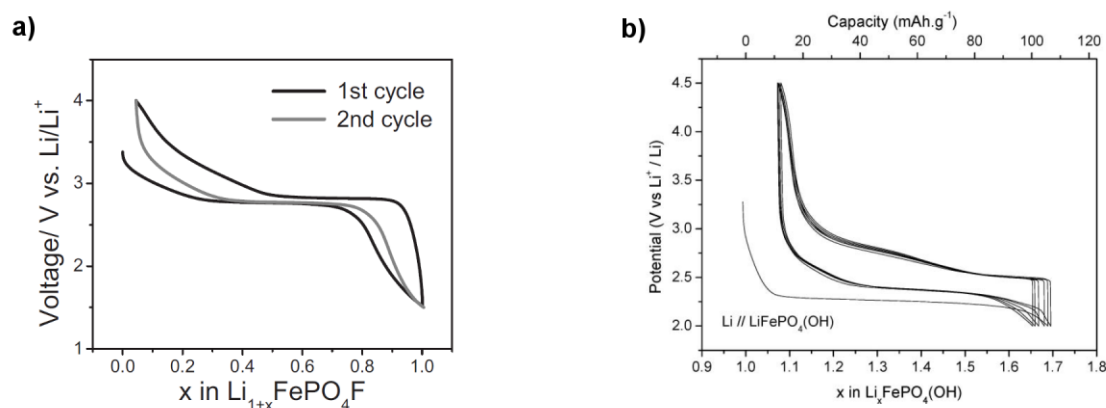
Figure I.23: Lithium insertion-deinsertion curves of (a) $LiFePO_4F$ (from **[309]**) and (b) $LiFePO_4OH$ (from **[312]**).

I.2.3.5.2 Lithium-based hydroxyphosphates

Electrochemical properties of the *tavorite* mineral's composition $LiFePO_4OH$ were tested as soon as 2001 by Whittingham's group **[313]**, but they observed no capacity between 1.9 and 4.1 V *vs.* Li^+/Li^0. No more attempts were reported until Delmas and co-workers reinvestigated this compound in 2009 and found interesting electrochemical activity **[312]**. Using a C/50 rate, they obtained a 90 mAh/g reversible capacity (i.e. ~60 % of the theoretical one) at an average voltage of ~2.5 V *vs.* Li^+/Li^0 (**Figure I.23.b**). An intriguing feature is the 0.12 V potential increase observed in the discharge curve after the first cycle, which was explained by an amorphization of the active material upon the first discharge **[310]**. Moreover, one can notice here that the 2.5 V potential of $LiFePO_4OH$ is about 0.3 V lower than the one reported for the $LiFePO_4F$. This illustrates the effect of replacing an hydroxyl group OH^- for a more electronegative fluorine ion F^- on the redox potential for two isostructural compounds. This observation is further supported by a recently-reported mixed hydroxy-fluoro-phosphate $LiFePO_4(OH)_{0.4}F_{0.6}$ of *tavorite* structure, which inserts lithium at an average voltage intermediate between those of $LiFePO_4OH$ and $LiFePO_4F$ **[314]** (**Figure I.24**). It is also worth noting the sloping shape of the cycling curve of $LiFePO_4(OH)_{0.4}F_{0.6}$, which undergoes a single-phase (solid-solution) lithium extraction/insertion mechanism, in contrast with the flat-like curves of the two end-members $LiFePO_4OH$ and $LiFePO_4F$. Such a charge/discharge profile, rather rare among polyanion compounds, constitutes an advantage for an electrode material at both material and practical point of views: first, it is associated with less strains within the particles, which favors better

reversibility and longer cycle life, and second, it permits facile monitoring of the state of charge of the full cell, as the operating voltage can be directly correlated to the remaining energy stored in it.
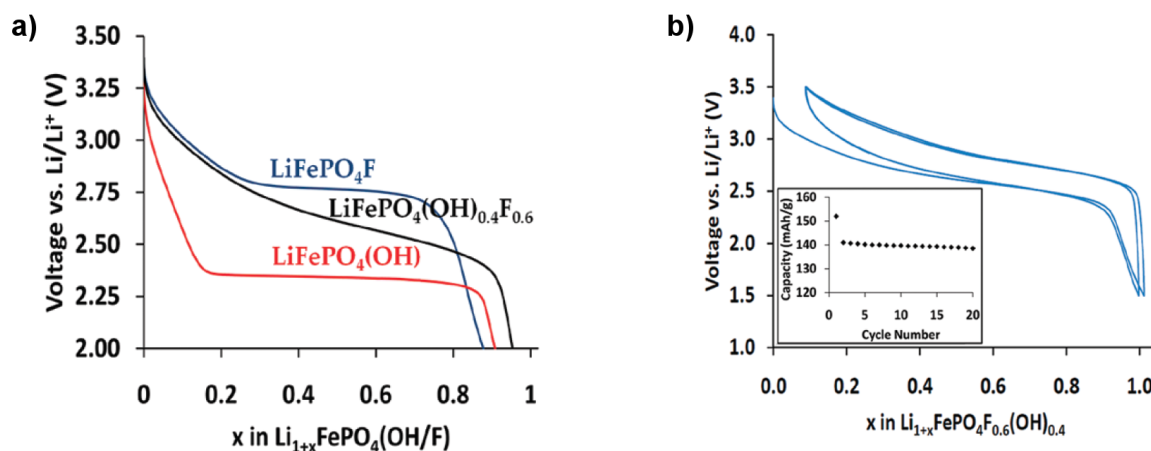
Figure I.24: (a) Voltage profiles on first discharge of LiFePO$_4$F, LiFePO$_4$OH, and LiFePO$_4$(OH)$_{0.4}$F$_{0.6}$ (from **[314]**). (b) Electrochemical cycling of LiFePO$_4$(OH)$_{0.4}$F$_{0.6}$ versus lithium. Inset: discharge capacity at a C/10 rate for the first 20 cycles. (from **[314]**).

Finally, the lithium manganese hydroxyphosphate LiMnPO$_4$OH was also investigated **[315]** with the hope of using both Mn^{III+}/Mn^{II+} and Mn^{IV+}/Mn^{III+} redox couples, as for LiVPO$_4$F. However, this material was found to present poorer electrochemical properties than LiFePO$_4$OH, with a reversible capacity of about 100 mAh/g at a very slow rate of C/100. Moreover, after a first charge occurring between 3.5 and 4.5 V *vs.* Li$^+$/Li^0, the discharge and charge curves become more sloping and are centered at an average voltage of 3.4 V *vs.* Li$^+$/Li^0. This drastic change in the curve profile should indicate a modification of the electrode material that has not been elucidated yet. Similar behavior and performances were also observed later for the mixed phase LiFe$_{1-x}$Mn$_x$PO$_4$OH **[316]**.

I.2.3.5.3 Sodium-based fluorophosphates

The sodium-based iron fluorophosphate has the general formula Na$_2$FePO$_4$F and does not crystallize in the *tavorite* structure, but in an orthorhombic unit cell (space group: *Pbcn*). It presents a layered-like two-dimensional framework, composed of FeO$_7$F$_2$ units made of face-sharing FeO$_4$F$_2$ octahedra. These units are connected *via* bridging fluorine atoms to form chains, which are joined by PO$_4$ tetrahedra to give (FePO$_4$F)$_n$ infinite layers. The two sodium atoms, which are located in the interlayer spaces, possess facile 2D migration pathways.

Na$_2$FePO$_4$F was first tested as positive electrode material against lithium **[260]**, providing 124 mAh/g at an average potential of ~3.3 V vs. Li$^+$/Li^0 for 50 cycles at C/10. This demonstrated the feasibility of directly using sodium-based compounds as cathode materials for Li-ion batteries, in particular when lithium equivalent cannot be synthesized directly, without prior ion exchange. Na$_2$FePO$_4$F was later

incorporated in Na-ion batteries by Recham *et al.*, who obtained about 100 mAh/g at an average voltage of 3 V vs. Na^+/Na^0 (**Figure I.25**) **[306,308,317,318]**. The removal of one sodium is associated with only a 3.7 % cell volume reduction. The remaining sodium atom, which cannot be electrochemically removed owing to the inaccessibly high potential of the Fe^{IV+}/Fe^{III+} redox couple, acts as a pillar between the layers.
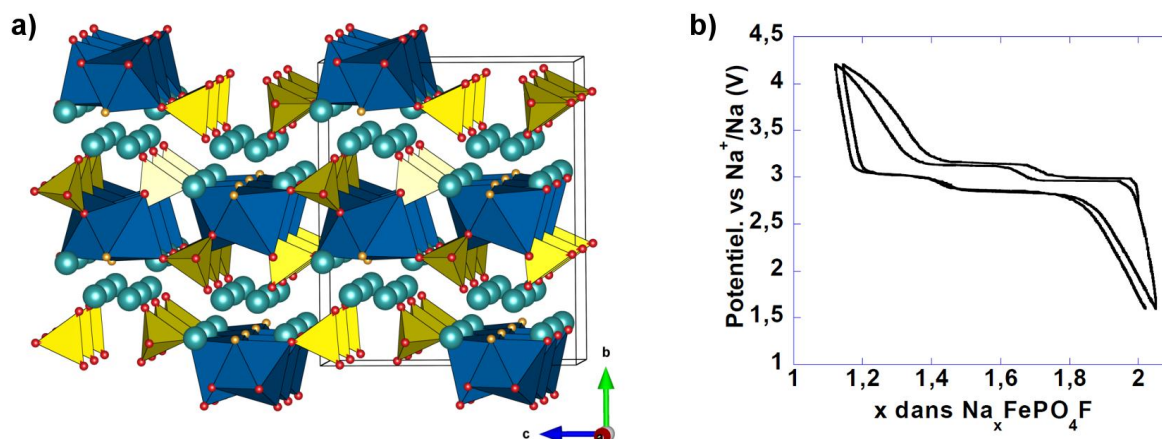
Figure I.25: (a) Structure of Na_2FePO_4F, and (b) electrochemical curve obtained when cycling Na_2FePO_4F *versus* sodium (from **[318]**).

I.2.3.6   Fluoro- and hydroxy-sulfates A_xMSO_4X (A = Li, Na, M = Fe, Co, Ni, Mn, Zn and X = F, OH)

At this stage, if we remind the 0.8 V shift observed by Goodenough *et al.* on the redox potentials when substituting phosphate groups by sulfates in NASICON compounds **[232]**, an evident continuation of the work done on fluoro- and hydroxy-phosphates was naturally to explore the sulfate analogues.

I.2.3.6.1 Lithium-based fluorosulfates

The first fluorosulfate of *tavorite* structure to be synthesized was the $LiMgSO_4F$ phase and was reported in 2002 by Sebastian *et al.* **[319]**. Based on their conductivity measurements, they predicted that "isostructural transition metal analogues, LiMSO_4F (M = Mn, Fe, Co), would be important for redox extraction/insertion of lithium involving M^{II}/M^{III} oxidation states", but they could not prepare them using ceramic methods. Eight years later, Tarascon and co-workers eventually obtained the *tavorite* $LiFeSO_4F$ phase by employing an unusual ionothermal route **[308,318,320,321]**. Indeed, this new phase was then found to decompose at temperature beyond 375°C and to be soluble in water, which explains the difficulties encountered to isolate it with classical ceramic approaches or low-temperature solution chemistry in aqueous media. Moreover, the authors also noticed that one of the determinant factors for the success of the synthesis was the use of monohydrate iron sulfate and lithium fluoride as the precursors. They pointed out that the *szomolnokite*-type structure of $FeSO_4 \cdot H_2O$ **[322]** was in fact closely related to that of the *tavorite* $LiFeSO_4F$ **[323]**, as seen in

Figure I.**26**. During the reaction, the water molecules that link adjacent $FeO_4(H_2O)_2$ octahedra in the mother phase $FeSO_4 \cdot H_2O$ are replaced by fluorine anions while lithium cation are inserted in the open cavities, thus forming the tavorite $LiFeSO_4F$.

FeSO₄·H₂O   **LiFeSO₄F**

F⁻   H₂O   Li⁺
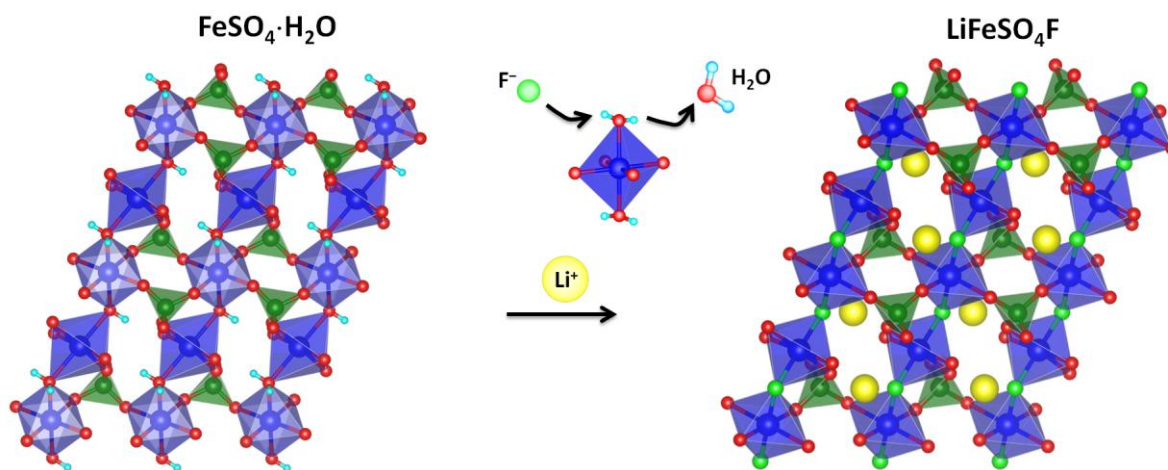
Figure I.26: Comparison of the *szomolnokite* structure of $FeSO_4 \cdot H_2O$ (on the left) and the one of the *tavorite* of $LiFeSO_4F$ (on the right).

Tavorite $LiFeSO_4F$ displays a high redox potential of 3.6 V *vs.* Li^+/Li^0, which is, as expected, 0.8 V greater than the one of the isostructural fluorophosphate $LiFePO_4F$. Nearly 0.9 lithium ions per formula unit (*i.e.* 135 mAh/g) can be reversibly extracted from the structure, with good capacity retention. The redox process follows a biphasic mechanism and leads to a delithiated $FeSO_4F$ phase, which conserves the *tavorite* framework although described in that case with a monoclinic cell (space group: $C2/c$); the resulting 8 % volume change between the lithiated and the delithiated phases is comparable with the ones of $LiFePO_4F$ and $LiFePO_4$.
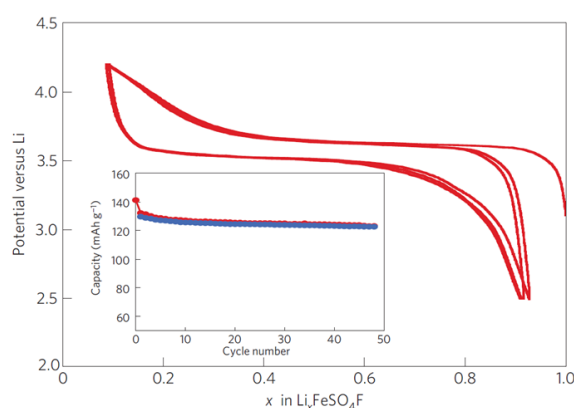
Figure I.27: Cycling of the *tavorite* $LiFeSO_4F$ (from **[321]**).

Therefore, with a potential slightly higher than that of the *olivine* $LiFePO_4$ and a similar energy density (*c.a.* 500 Wh/kg), and because such good electrochemical response is achieved with no need of carbon coating nor nanosizing of the particles, *tavorite* $LiFeSO_4F$ stood as a new promising positive

electrode. Therefore, a lot of work have been dedicated in developing alternative synthesis routes, ranging from low-temperature solid-state reaction **[324]** to the use of polymers **[325,326]** or polyols **[327,328]** as reacting media, in order to propose more scalable ways to produce the new electrode material.

These syntheses were consecutively extended to the preparation of other 3d-metal fluorosulfates LiMSO$_4$F (M = Co, Ni, Mn, Zn), which revealed the rich polymorphism of this family of compounds **[323]**. While the cobalt and nickel phases were additional members of the *tavorite* series **[321,329]**, the manganese compound was found to be isostructural to the *triplite* mineral **[330]** and the zinc counterpart to crystallize in a *sillimanite*-like structure **[323,331–333]**.

The structure of LiZnSO$_4$F is built on chains of corner-sharing ZnO$_4$F$_2$ octahedra bridged by SO$_4$ tetrahedra similarly to the *tavorite* structure (**Figure I.28**); the main difference resides in the orientation of the octahedra along the chains and the way these chains are connected through SO$_4$ tetrahedra, which results in a higher symmetry for the *sillimanite*-like LiZnSO$_4$F structure (monoclinic unit cell, space group: *Pnma*) and in narrower channels for lithium diffusion **[323]**.
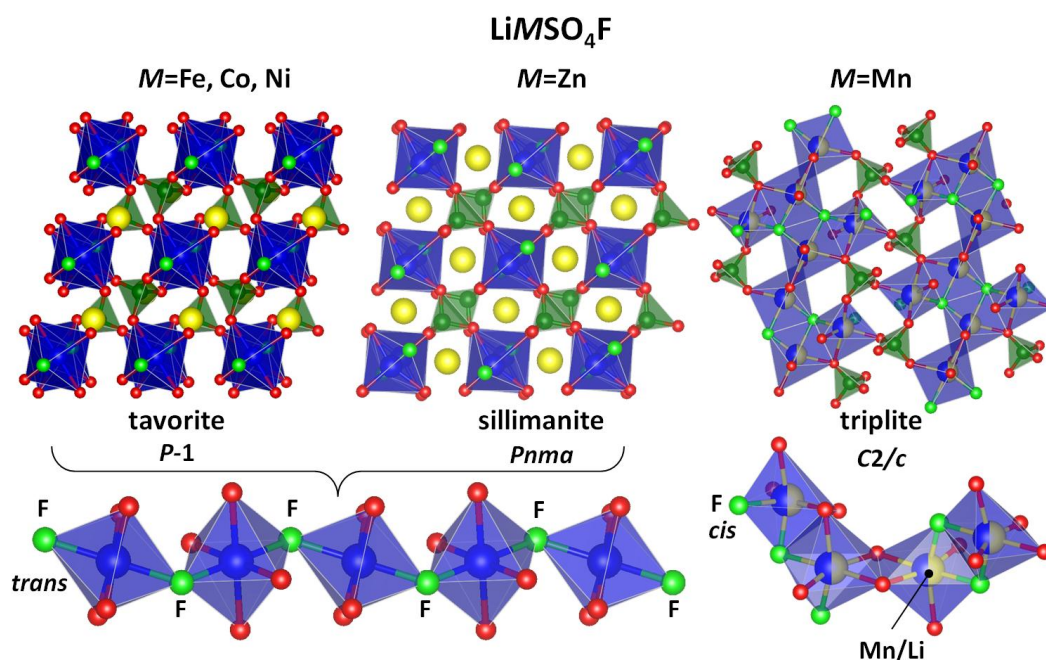
Figure I.28: Comparison of the *tavorite*, the *sillimanite*-like and the *triplite* structures (from **[323]**).

On the contrary, the *triplite* structure significantly differs from the *tavorite* and the *sillimanite*-like ones, as seen in **Figure I.28**. First, the 3d-metal and lithium atoms, which have well-defined crystallographic sites in the *tavorite* and the *sillimanite*-like structures, are statistically distributed on two octahedral sites (denoted M1 and M2) in the *triplite* structure. Second, fluorine atoms are

arranged in a *cis* configuration, rather than a *trans* one, within the strongly distorted $(Mi)O_4F_2$ octahedra. Finally, when the MO_4F_2 octahedra are only interconnected through corners in the *tavorite* and the *sillimanite*-like structures, in the *triplite* one they share edges, and form chains running along the [101] and [010] directions of the monoclinic unit cell (space group: $C2/c$).

Although expected for the zinc phase, the four new compounds LiMSO_4F (M = Co, Ni, Mn, Zn) were regrettably found to be electrochemically inactive up to 5 V *vs.* Li$^+$/Li^0. The solid solutions of *triplite* Li(Fe$_{1-x}$Mn$_x$)SO$_4$F (0.05 ≤ x ≤ 1) [330,334] and *sillimanite*-like Li(Fe$_{1-y}$Zn$_y$)SO$_4$F (0.15 ≤ y ≤ 1) [332] were then investigated in order to probe the influence of the structure on the redox potential of the Fe^{III+}/Fe^{II+} couple. These studies also revealed high operating voltages of 3.6 V *vs.* Li$^+$/Li^0 for the *sillimanite*-like structure and even 3.9 V *vs.* Li$^+$/Li^0 for the *triplite* polymorph, which is indeed the highest potential ever reported for the Fe^{III+}/Fe^{II+} redox couple in any inorganic compounds. Intense efforts were therefore dedicated to stabilize a pure LiFeSO$_4$F phase in the *triplite* structure. This was first achieved *via* solid-state routes [335,336] and later through spark plasma sintering (SPS) [337], mechanical billing[337] and ultra-rapid microwave synthesis [338], after that a thermodynamical study had showed that the formation of the *triplite* LiFeSO$_4$F polymorph rather than the *tavorite* one was entropy-driven [339].

With respect to the electrochemical performances, nearly 0.7 Li$^+$ ions per formula unit (*i.e.* ~105 mAh/g) can be reversibly removed from the *triplite* LiFeSO$_4$F. The oxidation/reduction process involves a biphasic mechanism and is associated with a very low volume change (ΔV/V ≈ 0.5 %), in contrast with the *tavorite* and *olivine* systems presented earlier. However, this low global volume change is the result of anisotropic changes of the lattice parameters, and there is therefore no guarantee that mechanical stress will be reduced upon cycling [323]. Still, the attractive operating voltage of 3.9 V *vs.* Li$^+$/Li^0 potential makes this *triplite* LiFeSO$_4$F polymorph an electrode material of high interest and may become, after electrode optimizations, a serious contender for the next generation of Li-ion batteries.
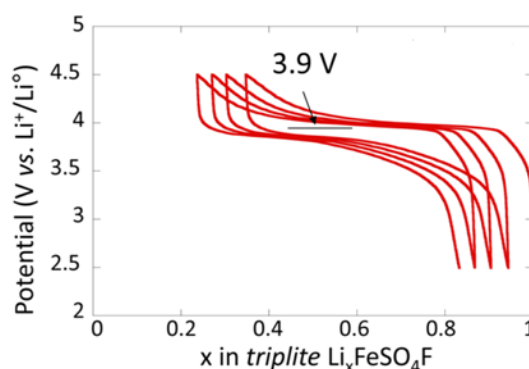
Figure I.29: Cycling of the *triplite* LiFeSO$_4$F (adapted from [323]).

I.2.3.6.2 <u>Lithium-based hydroxysulfates</u>

The exploration of the fluorosulfate family has led to two attractive $LiFeSO_4F$ electrode materials, which are currently under development. However, the presence of fluorine in these compounds may be opposed to stringent sustainable or safety requirements of specific applications. This point has thus motivated the investigation of fluorine-free sulfates, and this has been done by replacing the F^- ions for hydroxyl groups in the previously presented fluorosulfates.

Reversible lithium insertion into the monoclinic form of $FeSO_4OH$ was reported by the group of Pralong in 2009 [340]. This phase indeed presents the same FeO_6 and SO_4 framework as the *tavorite* structure, but without any Li^+ ions. First results showed a reversible capacity of ~110 mAh/g at a C/20 rate, involving two successive redox steps located around 3.3 and 3.2 V *vs.* Li^+/Li^0 (**Figure I.30**). If compared to the 2.5 V potential recorded for $LiFePO_4OH$ [312], this constitutes once again a clear illustration of the shift of the position of the Fe^{III+}/Fe^{II+} redox couple when $(PO_4)^{3-}$ polyanions are replaced by $(SO_4)^{2-}$ ones.

Subsequently, Tarascon's group confirmed and completed the results of Pralong, by studying the solid-solution $FeSO_4F_{1-y}OH_y$ [341]. First of all, they showed a gradual decrease of the average redox potentials with the OH content (*y*) from 3.6 V to 3.2 V *vs.* Li^+/Li^0 (**Figure I.30**). Next, the two-phase lithium insertion/extraction mechanism observed for the end-members $LiFeSO_4F$ and $LiFeSO_4OH$ were found to become a single-phase process for the F/OH mix compounds, as equally reported for the $LiFePO_4(OH)_{0.4}F_{0.6}$ phase [314]. Finally, similarly to what had been reported for $LiFePO_4OH$ [310,312], they observed for $FeSO_4F_{0.48}OH_{0.52}$ a slight shift of the discharge curve towards the high potentials after the first cycle, and explained here also this uncommon feature by local structural rearrangement.
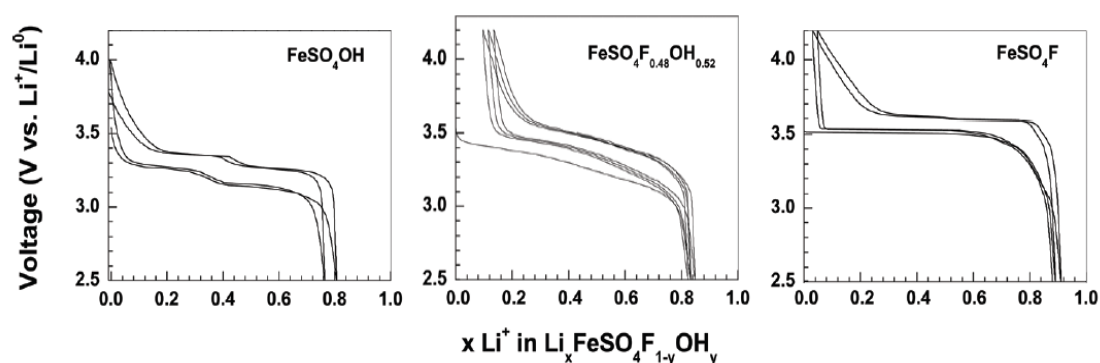
Figure I.30: Typical voltage-composition curves obtained for $FeSO_4OH$, $FeSO_4F_{0.48}(OH)_{0.52}$ and $FeSO_4F$ cycled at C/20 *versus* a Li metal anode (adapted from [341]).

Later, in an unsuccessful attempt to synthesize a *triplite* polymorph of $LiFeSO_4OH$, Tarascon's group stabilized a new lithium iron hydroxy-sulfate, which presents a layered structure [342]. Indexed in a

monoclinic ($P2_1/c$) unit cell, this $LiFeSO_4OH$ is built upon layers of FeO_6 octahedra parallel to the (bc) planes, which are sandwiched on both sides by SO_4 tetrahedra (Figure I.31.**a**). Within the sheets, FeO_6 octahedra share both corners and edges, thus forming zig-zag chains running along the [010] direction. Lithium atoms sit in the space between the layers and are tetrahedrally coordinated by oxygen atoms. The sloping electrochemical curve of $LiFeSO_4OH$, which inidcates a single-phase mechanism process, is centered around 3.6 V *vs.* Li^+/Li^0 and shows the reversible removal and uptake of 0.7 Li (*i.e.* ~110 mAh/g) at a rate of C/20 (Figure I.31.**b**).
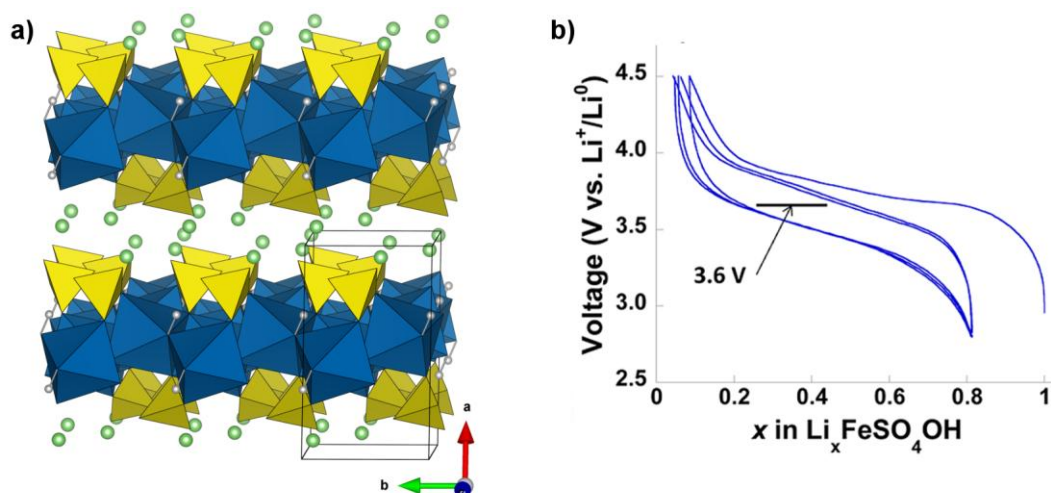
Figure I.31: (a) Structure and (b) electrochemistry of the layered $LiFeSO_4OH$ (from **[323]**).

I.2.3.6.3 Sodium-based fluorosulfates

Following on their work on $LiMSO_4F$, Tarascon and co-workers explored sodium-based fluorosulfates $NaMSO_4F$ (M = Fe, Co, Ni, Mn), which were first prepared by both ionothermal and solid-state syntheses **[320,331,343]**. These compounds present a *maxwellite* structure (space group: $C2/c$) having the same framework as the *tavorite*, but with the large Na^+ ions displaced towards the center of the tunnels as compared with the position occupied by Li^+ in $LiMSO_4F$ **[323]**. Among these sodium-based compounds, $NaFeSO_4F$ is the only one to display electrochemical activity, with a high redox potential centered around 3.5 V *vs.* Na^+/Na^0, but it is far from being impressive from the capacity point of view (~0.1 Na^+ per formula unit) **[327,331,343]**. This poor electrochemical properties are explained by limited ionic conductivity (1D Na^+ diffusion along the [101] chanel and Ea ≈ 0.6 eV, as compared to the 3D Li^+ diffusion and Ea < 0.4 eV for in the *tavorite* $LiFeSO_4F$) together with a high volume change of ~14 % between $NaFeSO_4F$ and $FeSO_4F$ **[344]**. This illustrates the difficulties of extending solid-state electrochemistry concepts from a lithium phase to a sodium analogue, even though they are almost isostructural.

Interestingly, the NaMSO$_4$F phases could also be obtained from the dehydration of the hydrated analogues NaMSO$_4$F·2H$_2$O (M = Fe, Co, Ni, Mn, Zn, Mg) [345–347], which isostructural to the mineral *uklonskovite* NaMgSO$_4$F·2H$_2$O. This structure is built upon MO$_4$F$_2$ octahedra linked together though the F atoms *sitting* in trans position, so as to form *tavorite*-like chains, with in addition two of the oxygen atoms constituting the equatorial plan being part of the H$_2$O moieties (**Figure I.32**). These chains are here linked via strongly distorted NaO(H$_2$O)$_2$F tetrahedra. The removal of water induces a condensation of the structure through the bridging of the MO$_4$F$_2$ octahedra and SO$_4$ tetrahedra so as to obtain the *maxwellite* structure of the anhydrous NaMSO$_4$F phases
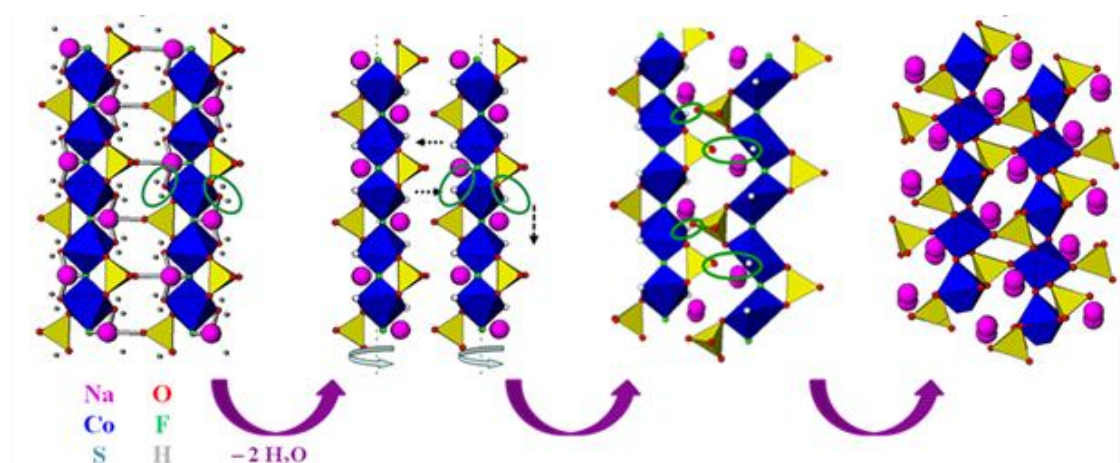
Figure I.32: Comparative structural diagrams illustrating the water removal mechanism from (left) the *uklonskovite* NaMSO$_4$F·2H$_2$O to (right) the *maxwellite* NaMSO$_4$F (adapted from [345]).

I.3   Conclusion

This first chapter intended to give the reader an insight of the battery research landscape at the time we have started this thesis towards the search for new positive electrode materials for Li- and Na-ion batteries. As it can be noticed from the short (non-exhaustive) overview of positive electrode materials given in this chapter, these two battery technologies rely on a rich and versatile chemistry. This offers the possibility of adjusting the material components of the battery to the requirements of the targeted application, and moreover opens a multitude of opportunities to chemists to imagine and design better materials for the next generations of batteries.

Generally speaking, the main positive electrode materials that have been investigated up to now can be divided into two groups: the oxides and the polyanionic compounds. Oxides, which were part of the first commercial success of the Li-ion batteries, provide high potentials and high energy densities. However, environmental and economic considerations have encouraged replacing these cobalt- and nickel-based compounds by electrode materials relying on sustainable, naturally abundant and

non-toxic elements, and this led to the successful development of $LiMn_2O_4$ which is now used in the large-scale application of zero-emission vehicles. Pursuing the search for other sustainable electrode materials based on iron, much research has been focused for the last decades in polyanionic compounds. As illustrated in this chapter, these offered several advantages as electrode materials, among which their robust frameworks that enable safe and extended cycling, as well as the possibility of tuning the potential of the redox couple by playing on their composition and their structure.

Although there is still no universal indicator capable of predicting the exact electrochemical performances of a given compound, several factors have been identified through the studies of different families of electrode materials for the last 25 years **[348]**. First of all, a common structural feature encountered among most of the compounds that have been previously presented is their open frameworks, which favor alkali ionic diffusion and allow for high cycling rates. These diffusion pathways may result from layers of transition metals (*e.g.* $LiCoO_2$), from the packing of transition metal chains (*e.g.* $LiFePO_4$, $LiFeSO_4F$), or through a coherent network of empty interstitials with close-packed anion lattice (*e.g.* $LiMn_2O_4$). Regarding the potential of the redox couple $M^{n+}/M^{(n+1)+}$, it is highly related to the iono-covalency of the M–O bond, which itself also depends on a variety of interdependent chemical and structural features: the packing of the structure (isolated, corner-, edge- or face-sharing MO_x polyhedra **[234,349]**), the presence and connectivity of electronegative elements and polyanionic groups around the redox center (inductive effect **[222,232,233]**), the position of the guest cation in the structure **[113,115,349,350]**, *etc*. They are widely used as tools to explain the general trends observed through the different families of electrode materials, but they should be employed prudently for voltage prediction since unfortunately none of them is fully infallible individually, and the redox potential observed for a given compound is often the result of a combination of various parameters.

Keeping in mind these observations, several strategies can be pursued to efficiently design new attractive materials. One relies on high-throughput materials computation to predict the structures of thousands of random compositions and calculate their physical chemistry properties with the goal of identifying the "magic phase composition" having both a high voltage and a high capacity **[351–354]**. First results of such theoretical studies have been reported for the last few years **[288,355–357]**, but success is still limited. Another approach, mainly pursued by experimental chemists, consists in browsing through the structures of known compounds (*e.g.* already synthesized phases, minerals) to spot families of materials having attractive structural features for ion transport. In the work presented herein, we opted for the second option, making use of the about 4000 identified mineral species on Earth to design new electrode materials. In addition to the fact that minerals'

structures are usually well known, understanding the conditions of their formation may suggest a starting point for their artificial synthesis, which could be generalized to their structural derivates. Here it is also interesting to note that many of the polyanionic compounds presented in the previous pages display original structures of minerals. The next chapter presents indeed one illustration of the feasibility of taking example from minerals structures to design new electrode materials having high redox potentials.

Chapter II.   Design of new electrode materials from bimetallic sulfate minerals

II.1   Introduction

We have seen in the previous chapter that polyanionic compounds can provide attractive positive electrode materials based on sustainable elements, in particular because they enable to tune the potential of the Fe^{III+}/Fe^{II+} redox center thanks to the inductive effect of the polyanionic groups $(XO_4)^{n-}$ [222,232,233]. From the different examples aforementioned, one can notice that sulfate-based compounds generally display higher potentials than phases with other polyanionic groups. This is explained by the fact that sulfur is more electronegative than other elements X involved in polyanionic groups (phosphorous, boron, silicon, *etc.*). Fluorosulfates, which combine the inductive effect of the sulfate group and the high electronegativity of the fluorine, provide indeed the highest potentials ever reported for the Fe^{III+}/Fe^{II+} redox couple (3.9 V *vs.* Li^+/Li^0 for *triplite* $LiFeSO_4F$ [330,335] and 3.5 V *vs.* Na^+/Na^0 for *maxwellite* $NaFeSO_4F$ [331]). However, growing reluctances to employ fluorine-containing compounds for safety reasons encouraged us to search for other high-voltage electrode materials based on sulfate but free of fluorine. Interestingly, we have seen in the previous chapter that although fluorine is the most electronegative element and is thus expected to enhance the redox potential of the neighboring redox center, fluorophosphates do not systematically display higher voltages than phosphate compounds that contain no fluorine (*e.g.* $LiFePO_4F$, 2.8 V *vs.* Li^+/Li^0, *versus* $Li_3Fe(PO_4)_3$ and $LiFePO_4$, 2.8 V and 3.45 V respectively). We were thus reasonably confident in the possibility of finding fluorine-free sulfate compounds without severe voltage penalty.

Working towards this goal, we decided to seek inspiration from minerals, encouraged by the fact that many positive electrode materials present the structure of mineral species (*cf.* Chapter I, in particular § I.2.3 Polyanions from page 20) as well as by the existence of numerous well documented sulfate-based minerals [358]. More specifically, we focused on naturally-occurring sulfate compounds that contain both alkali (Na or K) and 3d transition metal or magnesium cations, as presented in **Table II.1**. These phases reveal a rich crystallochemistry with different levels of hydration and a great diversity of structures, which present MO_6 octahedra and SO_4 tetrahedra organized either in isolated cluster, in chains or in infinite sheets, thus giving rise to wide pathways in which alkali ions could diffuse. Thus, we explored the possibility of preparing new electrode materials from these polyanionic frameworks using metal substitution and dehydration processes.

Table II.1: Selection of sulfate-based minerals having both alkali and 3d transition metal (or magnesium) cations, arranged according to the Nickel-Strunz classification [359–361].

General formula	Sodium-based minerals	Potassium-based mineral
Hydrated sulfates without additional anions, and with medium-sized (M) and large (A) cations		
$A_2M^{II+}(SO_4)_2 \cdot 2H_2O$	*kröhnkite* $Na_2Cu(SO_4)_2 \cdot 2H_2O$	
$A_2M^{II+}(SO_4)_2 \cdot 4H_2O$	*bloedite* (*astrakhanite*) $Na_2Mg(SO_4)_2 \cdot 4H_2O$ *changoite* (*zincbloedite*) $Na_2Zn(SO_4)_2 \cdot 4H_2O$ *nickelbloedite* $Na_2(Mg,Ni)(SO_4)_2 \cdot 4H_2O$	*leonite* $K_2Mg(SO_4)_2 \cdot 4H_2O$ *mereiterite* $K_2Fe(SO_4)_2 \cdot 4H_2O$
$A_2M^{II+}(SO_4)_2 \cdot 5H_2O$	*konyaite* $Na_2Mg(SO_4)_2 \cdot 5H_2O$	
$A_2M^{II+}(SO_4)_2 \cdot 6H_2O$ (Tutton's salts [362])		*cyanochroite* $K_2Cu(SO_4)_2 \cdot 6H_2O$ *picromerite* (*schoenite*) $K_2Mg(SO_4)_2 \cdot 6H_2O$
$A_{12}M^{II+}_7(SO_4)_{13} \cdot 15H_2O$	*loweite* $Na_{12}Mg_7(SO_4)_{13} \cdot 15H_2O$	
$AM^{III+}(SO_4)_2 \cdot H_2O$		*krausite* $KFe(SO_4)_2 \cdot H_2O$
$AM^{III+}(SO_4)_2 \cdot 4H_2O$		*goldichite* $KFe(SO_4)_2 \cdot 4H_2O$
$AM^{III+}(SO_4)_2 \cdot 6H_2O$	*amarillite* $NaFe(SO_4)_2 \cdot 6H_2O$	
$A_3M^{III+}(SO_4)_3 \cdot 3H_2O$	*ferrinatrite* $Na_3Fe(SO_4)_3 \cdot 3H_2O$	
Anhydrous sulfates without additional anions, and with medium-sized (M) and large (A) cations		
$A_2M^{II+}_2(SO_4)_3$		*langbeinite* $K_2Mg_2(SO_4)_3$ *manganolangbeinite* $K_2Mn_2(SO_4)_3$
$A_6M^{II+}(SO_4)_4$	*vanthoffite* $Na_6Mg(SO_4)_4$	
$AM^{III+}(SO_4)_2$	*eldfellite* $NaFe(SO_4)_2$	*yavapaiite* $KFe(SO_4)_2$

In this chapter, we present two new electrode materials elaborated from the *bloedite* mineral $Na_2Mg(SO_4)_2 \cdot 4H_2O$: the iron analogue $Na_2Fe(SO_4)_2 \cdot 4H_2O$ and its dehydrated derivate α-$Na_2Fe(SO_4)_2$, whose crystal structure has been solved [363,364]. Both of them are electrochemically active against both lithium and sodium metal anodes. In the last part of the chapter, we also report on the electrochemical properties of the *eldfellite* and *yavapaiite* mineral compounds $AFe(SO_4)_2$ (*A* = Na, K).

II.2   *Bloedite* compounds Na$_2$M(SO$_4$)$_2$·4H$_2$O (M = Mg, Zn, Co, Fe, Ni)

Bloedite-type compounds having the general formula Na$_2$M(SO$_4$)$_2$·4H$_2$O (M = Mg, Zn, Ni, Co, Fe) have been widely studied since the 1940s. The first crystallographic study on the *bloedite* mineral Na$_2$Mg(SO$_4$)$_2$·4H$_2$O was reported by Lauro in 1940 **[365]**. Rumanova and Malitskaya determined its structure in 1958 **[366]**, while Giglio reported the same year the one of the synthetic zinc-based phase Na$_2$Zn(SO$_4$)$_2$·4H$_2$O and mentioned that it was isostructural to the magnesium, cobalt, nickel and iron synthetic analogues **[367]**. These structural models were later revisited by different groups from the 1970's to the end of the 2000's **[368–375]**. In the 1960's, Cot and co-workers carried out a detailed study of the thermal stability of these Na$_2$M(SO$_4$)$_2$·4H$_2$O phases (M = Co, Ni, Zn, Fe) and proposed the formation of several anhydrous compounds Na$_2$M(SO$_4$)$_2$ upon water removal from the hydrated parents **[376–381]**. Except for the zinc system, for which a crystal structure has been reported **[382]**, none of these water-free phases was further investigated. We revisit herein these hydrated phases Na$_2$M(SO$_4$)$_2$·4H$_2$O phases (M = Mg, Zn, Ni, Co, Fe), paying special attention to the iron analogue for its electrochemical properties.

II.2.1   Syntheses

Several procedures had been employed in the past to prepare the Na$_2$M(SO$_4$)$_2$·4H$_2$O (M = Mg, Zn, Co, Ni) phases **[367–369,372–374,380,381]**. In our case, we first chose a simple process inspired from natural sedimentation, which consists in slowly evaporating an equimolar solution of commercial sodium sulfate Na$_2$SO$_4$ and metal sulfate heptahydrate MSO$_4$·7H$_2$O at temperatures ranging from 20°C to 90°C. Later, we experienced that the targeted phases were more rapidly obtained by precipitating these solutions of sulfate precursors in ethanol. Alternatively, we equally succeeded in preparing pure phases of Na$_2$M(SO$_4$)$_2$·4H$_2$O by ball-milling (Spex 8000M®) for 20 minutes equimolar amounts of the two aforementioned precursors **[363]**.

Whatever the synthetic route used, these hydrated phases form accordingly to the following reaction:

$$Na_2SO_4 + M^{II}SO_4·7H_2O \rightarrow Na_2M^{II}(SO_4)_2·4H_2O + 3H_2O$$

Given the great aptitude of Fe(II+)-based precursors to oxidize, we prepared the iron analogue Na$_2$Fe(SO$_4$)$_2$·4H$_2$O using similar routes, but carrying the reaction out under inert conditions. This was achieved by employing degassed solvents and adding ascorbic acid for the solution-precipitation route, and by closing the ball-milling jar under argon for the mechanical milling route **[363]**.

II.2.2   Samples characterization

The as-prepared cobalt- and nickel-based phases present bright pink and green colors, respectively (**Figure II.1.a**). Conversely, the magnesium-, zinc- and iron-based compounds are white, any coloration indicating a non-pure sample. The $Na_2M(SO_4)_2 \cdot 4H_2O$ (M = Mg, Zn, Ni, Co, Fe) powders obtained through solution routes present heterogeneous particle sizes, ranging from one to several dozens of microns (**Figure II.1.b**), while the ones prepared *via* mechanical milling are more homogeneous with particles smaller than one micron (**Figure II.1.c**).
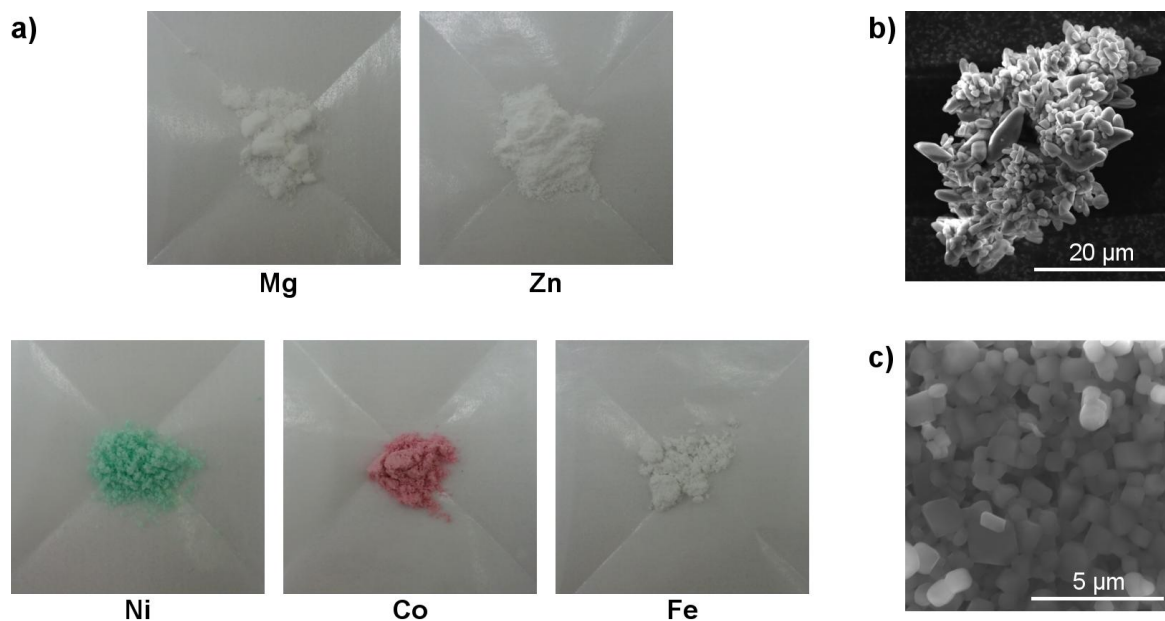
Figure II.1: (a) Powders of $Na_2M(SO_4)_2 \cdot 4H_2O$ (M = Mg, Zn, Ni, Co, Fe). (b) and (c) SEM images of $Na_2Fe(SO_4)_2 \cdot 4H_2O$ samples obtained *via* solution-precipitation and ball-milling routes, respectively.

The presence of structural water was confirmed using infra-red spectroscopy (FTIR), and thermogravimetric analyses (TGA) coupled to mass spectroscopy (MS) verified the amount of four H_2O moieties per formula unit. As seen in **Figure II.2**, the ATG-MS curves revealed two different water-loss mechanisms for the five $Na_2M(SO_4)_2 \cdot 4H_2O$ compounds: on the one hand the water departure of the magnesium, zinc and nickel phases occurs in two-steps, while on the other hand the cobalt and iron analogues release the majority of their structural water in one step, although the water removal is complete only after the long tail seen in the curves until ~280°C.
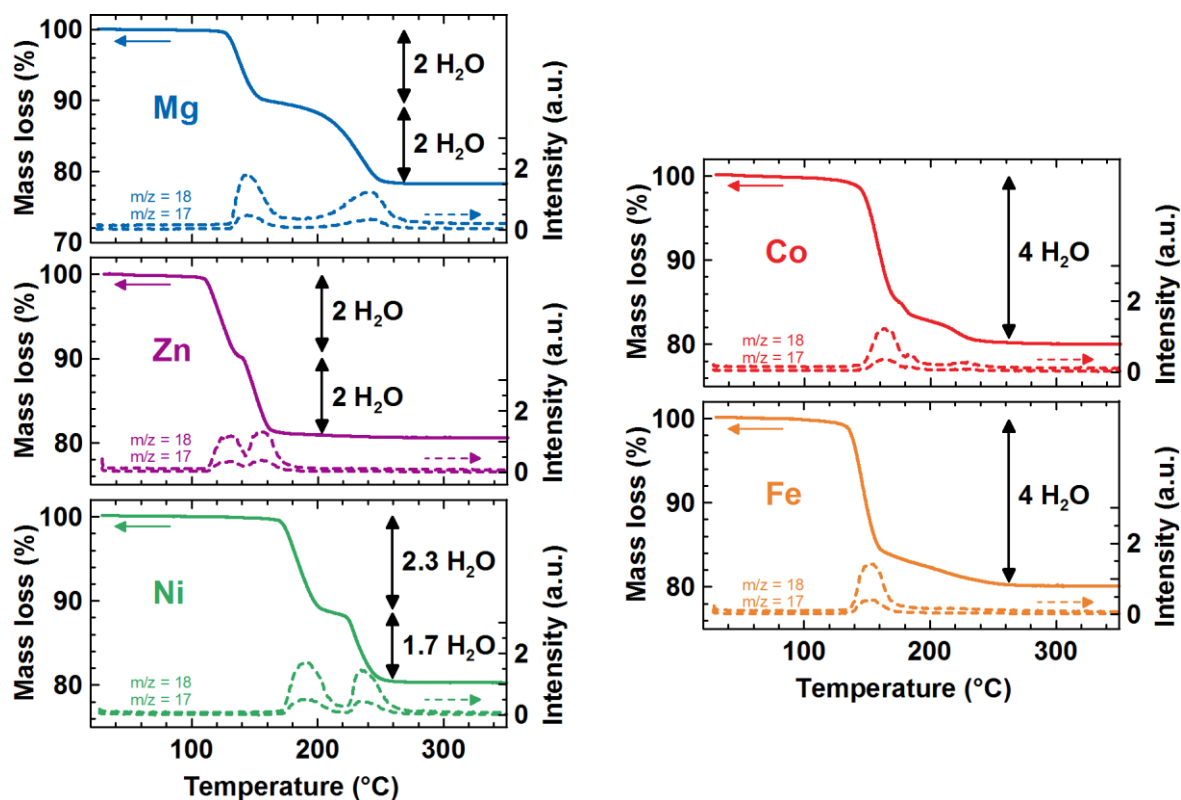
Figure II.2: TGA-MS curves of the five compounds Na$_2$M(SO$_4$)$_2$·4H$_2$O (M = Mg, Zn, Ni, Co, Fe), demonstrating the loss of four molecules of water between 100 and 300°C. Full lines correspond to the mass loss in percentages, while the dotted lines represent the mass curves for m/z = 18 and 17, which correspond to the detection of H$_2$O$^-$ and OH$^-$ ions, respectively.

Purity of the samples was first checked by X-ray diffraction (XRD). The profiles of these laboratory XRD patterns were simulated using the Le Bail method as implemented in the FullProf program **[383,384]** (*cf.* Annexes: § A.3.4 Diffraction data treatment, page 166). They could be fully indexed with the monoclinic cell (space group: P2$_1$/c) previously reported for the *bloedite*-type compounds **[372]**. Taking advantage of the great crystallinity of a Na$_2$Co(SO$_4$)$_2$·4H$_2$O sample, we performed Synchrotron X-ray diffraction at the CRISTAL beamline of SOLEIL Synchrotron (Saint-Aubin, France; *cf.* Annexes: § A.3.2.2 page 164) and neutron powder diffraction on the D2B diffractometer of the Institut Laue Langevin (Grenoble, France; *cf.* Annexes: § A.3.3 page 165). A joint Rieveld refinement **[385]** of these data, conducted using the FullProf program **[383,384]**, enabled to refine the hydrogen positions without any constraints (see **Figure II.3** and **Table II.2**). The resulting structural model was then used to refine the XRD patterns of the other four compounds Na$_2$M(SO$_4$)$_2$·4H$_2$O (M = Zn, Mg, Ni, Fe). The results of these refinements are presented in **Table II.3** to **Table II.6**. One can observe a smooth increase in the unit cell volume as the ionic radii of the 3d-metal cations M(II+) **[111]** become bigger in the series Ni-Zn-Co-Fe (**Figure II.4**). As previously reported by Stoilova and Wildner **[372]**, the magnesium analogue makes an exception as it does not follow this trend.
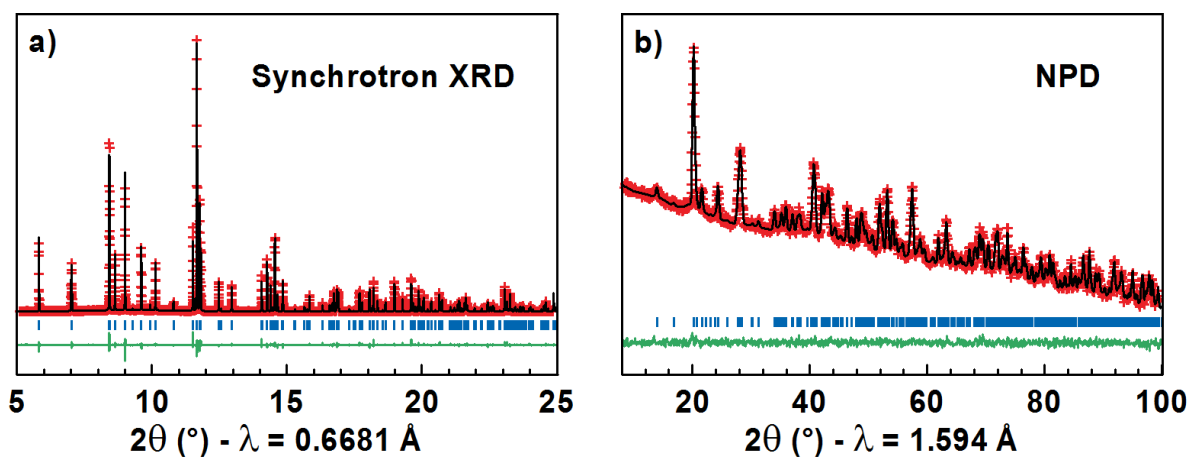
Figure II.3: Results of the joint Rietveld refinement of the (a) Synchrotron X-ray diffraction (XRD) and (b) neutron powder diffraction (NPD) data for $Na_2Co(SO_4)_2 \cdot 4H_2O$. The blue sticks represent the Bragg peak positions of the phase, the red crosses and the black line are the experimental and the simulated patterns, respectively; the difference between these two patterns is shown with the green line (note that this color coding will be used in the rest of the manuscript).
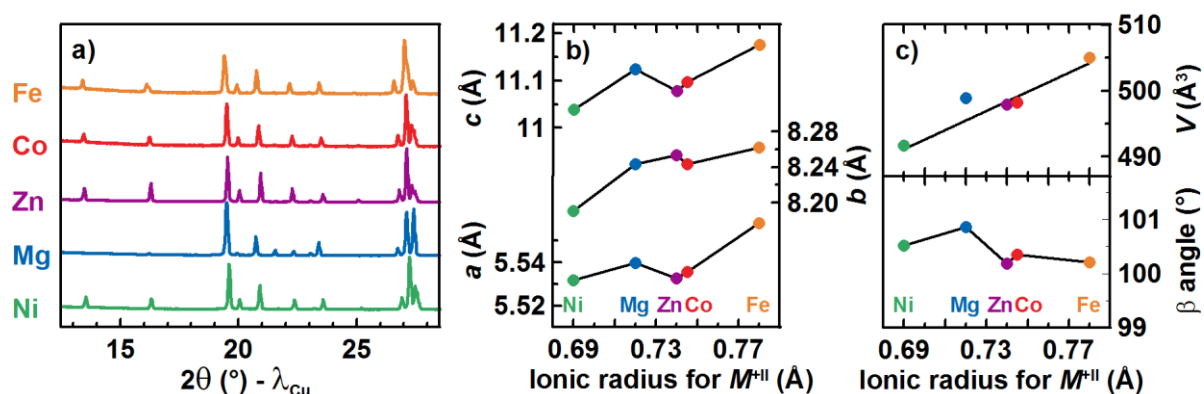
Figure II.4: (a) Comparison of the XRD patterns of the five *bloedite* phases $Na_2M(SO_4)_2 \cdot 4H_2O$ (M = Ni, Mg, Zn, Co, Fe). (b) and (c) Variation of the lattice parameters a, b, c, β and the cell volume V as a function of the ionic radii of M^{II+} [111] (note that error bars are smaller than the points displayed on the graphs).

Table II.2: Crystallographic data and atomic positions of $Na_2Co(SO_4)_2 \cdot 4H_2O$ deduced from a combined Rietveld refinement of SOLEIL Synchrotron X-ray diffraction ($\lambda = 0.6681$ Å) and ILL neutron diffraction ($\lambda = 1.594$ Å) data. Bond Valence Sum analysis (BVS) is also indicated.

$Na_2Co(SO_4)_2 \cdot 4H_2O$					
Space group $P2_1/c$			$\chi^2 = 1.37$		$R_{Bragg} = 5.72$ %
$a = 5.5356(4)$ Å	$b = 8.2436(5)$ Å	$c = 11.0978(6)$ Å	$\beta = 100.356(5)°$		$V = 498.18(5)$ Å^3

Atom	Wyckoff site	x/a	y/b	z/c	B_{iso} (Å^2)	BVS
Na	4e	0.1290(12)	0.0700(9)	0.3617(5)	0.99(15)	1.11(2)
Co	2a	0	0	0	0.31(6)	2.00(2)
S	4e	0.3701(9)	0.2879(5)	0.1361(4)	0.47(9)	5.93(9)
O1	4e	0.3462(15)	0.2704(12)	0.2676(9)	1.1(2)	2.13(4)
O2	4e	0.2026(15)	0.4151(12)	0.0789(9)	1.0(2)	2.04(4)
O3	4e	0.3148(15)	0.1319 (12)	0.0725(9)	0.9(2)	1.80(4)
O4	4e	0.6280(18)	0.3299(12)	0.1320(9)	1.0(2)	2.31(4)
O5	4e	0.1277(15)	0.5392(12)	0.3379(9)	0.8(2)	1.66(4)
O6	4e	0.1760(15)	0.7861(12)	0.0815(9)	0.9(2)	1.58(4)
H1	4e	0.230(9)	0.445(5)	0.321(4)	2.2(9)	0.93(3)
H2	4e	0.227(9)	0.636(5)	0.344(4)	3.2(9)	1.05(4)
H3	4e	0.683(9)	0.303(6)	0.359(5)	3.1(9)	1.03(3)
H4	4e	0.237(9)	0.719(6)	0.021(4)	3.2(9)	0.98(4)

Table II.3: Crystallographic data and atomic positions of $Na_2Zn(SO_4)_2 \cdot 4H_2O$ deduced from a Rietveld refinement of SOLEIL Synchrotron data ($\lambda = 0.6681$ Å). Bond Valence Sum analysis (BVS) is also indicated. Hydrogen atomic positions were not refined but fixed at the values determined from the joint refinement of data for the cobalt analogue.

$Na_2Zn(SO_4)_2 \cdot 4H_2O$					
Space group $P2_1/c$			$\chi^2 = 1.70$		$R_{Bragg} = 4.60$ %
$a = 5.5328(2)$ Å	$b = 8.2536(2)$ Å	$c = 11.0771(2)$ Å	$\beta = 100.185(2)°$		$V = 497.87(2)$ Å^3

Atom	Wyckoff site	x/a	y/b	z/c	B_{iso} (Å^2)	BVS
Na	4e	0.1283(7)	0.0698(5)	0.3616(4)	1.10(12)	1.12(2)
Zn	2a	0	0	0	0.58(4)	2.05(2)
S	4e	0.3723(5)	0.2882(4)	0.1362(3)	0.54(6)	5.98(3)
O1	4e	0.3487(12)	0.2699(7)	0.2676(6)	0.83(7)	2.14(4)
O2	4e	0.2069(11)	0.4158(8)	0.0791(6)	0.83(7)	1.94(3)
O3	4e	0.3177(11)	0.1327(8)	0.0717(6)	0.83(7)	1.97(4)
O4	4e	0.6296(12)	0.3300(8)	0.1318(6)	0.83(7)	2.20(4)
O5	4e	0.1267(12)	0.5380(9)	0.3373(6)	0.83(7)	1.87(6)
O6	4e	0.1736(12)	0.7866(9)	0.0823(6)	0.83(7)	1.75(6)
H1	4e	0.230	0.4452	0.3208	2.2	0.94(5)
H2	4e	0.227	0.6359	0.3438	3.2	1.05(5)
H3	4e	0.683	0.3027	0.3587	3.1	0.89(3)
H4	4e	0.237	0.7186	0.0206	3.2	0.87(6)

Table II.4: Crystallographic data and atomic positions of $Na_2Mg(SO_4)_2\cdot4H_2O$ deduced from a Rietveld refinement of laboratory XRD data (Co source: $\lambda_{K\alpha1}$ = 1.78897 Å, $\lambda_{K\alpha2}$ = 1.79285 Å). Bond Valence Sum analysis (BVS) is also indicated. Hydrogen atomic positions were not refined but fixed at the values determined from the joint refinement of data for the cobalt analogue.

$Na_2Mg(SO_4)_2\cdot4H_2O$						
Space group $P2_1/c$				χ^2 = 3.08		R_{Bragg} = 7.71 %
a = 5.5398(2) Å	b = 8.2432(2) Å		c = 11.1242(2) Å	β = 100.868(2)°		V = 498.88(2) Å^3
Atom	Wyckoff site	x/a	y/b	z/c	B_{iso} (Å^2)	BVS
Na	4e	0.134(2)	0.071(2)	0.361(2)	1.93(18)	1.09(2)
Mg	2a	0	0	0	2.1(2)	1.97(2)
S	4e	0.369(2)	0.290(2)	0.139(2)	1.17(12)	5.91(10)
O1	4e	0.344(2)	0.271(2)	0.264(2)	1.67(15)	2.43(6)
O2	4e	0.210(2)	0.425(2)	0.075(2)	1.67(15)	1.88(4)
O3	4e	0.312(2)	0.139(2)	0.068(2)	1.67(15)	1.93(5)
O4	4e	0.634(2)	0.327(2)	0.131(2)	1.67(15)	2.17(5)
O5	4e	0.123(2)	0.535(2)	0.340(2)	1.67(15)	1.79(2)
O6	4e	0.176(2)	0.796(2)	0.082(2)	1.67(15)	1.71(2)
H1	4e	0.230	0.445	0.321	2.2	0.93(2)
H2	4e	0.227	0.636	0.344	3.2	1.03(2)
H3	4e	0.683	0.303	0.359	3.1	1.03(2)
H4	4e	0.237	0.719	0.021	3.2	0.95(2)

Table II.5: Crystallographic data and atomic positions of $Na_2Ni(SO_4)_2\cdot4H_2O$ deduced from a Rietveld refinement of laboratory XRD data (Co source: $\lambda_{K\alpha1}$ = 1.78897 Å, $\lambda_{K\alpha2}$ = 1.79285 Å). Bond Valence Sum analysis (BVS) is also indicated. Hydrogen atomic positions were not refined but fixed at the values determined from the joint refinement of data for the cobalt analogue.

$Na_2Ni(SO_4)_2\cdot4H_2O$						
Space group $P2_1/c$				χ^2 =1.63		R_{Bragg} =2.72 %
a = 5.5316(2) Å	b = 8.1906(2) Å		c = 11.0379(2) Å	β = 100.513(2)°		V = 491.71(2) Å^3
Atom	Wyckoff site	x/a	y/b	z/c	B_{iso} (Å^2)	BVS
Na	4e	0.130(2)	0.070(2)	0.362(2)	1.22(13)	1.14(2)
Ni	2a	0	0	0	0.03(7)	2.00(2)
S	4e	0.373(2)	0.287(2)	0.137(2)	0.68(8)	5.71(8)
O1	4e	0.349(2)	0.268(2)	0.268(2)	1.03(10)	2.21(5)
O2	4e	0.204(2)	0.416(2)	0.078(2)	1.03(10)	1.98(4)
O3	4e	0.319(2)	0.127(2)	0.070(2)	1.03(10)	1.81(3)
O4	4e	0.631(2)	0.329(2)	0.129(2)	1.03(10)	2.29(4)
O5	4e	0.124(2)	0.535(2)	0.340(2)	1.03(10)	1.82(2)
O6	4e	0.177(2)	0.790(2)	0.031(2)	1.03(10)	1.73(2)
H1	4e	0.230	0.445	0.321	2.2	0.93(2)
H2	4e	0.227	0.636	0.344	3.2	1.04(2)
H3	4e	0.683	0.303	0.359	3.1	1.04(2)
H4	4e	0.237	0.719	0.021	3.2	0.98(2)

Table II.6: Crystallographic data and atomic positions of $Na_2Fe(SO_4)_2 \cdot 4H_2O$ deduced from a Rietveld refinement of laboratory XRD data (Co source: $\lambda_{K\alpha1}$ = 1.78897 Å, $\lambda_{K\alpha2}$ = 1.79285 Å). Bond Valence Sum analysis (BVS) is also indicated. Hydrogen atomic positions were not refined but fixed at the values determined from the joint refinement of data for the cobalt analogue.

$Na_2Fe(SO_4)_2 \cdot 4H_2O$						
Space group $P2_1/c$				χ^2 = 15.1		R_{Bragg} = 10.3 %
a = 5.5581(3) Å		b = 8.2622(5) Å	c = 11.1753(6) Å	β = 100.210(4)°		V = 505.06(5) Å^3
Atom	**Wyckoff site**	**x/a**	**y/b**	**z/c**	**B_{iso} (Å^2)**	**BVS**
Na	4e	0.129(3)	0.068(2)	0.362(2)	1.0(5)	1.22(4)
Fe	2a	0	0	0	3.8(5)	1.74(5)
S	4e	0.368(3)	0.290(2)	0.139(2)	0.1(3)	6.3(3)
O1	4e	0.341(5)	0.266(3)	0.265(3)	0.34(11)	2.29(15)
O2	4e	0.206(5)	0.416(3)	0.070(2)	0.34(11)	1.96(10)
O3	4e	0.336(5)	0.150(3)	0.073(2)	0.34(11)	2.25(16)
O4	4e	0.631(6)	0.330(3)	0.124(3)	0.34(11)	2.10(12)
O5	4e	0.110(5)	0.537(3)	0.327(2)	0.34(11)	1.64(3)
O6	4e	0.178(5)	0.788(3)	0.088(3)	0.34(11)	1.58(3)
H1	4e	0.230	0.445	0.321	2.2	0.90(2)
H2	4e	0.227	0.636	0.344	3.2	1.01(2)
H3	4e	0.683	0.303	0.359	3.1	1.04(2)
H4	4e	0.237	0.719	0.021	3.2	0.95(2)

The *bloedite* structure is built upon isolated units made of one MO_6 octahedron surrounded by four water moieties in the equatorial plane and two axial SO_4 tetrahedra. These individual units are aligned along the *a*-axis, as seen in **Figure II.5**. The distance between two metals is above 5 Å, and thus the $M(SO_4)_2(H_2O)_4$ units are rather spaced one from another. Such a low connectivity between the 3d transition metals is likely to result in poor electronic conductivity properties. Conversely, ionic transport could be favored by the fact that the sodium ions sit in the large channels running along the [100] direction. Each sodium atom is coordinated by six oxygen atoms, which form distorted NaO_6 octahedra that are linked two by two through edges, thus generating isolated Na_2O_{10} bi-octahedra.
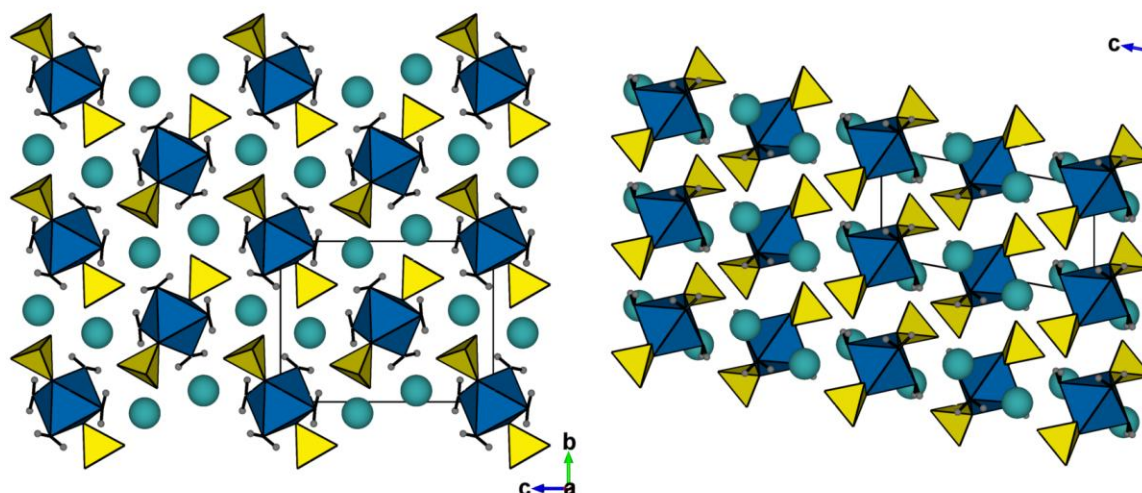
Figure II.5: Representation of the *bloedite* structure, along the *a*-axis (left) and along the *b*-axis (right).

II.2.3   Electrochemistry of Na$_2$Fe(SO$_4$)$_2$·4H$_2$O

To explore the feasibility of sodium removal from these large channels, we studied the electrochemical properties of the Na$_2$M(SO$_4$)$_2$·4H$_2$O (*M* = Mg, Zn, Ni, Co, Fe) compounds against both lithium and sodium metal anodes. However, we found that the iron-based phase was the only one to show electrochemically activity against both lithium and sodium **[363,364]**.

The electrode materials were prepared by ball-milling for 20 minutes under argon a 70:30 mass ratio of the active material Na$_2$Fe(SO$_4$)$_2$·4H$_2$O and carbon SP. The as-prepared positive electrode materials were loaded in Swagelok® cells (*cf.* Annexes: § A.2 Electrochemical characterizations, page 158) and tested against lithium and sodium metals with several electrolytes. Initial attempts to use classical LiPF$_6$-based electrolytes (*e.g.* LP30) in lithium half-cells failed as a drastic voltage drop appeared when nearly ~0.4 Na$^+$ ion was extracted from the material (**Figure II.6.a**). *In situ* XRD measurements of the electrode material at different states of charge showed that this voltage drop was associated with the reaction of Na$_2$Fe(SO$_4$)$_2$·4H$_2$O with the electrolyte, as indicated in particular by the apparition of Li$_2$SO$_4$ and FeSO$_4$·H$_2$O in the XRD patterns (**Figure II.6.b**). Therefore, we believe that at this stage of Na$^+$-ion removal the structural water may become more labile and reacts with the PF$_6^-$ anion of the electrolyte salt; PF$_6^-$ would decompose into PF$_5$ + HF, with the latter attacking at its turn our electrode material.
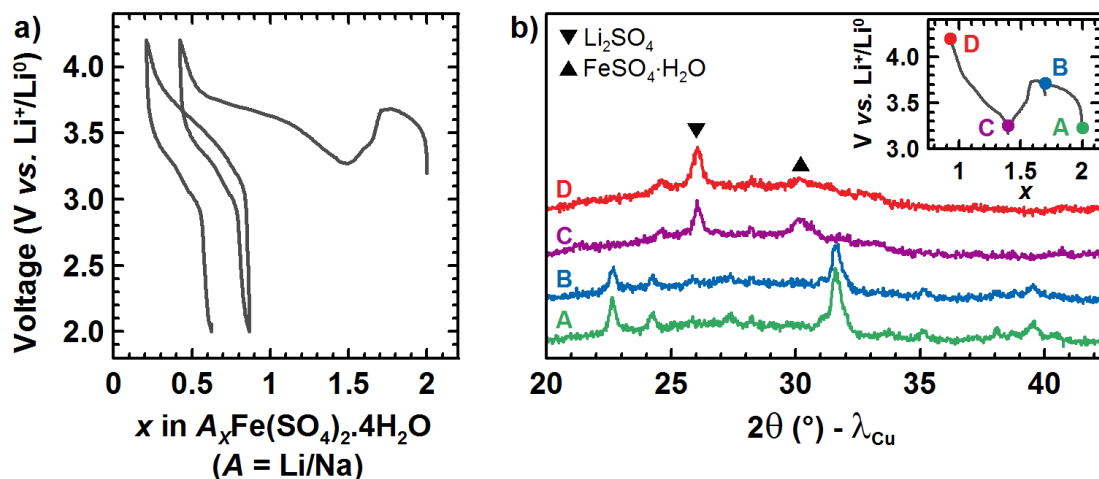
Figure II.6: (a) Galvanostatic curve obtained for a Li // LP30 // $Na_2Fe(SO_4)_2 \cdot 4H_2O/C_{SP}$ cell showing the uncommon drop in voltage near $\Delta x \approx 0.4$ as described in the text. (b) *In situ* XRD patterns of the positive electrode material at different states of charge.

To circumvent this problem, we envisaged the use of PF_6^--free electrolytes, such as LiTFSI 1M in EC/DMC and $LiClO_4$ or $NaClO_4$ 1M in PC. We eventually found that $Na_2Fe(SO_4)_2 \cdot 4H_2O$ successfully cycles *versus* both lithium and sodium metals using these electrolytes at a slow cycling rate of one electron in 50 hours (**Figure II.7**). Whatever the nature of the negative electrode (Li or Na metals), the first charge, whose amplitude nearly approaches one sodium, is flat (in red in **Figure II.7**). This contrasts with the following discharge and subsequent charge/discharge curves that show an S-type shape (in blue and green in **Figure II.7**). This phenomenon is highlighted when plotting the derivatives (dx/dV): they show a sharp peak for the first charge, which becomes much broader for the subsequent cycles. From both the voltage-composition and the derivative curves, one can deduce that the electrochemical activity of $Na_2Fe(SO_4)_2 \cdot 4H_2O$ is centered near 3.6 V *versus* Li^+/Li^0 and 3.3 V *versus* Na^+/Na^0. These potentials are higher than the one of $LiFePO_4$ (3.45 V *vs.* Li^+/Li^0 **[233]**) and compare well with other sulfate compounds, such as the NASICON-type $Fe_2(SO_4)_3$ (3.6 V *vs.* Li^+/Li^0 **[222,223]**), the *tavorites* $LiFeSO_4F$ (3.6 V *vs.* Li^+/Li^0 **[321]**) and $FeSO_4OH$ (3.2 V *vs.* Li^+/Li^0 **[340]**), the layered $LiFeSO_4OH$ (3.6 V *vs.* Li^+/Li^0 **[342]**), and the *maxwellite* $NaFeSO_4F$ (~3.5 V *vs.* Na^+/Na^0 **[331]**). Note that the 300-mV difference observed between the lithium and the sodium half-cells falls within the range of the voltage differences observed and/or expected for other polyanionic materials, as commented in Chapter I and in the following references **[317,318,386,387]**. Last, the shift to the left of the voltage-composition curves suggests a progressive solvent decomposition upon charging, with this effect being more pronounced for Na- than Li-based cells. The use of other (better) electrolytes could alleviate this issue, however we did not judge highly relevant to perform advanced electrode and electrolyte optimizations given that the limited cycling performances of $Na_2Fe(SO_4)_2 \cdot 4H_2O$, as suggested by its poor kinetics (slow cycling rate, need of 30 %wt of conductive carbon) and its low reversible capacity (≤ 50 mAh/g for the first five cycles).
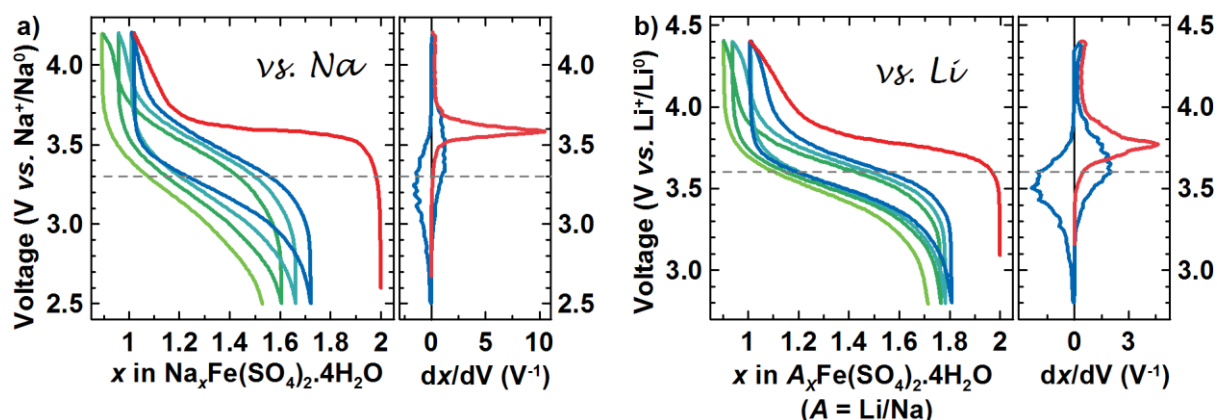
Figure II.7: Electrochemistry of $Na_2Fe(SO_4)_2 \cdot 4H_2O$ (a) *versus* sodium and (b) *versus* lithium, using $NaClO_4$ in PC and $LiClO_4$ in PC as the electrolytes, respectively, and a C/50 cycling rate. The left panels show the voltage-composition traces, with a flat-like first charge (in red) and more sloping subsequent discharge and charges (blue to green), while the right panels display the corresponding derivative curves (dx/dV).

To grasp insights into the evolution of the voltage-composition curves from flat to S-type between the first charge and the subsequent discharge, *ex situ* X-ray diffraction measurements were carried out. For that purpose, Na // 1M $NaClO_4$ in PC // $Na_2Fe(SO_4)_2 \cdot 4H_2O$/C cells were assembled, stopped at different states of charge and discharge, and the positive electrodes were then recovered, washed and X-rayed. The collected diffraction patterns are shown in **Figure II.8**. They show the progressive amorphization of the active material $Na_xFe(SO_4)_2 \cdot 4H_2O$ upon charging, which goes with a growth of the background in the range $20 \leq 2\theta \leq 45°$. Such an amorphization is consistent with the onset of the S-type voltage-composition curve once the first charge is achieved. Note that featureless XRD patterns were equally obtained for $Na_1Fe(SO_4)_2 \cdot 4H_2O$ samples that were prepared from chemical oxidation of $Na_2Fe(SO_4)_2 \cdot 4H_2O$ using NO_2BF_4 in acetonitrile as the oxidizing agent.
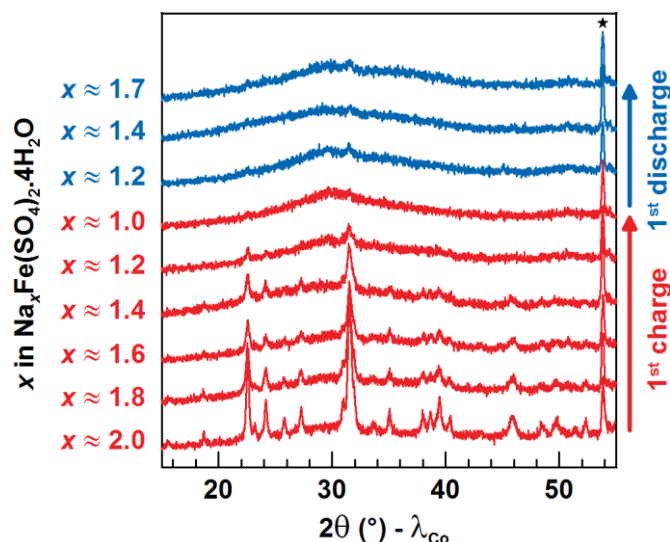
Figure II.8: *Ex situ* X-ray diffraction patterns of the $Na_xFe(SO_4)_2 \cdot 4H_2O/C_{SP}$ electrodes recovered at different states (x) of the first charge and the first discharge. The star indicates a reflection of Be, due to the beryllium window of the XRD sample holder (*cf.* Annexes: § A.3.1.2 page 162).

^{57}Fe Mössbauer spectroscopy[*] was used to gain access to the changes in the local environment and the oxidation state of the iron upon sodium removal and uptake (*cf.* Annexes: § A.4.1 ^{57Fe} Mössbauer Spectrosocopy, page 167). All the recorded spectra were fitted with Lorentzian lines using the FullHam program. First, the spectrum recorded for the pristine $Na_2Fe(SO_4)_2 \cdot 4H_2O$ (**Figure II.9.a**) presents a single and narrow doublet of a Fe(II+) in high-spin configuration, confirming that there is a unique iron site in the structure (**Table II.7**). Whatever the synthesis route employed, no trace of Fe(III+) was detected, confirming the purity of the pristine phase $Na_2Fe(SO_4)_2 \cdot 4H_2O$. Next, the Mössbauer spectrum of the chemically oxidized phase $Na_1Fe(SO_4)_2 \cdot 4H_2O$ shows that iron is fully oxidized, but the large width of the signal suggests a distribution of iron environments, which is in agreement with the amorphous nature of the sample (**Figure II.9.b** and **Table II.7**).
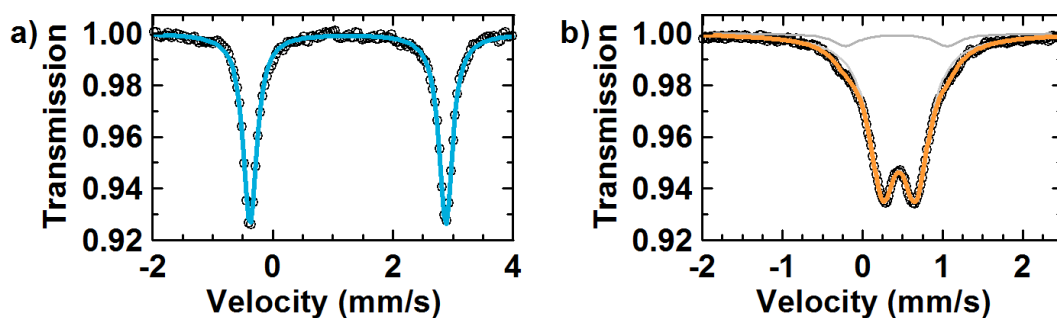
Figure II.9: ^{57}Fe Mössbauer spectra of (a) the as-prepared $Na_2Fe(SO_4)_2 \cdot 4H_2O$ and (b) the $Na_1Fe(SO_4)_2 \cdot 4H_2O$ obtained from chemical oxidation of the pristine sample.

---

[*] All Mössbauer spectroscopy experiments presented in this manuscript were conducted in collaboration with Dr. Moulay Tahar Sougrati at the Institut Charles Gerhardt (UMR 5253), Université de Montpellier 2, Montpellier, France.

Table II.7: Room temperature ^{57}Fe Mössbauer parameters for the pristine $Na_2Fe(SO_4)_2 \cdot 4H_2O$, the chemically oxidized phase $Na_1Fe(SO_4)_2 \cdot 4H_2O$, and the electrode materials $Na_xFe(SO_4)_2 \cdot 4H_2O/C_{SP}$ at different states of charge and discharge. δ represents the isomer shift relative to metallic iron standard at room temperature, while ΔE_q and Γ indicate the quadrupole splitting and the line width, respectively.

	Attribution	δ (mm/s)	ΔEq (mm/s)	Γ (mm/s)	Molar fraction (%)
$Na_2Fe(SO_4)_2 \cdot 4H_2O$ *pristine*	Fe(II+)·A	1.25(1)	3.25(1)	0.27(1)	100(−)
$Na_1Fe(SO_4)_2 \cdot 4H_2O$ *chemically oxidized*	Fe(III+)·A	0.45(1)	0.41(1)	0.41(1)	92(2)
	Fe(III+)·B	0.42(2)	1.27(4)	0.38(6)	8(2)
$Na_2Fe(SO_4)_2 \cdot 4H_2O/C_{SP}$ *electrode material*	Fe(II+)·A	1.26(1)	3.25(1)	0.31(2)	52(3)
	Fe(II+)·B	1.22(2)	2.31(5)	0.73(6)	39(3)
	Fe(III+)·C	0.55(4)	0.45(5)	0.49(−)	9(6)
$Na_{\sim 1}Fe(SO_4)_2 \cdot 4H_2O/C_{SP}$ *end of the 1st charge*	Fe(III+)·A′	0.42(1)	0.51(2)	0.49(3)	100(−)
$Na_{\sim 1.7}Fe(SO_4)_2 \cdot 4H_2O/C_{SP}$ *end of the 1st discharge*	Fe(II+)·B	1.15(2)	2.39(4)	0.66(7)	72(4)
	Fe(III+)·A′	0.42(−)	0.51(−)	0.49(−)	28(4)

The $Na_xFe(SO_4)_2 \cdot 4H_2O/C_{SP}$ samples prepared for the *ex situ* XRD experiment were also analyzed by Mössbauer spectroscopy. **Figure II.10** presents the results of the fits of the collected spectra. First, one can notice that the spectrum of the electrode material $Na_2Fe(SO_4)_2 \cdot 4H_2O/C_{SP}$ differs from the one recorded for the pristine $Na_2Fe(SO_4)_2 \cdot 4H_2O$: the doublet of Fe(II+) (labelled Fe(II+)·A) observed for the pristine sample is still present, but it is accompanied by an additional broad doublet of Fe(II+) (labelled Fe(II+)·B) as well as a small doublet of an oxidized Fe(III+) (**Table II.7**). The presence of a second signal of divalent iron indicates that the environment of part of the Fe(II+) in the active material is modified during the electrode preparation. To assess the influence of the milling time on the amount of $Na_2Fe(SO_4)_2 \cdot 4H_2O$ that is altered, we prepared several electrode materials by ball-milling the active material with carbon for 10, 20, 40 and 60 minutes, and we found that 40 to 45 % of the iron had its local environment modified whatever the ball-milling time.

Figure II.11 shows the evolution of the relative contribution of each of the three signals (Fe(II+)·A, Fe(II+)·B and Fe(III+)·A′) as a function of the state of charge and state of discharge. When charging the electrode material, the two signals of Fe(II+) decrease simultaneously while the signal of Fe(III+) increases. The spectrum at the end of the charge ($x \approx 1.0$) shows no trace of Fe(II+), and its large doublet of Fe(III+) (denoted Fe(III+)·A′) presents a quadrupole splitting slightly different from the one obtained for the chemically oxidized sample (Fe(III+)·A), which may suggest different iron environments (**Table II.7**). During the subsequent discharge, the Fe(III+) signal decreases at its turns in favor of the rise of the broad doublet of Fe(II+)·B, while no trace of Fe(II+)·A is detected. Again, such a broad signal indicates a diversity of similar iron environments, in agreement with the amorphous nature of the sample as concluded from the diffraction observations.
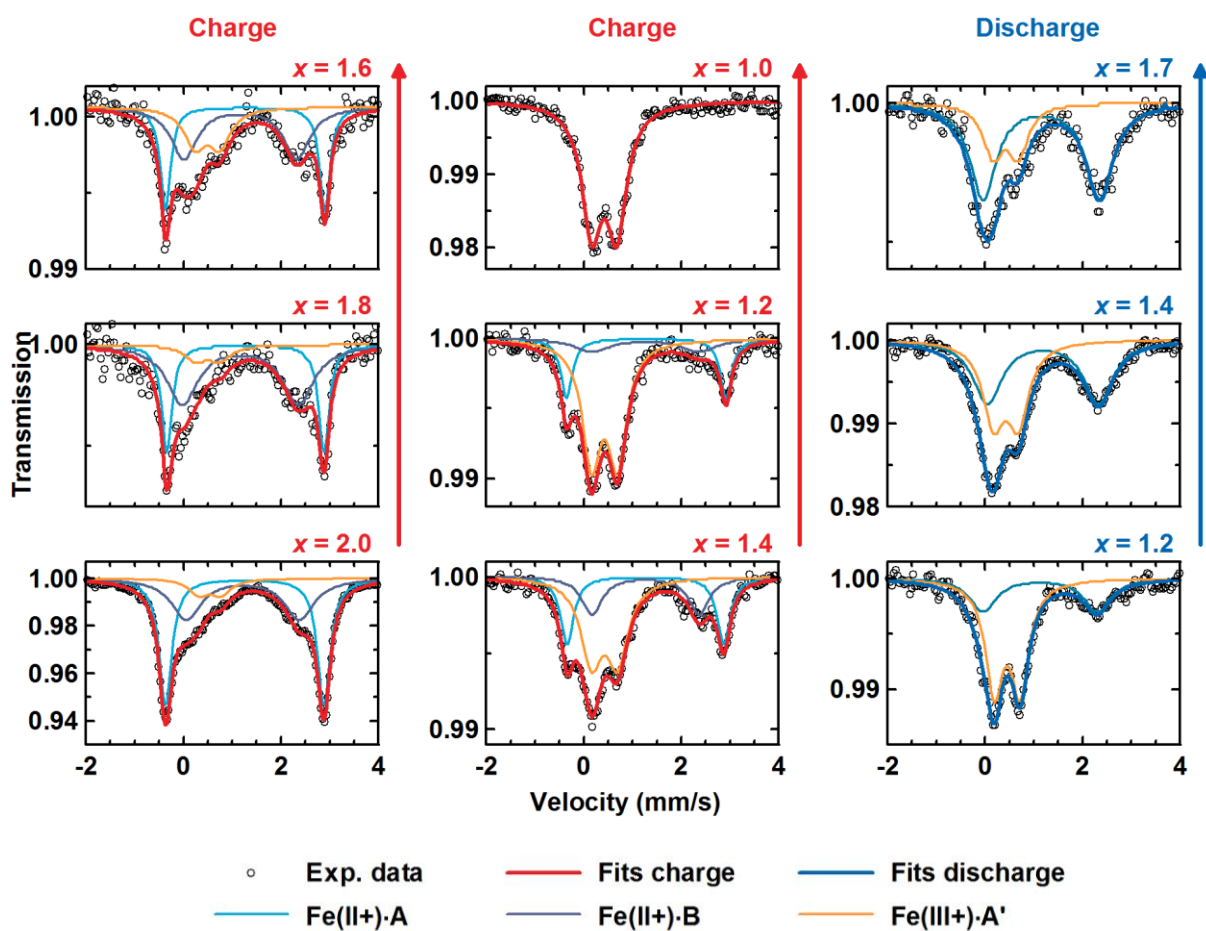
Figure II.10: *Ex situ* [57]Fe Mössbauer spectra of the electrode material recovered at different states (*x*) of the first charge and the first discharge. Black circles represent the experimental data; the bold red (for charge) and blue (for discharge) lines are the simulated spectra, and are deconvoluted into thin blue and orange lines, which represent the Fe(II+) and Fe(III+) contributions, respectively. Note that the poor statistic of some of the spectra is due to the very small amount of sample available.
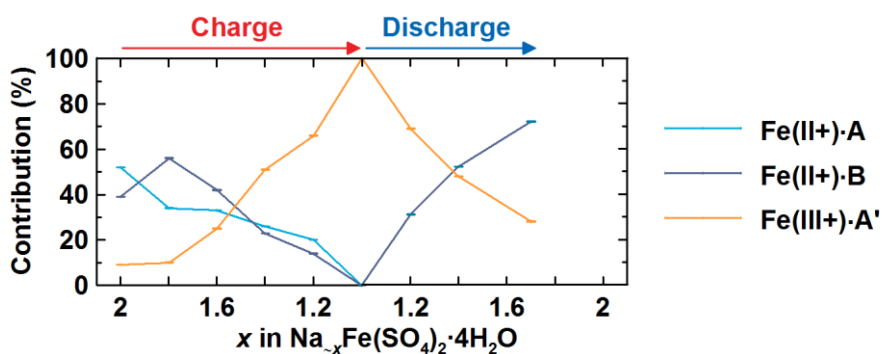
Figure II.11: Evolution of the relative contribution of the three sub-spectra denoted Fe(II+)·A, Fe(II+)·B and Fe(III+)·A' to the [57]Fe Mössbauer spectra of the electrode material as a function of the state (*x*) of charge and discharge during the first cycle.

To complete the characterization of the electrode material during the first charge/discharge cycle, we probed the presence of water by combining infra-red spectroscopy and thermogravimetric analyses coupled to mass spectroscopy. The presence in the FTIR spectra of the chemically oxidized $Na_1Fe(SO_4)_2\cdot4H_2O$ samples, of both a broad signal above 3000 cm^{-1} and a sharp band at around 1700 cm^{-1} (indicated with black arrows in **Figure II.12**), as equally observed for the pristine $Na_2Fe(SO_4)_2\cdot4H_2O$ ones, unambiguously indicated that the water was maintained into the structure after the removal of sodium. Moreover, ATG-MS measurements confirmed the amount of four molecules in these samples. However, to our surprise, both FTIR and ATG-MS analyses showed that conversely the electrode materials recovered after the first charge present no trace of water (**Figure II.12**). After verifying that $Na_2Fe(SO_4)_2\cdot4H_2O$ and the chemically oxidized phase $Na_1Fe(SO_4)_2\cdot4H_2O$ do not dehydrate when submerged into the electrolyte during extended time, we concluded that the loss of the structural water of our electrode material occurs concurrently to the electrochemical sodium removal and the amorphization of the structure, these concurrent phenomena being expressed in the peculiar flat-like trace of the first charge. However we have no explanation for the different behavior observed when the sample is oxidized chemically yet.
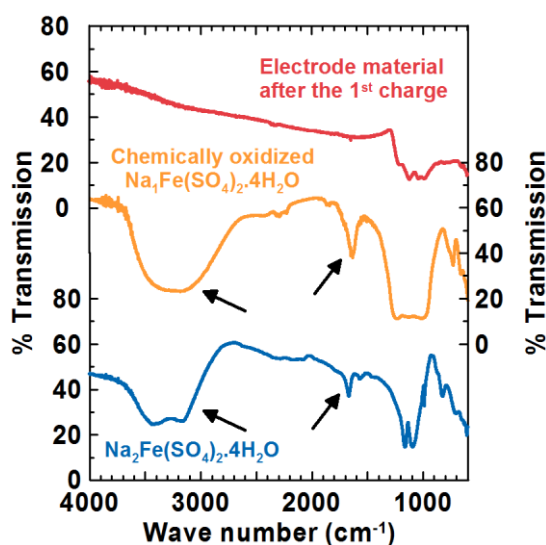
Figure II.12: Infra-red spectra of the pristine $Na_2Fe(SO_4)_2\cdot4H_2O$ (in blue), the chemically oxidized phase $Na_1Fe(SO_4)_2\cdot4H_2O$ (in orange) and the electrode material recovered after the first charge (in red). The black arrows indicate the broad signal above 3000 cm^{-1} and the sharp band at around 1700 cm^{-1}, which indicate the presence of structural water in the two first samples. These features are not visible in the third sample. Strong bands in the region 900-1300 cm^{-1} and medium bands below 800 cm^{-1} are attributed to the sulfate groups.

At this stage, knowing that $Na_2Fe(SO_4)_2\cdot4H_2O$ can lose its structural water either by thermal treatment or through electrochemical oxidation, an obvious prolongation of this work was to prepare a dehydrated $Na_2Fe(SO_4)_2$ phase (theoretical specific capacity of ~91 mAh/g *versus* ~73 mAh/g for the hydrated phase) to study its electrochemical behavior. Cot had previously reported the existence of such anhydrous phases $Na_2M(SO_4)_2$ (*M* = Co, Ni, Fe, Zn) **[376–379,381]**, but their structures were not

solved. We therefore embarked in the preparation of high purity and well crystallized samples, which required to previously understand the water removal process.

II.3   Anhydrous *bloedite*-derivatives α-Na$_2$$M$(SO$_4$)$_2$ (M = Co, Fe)

II.3.1   Dehydration of the *bloedite* phases Na$_2$$M$(SO$_4$)$_2$·4H$_2$O ($M$ = Co, Fe) and preparation of the anhydrous derivatives α-Na$_2$$M$(SO$_4$)$_2$ (M = Co, Fe)

Previous thermogravimetric analyses had shown that the four water moieties of the *bloedite* compounds Na$_2$$M$(SO$_4$)$_2$·4H$_2$O ($M$ = Mg, Zn, Ni, Co, Fe) were released between 100 and 300°C (**Figure II.2** page 47), thus supporting the feasibility of preparing the corresponding anhydrous Na$_2$$M$(SO$_4$)$_2$ phases. Moreover, these measurements suggested that these water removals occurred according to two different mechanisms depending on the nature of the divalent metal. For this reason, we decided to focus on the cobalt and iron systems, which present similar water-loss behaviors.

To obtain further insight into the dehydration process, we monitored the evolution of the XRD patterns as a function of the heating temperature. These measurements were conducted using a special furnace chamber adapted to the diffractometer (see more details in Annexes: § A.3.1.4 High-temperature XRD measurements, page 163), which enabled to slowly heat the Na$_2$$M$(SO$_4$)$_2$·4H$_2$O powder compounds either under air (M = Co) or under nitrogen flow (M = Fe) while recording the XRD patterns at different temperature steps. As one can see in **Figure II.13**, both iron and cobalt samples display a similar behavior upon water departure. The beginning of the dehydration process is associated with a radical change of the XRD patterns (green patterns in **Figure II.13**), from which we could identify a certain quantity of Na$_2$SO$_4$ and MSO$_4$·H$_2$O (M = Co or Fe) among other unknown phases. At the end of the dehydration, we observed the crystallization of a new phase whose pattern (shown in red in **Figure II.13**) matches with the Debye-Scherrer pattern reported by Cot for α-Na$_2$Co(SO$_4$)$_2$ **[376,381]**. Note that the dehydration of the Na$_2$$M$(SO$_4$)$_2$·4H$_2$O phases to α-Na$_2$$M$(SO$_4$)$_2$ is accompanied by a change in color of the powder samples, turning from pale pink to purple for the cobalt system and from white to sandy-grey for the iron one. TGA-MS and FTIR analyses on the recovered samples confirmed the removal of water (**Figure II.14**), and the nominal composition Na$_2$$M$(SO$_4$)$_2$ was verified by EDX analysis, performed with a transmission electron microscope using short time exposure to prevent the gradual loss of sodium.

Figure II.13: Evolution of the XRD patterns upon the dehydration process of (a) $Na_2Co(SO_4)_2 \cdot 4H_2O$ and (b) $Na_2Fe(SO_4)_2 \cdot 4H_2O$. Blue patterns correspond to the $Na_2M(SO_4)_2 \cdot 4H_2O$ phases, green patterns to the intermediate step described in the text and red patterns to the α-$Na_2M(SO_4)_2$ phases. Blue sticks indicate the position of the Bragg reflections of the $Na_2M(SO_4)_2 \cdot 4H_2O$ phases, while the first and second raw of green sticks correspond to the Bragg reflections of $M(SO_4) \cdot H_2O$ (M = Co, Fe) and Na_2SO_4, respectively.

Figure II.14: FTIR spectra of the hydrated $Na_2M(SO_4)_2 \cdot 4H_2O$ and anhydrous α-$Na_2M(SO_4)_2$ phases, for the (a) cobalt and (b) iron systems. Note that the small bumps observed above 3000 cm^{-1} for the dehydrated $Na_2M(SO_4)_2$ phases are more likely due to humidity at the surface of the IR pellet than to remaining structural water as no peak is seen at ~1700 cm^{-1}.

Before pursuing the discussion on these α-$Na_2M(SO_4)_2$ phases, it is worth mentioning that these systems seem to be subject to thermodynamic and kinetic competition. Indeed, we experienced that, with further annealing at 300°C for several hours, the α-$Na_2M(SO_4)_2$ phases (M = Co, Fe) undergo a phase transformation, with the resulting XRD patterns being comparable to the Debye-Scherrer patterns that Cot attributed to a second polymorph β-$Na_2M(SO_4)_2$ (M = Co, Fe) **[376,378,381]**. We also obtained similar samples from stoichiometric mixtures of anhydrous precursors Na_2SO_4 and MSO_4 pressed into a pellet and heated between 250 and 350°C either under air (M = Co, Mn) or in quart-tube sealed under vacuum (M = Fe). However, we have doubts about the fact that these

samples were really single-phased, as we were not able to find any unit cell that could index all the reflections of their XRD patterns. Besides, we also managed to prepare the α-Na$_2$Co(SO$_4$)$_2$ phase directly from a stoichiometric mixture of Na$_2$SO$_4$ and CoSO$_4$ annealed above 400°C for a few hours, but all our attempts to stabilize the iron analogue α-Na$_2$Fe(SO$_4$)$_2$ from its anhydrous precursors failed, suggesting that the formation of this phase is favored by the presence of water in the starting materials. Finally, despite many tries, α-Na$_2$Fe(SO$_4$)$_2$ could not be obtained as a pure phase from Na$_2$Fe(SO$_4$)$_2$·4H$_2$O, as an unidentified phase tended to grow in competition with the targeted one. However, by adjusting the dehydration conditions (temperature ramp, nitrogen flow, quantity of sample, etc), we were able to prepare samples which mainly contained the α-Na$_2$Fe(SO$_4$)$_2$ phase, so that we could probe its electrochemical behavior.

II.3.2   Structural determination of α-Na$_2$Co(SO$_4$)$_2$

The structural determination of α-Na$_2$M(SO$_4$)$_2$ (M = Co, Fe) [364] was carried out on the cobalt-based compound because this sample was better crystallized and less sensitive to oxidation upon air exposure, which made it easier to handle.

High quality data were actually needed to resolve the precise structure of α-Na$_2$Co(SO$_4$)$_2$. A Synchrotron X-ray powder diffraction pattern ($\lambda = 0.6681$ Å) was thus collected at the CRISTAL beamline at SOLEIL Synchrotron (*cf.* Annexes: § A.3.2.2 CRISTAL beamline at SOLEIL Synchrotron, page 164). We first tried to refine the α-Na$_2$Co(SO$_4$)$_2$ pattern starting from the structure proposed for Na$_2$Zn(SO$_4$)$_2$ by Berg and Thorup [382]. This model led to acceptable Rietveld refinement of the main reflections, with the following parameters: S.G.: *P*2/*n*, $a = 8.9725(2)$ Å, $b = 10.3834(2)$ Å, $c = 15.0443(2)$ Å, $\beta = 90.235(5)$°, $V = 1401.62(4)$ Å^3; however, it did not allow to describe weak reflections, which could be attributed to the existence of a superstructure (**Figure II.15.a**). This assumption was confirmed with neutron powder diffraction (NPD), that we performed on the D2B diffractometer at the Institut Laue Langevin (*cf.* Annexes: § A.3.3.1 D2B diffractometer at ILL, page 165). Indeed, this technique provides better contrast between the different elements which constitute the phase, since cobalt scatters neutrons less efficiently ($b_{Co} = 2.49$ fm) than X-ray, and Na, S and O give strong contributions to the intensities of the neutron Bragg reflections ($b_{Na} = 3.63$ fm, $b_S = 2.847$ fm, $b_O = 5.803$ fm). The Rietveld refinement of the high-resolution NPD pattern of α-Na$_2$Co(SO$_4$)$_2$ using the Na$_2$Zn(SO$_4$)$_2$ model was poor, especially for reflections in the range $35 \leq 2\theta \leq 60$° (**Figure II.15.b**). This was therefore a confirmation that α-Na$_2$Co(SO$_4$)$_2$ adopts a structure different from the one reported for the zinc analogue [382], with the main difference between both models not resting in the transition metal position, as the XRD refinement is acceptable, but rather in the Na, S and O distribution.

Figure II.15: Results of the Rietveld refinements of (a) the Synchrotron X-ray powder diffraction and (b) the neutron powder diffraction patterns of α-Na$_2$Co(SO$_4$)$_2$ using the Berg and Thorup's Na$_2$Zn(SO$_4$)$_2$ model **[382]**, as described in the text.

At this juncture, attempts to find the proper unit cell for α-Na$_2$Co(SO$_4$)$_2$ from complementary Synchrotron XRD and NPD patterns lead to numerous possibilities, with cells having large volumes (2500-3000 Å^3). To sort out between these different options, Dr. Artem M. Abakumov and Pr. Gustaaf Van Tendeloo[*] performed transmission electron microscopy (TEM) on a α-Na$_2$Co(SO$_4$)$_2$ sample.

Using very weak and widely spread electron beam to avoid the alteration of the compound (as gradual loss of sodium had been observed when standard exposition conditions were employed), tilt series of selected area electron diffraction (SAED) patterns were collected and used for a reconstruction of the 3D reciprocal lattice. As seen in **Figure II.16**, the patterns present two groups of reflections with different intensities, confirming the existence of a superstructure. All bright reflections in the electron diffraction patterns could be indexed with the subcell derived from the Na$_2$Zn(SO$_4$)$_2$ model proposed by Berg and Thorup **[382]**. Indexation of the weaker reflections required a new monoclinic supercell, with the lattice vectors related to the vectors of the subcell as **a**$_{super}$ = 2**a**$_{sub}$ + **c**$_{sub}$, **b**$_{super}$ = -**b**$_{sub}$, and **c**$_{super}$ = **a**$_{sub}$ - **c**$_{sub}$. This lead to the supercell lattice parameters: a_{super} ≈ 23.3 Å, b_{super} ≈ 10.3 Å, c_{super} ≈ 17.4 Å, β ≈ 99.0°, which corresponds to a cell volume three times larger than the subcell (V_{super} ≈ 4204 Å^3 *versus* V_{sub} ≈ 1402 Å^3).

---

[*] Electron Microscopy for Materials Science, University of Antwerp, Antwerp, Belgium.

Figure II.16: SAED patterns of a α-Na$_2$Co(SO$_4$)$_2$ sample. They are indexed in the monoclinic supercell as described in the text.

The Berg and Thorup's Na$_2$Zn(SO$_4$)$_2$ atomic positions were then transformed into this supercell, and the space group was determined to be *C*2/*c* (**Table II.8**). Note that this supercell contains 40 independent atoms, which could hardly be refined with laboratory powder X-ray diffraction pattern but require high-quality data. The Rietveld refinement of the Synchrotron XRD data using this model with soft constraints on the S–O distances of the sulfate group enabled to fit almost all weak superlattice reflections of the pattern; a few very weak reflections remain unindexed and may be attributed to a possible admixture. Then, this supercell was also checked against our neutron powder diffraction data, and it was found to perfectly match. Finally, a joint Rietveld refinement was performed against both the Synchrotron XRD and the NPD data; the corresponding results are given in **Figure II.17** and **Table II.8**.


Figure II.17: Results of the combined Rietveld refinement of the Synchrotron X-ray powder diffraction and the neutron powder diffraction patterns of α-Na$_2$Co(SO$_4$)$_2$ against the monoclinic supercell described in the text.

Table II.8: Crystallographic data and atomic positions of α-Na$_2$Co(SO$_4$)$_2$ deduced from a joint Rietveld refinement of SOLEIL Synchrotron X-ray diffraction (λ = 0.6681 Å) and ILL neutron powder diffraction (λ = 1.594 Å) data. Bond Valence Sum analysis (BVS) is also indicated. Note that the S–O distances were controlled with soft constraints.

α-Na$_2$Co(SO$_4$)$_2$					
Space group C 2/c	χ^2 = 3.26		R$_{Bragg}$ = 5.49 %	*V* = 4121.4(6) Å^3	
a = 23.262(2) Å	*b* = 10.3057(9) Å		*c* = 17.4047(15) Å	β = 98.972(6)°	
Atom	**Wyckoff site**	***x/a***	***y/b***	***z/c***	**B$_{iso}$ (Å^2)**	**BVS**
Co1	8*f*	0.4288(6)	0.1048(13)	0.0600(8)	1.41(10)	1.74(7)
Co2	8*f*	0.4002(6)	0.3842(14)	0.2728(9)	1.41(10)	1.90(8)
Co3	8*f*	0.2359(7)	0.1286(12)	0.1198(8)	1.41(10)	2.01(8)
Na1	4*e*	0	0.144(5)	¼	3.2(3)	0.83(4)
Na2	8*f*	0.1684(19)	0.340(3)	0.428(2)	3.2(3)	0.98(6)
Na3	8*f*	0.4007(17)	0.107(4)	0.396(2)	3.2(3)	0.93(5)
Na4	8*f*	0.0626(15)	0.118(4)	0.077(2)	3.2(3)	1.10(6)
Na5	8*f*	0.2392(16)	0.379(4)	0.234(2)	3.2(3)	1.08(7)
Na6	4*e*	0	0.589(5)	¼	3.2(3)	1.03(5)
Na7	8*f*	0.3365(18)	0.449(3)	0.072(3)	3.2(3)	0.64(5)
S1	8*f*	0.4735(8)	0.3789(18)	0.1246(10)	1.43(15)	6.3(3)
O11	8*f*	0.4763(15)	0.239(2)	0.1319(19)	1.55(6)	2.03(13)
O12	8*f*	0.0325(11)	0.074(3)	0.6431(18)	1.55(6)	2.17(14)
O13	8*f*	0.4438(14)	0.421(3)	0.0502(15)	1.55(6)	2.02(15)
O14	8*f*	0.4428(14)	0.433(3)	0.1843(17)	1.55(6)	1.99(17)
S2	8*f*	0.1901(8)	0.3780(17)	0.0249(10)	1.43(15)	5.9(3)
O21	8*f*	0.3531(13)	0.208(3)	0.0191(18)	1.55(6)	1.94(14)
O22	8*f*	0.1676(13)	0.506(3)	0.0388(17)	1.55(6)	1.91(15)
O23	8*f*	0.2109(14)	0.321(3)	0.1024(14)	1.55(6)	1.98(13)
O24	8*f*	0.2559(11)	0.106(4)	0.0089(18)	1.55(6)	1.97(14)
S3	8*f*	0.3619(8)	0.1042(17)	0.2144(10)	1.43(15)	5.9(3)
O31	8*f*	0.3143(13)	0.185(3)	0.1754(18)	1.55(6)	1.92(14)
O32	8*f*	0.3430(14)	0.010(3)	0.2692(16)	1.55(6)	1.79(15)
O33	8*f*	0.4077(12)	0.187(3)	0.2573(18)	1.55(6)	2.14(14)
O34	8*f*	0.3875(14)	0.031(2)	0.1552(16)	1.55(6)	1.80(14)
S4	8*f*	0.1818(8)	0.1047(17)	0.5879(10)	1.43(15)	6.1(3)
O41	8*f*	0.1579(14)	0.025(3)	0.0748(19)	1.55(6)	2.14(14)
O42	8*f*	0.2604(11)	0.424(3)	0.3706(19)	1.55(6)	2.15(15)
O43	8*f*	0.3511(13)	0.316(3)	0.3633(17)	1.55(6)	1.84(15)
O44	8*f*	0.1868(14)	0.179(4)	0.5185(15)	1.55(6)	1.80(15)
S5	8*f*	0.0047(8)	0.3694(17)	0.4150(10)	1.43(15)	6.0(3)
O51	8*f*	0.0108(14)	0.490(3)	0.1289(16)	1.55(6)	1.95(13)
O52	8*f*	0.0601(11)	0.391(3)	0.4641(17)	1.55(6)	2.02(14)
O53	8*f*	0.0393(13)	0.341(4)	0.0338(17)	1.55(6)	2.01(16)
O54	8*f*	0.0069(14)	0.261(3)	0.3636(17)	1.55(6)	1.99(16)
S6	8*f*	0.1624(8)	0.1104(17)	0.2667(11)	1.43(15)	6.1(3)
O61	8*f*	0.3246(15)	0.475(3)	0.2093(18)	1.55(6)	2.15(13)
O62	8*f*	0.1604(15)	0.186(4)	0.3374(16)	1.55(6)	1.81(15)
O63	8*f*	0.1073(11)	0.100(4)	0.2157(19)	1.55(6)	2.05(15)
O64	8*f*	0.2094(13)	0.160(3)	0.2279(18)	1.55(6)	2.05(16)

Figure II.18: Crystal structure of α-Na$_2$Co(SO$_4$)$_2$ represented with the monoclinic supercell described in the text. (a), (d) and (e) Projections along the *b*-axis, and the [1 0 -2] and [1 0 1] directions, respectively. CoO$_6$ and SO$_4$ groups are displayed as blue octahedra and yellow tetrahedra, respectively. Cyan spheres correspond to the sodium atoms. (b) Chains of CoO$_6$ octahedra and SO$_4$ tetrahedra, which are alternatively connected through corners and edges. Na atoms are not displayed for clarity. (c) Enlargement of one chain, where oxygen atoms are represented as small red balls. The edges shared by CoO$_6$ octahedra and SO$_4$ tetrahedra are highlighted with red segments.

The structure of α-Na$_2$Co(SO$_4$)$_2$ as determined above is illustrated in **Figure II.18**. No obvious structural relation with its precursor phase Na$_2$Co(SO$_4$)$_2$·4H$_2$O was found. The structure consists in a complicated arrangement of CoO$_6$ octahedra and SO$_4$ tetrahedra, which are alternately connected either by corners and edges or by corners only, and give rise to small chains as shown in **Figure II.18.c**. Thus, each CoO$_6$ octahedron is linked to four SO$_4$ groups by vertices and shares an edge with a fifth SO$_4$ tetrahedron. As for the sulfate groups, they are connected either to two CoO$_6$ octahedra (through one corner and one edge) or to three different CoO$_6$ octahedra (through corners only); in both cases, the fourth oxygen of the SO$_4$ tetrahedra points to small cavities where the Na atoms sit. Overall, the main difference between the structure of α-Na$_2$Co(SO$_4$)$_2$ and the one reported for Na$_2$Zn(SO$_4$)$_2$ **[382]** resides in the orientation of the SO$_4$ groups, which explains why the mismatch was barely noticeable from X-ray diffraction but was much more obvious with neutron powder diffraction.

II.3.3 Electrochemistry of α-Na₂Fe(SO₄)₂

The electrochemical activity of the α-Na$_2$$M$(SO$_4$)$_2$ phases (M = Co, Fe) was tested against both sodium and lithium metal negative electrodes. For the cobalt counterpart, alike the hydrated phase, no electrochemical activity could be detected up to 4.8 V $vs.$ Li$^+$/Li^0, $i.e.$ the electrochemical stability limit of our electrolyte. This contrasts with the iron-based phase α-Na$_2$Fe(SO$_4$)$_2$, whose electrochemical activity is within the 2.5–4.5 V range (**Figure II.19**) [364]. The voltage-composition traces show here again high experimental potentials, which are centered around 3.6 V $vs.$ Li$^+$/Li^0 and 3.4 V $vs.$ Na$^+$/Na^0. Almost one sodium can be extracted from the structure and nearly 0.7 Li$^+$ or Na$^+$ ion ($i.e.$ ~64 mAh/g) can be reversibly re-inserted at a rate of C/20. The discharge capacities remain stable upon cycling but one should note that, as for the hydrated parent phase, the curves are "walking to the left" as a result of a longer charge than discharge, and this effect is highly enhanced for sodium cells. We believe that it is linked to electrolyte degradation issues that we have not yet mastered. As for the profile of the electrochemical curves, it differ from the one obtained with the hydrated phase Na$_2$Fe(SO$_4$)$_2$·4H$_2$O. For the latter, the first flat-like charge neatly contrasted with the subsequent discharges and charges (see **Figure II.7** page 54), whereas in the case of α-Na$_2$Fe(SO$_4$)$_2$ the electrochemical curves already show an S-shape at the first charge (**Figure II.19**). Moreover, preliminary $in\ situ$ XRD experiments seem to show no sign of amorphization of α-Na$_2$Fe(SO$_4$)$_2$ during cycling, though the poor crystallinity of the electrode material does not enable to judge the exact nature of the charge-discharge mechanism.
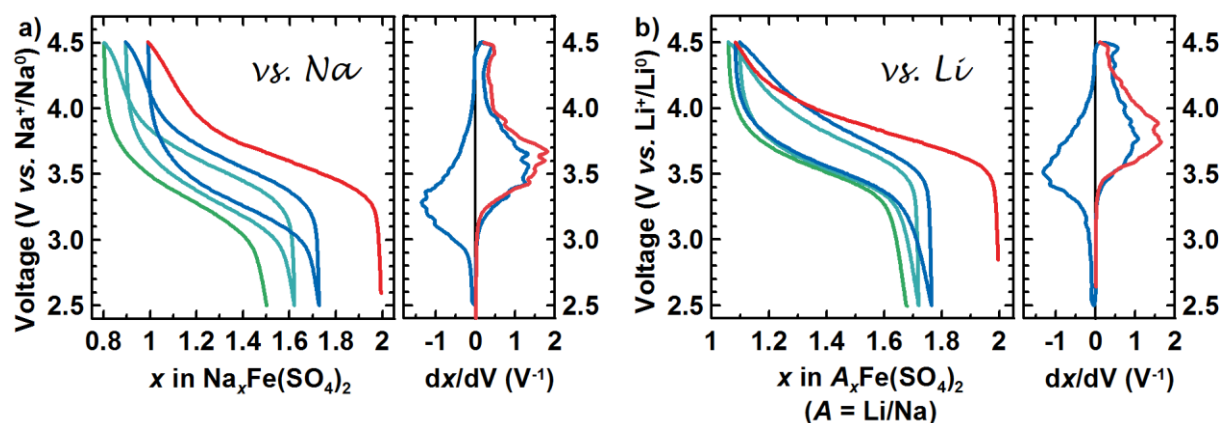
Figure II.19: Electrochemical characterization of α-Na$_2$Fe(SO$_4$)$_2$ (a) $versus$ sodium and (b) $versus$ lithium. The first charge is displayed in red, and the subsequent discharges and charges are colored from blue to green. The corresponding derivative dx/dV curves are shown at the right of each galvanostatic curve.

At this stage, we got interested in probing the electrochemical properties of another mineral compound, namely the *eldfellite* NaFe(SO$_4$)$_2$, which has the same composition as the α-Na$_2$Fe(SO$_4$)$_2$ phase would have after oxidation, but presents a layered structure as opposed with the 3D framework of the latter.

II.4   Syntheses and electrochemical properties of other sodium iron sulfates inspired from minerals

Eldfellite NaFe(SO$_4$)$_2$, unnamed Na$_3$Fe(SO$_4$)$_3$ and *yavapaiite* KFe(SO$_4$)$_2$ are rare mineral species that occur as high-temperature fumarolic phases in the neighborhood of volcanoes **[388–393]**. Although recently discovered as naturally-occurring compounds, these phases have been known since the 1940s as they are involved in highly corrosive deposits in industrial boiler furnaces **[394,395]**, and their syntheses were described as soon as 1945 **[396–399]**. The crystal structure of KFe(SO$_4$)$_2$ was reported in the 1970s **[392,393]** while the ones of the sodium compounds NaFe(SO$_4$)$_2$ and Na$_3$Fe(SO$_4$)$_3$ were determined only few years ago **[389,400]**. At the end of the 1990s, Barker patented the use of NaFe(SO$_4$)$_2$ and Na$_3$Fe(SO$_4$)$_3$ as positive electrode materials for Li-ion batteries **[401]**, but to the best of our knowledge, no electrochemical data were ever reported. We therefore embarked in the synthesis and characterization of these phases.

II.4.1   Syntheses

To synthesize the three NaFe(SO$_4$)$_2$, Na$_3$Fe(SO$_4$)$_3$ and KFe(SO$_4$)$_2$ phases, we employed a solid-state route similar to the one described by Perret and Couchot **[398]**, using anhydrous iron (III+) sulfate and sodium/potassium sulfates as starting reagents to carry out the following reactions:

$$A_2SO_4 + Fe_2(SO_4)_3 \rightarrow 2\ A Fe(SO_4)_2 \quad (A = \text{Na, K})$$

$$3\ Na_2SO_4 + Fe_2(SO_4)_3 \rightarrow 2\ Na_3Fe(SO_4)_3$$
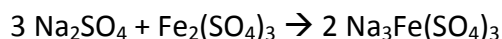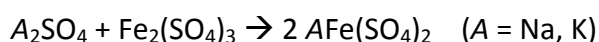
The Fe$_2$(SO$_3$)$_4$ precursor was prepared from the commercial product Fe$_2$(SO$_3$)$_4$.nH$_2$O ($n \approx 5$, CAS number: 15244-10-7), which was first washed several times with absolute ethanol to eliminate impurities, and in particular to avoid the formation of FeSO$_4$OH, before being dehydrated by thermal treatment at 300°C under air for a dozen hours. Stoichiometric amounts of A_2SO$_4$ (A = Na, K) and Fe$_2$(SO$_4$)$_3$ were then thoroughly mixed using a Spex 8000 ball-miller, pressed into pellets and annealed at 400°C for one night. Note that the samples had to be removed from the oven at high-temperature and immediately crushed with a mortar, since we experienced that the surface of the pellet got hydrated when slowly cooling down, resulting in an amorphous yellow slurry. Afterwards, the samples were safely stored in an argon-filled glove-box.

II.4.2   Characterizations

Purity of the samples was first checked by laboratory X-ray diffraction, and we confirmed the crystal structures reported for the three phases **[389,392,393,400]** using neutron powder diffraction (NPD) performed on the D20 diffractometer of the Institut Laue Langevin (ILL, Grenoble, France; *cf.* Annexes: A.3.3.2 D20 diffractometer at ILL, page 165). The results of these Rietveld refinements are shown in **Figure II.20** and **Figure II.21**, and in **Table II.9** to **Table II.11**. BVS analyses, using b_0 parameters from Brown **[402]** (*cf.* Annexes: A.3.4.1 Refinement of the structures from XRD and NPD patterns, page 166), indicated that the Fe–O bond lengths are in good agreement with iron in the III+ oxidation state, as also confirmed by Mössbauer spectroscopy (**Figure II.22** and **Table II.12**).
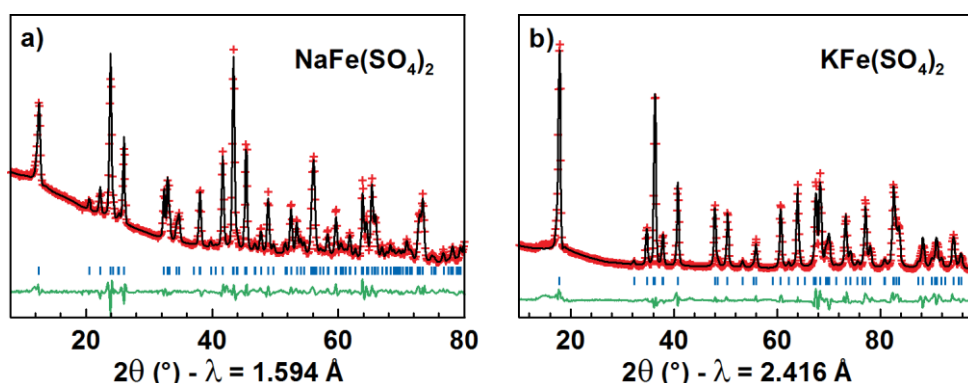
Figure II.20: Results of the Rietveld refinements of the NPD data of (a) $NaFe(SO_4)_2$ and (b) $KFe(SO_4)_2$.
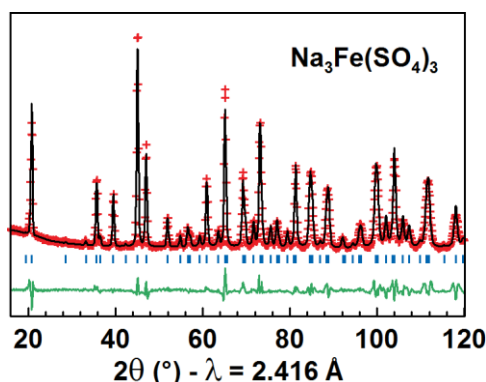
Figure II.21: Results of the Rietveld refinements of the NPD data of $Na_3Fe(SO_4)_3$.
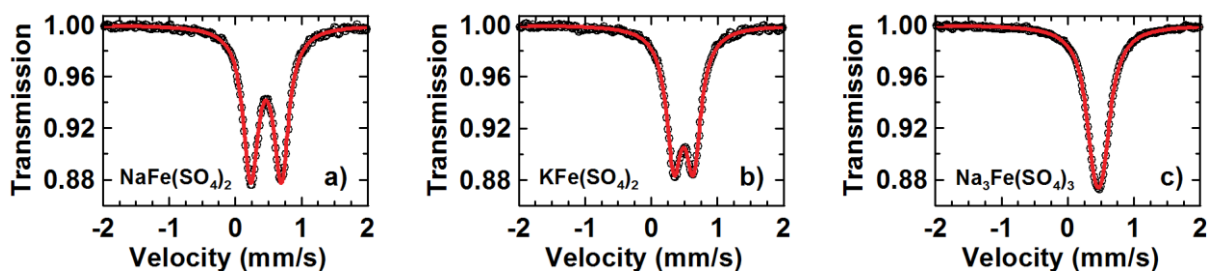
Figure II.22: ^{57}Fe Mössbauer spectra of (a) $NaFe(SO_4)_2$, (b) $KFe(SO_4)_2$, and (c) $Na_3Fe(SO_4)_3$.

Table II.9: Crystallographic data and atomic positions of NaFe(SO$_4$)$_2$ deduced from the Rietveld refinement of the D20 NPD data (λ = 1.594 Å, T = 50 K). Bond Valence Sum analysis (BVS) is also indicated.

NaFe(SO$_4$)$_2$					
Space group *C*2/*m*		χ^2 = 23.8	R$_{Bragg}$ = 3.01 %	B$_{iso}$ = 0.30(12)	
a = 7.997(2) Å	*b* = 5.163(2) Å	*c* = 7.094(2) Å	β = 91.939(6)°	V = 292.70(4) Å^3	
Atom	**Wyckoff site**	***x/a***	***y/b***	***z/c***	**BVS**
Na	2*c*	0	0	½	0.96(2)
Fe	2*a*	0	0	0	2.96(3)
S	4*i*	0.362(3)	0	0.218(3)	6.03(18)
O1	4*i*	0.240(2)	0	0.060(2)	2.11(10)
O2	4*i*	0.288(2)	0	0.403(2)	1.77(10)
O3	8*j*	0.470(2)	0.233(2)	0.204(2)	2.05(6)

Table II.10: Crystallographic data and atomic positions of KFe(SO$_4$)$_2$ deduced from the Rietveld refinement of the D20 NPD data (λ = 2.416 Å, T = 7 K). Bond Valence Sum analysis (BVS) is also indicated.

KFe(SO$_4$)$_2$					
Space group *C*2/*m*		χ^2 = 48.9	R$_{Bragg}$ = 6.41 %	B$_{iso}$ = 0.6(2)	
a = 8.127(2) Å	*b* = 5.154(2) Å	*c* = 7.829(2) Å	β = 95.067(8)°	V = 326.62(6) Å^3	
Atom	**Wyckoff site**	***x/a***	***y/b***	***z/c***	**BVS**
K	2*c*	0	0	½	0.9(2)
Fe	2*a*	0	0	0	3.0(2)
S	4*i*	0.36(4)	0	0.20(4)	6.0(3)
O1	4*i*	0.238(2)	0	0.056(3)	2.4(2)
O2	4*i*	0.313(3)	0	0.370(3)	1.8(2)
O3	8*j*	0.477(2)	0.231(3)	0.182(2)	1.9(2)

Table II.11: Crystallographic data and atomic positions of Na$_3$Fe(SO$_4$)$_3$ deduced from the Rietveld refinement of the D20 NPD data (λ = 2.416 Å, T = 2 K). Bond Valence Sum analysis (BVS) is also indicated.

Na$_3$Fe(SO$_4$)$_3$					
Space group *R*-3		χ^2 = 10.8	R$_{Bragg}$ = 4.15 %	B$_{iso}$ = 0.5(3)	
a = 13.365(2) Å	*c* = 9.082(2) Å			V = 1405.0(3) Å^3	
Atom	**Wyckoff site**	***x/a***	***y/b***	***z/c***	**BVS**
Na	18*f*	0.224(3)	0.303(4)	0.156(3)	1.0(2)
Fe1	3*a*	0	0	0	3.1(2)
Fe2	3*b*	0	0	½	3.0(2)
S	18*f*	0.186(5)	0.019(7)	0.260(8)	5.9(6)
O1	18*f*	0.033(3)	0.138(3)	0.381(3)	2.1(3)
O2	18*f*	0.248(3)	0.149(3)	0.276(3)	1.7(3)
O3	18*f*	0.028(3)	0.291(2)	0.259(4)	2.2(4)
O4	18*f*	0.120(3)	0.989(3)	0.115(4)	1.9(3)

Table II.12: Room temperature [57]Fe Mössbauer parameters of $NaFe(SO_4)_2$, $KFe(SO_4)_2$, and $Na_3Fe(SO_4)_3$. δ represents the isomer shift relative to metallic iron standard at room temperature, while ΔE_q and Γ indicate the quadrupole splitting and the line width, respectively. Note that [57]Fe Mössbauer parameters obtained for the two sodium-based compounds are in good agreement with those reported by Zboril *et al.* **[403]**.

	Attribution	δ (mm/s)	ΔEq (mm/s)	Γ (mm/s)	Molar fraction (%)
$NaFe(SO_4)_2$	Fe(III+)	0.46(1)	0.46(1)	0.27(1)	100(–)
$KFe(SO_4)_2$	Fe(III+)	0.49(1)	0.29(1)	0.28(1)	100(–)
$Na_3Fe(SO_4)_3$	Fe(III+)	0.46(1)	0.12(1)	0.33(1)	100(–)

The *yavapaiite* $KFe(SO_4)_2$ and *eldfellite* $NaFe(SO_4)_2$ compounds are isostructural and crystallize in a monoclinic unit cell (space group: $C2/m$). Their structure is built upon layers of FeO_6 octahedra and SO_4 tetrahedra parallel to the (001) plane, inbetween which the alkali (K^+ or Na^+) cations lie in distorted octahedral coordination (**Figure II.23.a**). Within the $[FeSO_4]_n$ sheets, the FeO_6 octahedra are isolated one from each other and are connected through the sulfate groups (**Figure II.23.b**). Each SO_4 tetrahedron is thus linked to three different FeO_6 octahedra *via* its vertices, and its fourth corner points to the sodium layer.
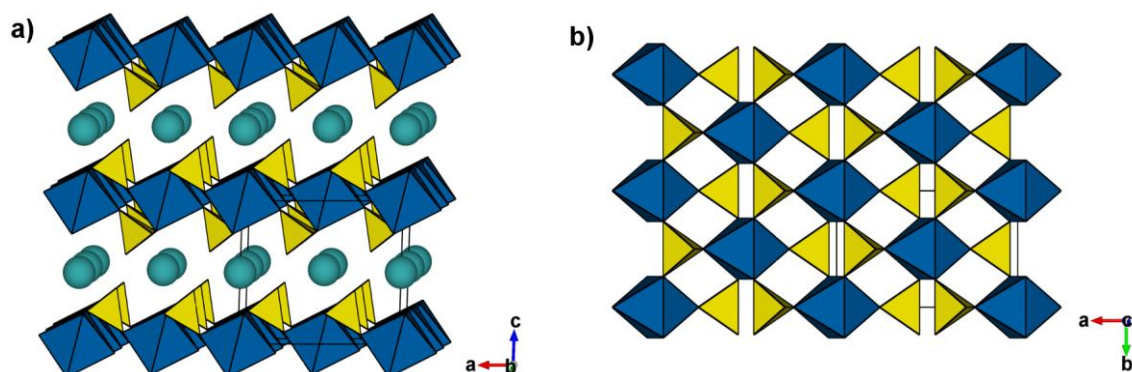
Figure II.23: Representation of the structure of the *yavapaiite* $KFe(SO_4)_2$ and the *eldfellite* $NaFe(SO_4)_2$ viewed along (a) the *b*- and (b) the *c*-axes.

$Na_3Fe(SO_4)_3$ crystallizes in a rhombohedral structure (space group: R-3). It is built upon chains of FeO_6 octahedra and SO_4 tetrahedra running along the *c*-axis, as seen in **Figure II.24**. The way the FeO_6 and SO_4 groups share their corners recall the $Fe_2(SO_4)_3$ lantern units of the NASICON-type structures (Chapter I § I.2.3.1 The NASICON-type compounds AxM2(*XO4*)$_3$ page 20), and give rise to a star or pinwheel pattern when viewed along the *c*-axis. Sodium atoms sit in between these $[Fe(SO_4)_3]_n$ chains in a highly distorted octahedral environment.
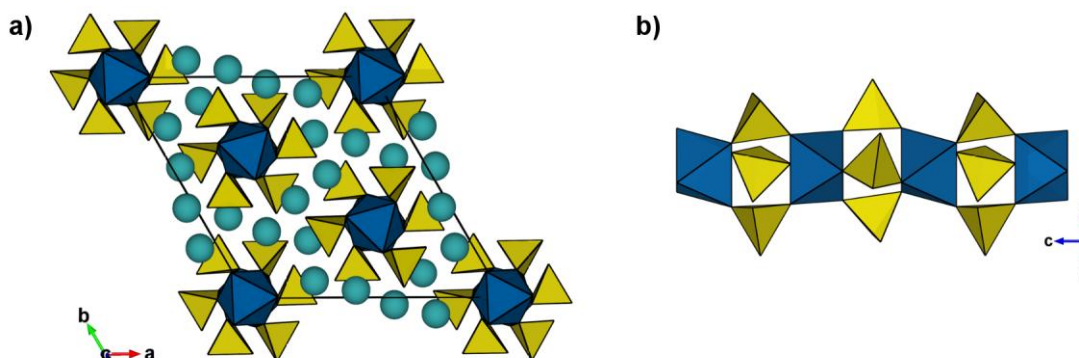
Figure II.24: (a) Representation of the structure of $Na_3Fe(SO_4)_3$ viewed along the *c*-axis. (b) Chains of FeO_6 octahedra and SO_4 tetrahedra that run along the the *c*-axis.

II.4.3   Electrochemistry

The electrochemical properties of the three compounds $NaFe(SO_4)_2$, $KFe(SO_4)_2$ and $Na_3Fe(SO_4)_3$ were probed in lithium and sodium half-cells (**Figure II.25** and **Figure II.26**). All of them were found to be electrochemically active, although very limited amount of lithium (or sodium) could be effectively inserted and extracted in these compounds. This is mostly due to the fact that their structures can not accomodate extra alkali cations and to the difficulty of oxidizing Fe^{III+} into Fe^{IV+}. This therefore reminds that choosing open 3D frameworks favoring the ionic diffusion is a good but not sufficient criterion to make good alkali hosts. Nevertheless, the three compounds $NaFe(SO_4)_2$, $KFe(SO_4)_2$ and $Na_3Fe(SO_4)_3$ are still interesting electrode materials from a fundamental point of view as their all display high redox potentials of about 3.5 V *vs.* Li^+/Li^0 and 3.2 V *vs.* Na^+/Na^0, thus confirming once again that sulfate-based materials enable to reach elevated voltages for the Fe^{III+}/Fe^{II+} redox couple.
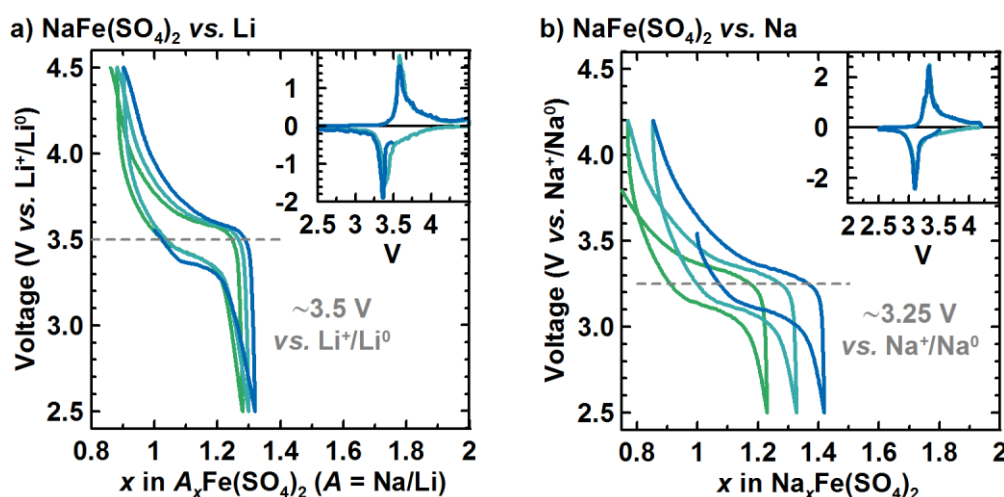
Figure II.25: Typical voltage-composition curves obtained for $NaFe(SO_4)_2$ cycled against (a) a lithium metal and (b) a sodium metal anodes. The corresponding derivative d*x*/dV curves for the two first cycles are shown in insets.
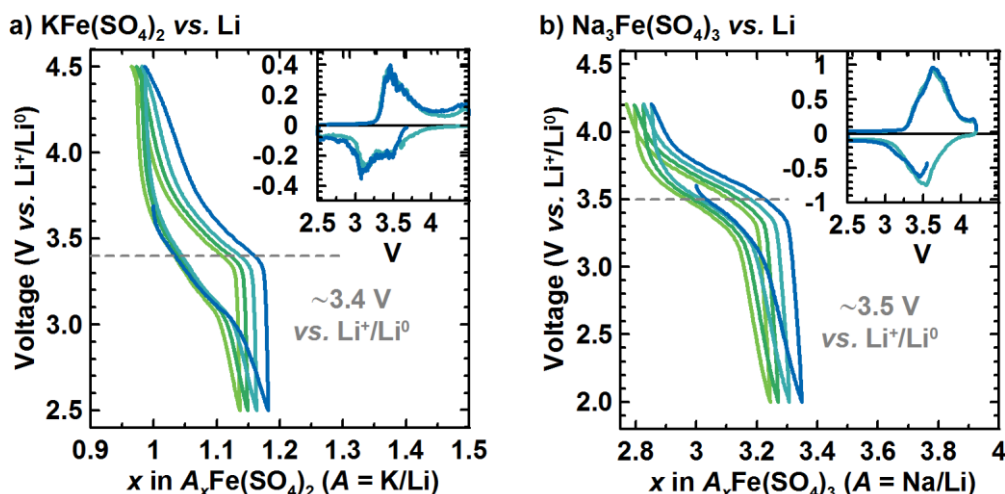
Figure II.26: Typical voltage-composition curves obtained for (a) $KFe(SO_4)_2$ and (b) $Na_3Fe(SO_4)_3$ against lithium. The corresponding derivative dx/dV curves for the two first cycles are shown in insets.

II.5   Conclusion

In this chapter, we have demonstrated the possibility of preparing new electrode materials based on abundant and sustainable elements (sodium, iron, sulfur and oxygen) from mineral species, and thus revealed that mineral compounds indeed constitute a rich structural database from which researchers can get inspiration to design new functional materials.

We reported on the synthesis of *bloedite*-type compounds $Na_2M(SO_4)_2 \cdot 4H_2O$ (M = Mg, Zn, Ni, Co, Fe) and their dehydrated derivatives $Na_2M(SO_4)_2$ (M = Co and Fe), for which we have solved the complete structure for the first time. We also prepared the mineral phases $NaFe(SO_4)_2$ and $Na_3Fe(SO_4)_3$ in order to probe their properties in sodium and lithium half-cells. All the four iron-based compounds presented herein were found to be electrochemically active *versus* both lithium and sodium metal anodes. The low reversible capacities offered by these compounds (below 80 mAh/g) make them of limited interest for practical electrode materials, but they display however attractive voltages of 3.5-3.6 V *vs.* Li^+/Li^0 and 3.3-3.4 V *vs.* Na^+/Na^0, for which these new electrode materials should not be disregarded.

These Fe^{III+}/Fe^{II+} redox potentials exceed indeed the benchmarked values obtained with phosphate-based compounds ($LiFePO_4$: 3.45 V *vs.* Li^+/Li^0, $NaFePO_4$ and Na_2FePO_4F: ~3.0 V *vs.* Na^+/Na^0) and compare with the potentials reported for other sulfate-based electrode materials (NASICON-type $Fe_2(SO_4)_3$, layered $LiFeSO_4OH$ and *tavorite* $LiFeSO_4F$: 3.6 V *vs.* Li^+/Li^0, *maxwellite* $NaFeSO_4F$: ~3.5 V *vs.* Na^+/Na^0). Therefore, these results corroborate previous observations that sulfate-based electrode materials enable to reach the highest potential values for the Fe^{III+}/Fe^{II+} redox couple among inorganic compounds. Moreover, they confirm once again that incorporation of fluorine into electrode materials is not necessary to obtain high voltages.

At this stage, an obvious prolongation of this work was to explore the possibility of preparing lithium analogues to the sodium compounds presented above, in order to check if they adopt the same structures and to probe whether they equally offer high redox potentials.

Chapter III.   A new family of lithium metal sulfate compounds: Li$_2$$M$(SO$_4$)$_2$ (M = Co, Fe, Mn, Ni, Zn, Mg)

III.1   Introduction

In the previous chapter, we presented the electrochemical properties of sodium iron sulfate compounds inspired from mineral species. These compounds can be employed as positive electrode materials against both sodium and lithium anodes, and display high Fe^{III+}/Fe^{II+} redox potentials as compared with other polyanionic compounds. An obvious prolongation of this work was thus to investigate the possibility of preparing lithium analogues to these compounds.

First attempts consisting in synthesizing hydrated lithium metal sulfates using the same routes as employed for the preparation of the *bloedite* phases Na$_2$$M$(SO$_4$)$_2$·4H$_2$O were totally unfruitful. Li ↔ Na ionic exchange experiments conducted on both hydrated and anhydrous sodium-based phases were not more successful, although somewhat surprising since we were able to cycle these phases in lithium cells. Indeed all reactions performed with LiCl or LiNO$_3$ in acetonitrile resulted in partial decomposition of the compounds, with in particular formation of lithium sulfate. Annealing at 200°C pellets of α-Na$_2$Co(SO$_4$)$_2$ with the same reagents equally ended up with the decomposition of the phase, but we noticed however the presence of new diffraction peaks in the XRD patterns, which could be compared to the pattern reported by Touboul *et al.* for a phase having the composition Li$_2$Co(SO$_4$)$_2$ **[404,405]**. This was an impetus for the exploration of such Li$_2$$M$(SO$_4$)$_2$ compounds.

In the 1980s, after the first reports on the LISICON compound Li$_{3.5}$Zn$_{0.25}$GeO$_4$ which presents high ionic conductivity at high temperature (*i.e.* ~0.13 S/cm at 300°C) **[406,407]**, much efforts were dedicated to the search of new lithium compounds to be employed as solid electrolytes in high-voltage electrochemical devices. In this context, several groups worked on sulfate phases because the high-temperature polymorph of lithium sulfate (the cubic α-Li$_2$SO$_4$, stable at T > 572°C) had also been shown to present high ionic conductivity (*i.e.* ~1.08 S/cm at 600°C) **[408–413]**. Thus, in the search for new lithium-based sulfate phases, they extensively explored the binary systems Li$_2$SO$_4$–M^{n+}(SO$_4$)$_{n/2}$ (M = Na, K, Rb, Cs, Ag, Mg, Ca, Zn, Cd, Mn, *etc.*) **[404,405,410,414–424]**. To the best of our knowledge, only three phases having the general formula Li$_2$$M$(SO$_4$)$_2$ were reported in the course of these studies: a zinc, a cobalt and a nickel counterparts **[414,404,405]**. However, as these phases presented no outstanding conductivity properties, they drew very limited interest at that time, and only the structure of the nickel compound Li$_2$Ni(SO$_4$)$_2$ was reported at the beginning of the 2000s **[425]**.

Knowing that cobalt and iron usually display similar chemistry among the polyanion compounds (*cf.* Chapter I and Chapter II), we decided to focus first on isolating the Li$_2$Co(SO$_4$)$_2$ phase, and to try next to extend its synthesis to an iron analogue and probe its electrochemical properties.

III.2   Syntheses of the Li$_2$M(SO$_4$)$_2$ phases (M = Co, Fe)

III.2.1   Li$_2$Co(SO$_4$)$_2$

In an attempt to isolate Li$_2$Co(SO$_4$)$_2$, we started by combining cobalt sulfate CoSO$_4$ with various amounts of lithium sulfate Li$_2$SO$_4$. These mixtures were pressed into pellets and heated under air at various temperatures and for several annealing times. It was found that, when heated at temperatures above 300°C for more than 12 hours, stoichiometric ratios yield to almost pure samples of Li$_2$Co(SO$_4$)$_2$, as deduced from powder X-ray diffraction and confirmed with atomic absorption and EDX measurements **[426]**.

III.2.2   Li$_2$Fe(SO$_4$)$_2$

The synthesis of Li$_2$Fe(SO$_4$)$_2$ revealed to be more tricky, especially because of the greater propensity of divalent iron to oxidize. Indeed, our group had previously experienced the critical importance of working under inert conditions and using precursors of high-purity to produce pure Fe(II+)-based fluorosulfates phases **[321,324,335,427,337]**. For the synthesis of our new lithium iron sulfate, we decided therefore to employ the same precautions and explore similar routes to the ones used for the preparation of these fluorosulfates.

Ionothermal synthesis

Our first attempts to prepare Li$_2$Fe(SO$_4$)$_2$ thus consisted in reacting stoichiometric mixtures of FeSO$_4$·H$_2$O and LiSO$_4$·H$_2$O, assuming that the departure of water could favor the reaction, as previously observed in the synthesis of *tavorite* LiFeSO$_4$F **[321,324,427]**.

Monohydrate iron sulfate FeSO$_4$·H$_2$O precursors were prepared from the commercial heptahydrate compound FeSO$_4$·7H$_2$O, using a procedure previously reported **[324]** that had proved to reliably provide the targeted compound free of any Fe(III+) traces. First, FeSO$_4$·7H$_2$O powder was dissolved into a small volume of degassed water. A small amount of ascorbic acid was subsequently added to this solution in order to complex any traces of Fe(III+), and the latter was then precipitated into absolute ethanol. After being dried under vacuum, the recovered pale green powder was immersed under an ionic liquid (1-Ethyl-3-MethylImidazolium bis(TriFluoromethylSulfonyl)Imide, commonly called EMI-TFSI), and slowly heated until 160°C to complete the dehydration. The recovered FeSO$_4$·H$_2$O powder was finally washed several times with ethyl acetate or dichloromethane, dried under vacuum and kept under argon until its use to prevent possible oxidation.

For the Li$_2$Fe(SO$_4$)$_2$ synthesis, the as-prepared FeSO$_4$·H$_2$O was then ball-milled with Li$_2$SO$_4$·H$_2$O in a stainless steel jar closed under argon. This powder mixture was immersed in EMI-TFSI, and heated at around 270-300°C for several hours to several days. With the XRD patterns of the recovered samples, we verified the formation of a certain amount of the Li$_2$Fe(SO$_4$)$_2$ phase, which presented XRD reflections close to those observed for the cobalt counterpart, but reactions were incomplete, since remaining unreacted precursors were also found in the diffraction patterns.

Ceramic route

The use of hydrated precursors being unsuccessful, we attempted to prepare Li$_2$Fe(SO$_4$)$_2$ from anhydrous iron and lithium sulfates. Li$_2$SO$_4$ was easily obtained by dehydrating the commercial monohydrate under air at 350°C for a couple of hours. For FeSO$_4$, the FeSO$_4$·H$_2$O prepared through the aforementioned procedure was slowly heated under dynamical primary vacuum up to 280°C with a ~1°C/min temperature ramp and maintained at this temperature for one night.

The two as-prepared anhydrous sulfate precursors were then thoroughly ball-milled under argon and the resulting powder pressed into pellets, which were then sealed under vacuum into quartz tubes and annealed for two days at 310°C. After cooling, the recovered sandy-grey powder was X-rayed to check the completion of the reaction and the nominal composition Li$_2$Fe(SO$_4$)$_2$ was confirmed by complementary atomic absorption and EDX measurements **[426,428]**.

SPS route

Later, we managed to considerably reduce the preparation time of Li$_2$Fe(SO$_4$)$_2$ by employing Spark Plasma Sintering (abbreviated SPS, *cf.* Annexes: § A.1.2 SPS page 157). For this synthesis, about 300 mg of the same Li$_2$SO$_4$–FeSO$_4$ mixture as described above was placed between two carbon paper disks (Papyex®) and introduced in a 10-mm diameter carbon matrix (Mersen® 2333). The powder was thus pressed to 50 MPa and annealed at 320°C (75°C/min via a sequence of 1 pulse of 1 ms of DC polarization) for 15 minutes with an HPD 10 FCT SPS machine(*cf.* Annexes: § A.1.2 SPS page 157). The samples of Li$_2$Fe(SO$_4$)$_2$ prepared using this method were of the same degree of purity and displayed the same properties as the ones prepared *via* the ceramic route **[337,363]**.

III.3   Characterizations of the Li$_2M$(SO$_4$)$_2$ phases (M = Co, Fe)

III.3.1   Structure determination

Although the existence of the Li$_2$Co(SO$_4$)$_2$ phase had been reported at the beginning of the 1990s **[404,405]**, its structure remained unknown at the beginning of our study. We therefore embarked in the search of a unit cell for Li$_2$Co(SO$_4$)$_2$ using the Dicvol program **[429,430]** as implemented in the FullProf suite of software **[383,384]** (*cf.* Annexes: § A.3.4 Diffraction data treatment, page 166). We determined that all the reflections of its XRD pattern could be indexed with a monoclinic cell with the following parameters: space group $P2_1/n$, $a \approx 7.47$ Å, $b \approx 8.11$ Å, $c \approx 4.98$ Å, $\beta \approx 92.68°$ and $V \approx 301.37$ Å^3. Here we should mention that these unit cell parameters are different from those reported by Isasi *et al.* for Li$_2$Ni(SO$_4$)$_2$ **[425]**, but are similar to the ones proposed by Lundén *et al.* to index the XRD pattern the Li$_2$Zn(SO$_4$)$_2$ phase **[414]**, though no structural data were provided for this latter. The structure of Li$_2$Co(SO$_4$)$_2$ was then solved through global optimization (*ab initio* method) with the program FOX **[431,432]**, assuming the presence of rigid SO$_4$ tetrahedra within the unit cell. Note that direct methods using the program EXPO **[433–435]** led to the same solution. This structure was then standardized to the $P2_1/c$ space group using the STRUCTURE TIDY program **[436]** and finally refined against the XRD pattern using the Rietveld method **[385]** with the FullProf program **[383,384]**. The accuracy of this structure was later confirmed with Synchrotron XRD data, which were obtained through the mail-in service of the 11-BM beamline of the Advanced Photon Source of the Argonne National Laboratories (Argonne, USA; *cf.* Annexes: § A.3.2.1 page 163) **[426]**; the results of the Rietveld refinement of these data are presented in **Figure III.1** and **Table III.1**.
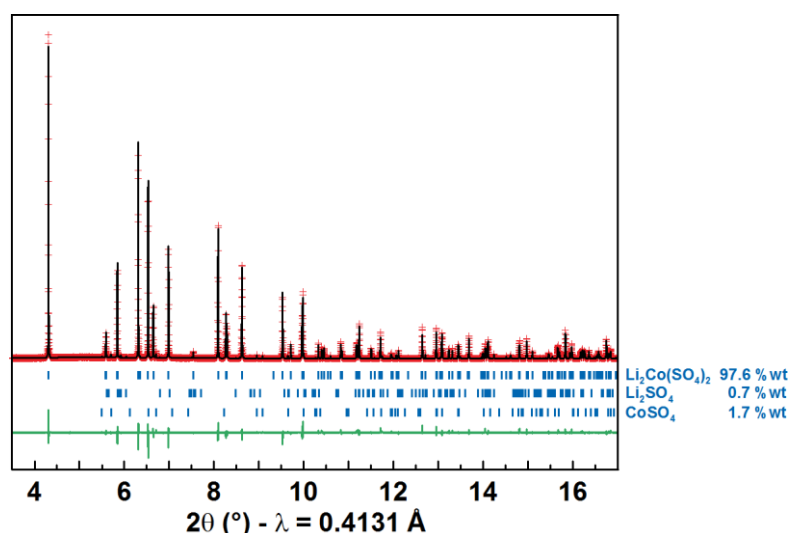
Figure III.1: Result of the Rietveld refinement of the structure determined for Li$_2$Co(SO$_4$)$_2$ against the 11-BM Synchrotron XRD data.

Table III.1: Crystallographic data and atomic positions of Li$_2$Co(SO$_4$)$_2$ determined from the Rietveld refinement of its 11-BM Synchrotron XRD pattern (λ = 0.4131 Å). Bond Valence Sum analysis (BVS) is also given.

Li$_2$Co(SO$_4$)$_2$						
Space group P2$_1$/c				χ² = 2.30		R$_{Bragg}$ = 4.79 %
a = 4.9787(2) Å		b = 8.1113(2) Å		c = 8.7831(2) Å	β = 121.811(2)°	V = 301.416(2) Å³
Atom	**Wyckoff site**	**Occupancy**	**x/a**	**y/b**	**z/c**	**B$_{iso}$ (Å²)**	**BVS**
Li	4e	1.0	0.002(2)	0.638(2)	0.103(2)	1.16(11)	1.19(2)
Co	2a	1.0	0	0	0	0.65(2)	1.92(2)
S	4e	1.0	0.3361(2)	0.3046(13)	0.3024(2)	0.68(2)	5.97(2)
O1	4e	1.0	0.1829(4)	0.4185(3)	0.1530(3)	0.70(4)	2.12(2)
O2	4e	1.0	0.2048(5)	0.1365(2)	0.2466(3)	0.85(4)	1.97(2)
O3	4e	1.0	0.2834(4)	0.3506(2)	0.4501(3)	0.73(4)	1.92(2)
O4	4e	1.0	0.6794(4)	0.3022(2)	0.3748(3)	0.46(4)	2.04(2)
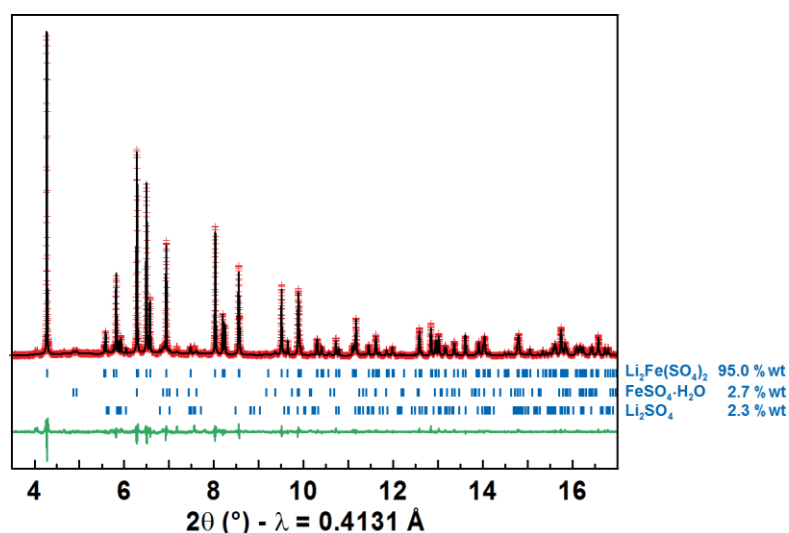
Figure III.2: Results of the Rietveld refinement of the 11-BM Synchrotron XRD pattern of a Li$_2$Fe(SO$_4$)$_2$ sample.

Table III.2: Crystallographic data and atomic positions of Li$_2$Fe(SO$_4$)$_2$. Results of the Rietveld refinement of the 11-BM X-ray diffraction pattern (λ = 0.4131 Å).

Li$_2$Fe(SO$_4$)$_2$						
Space group P2$_1$/c				χ² = 1.78		R$_{Bragg}$ = 2.62 %
a = 4.9886(2) Å		b = 8.2062(2) Å		c = 8.8293(2) Å	β = 121.7499(2)°	V = 307.359(2) Å³
Atom	**Wyckoff site**	**Occupancy**	**x/a**	**y/b**	**z/c**	**B$_{iso}$ (Å²)**	**BVS**
Li	4e	1.0	0.0176(12)	0.6307(7)	0.1060(7)	1.30(12)	1.14(2)
Fe	2a	1.0	0	0	0	0.49(2)	1.94(2)
S	4e	1.0	0.3340(2)	0.3040(13)	0.3015(2)	0.49(2)	5.94(2)
O1	4e	1.0	0.1779(4)	0.4183(2)	0.1501(2)	0.48(4)	2.08(2)
O2	4e	1.0	0.2007(4)	0.1376(2)	0.2482(2)	0.37(4)	1.95(2)
O3	4e	1.0	0.2879(4)	0.3517(2)	0.4470(2)	0.63(5)	1.95(2)
O4	4e	1.0	0.6762(4)	0.3003(2)	0.3703(3)	0.42(4)	2.03(2)

As expected, the Li$_2$Fe(SO$_4$)$_2$ phase was found to be isostructural to the cobalt counterpart **[426]**. The structure determined above for Li$_2$Co(SO$_4$)$_2$ was therefore refined against the 11-BM Synchrotron XRD data obtained for the iron analogue. The atomic positions and crystallographic parameters resulting from this Rietveld refinement are shown in **Figure III.2** and **Table III.2**.

The structure of the Li$_2$M(SO$_4$)$_2$ (M = Co, Fe) phases is illustrated in **Figure III.3**. It is built upon isolated MO$_6$ octahedra that are linked one to the other through SO$_4$ tetrahedra. This 3D framework gives rise to large open channels running along the [100] direction, in which the Li$^+$ cations sit. Each octahedron is linked to six sulfate groups through their vertices. Conversely, each SO$_4$ group is only bounded to three MO$_6$ octahedra, and the non-shared fourth corner of the tetrahedra points towards the channels where the lithium resides. This peculiar arrangement of corner-sharing MO$_6$ octahedra and SO$_4$ tetrahedra results in an open framework, as reflected by the low density of these compounds (ρ ≈ 2.8 g/cm^3). Overall, the structure of the Li$_2$M(SO$_4$)$_2$ (M = Co, Fe) compounds can be considered topologically similar to the phases Mg(HSO$_4$)$_2$ and Zn(HSO$_4$)$_2$ **[437,438]**, although the Li site of the former is non-equivalent to the H site in the latter. This is the reason why the monoclinic structure determined for the Li$_2$M(SO$_4$)$_2$ (M = Co, Fe) phases, which will be referred to as the *marinite* structure[*] herein, can be viewed as a novel structure.
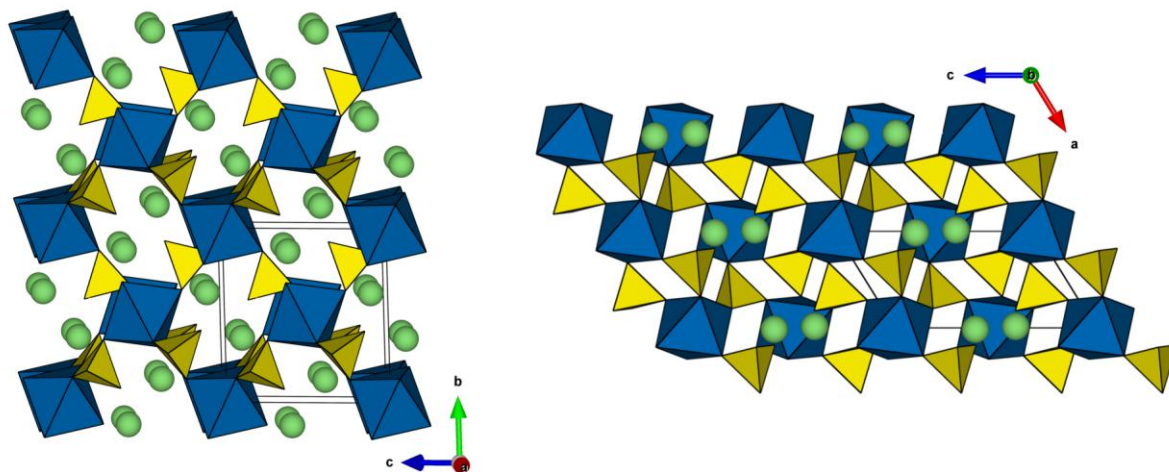
Figure III.3: Representation of the monoclinic *marinite* structure of Li$_2$M(SO$_4$)$_2$ (M = Co, Fe), viewed along the *a*- and the *b*-axes.

[*] For the sake of the anecdote, we incidentally invented the name "*marinite*" in the course of one of our weekly group meetings after having spelled aloud the general formula "Li$_2$M(SO$_4$)$_2$" for several dozens times when comparing these new compounds with the *bloedite* (Na$_2$M(SO$_4$)$_2$·4H$_2$O, M = Mg, Co, Fe, Ni, Zn), the *triplite* (LiMSO$_4$F, M = Fe, Mn), the *tavorite* (LiMSO$_4$F, M = Fe, Co, Ni), the *sillimanite* (LiMSO$_4$F, M = Zn), *olivine* (LiMPO$_4$, M = Fe, Co), *etc.* families of compounds, for which isostructural mineral species were known. This convenient code-name accidentally escaped from our group meetings, and it eventually started to be used by the European battery community to design the Li$_2$M(SO$_4$)$_2$ compounds in meetings, in congresses and even in review papers **[105,323]**.

III.3.2   Mössbauer spectroscopy

[57]Fe Mössbauer spectroscopy[*] was used to probe the oxidation state and the environment of the iron in Li$_2$Fe(SO$_4$)$_2$. **Figure III.4** shows an example of the typical spectra obtained for our samples. It shows a main doublet of divalent iron (noted Fe(II+)·A in **Table III.3** and displayed in blue in **Figure III.4**), which accounts for about 90 % of the iron present in the sample. It is attributed to the iron sitting in an octahedral environment in the crystalline phase Li$_2$Fe(SO$_4$)$_2$.

Table III.3: Room temperature [57]Fe Mössbauer parameters of Li$_2$Fe(SO$_4$)$_2$. δ represents the isomer shift relative to metallic iron standard at room temperature, while ΔE_q and Γ are the quadrupole splitting and the line width, respectively. The stars * at the right of the value numbers indicate that the corresponding parameters were constrained for the fit of the spectrum.

	Attribution	δ (mm/s)	ΔEq (mm/s)	Γ (mm/s)	Atomic fraction (%)
Li$_2$Fe(SO$_4$)$_2$ pristine	Fe(II+)·A	1.30(1)	1.16(1)	0.27(1)	92(3)
	Fe(II+)·B1	1.30(5)	2.47(15)	0.26(7)*	2(1)
	Fe(II+)·B2	1.30(2)	2.85(6)	0.26(7)*	6(2)
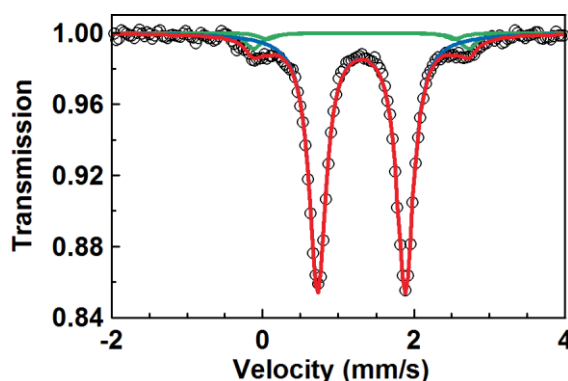
Figure III.4: Typical [57]Fe Mössbauer spectra recorded for Li$_2$Fe(SO$_4$)$_2$. The black circles and the red line represent the experimental and the simulated spectra, respectively. The blue subspectrum corresponds to the contribution denoted Fe(II+)·A, while the Fe(II+)·B1 and B2 subspectra are displayed in green.

Whatever the synthesis route chosen (*e.g.* ceramic, ionothermal, SPS), the annealing temperature (*e.g.* 270 to 380°C) and the time reaction (*e.g.* 24 hours to several days), the spectra of all our Li$_2$Fe(SO$_4$)$_2$ samples present shoulders surrounding the main doublet of Fe(II+)·A. This small signal was fitted with two doublets having large quadrupole splittings (noted Fe(II+)·B1 and Fe(II+)·B2 in **Table III.3**) and corresponds to about 8-12 % of the iron of the sample. The exact origin of this second kind of signal (intrinsic to Li$_2$Fe(SO$_4$)$_2$ or other phase(s)) is not fully understood at this stage. Note that the Mössbauer parameters of doublet Fe(II+)·B2 are close to the ones of the FeSO$_4$·H$_2$O phase ($\delta \approx 1.26$ mm/s and $\Delta Eq \approx 2.72$ mm/s; reference **[324]** and personal results not shown here),

---

[*] Mössbauer spectroscopy was performed in collaboration with Dr. Moulay Tahar Sougrati at the Institut Charles Gerhadt (UMR 5253), Université de Montpellier 2, Montpellier, France (*cf.* Annexes: § A.4.1 page 167).

however the presence of this hydrated sulfate is excluded since the samples were prepared at temperatures beyond its temperature of dehydration and were prevented from moisture exposure afterwards (contrary to the sample used for the structure determination in **Figure III.2**).

III.3.3   Thermal stability

Thermal gravimetric analysis (TGA) coupled with mass spectrometry (MS) and differential scanning calorimetry (DSC) were used to assess the thermal stability of both Li$_2$Co(SO$_4$)$_2$ and Li$_2$Fe(SO$_4$)$_2$ under argon. The cobalt sample showed no decomposition before melting at 585°C, whereas the iron-based one was found to decompose above 420°C (**Figure III.5.a**). Complementary high-temperature XRD measurements were performed under flowing N$_2$ for the iron phase. They showed evidence of decomposition of Li$_2$Fe(SO$_4$)$_2$ into Li$_2$SO$_4$ + Fe$_2$O$_3$, as seen in **Figure III.5.b**.
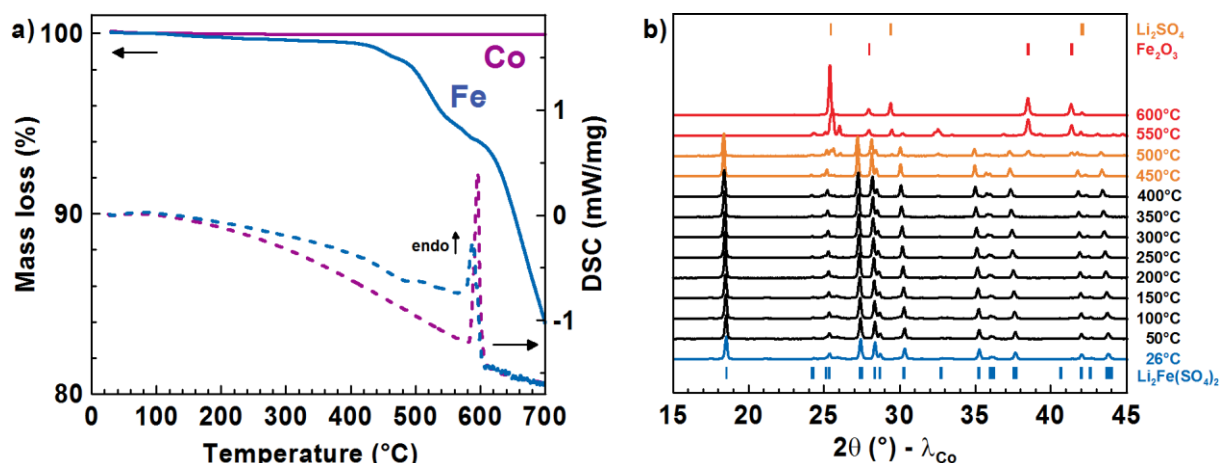
Figure III.5: (a) TGA (solid lines) and DSC (dotted lines) measurements recorded for the Li$_2$Co(SO$_4$)$_2$ (in purple) and the Li$_2$Fe(SO$_4$)$_2$ (in blue) samples (b) Evolution of the XRD patterns upon heating Li$_2$Fe(SO$_4$)$_2$. The blue, orange and red sticks represent the Bragg positions expected for the Li$_2$Fe(SO$_4$)$_2$, Li$_2$SO$_4$, and Fe$_2$O$_3$ phases, respectively.

III.3.4   Electrochemical properties of Li$_2$Fe(SO$_4$)$_2$

For electrochemical testing, electrode materials were simply prepared by ball-milling for 20 minutes under argon the active material with carbon SP, taken in a mass ratio of 80:20. They were cycled in half-cells against lithium metal, using LiClO$_4$ 1M in PC or EC/DMC as the electrolyte, since first attempts with LP30 appeared to have a slight reactivity with the active material.

A typical voltage-composition trace of the *marinite* Li$_2$Fe(SO$_4$)$_2$ cycled at a rate of one lithium per 20 hours (C/20) is shown in **Figure III.6**. During the first charge, nearly 1 Li$^+$ ion is removed from the structure, while 0.86 Li$^+$ ions are reinserted on discharge, which gives a reversible capacity of about 88 mAh/g (theoretical specific capacity of 102 mAh/g). The electrochemical activity is centered around 3.83 V *vs.* Li$^+$/Li^0 **[426,428]**, as confirmed by the dx/dV derivative curve (**Figure III.6**) and by GITT experiments (**Figure III.7.a**; *cf.* Annexes: § A.2.3.2 Galvanostatic Intermittent Titration Technique

(GITT) tests, page 161). Note that this 3.83 V potential is in fact the highest potential ever reported for the Fe^{III+}/Fe^{II+} redox couple in a fluorine-free inorganic material **[105,323,426,428]**, and it is only overstepped by the *triplite* form of LiFeSO$_4$F (3.9 V *vs.* Li$^+$/Li^0, **[330,335]**).
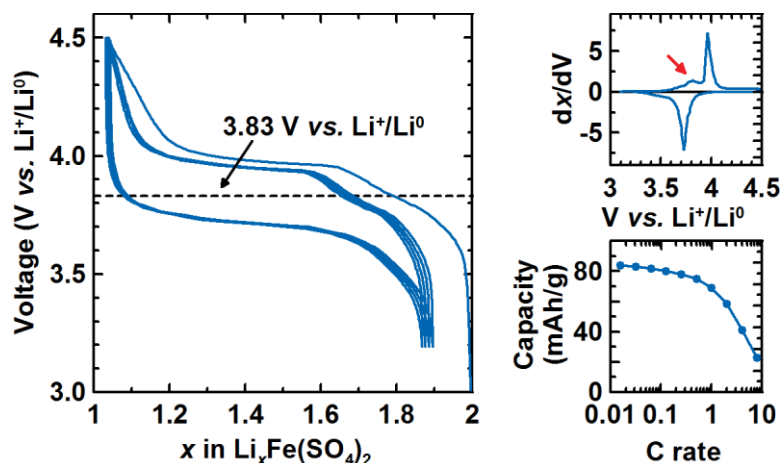
Figure III.6: Electrochemical characterization of *marinite* Li$_2$Fe(SO$_4$)$_2$. Left: galvanostatic curve of Li$_2$Fe(SO$_4$)$_2$ *versus* lithium metal cycled at a C/20 rate. Upper right: corresponding derivative curve d*x*/dV. The red arrow indicates the feature discussed in the text. Bottom right: discharge capacity as function of the cycling rate.

Therefore, if one takes into account the usual gap (~1.3 V) observed between the potentials of iron- and cobalt-based compounds, the potential related to the Co^{III+}/Co^{II+} redox couple in *marinite* Li$_2$Co(SO$_4$)$_2$ would be well outside the stability range of the electrolyte, hence the absence of any electrochemical activity observed for this phase. Recent DFT calculations have shown that its potential would indeed lie around 5.2 V *vs.* Li$^+$/Li^0 **[439]**. The same trend was observed for the *olivine* LiCoPO$_4$ and the *tavorite* LiCoSO$_4$F, for which redox potentials about 1.3 V larger than their iron counterparts were measured or calculated **[252,254,318,331,427,440]**.
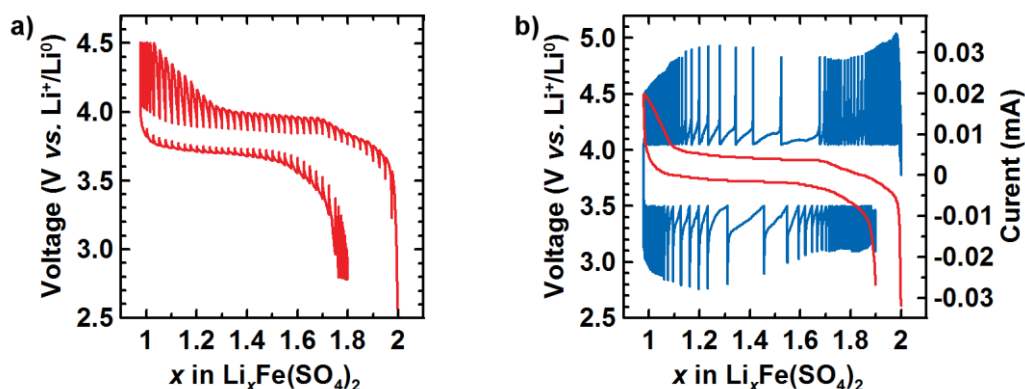
Figure III.7: (a) GITT and (b) PITT responses obtained from Li$_2$Fe(SO$_4$)$_2$ in lithium half-cells.

Besides, in order to test the electrode kinetics, we probed the rate capability of the iron phase Li$_2$Fe(SO$_4$)$_2$; the corresponding results are shown in **Figure III.6** at the bottom right. Given that the electrode contained only 20% carbon and that a thorough optimization of the electrode composition

was not performed, the fact that 85% of the initial capacity was retained at a 1C rate reflects good kinetics for Li$^+$ insertion.

Regarding the Li$^+$ removal/uptake mechanism, the plateau observed in the voltage-composition trace on charge and on discharge (**Figure III.6**) is suggestive of a two-phase intercalation process, as also supported by PITT measurements (**Figure III.7.b**). However, one should notice the presence of a sloped region at the beginning of each charge ($2 \leq x \leq 1.7$), which is not visible in the discharge curves. This is more noticeable in the derivative curve, as indicated with a red arrow in **Figure III.6**. Such features which are clearly visible on charge but less so on discharge are not unprecedented, as similar observations were reported for the *tavorite* LiVPO$_4$F **[302,441]**, the *maricite* NaFePO$_4$ **[261]** (see in Chapter I: **Figure I.18** page 26), or also the rhombohedral form of Fe$_2$(SO$_4$)$_3$ **[224,230]** (see in Chapter I: **Figure I.11.b** page 21); in these cases, the kinetics of Li$^+$ insertion and removal have been suggested to play a role but no definitive explanation has been established. Further investigation of the charge/discharge mechanism of the *marinite* Li$_2$Fe(SO$_4$)$_2$ will be presented in section III.3.7 (page 92), but before to address this point, we will first examine the oxidized phase Li$_1$Fe(SO$_4$)$_2$.

III.3.5 The delithiated phase Li$_1$Fe(SO$_4$)$_2$

III.3.5.1 Preparation

Li$_1$Fe(SO$_4$)$_2$ can be made from both chemical and electrochemical oxidation of Li$_2$Fe(SO$_4$)$_2$. To characterize this delithiated phase, samples prepared from chemical oxidation of the pristine phase were preferred to the ones obtained from electrochemical oxidation (*i.e.* electrode materials recovered at the end of the first charge in lithium half-cells), because the former were free of carbon and traces of electrolyte, and better crystallized than the latter, as seen in **Figure III.8**.
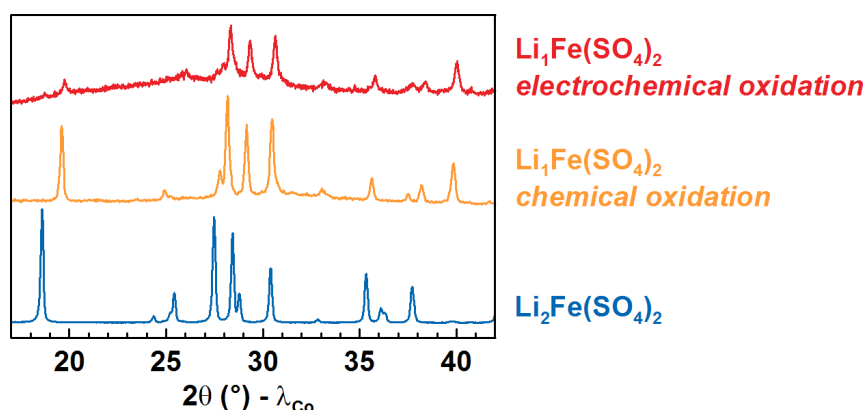
Figure III.8: Comparison of the XRD patterns of the pristine Li$_2$Fe(SO$_4$)$_2$ (blue pattern), the delithiated phase Li$_1$Fe(SO$_4$)$_2$ obtained through chemically oxidation (yellow pattern) or electrochemical oxidation (red pattern).

To prepare these "chemically oxidized" samples, powders of Li$_2$Fe(SO$_4$)$_2$ were reacted in acetonitrile with NO$_2$BF$_4$, which were employed as an oxidizing agent. This solution was stirred for at least 12 hours at room temperature in an argon-filled glove-box. The oxidized sample was then recovered by centrifugation and washed several times with acetone.

Atomic absorption and EDX measurements performed on the resulting sandy-grey powders verified the nominal composition of Li$_1$Fe(SO$_4$)$_2$, and Mössbauer spectroscopy confirmed that the all the iron was oxidized into Fe(III+) (**Figure III.9**), in good agreement with electrochemical observations. Note however that the Mössbauer spectrum of the oxidized phase suggests the presence of three different iron environments (**Table III.4**); the main doublet is attributed to the Li$_1$Fe(SO$_4$)$_2$ phase and accounts for ~85 % of the Fe(III+) present in the sample (orange subspectrum in **Figure III.9**, labeled Fe(III+)·A in **Table III.4**), while the other two may be related to the iron labeled Fe(II+)·B in the pristine phase Li$_2$Fe(SO$_4$)$_2$, although no evidence have been established yet to confirm this assumption.
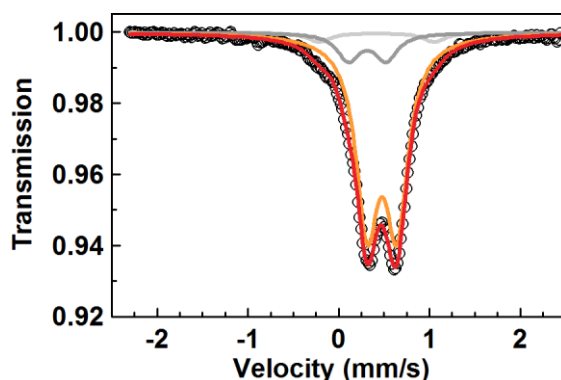
Figure III.9: Typical ^{57}Fe Mössbauer spectrum recorded for a chemically oxidized Li$_1$Fe(SO$_4$)$_2$ sample. Orange subspectrum is attributed to Li$_1$Fe(SO$_4$)$_2$, which is labeled Fe(III+)·A in **Table III.4**, while the dark and light grey subspectra correspond to the Fe(III+)·B and Fe(III+)·C contributions, respectively.

Table III.4: Room temperature ^{57}Fe Mössbauer parameters of Li$_1$Fe(SO$_4$)$_2$. δ represents the isomer shift relative to metallic iron standard at room temperature, while ΔE_q and Γ are the quadrupole splitting and the line width, respectively. The stars * at the right of the value numbers indicate that the corresponding parameters were constrained for the fit of the spectrum.

	Attribution	δ (mm/s)	ΔEq (mm/s)	Γ (mm/s)	Atomic fraction (%)
	Fe(III+)·A	0.47(1)	0.33(1)	0.30(1)*	84(2)
Li$_1$Fe(SO$_4$)$_2$	Fe(III+)·B	0.32(1)	0.42(2)	0.30(1)*	12(2)
	Fe(III+)·C	0.41(2)	1.26(4)	0.30(1)*	4(1)

III.3.5.2 Structure of $Li_1Fe(SO_4)_2$

All reflections of the XRD pattern of $Li_1Fe(SO_4)_2$ could be indexed using the same monoclinic unit cell as the *marinite* $Li_2M(SO_4)_2$ (M = Co, Fe) compounds (space group: $P2_1/c$), with the following lattice parameters: a = 4.789(2) Å, b = 8.350(2) Å, c = 7.902(2) Å, β = 121.45(2)°, V = 269.60(4) Å^3 **[426]**. This corresponds to a cell volume reduction of about 12 % between $Li_2Fe(SO_4)_2$ and $Li_1Fe(SO_4)_2$, which is bigger than the changes observed in other Li^+-insertion compounds such as $LiFePO_4$ ($\Delta V/V \approx 8$ %, **[237]**) or *tavorite* $LiFeSO_4F$ ($\Delta V/V \approx 8$ %, **[321]**). The quality of the laboratory XRD data did not allow however to accurately refine the structure of $Li_1Fe(SO_4)_2$, and in particular localize the position of the lithium atoms within the unit cell **[426]**. For this purpose, we performed neutron powder diffraction (NPD) on the high-resolution powder diffractometer D2B at the Institut Laue Langevin (Grenoble, France; *cf.* Annexes: § A.3.3.1 D2B diffractometer at ILL, page 165) **[442]**. We first started the refinement of the NPD pattern of $Li_1Fe(SO_4)_2$ using solely the FeO_6 octahedra and SO_4 tetrahedra framework pertaining to the *marinite* structure of $Li_2Fe(SO_4)_2$, without any lithium atom in the cell. Calculations of Fourier differential maps were performed with the GFourier program **[443]** of the FullProf Suite **[383,384]**, and permitted to precisely localize the position of the lithium within the channels running along the *a*-axis. **Figure III.10** presents two sections of the calculated Fourier differential maps, which unambiguously showed a peak in nuclear density (*i.e.* a missing atom) having an elongated ellipsoidal shape around the (½,0,½) position.
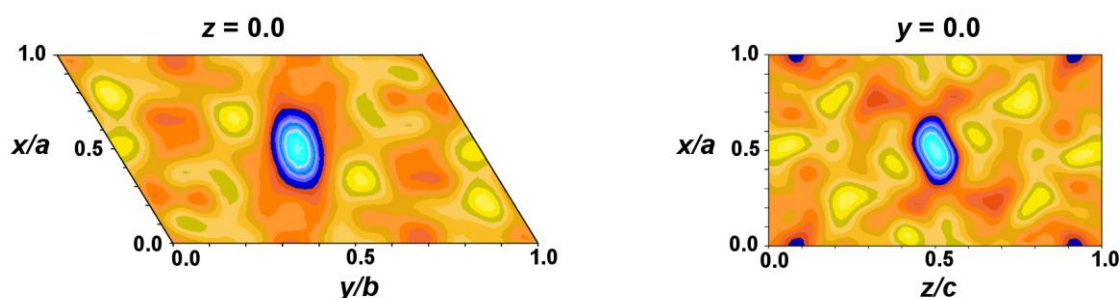
Figure III.10: Sections of the Fourier difference maps obtained from the refinement of the NPD pattern of $Li_1Fe(SO_4)_2$ against the FeO_6 octahedra and SO_4 tetrahedra framework pertaining to $Li_2Fe(SO_4)_2$ structure. The blue ellipsoid shows the position of the missing Li atom.

Refinement of the structure with one lithium atom placed in the 2*d* Wyckoff site (½, 0, ½) resulted in an important anisotropic displacement (equivalent isotropic temperature factor $B_{iso} \approx 8$ Å^2), with the main direction of this ellipsoid being elongated along the <5 1 2> directions (**Figure III.11.a**). This suggested that the lithium ions were more likely distributed on a general position 4*e* with half occupancy and located in the vicinity of the (½, 0, ½) position. Refinement of this model led to a much lower temperature factor ($B_{iso} \approx 1.1$ Å^2) **[442]**, and the resulting structure is displayed in **Figure III.11.b**. Note that in this second model, the two half-occupied lithium positions around the

(½, 0, ½) site are separated by a distance of 0.7 Å, which is consistent with the anisotropic displacement calculated with the first model.
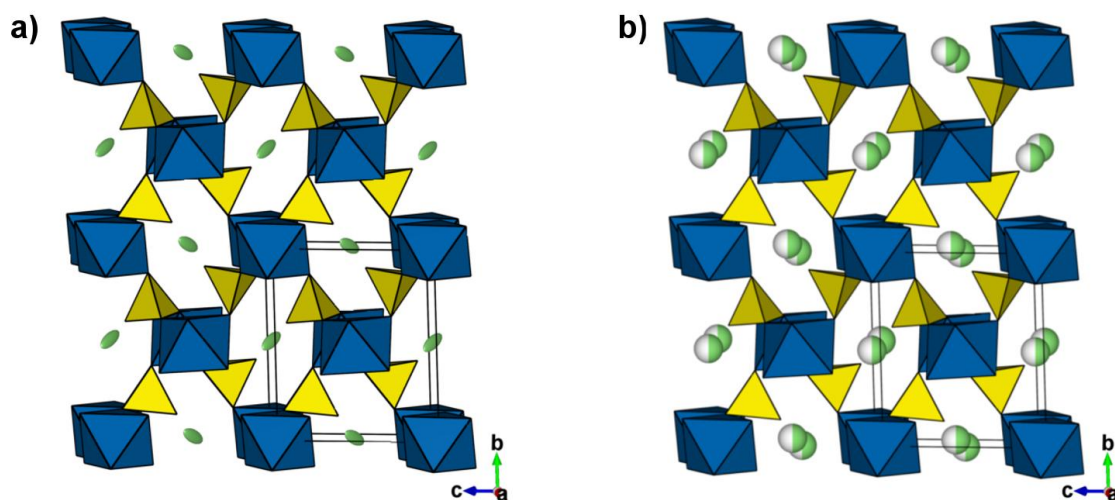
Figure III.11: Comparison of the two hypotheses for the lithium position in the structure of Li$_1$Fe(SO$_4$)$_2$, as described in the text: (a) Li in the 2*d* Wyckoff site, with an large anisotropic displacement (green elongated ellipsoids), and (b) Li in a half-occupied 4*e* Wyckoff site (half-colored green balls).

Finally, a joint Rietveld refinement of the structure was performed against both the D2B NPD data and Synchrotron XRD data obtained through the 11-BM mail-in service of the Argonne Photon Source (Argonne, USA, see Annexes). The results of this refinement are presented in **Table III.5** and **Figure III.12**. Note that the bond valence sum (BVS) analysis, using b$_0$ parameters from Brown **[402]** (*cf.* Annexes: § A.3.4.1 Refinement of the structures from XRD and NPD patterns, page 166), indicated that the Fe−O bond lengths are in excellent agreement with iron in the III+ oxidation state, as previous deduced from Mössbauer spectroscopy (**Figure III.9**).
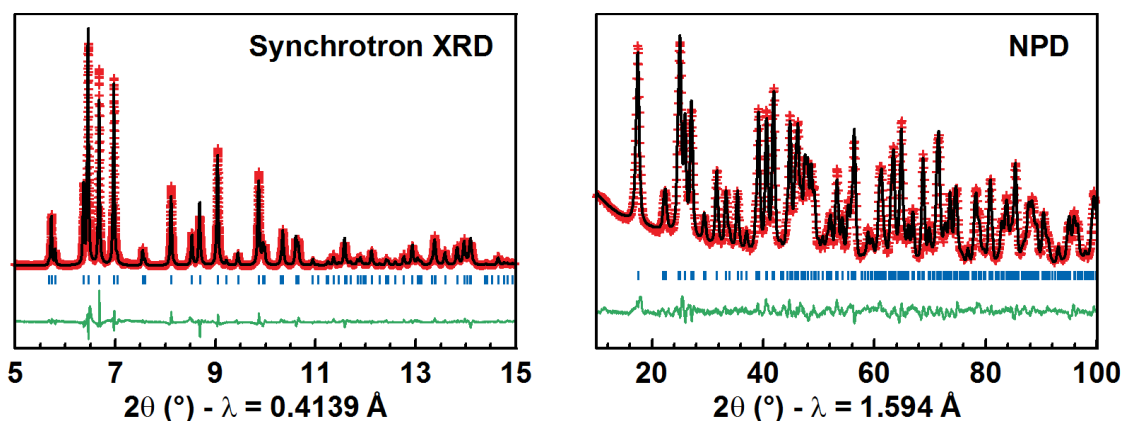
Figure III.12: Results of the joint Rietveld refinement of Li$_1$Fe(SO$_4$)$_2$ against the 11-BM Synchrotron X-ray diffraction pattern (left) and the D2B neutron powder diffraction pattern (right). The red crosses and the black line represent the experimental and the calculated patterns, respectively. The green line is the difference curve of these two patterns. Bragg positions are shown as blue sticks.

Table III.5: Crystal structure of $Li_1Fe(SO_4)_2$ resulting from the joint refinement of both D2B NPD (high-resolution mode, λ = 1.594 Å, T = RT) and 11-BM Synchrotron XRD (λ = 0.4139 Å, T = RT) data.

Li₁Fe(SO₄)₂							
Space group $P2_1/c$				χ^2 = 5.81		R_{Bragg} = 4.66 %	
a = 4. 7966(2) Å		b = 8. 3628(2) Å		c = 7. 9059(2) Å	β = 121.475(5)°	V = 270.465(3) Å³	
Atom	**Wyckoff site**	**Occupancy**	**x/a**	**y/b**	**z/c**	**B_{iso} (Å²)**	**BVS**
Li	4e	0.5	0.560(3)	0.0236(14)	0.5258(18)	1.1(3)	1.12(3)
Fe	2a	1.0	0	0	0	0.49 (2)	3.00 (2)
S	4e	1.0	0.3048 (3)	0.1783 (2)	0.7613 (2)	0.27 (2)	5.95 (2)
O1	4e	1.0	0.0455 (4)	0.1275 (2)	0.7997 (3)	0.69 (4)	1.99 (2)
O2	4e	1.0	0.2632 (4)	0.1033 (2)	0.5854 (3)	0.66 (4)	2.00 (2)
O3	4e	1.0	0.2824 (4)	0.3572 (2)	0.7377 (3)	0.57 (4)	2.02 (2)
O4	4e	1.0	0.3757 (4)	0.6422 (2)	0.5594 (2)	0.55 (4)	2.01 (2)
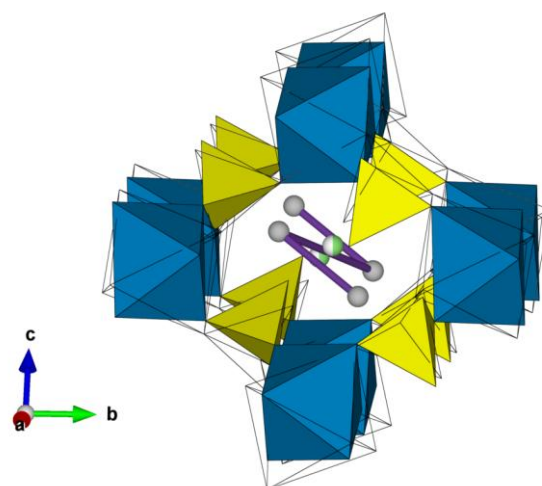
Figure III.13: Comparison of the structures of $Li_1Fe(SO_4)_2$ (colored filled polyhedra) and $Li_2Fe(SO_4)_2$ (open polyhedra). In the delithiated phase, lithium atoms (half-colored green balls) sit in a half-occupied position in the middle of the channels running along the a-axis. Grey balls indicate the position of the lithium atoms in the lithiated phase. The violet lines represent the Li^+ diffusion pathways calculated for $Li_2Fe(SO_4)_2$ **[439]**.

Overall, the structure of $Li_1Fe(SO_4)_2$ presents the same framework of FeO_6 octahedra and SO_4 tetrahedra as its parent lithiated phase, but as shown in **Figure III.13**, the octahedra and tetrahedra in $Li_1Fe(SO_4)_2$ are slightly tilted compared to $Li_2Fe(SO_4)_2$. After the removal of one lithium, the remaining Li^+ ion of $Li_1Fe(SO_4)_2$ shifts towards the middle of the tunnel in a split position with half occupancy. The lithium is therefore coordinated by five oxygen atoms, which is more preferable than the highly elongated octahedral coordination that lithium would adopt in the (½, 0, ½) 2d Wyckoff position. Moreover, this five-coordination is geometrically similar to the coordination of the lithium in the pristine $Li_2Fe(SO_4)_2$ compound. Besides, it is interesting to note that the position determined for the lithium cations in the delithiated phase $Li_1Fe(SO_4)_2$ is placed just in the middle of the lithium diffusion pathway calculated for the lithiated phase $Li_2Fe(SO_4)_2$ (violet lines in **Figure III.13**) **[439]**; this

is certainly not fortuitous, and we believed that further theoretical investigations of the delithiated phase Li$_1$Fe(SO$_4$)$_2$ could be of great interest to explain this observation. Such calculations could also find out whether the split lithium site determined from diffraction experiments is the result of a static or a dynamic disorder.

Another interesting point to address here is to compare the structure this new Li$_1$Fe(SO$_4$)$_2$ phase (the "delithiated *marinite*") with the one of the *eldfellite* NaFe(SO$_4$)$_2$ and the *yavapaiite* KFe(SO$_4$)$_2$, which were presented in the previous chapter (*cf.* Chapter II: § II.4 Syntheses and electrochemical properties of other sodium iron sulfates inspired from minerals, from page 67). At a first sight, the layered structure of the (Na/K)Fe(SO$_4$)$_2$ compounds (*cf.* Chapter I: **Figure II.23** page 70) strongly differ from the 3D framework of the *marinite* Li$_1$Fe(SO$_4$)$_2$ (**Figure III.11.b** page 87). However, when the Li$_1$Fe(SO$_4$)$_2$ structure is viewed along the *a*-axis (**Figure III.14.a**) and the (Na/K)Fe(SO$_4$)$_2$ structure is oriented along the [1 -1 0] direction (**Figure III.14.c**), some similarities begin to appear. Next, if one imagine a site exchange between half of the Fe and half of the Na/K atoms in the *eldfellite/yavapaiite* structure, as represented with the thin red arrows in **Figure III.14.c** (*i.e.* the alkali and the iron atoms alternately occupy the 2*a* and 2*c* Wyckoff sites of the *C*2/*m* unit cell, respectively), then the resulting hypothetical structure (**Figure III.14.b**) is topologically very close to the one of Li$_1$Fe(SO$_4$)$_2$ (**Figure III.14.b**). Therefore, one can consider that the *marinite* and the *eldfellite/yavapaiite* are structurally related, but with a different distribution of the alkali and iron cations in the octahedral sites, which may be due to the size of cations since Fe^{III+} and Li$^+$ present similar ionic radii (0.645 Å and 0.76 Å, respectively **[111]**) whereas the ones of Na$^+$ and K$^+$ are much larger (1.02 Å and 1.38 Å, respectively **[111]**).
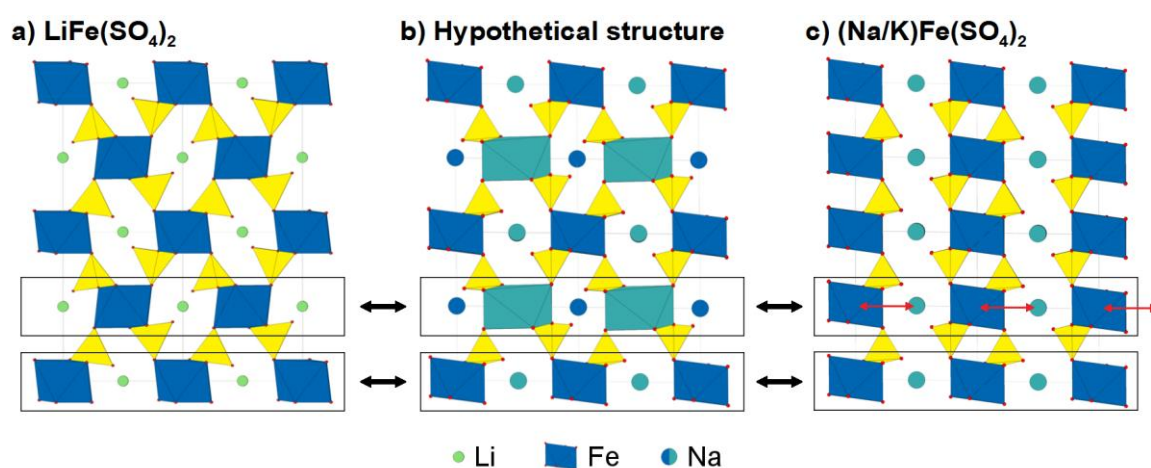
Figure III.14: Comparison of (a) the *marinite* structure of Li$_1$Fe(SO$_4$)$_2$ viewed along the *a*-axis and (c) the *eldfellite/yavapaiite* structure of (Na/K)Fe(SO$_4$)$_2$ viewed along the [1-10] direction. The red arrows illustrate the hypothetical site exchange of half of the iron with half of the alkali cations, as described in the text, and the resulting hypothetical structure is displayed in (b).

At this point, we should mention that we could not stabilize $Li_1Fe(SO_4)_2$ in the *eldfellite/yavapaiite* structure through chemical exchange from $NaFe(SO_4)_2$ or $KFe(SO_4)_2$, as here also, whatever the route employed (with either $LiCl$ or $LiNO_3$, either in acetonitrile or *via* solid-state reaction), all our attempts resulted in the decomposition of the material, with in particular the formation of Li_2SO_4. Finally, we can also remark the difference in thermal stability properties between the *marinite* $Li_1Fe(SO_4)_2$ and the *eldfellite/yavapaiite* $(Na/K)Fe(SO_4)_2$: the latter compounds are stable up to 600°C whereas the former decomposes above 150°C (see below, **Figure III.15**). Here, DFT calculations would also be of great interest in order to understand the differences between these three phases.

III.3.5.3 Stability properties of Li₁Fe(SO₄)₂

Several attempts have been made to prepare the delithiated *marinite* $Li_1Fe(SO_4)_2$ *via* direct synthesis from stoichiometric mixtures of Li_2SO_4 and $Fe_2(SO_4)_3$, but all of them failed. This was indeed understood when evaluating the thermal stability of the $Li_1Fe(SO_4)_2$ sample obtained from the chemical oxidation of $Li_2Fe(SO_4)_2$: high-temperature X-ray diffraction measurements performed under nitrogen flow indicated the decomposition of $Li_1Fe(SO_4)_2$ into Li_2SO_4 + $Fe_2(SO_4)_3$ at temperatures as low as 150°C (**Figure III.15**), suggesting that this phase would be in fact metastable.
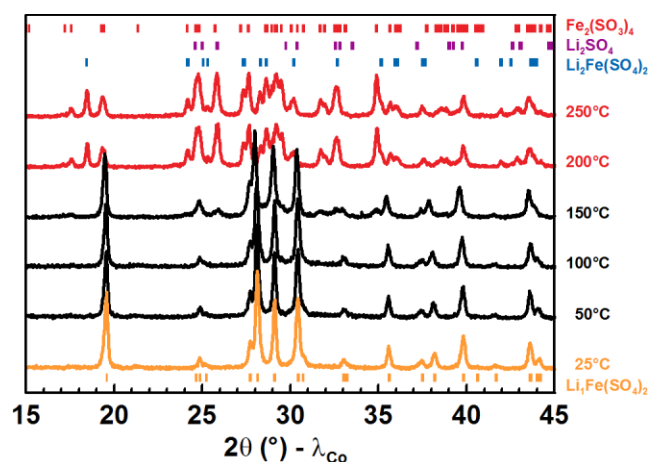
Figure III.15: Evolution of the XRD patterns upon heating $Li_1Fe(SO_4)_2$.

Moreover, contrary to the pristine $Li_2Fe(SO_4)_2$ phase, the delithiated compound $Li_1Fe(SO_4)_2$ was found to be moisture sensitive, with its XRD pattern evolving within a few hours when exposed to air (**Figure III.16**). The new reflections appearing in the XRD pattern can be compared to the pattern reported for the *rhomboclase* $HFe(SO_4)_2 \cdot 5H_2O$ **[444–446]**, and the presence of water in the sample was confirmed by TGA-MS analyses. As a result, $Li_1Fe(SO_4)_2$ had to be permanently stored in an argon-filled glove-box and characterizations had to be carried out with special care in order to keep the sample in an inert environment at any time.
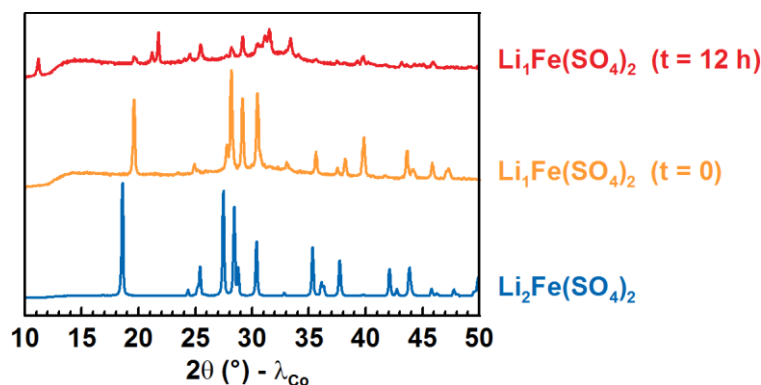
Figure III.16: Comparison of the XRD patterns of the pristine Li$_2$Fe(SO$_4$)$_2$ (blue pattern), the chemically oxidized phase Li$_1$Fe(SO$_4$)$_2$ (yellow pattern) and the same sample after air exposure (red pattern).

III.3.6 Sodium insertion into Li$_1$Fe(SO$_4$)$_2$

Having remarked the structural relation existing between the delithiated *marinite* Li$_1$Fe(SO$_4$)$_2$ and the *eldfellite*/*yavapaiite* (Na/K)Fe(SO$_4$)$_2$ compounds as discussed in the previous section, it was tempting to check whether sodium could be inserted into the *marinite* structure. We therefore assembled a sodium half-cell with Li$_1$Fe(SO$_4$)$_2$/C$_{SP}$ at the positive electrode material, and a solution of 1 M NaClO$_4$ in PC as the electrolyte. Li$_1$Fe(SO$_4$)$_2$ was found to reversibly uptake up to ~0.7 Na$^+$ during the first cycle, but the reversible capacity rapidly decrease upon the subsequent cycles **[426]**. The average potential was centered around 3.4 V *vs.* Na$^+$/Na^0 (**Figure III.17**), with an approximately 400 mV difference compared to the 3.83 V *vs.* Li$^+$/Li^0 falling within the range of what is expected and usually observed when changing a lithium metal anode for a sodium metal one (see Chapter I and references **[317,318,386,387]**).
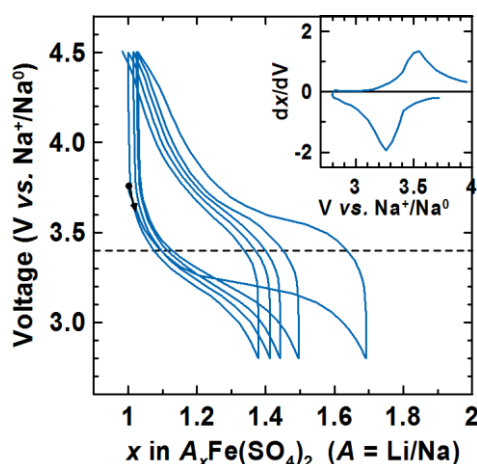
Figure III.17: Galvanostatic curve obtained from Li$_1$Fe(SO$_4$)$_2$ cycled *versus* a sodium metal anode. The derivative d*x*/dV corresponding to the first cycle is shown in inset.

Figure III.18 compares the XRD pattern of the positive electrode material recovered from a Na // NaClO$_4$ 1M in PC // Li$_1$Fe(SO$_4$)$_2$/C$_{SP}$ cell after a first discharge, labelled "Li$_1$Na$_1$Fe(SO$_4$)$_2$", with the ones of the pristine Li$_2$Fe(SO$_4$)$_2$ and the oxidized phase Li$_1$Fe(SO$_4$)$_2$. The similarity of the three patterns

suggests that the general structure framework of the *marinite* is maintained after sodium insertion, with a unit cell volume that should be intermediate between the ones of the lithiated Li$_2$Fe(SO$_4$)$_2$ and the delithiated Li$_1$Fe(SO$_4$)$_2$ phases. However we have not determined the exact unit cell parameters yet.
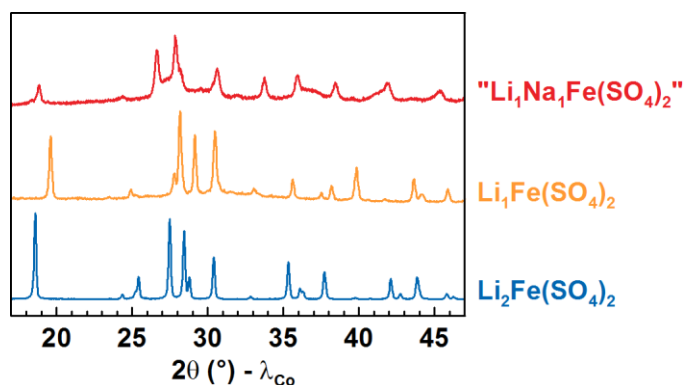
Figure III.18: Comparison of the XRD patterns of the pristine Li$_2$Fe(SO$_4$)$_2$ (blue pattern), the chemically oxidized phase Li$_1$Fe(SO$_4$)$_2$ (yellow pattern) and the phase "Li$_1$Na$_1$Fe(SO$_4$)$_2$" obtained by Na$^+$ electrochemical insertion into Li$_1$Fe(SO$_4$)$_2$ (red pattern).

Here again, all our attempts to prepared a LiNaFe(SO$_4$)$_2$ phase *via* direct synthesis failed, whatever the alkali-based precursors employed (Li$_2$SO$_4$ + Na$_2$SO$_4$ or LiNaSO$_4$) and the temperature of reaction (200-400°C). Synthesis of other members of the solid solution Li$_x$Na$_{1-x}$Fe(SO$_4$)$_2$ (0 ≤ x ≤ 1) were equally unsuccessful.

III.3.7   Towards the understanding the Li$^+$ extraction/insertion mechanism in Li$_2$Fe(SO$_4$)$_2$

The electrochemical signature of Li$_2$Fe(SO$_4$)$_2$ cycled against a lithium metal anode was previously presented in section III.3.4 (page 82). As commented therein, the electrochemical curve presents a plateau both on charge and on discharge (see **Figure III.6** page 83), suggesting a two-phase mechanism for Li$^+$ extraction/insertion in Li$_2$Fe(SO$_4$)$_2$. However, we also noticed the presence of a sloped region at the beginning of each charge (2 ≥ x ≥ 1.7), which is not visible on discharge. Understanding this feature called for further advanced characterizations.

III.3.7.1   In operando characterizations

X-ray diffraction

To gain better insight into the mechanism of Li$^+$ extraction/insertion in Li$_2$Fe(SO$_4$)$_2$, we first performed *in operando* XRD measurements while charging and discharging the electrode material Li$_2$Fe(SO$_4$)$_2$/C$_{SP}$ (**Figure III.19**). Despite the slopping region observed in the electrochemical curve no noticeable change in either the intensity or the position of the Bragg peaks in the XRD patterns was detected on charging up to x ≈ 1.7. This was somewhat surprising, since S-shaped electrochemical traces are usually the result of second-order mechanisms (*i.e.* solid-solution), which are generally reflected in

the XRD patterns by a gradual shift of the Bragg reflections upon lithium removal. Next, with further removal of lithium (for $1.7 \geq x \geq 1$), diffraction peaks of the Li$_2$Fe(SO$_4$)$_2$ phase progressively decrease in favor of the emergence of new peaks. At the end of the deinsertion process (near $x \approx 1$), the Li$_2$Fe(SO$_4$)$_2$ reflections had fully disappeared and the resulting XRD pattern (in yellow in **Figure III.19**) could be indexed with the unit cell previously determined for the Li$_1$Fe(SO$_4$)$_2$ phase. This confirms that the oxidation process associated with the plateau observed on the charge curve ($1.7 \geq x \geq 1$) occurs according to a two-phase mechanism. On the subsequent discharge, the reverse phenomenon occurs, and the similarity between the XRD pattern of the starting electrode material and the one obtained at the end of the charge–discharge cycle indicates the full reversibility of the process.
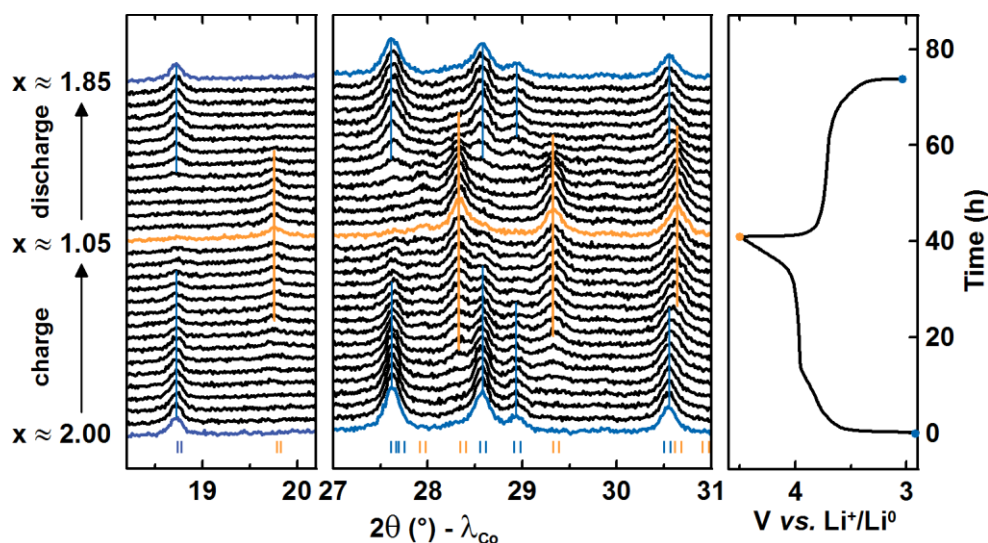
Figure III.19: *In operando* XRD patterns of the electrode material Li$_2$Fe(SO$_4$)$_2$/C$_{SP}$. Blue and yellow sticks represent the Bragg reflections of the Li$_2$Fe(SO$_4$)$_2$ and Li$_1$Fe(SO$_4$)$_2$ phases, respectively.

Mössbauer spectroscopy

As diffraction techniques did not provide any information about the feature observed at the beginning of the charge ($2 \geq x \geq 1.7$), we undertook an *in operando* ^{57}Fe Mössbauer spectroscopy experiment in order to probe the iron environment in the electrode material and follow its oxidation state upon cycling. The results of these measurements are presented in **Figure III.20** (page 95).

First of all, we noticed that the spectrum of the electrode material (Li$_2$Fe(SO$_4$)$_2$ ball-milled with C$_{SP}$; **Figure III.20.a**) is quite different from the one of the pristine phase Li$_2$Fe(SO$_4$)$_2$ (**Figure III.4**, page 81), suggesting that the electrode preparation step alters the active material, as previously observed with Na$_2$Fe(SO$_4$)$_2$·4H$_2$O (*cf.* Chapter I: § II.2.3 Electrochemistry of Na2Fe(SO4)$_2$·4H2O from page 52). Note that, here also, no new reflection could be observed in the XRD pattern of the electrode material Li$_2$Fe(SO$_4$)$_2$/C$_{SP}$ with compared to the one of the pristine phase Li$_2$Fe(SO$_4$)$_2$; the only noticeable difference being a broadening of the peaks, as usually observed after electrode preparation using

mechanical milling. The Mössbauer spectrum of the electrode material was fitted with four doublets of divalent iron, as shown in **Table III.6** and **Figure III.20.a**. In fact, the mechanical-milling seemed to enhance the small subspectrum labeled B in the spectrum of the pristine phase Li$_2$Fe(SO$_4$)$_2$ seen at the beginning of the chapter (**Figure III.4** and **Table III.3**, page 81); this contribution represented here about 32 % of the iron in the electrode material.

The electrode material was then charged and discharged at a C/50 rate, while recording the Mössbauer spectra. We can first remark that, conversely to the XRD patterns, the Mössbauer spectra start changing since the very beginning of the charge, and keep evolving until the all the iron +II is oxidized into iron +III (**Figure III.20.a to g**). The Mössbauer spectrum recorded for the oxidized phase at the end of the first charge (**Figure III.20.g** and **Table III.6**) was fitted with a doublet having a quadrupole splitting slightly larger than the one determined for the chemically oxidized Li$_1$Fe(SO$_4$)$_2$ phase presented earlier (Fe(III+)·A in **Table III.4** and **Figure III.9**, page 85). The other spectra acquired during the first charge/discharge cycle were fitted using a combination of the four doublets of divalent iron (labeled Fe(+II)·A1, A2, B1 and B3) and the doublet of trivalent iron (labeled Fe(+III)) (see **Table III.6**), which had been used to fit the spectra of the electrode material before cycling (**Figure III.20.a**) and at the end of the charge (**Figure III.20.g**), respectively; all the parameters were constrained, except the relative fractions of each contribution. This strategy enabled to well simulate all the spectra. The evolution of the relative fractions of the Fe(II+)·A, Fe(II+)·B and Fe(III+) contributions as a function of the state of charge/discharge is illustrated in the graph at the top right-hand corner of **Figure III.20**. This results provide interesting information. In fact, at the beginning of the charge (up to $x \approx 1.6$, *i.e.* the S-shape part of the curve, and **Figure III.20.a to c**), the Fe(III+) contribution arises at the expense of the Fe(+II)·B signals (*i.e.* the iron in this environment is oxidized) while the Fe(+II)·A contribution remains almost the same. Next, this latter gradually disappears in favor of further increase of the Fe(III+) signal (*i.e.* the iron in the Fe(+II)·A environment is oxidized) in the second part of the charge ($1.6 \geq x \geq 1$, *i.e.* on the plateau region, and **Figure III.20.c to g**). Conversely, on the subsequent discharge (**Figure III.20.g to j**) both Fe(+II)·A and Fe(+II)·B contributions grow simultaneously at the expense of the signal of Fe(III+).
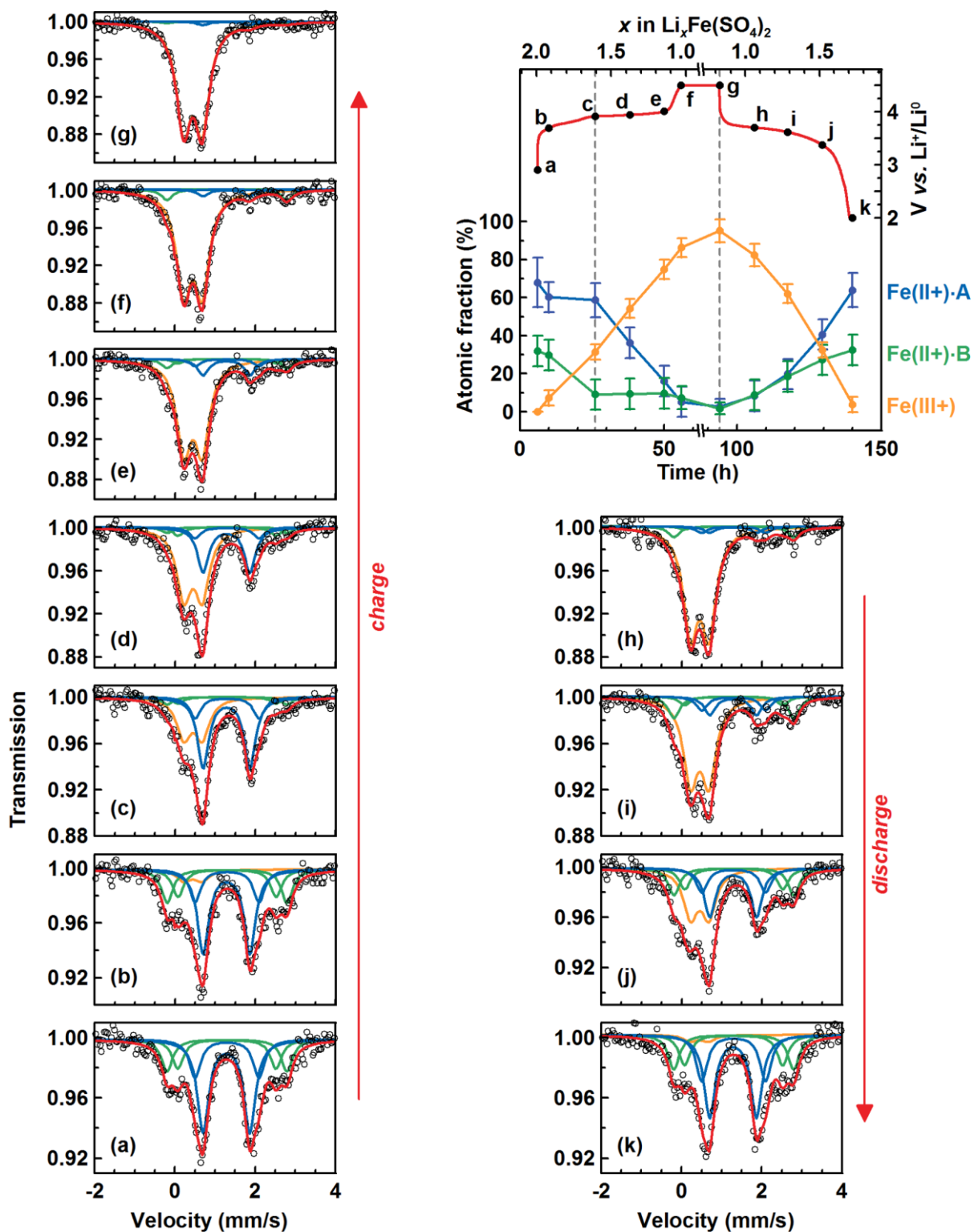
Figure III.20: *In operando* ^{57}Fe Mössbauer spectra of the Li₂Fe(SO₄)₂/C$_{SP}$ electrode material cycled in a lithium half-cell at a C/50 rate. The black circles and the red lines are the experimental and the simulated spectra, respectively. Blue subspectra corresponds to the contributions denoted Fe(II+)·A1 and A2, green subspectra represent the Fe(II+)·B1 and B2 ones. In the graph at the top right-hand corner, the state of charge/discharge corresponding to each spectrum is indicated by black points on the red electrochemical curve. The evolution of the atomic fractions of the Fe(II+)·A, Fe(II+)·B and Fe(III+) contributions upon cycling are represented in the same graph with the blue, green and yellow curves, respectively.

Table III.6: Room temperature ^{57}Fe Mössbauer parameters for the electrode material Li$_2$Fe(SO$_4$)$_2$/C$_{SP}$ before charging and at the end of the first charge. δ represents the isomer shift relative to metallic iron standard at room temperature, while ΔE_q and Γ are the quadrupole splitting and the line width, respectively. The stars * at the right of the numbers indicate that the corresponding parameters were constrained for the fitting of the spectrum.

	Attribution	δ (mm/s)	ΔEq (mm/s)	Γ (mm/s)	Atomic fraction (%)
Li$_2$Fe(SO$_4$)$_2$ *electrode material*	Fe(II+)·A1	1.28(1)	1.16(4)	0.34(4)*	48(7)
	Fe(II+)·A2	1.30(2)*	1.59(9)	0.34(4)*	20(6)
	Fe(II+)·B1	1.30(2)*	2.44(10)	0.34(4)*	15(4)
	Fe(II+)·B2	1.30(2)*	2.99(8)	0.34(4)*	17(4)
Li$_{\sim1.0}$Fe(SO$_4$)$_2$ *electrochemically oxidized*	Fe(II+)·A1	1.28(-)*	1.16(-)*	0.34(-)*	3(3)
	Fe(II+)·A2	1.30(-)*	1.59(-)*	0.34(-)*	<1
	Fe(II+)·B1	1.30(-)*	2.44(-)*	0.34(-)*	<1
	Fe(II+)·B2	1.30(-)*	2.99(-)*	0.34(-)*	2(2)
	Fe(III+)·A	0.45(1)	0.46(1)	0.43(1)	95(5)

Therefore, this *in operando* Mössbauer experiment shows that the electrode preparation using mechanical-milling was at the origin of a modified Fe(II+) environment (*i.e.* the signal labeled Fe(II+)·B, represented in green in the figures). The oxidation of the iron in this modified environment is reflected by a sloping region in the charge curve, whereas the iron remaining in the same Fe(II+) environment as in the crystalline *marinite* Li$_2$Fe(SO$_4$)$_2$ phase (labeled Fe(II+)·A, shown in blue in the figures) is oxidized on the plateau centered at 3.83 V of the electrochemical curve. To check this hypothesis, we undertook a careful study of the effect of the ball-milling time on the electrode material properties.

III.3.7.2   Influence of the ball-milling time on the electrode material

To test the influence of the ball-milling time on the electrode material properties, we prepared a new batch of *marinite* Li$_2$Fe(SO$_4$)$_2$, from which we made four different electrode materials by ball-milling the pristine material with carbon SP for 15, 30, 45 and 60 minutes (hereinafter denoted BM-15, BM-30, BM-45 and BM-60, respectively). Each sample was then characterized by X-ray diffraction, ^{57}Fe Mössbauer spectroscopy and ^{7}Li solid-state NMR, and was also cycled in lithium half-cells at a C/50 rate. The results of these characterizations are presented in **Figure III.21** and **Figure III.22** (page 97).
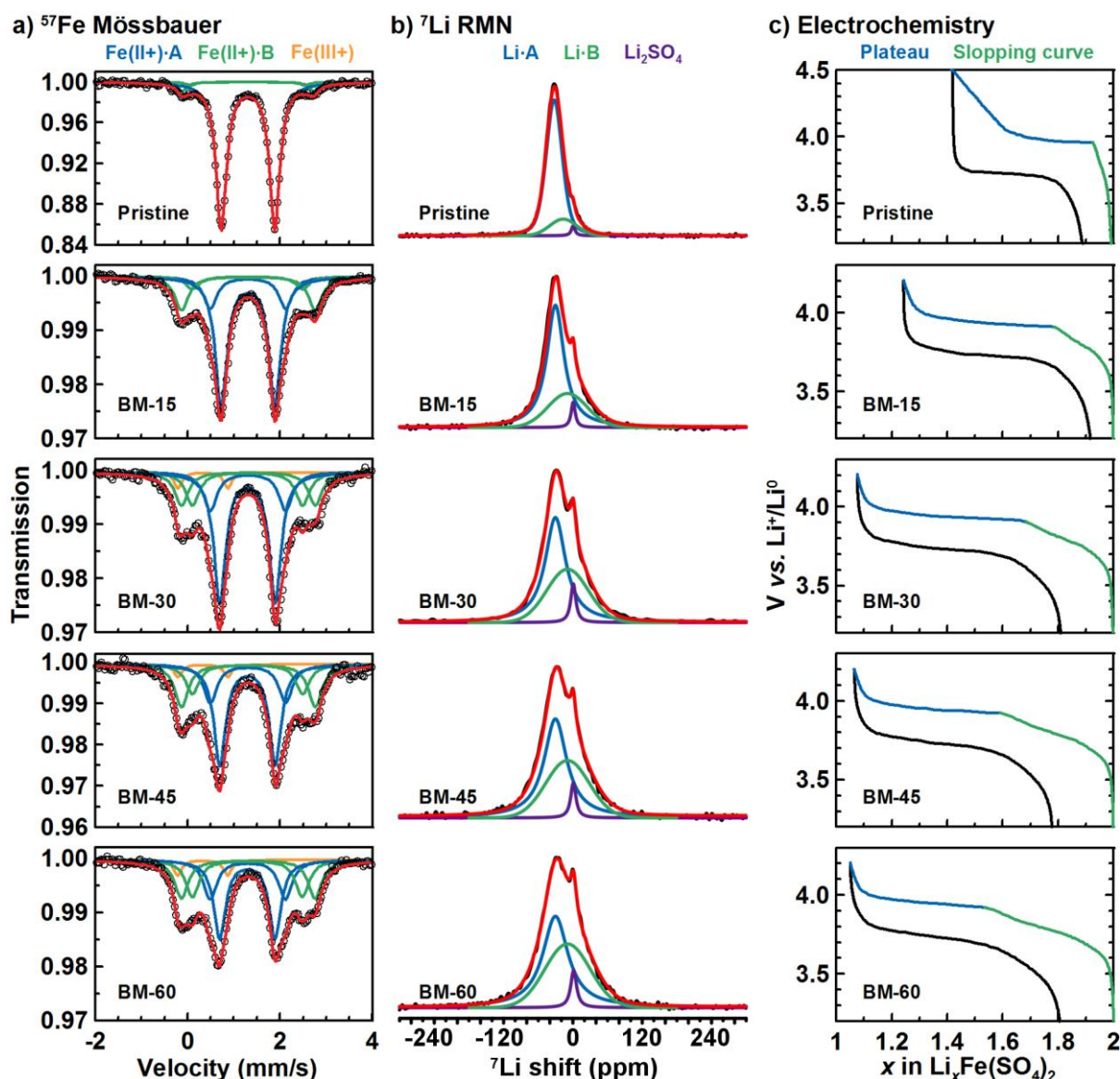
Figure III.21: Influence of the ball-milling time on the Li$_2$Fe(SO$_4$)$_2$/C$_{SP}$ electrode material properties.
(a) ^{57}Fe Mössbauer spectra, (b) solid-state ^{7}Li spin-echo NMR spectra and (c) electrochemical curves of (from top to bottom) the pristine Li$_2$Fe(SO$_4$)$_2$ and the electrode materials balled-milled for 15, 30, 45 and 60 minutes. Note that the upper voltage-composition trace correspond to the room-temperature carbon-coated Li$_2$Fe(SO$_4$)$_2$ electrode material.
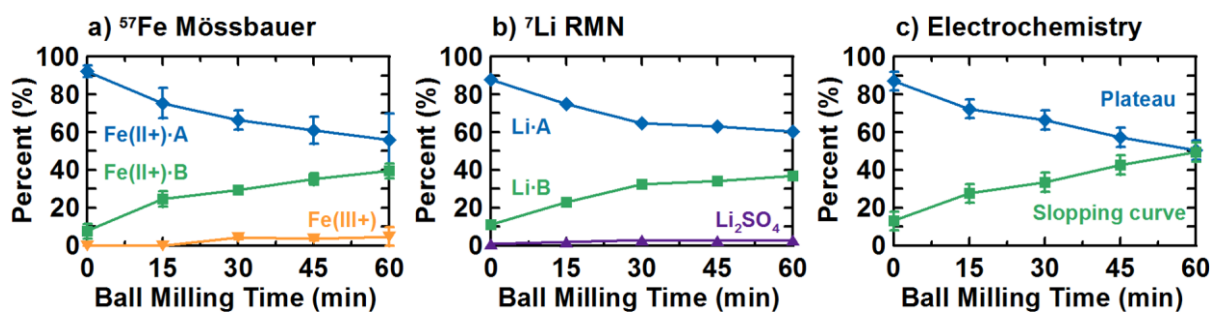
Figure III.22: Influence of the ball-milling time on the Li$_2$Fe(SO$_4$)$_2$ electrode material properties. Evolution with the ball-milling of the contribution of each component determined from the quantitative fitting of the (a) Mössbauer and (b) NMR spectra, as well as (c) the relative length of the sloping curve *versus* the plateau in the electrochemical curve. The color-code is the same as in **Figure III.21**.

X-ray diffraction and Mössbauer spectroscopy

As expected from the previous results, the XRD patterns of the four ball-milled electrode materials were found to be comparable with the one of the pristine sample, but with broader peaks (not shown here).

Mössbauer spectra were fitted with the same subspectra as determined for the electrode material in the previous experiment. They clearly showed that the ball-milling time favored the growth of the Fe(II+)·B signals at the expense of the Fe(II+)·A ones (**Figure III.21.a** and **Figure III.22.a**). Note however that the relative atomic fractions of these signals seem to stabilize after 45 minutes of ball-milling around a Fe(II+)·A/Fe(II+)·B ratio of 60/40 (**Figure III.22.a**).

^{7}Li solid-state NMR

^{7}Li solid-state NMR was conducted by Dr. Robert Messinger[*]. Solid-state ^{7}Li spin-echo spectra of the pristine *marinite* $Li_2Fe(SO_4)_2$ and the four ball-milled electrode materials were acquired on a 300 MHz spectrometer with ultra-fast 62.5 kHz magic-angle-spinning (*cf.* Annexes: § A.4.2 ^{7Li} solid-state NMR, page 168). **Figure III.21.b** shows that, here also, the spectra clearly evolve with the ball-milling time.

All the five spectra were deconvoluted into three components: two paramagnetic components labeled Li·A and Li·B, and a tiny diamagnetic signal which was attributed to a small amount of unreacted precursor Li_2SO_4. The fitting of the spectra were performed using in-house written programs run on the Maple® software. More precisely, the BM-60 spectrum was first fitted with all the parameters of the three components able to vary freely. The other BM samples were then fitted by fixing the paramagnetic shift anisotropy (PSA) and all other anisotropic parameters of the three subspectra, only the peak widths and intensities were let to vary. The line shape (*i.e.* the Gaussian/Lorentzian ratio) of the main contribution (Li·A) had to be modified between the pristine and the ball-milled samples, suggesting that $Li_2Fe(SO_4)_2$ may go through some initial changes upon the first minutes of ball-milling, as also supported by the splitting of the Fe(II+)·A signal in the Mössbauer spectra. Overall, this simple fitting model was robust and resulted in excellent fits.

The relative atomic fractions of each component (Li·A, Li·B and Li in Li_2SO_4; given in terms of lithium content in the different samples) are plotted **Figure III.22.b**. The main component (Li·A) accounts for roughly 88% of the lithium in the starting material, and is attributed to lithium in the cristalline *marinite* $Li_2Fe(SO_4)_2$ phase. It is compensated by the second paramagnetic signal (Li·B; ~11 %) and the small diamagnetic peak ascribed to Li_2SO_4 (~4 %). The Li·B component has a greater distribution of local lithium environments (*i.e.* its line width is broader) than the Li·A one, which means that this Li·B

---

[*] CEMHTI (Conditions Extrêmes et Matériaux: Haute Température et Irradiation), Site Haute Température, CNRS UPR 3079, Orléans, France.

environment is less well defined than the Li·A in the *marinite* Li$_2$Fe(SO$_4$)$_2$, and could for instance indicate that this lithium is in an amorphous phase. The contribution of the Li·B signal gradually increases with the ball-milling time at the expense of the Li·A one (note that the Li$_2$SO$_4$ contribution remains constant in the five samples). Here it is worth to remark that the NMR and Mössbauer data were acquired on the same samples and that, although they were processed independently, their respective quantitative results line up impressively well (**Figure III.22.a** and **b**). The similar trends observed in the appearance of both the Li·B and Fe(II+)·B contributions at the expense of the Li·A and Fe(II+)·A ones hence suggest that these lithium and iron both lie in the same modified electrode material.

Besides, 2D ^{7}Li{^{7}Li} EXSY* experiments were also conducted on the samples BM-30 and BM-60 with two different mixing times (1 ms and 8 ms, respectively) in order to probe chemical exchange between the lithium environments Li·A and Li·B. The spectrum acquired for the sample ball-milled for 30 minutes is shown in **Figure III.23**; a very similar spectrum was obtained for the second sample (not shown here). These results show no chemical exchange between the two lithium environments over 1 and 8 ms, which means that the lithium is not mobile between Li·A and Li·B over this time, and thus may suggest that they correspond to two different phases.
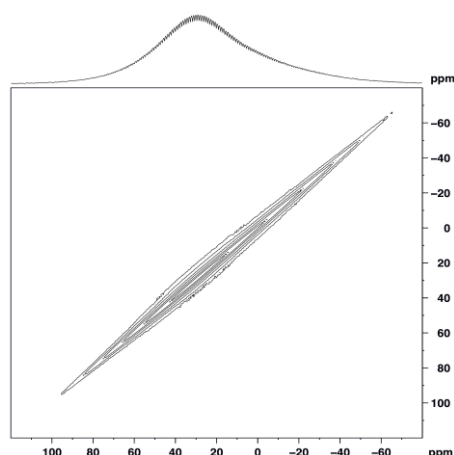
Figure III.23: 2D ^{7}Li{^{7}Li} EXSY spectrum obtained for the sample BM-30 with a 1-ms mixing time.

Electrochemical testings

Besides XRD, Mössbauer and NMR characterizations, the four electrode materials were also tested in lithium half-cells (**Figure III.21.c**) in order to look at the influence of the ball-milling time on the length of the sloping part (highlighted in green in **Figure III.21.c**) with respect to the length of the plateau at 3.83 V *vs.* Li$^+$/Li^0 (highlighted in blue in **Figure III.21.c**) in the charge curve. As expected, and as better seen from the graph in **Figure III.22.c**, the contribution of the sloping part increases

---

* EXchange SpectroscopY.

gradually with the ball-milling time, hence corroborating our prediction that the more the ball-milling time, the more iron in the modified Fe(II+)·B environment (Mössbauer data, **Figure III.22.a**) and the longer the sloping part in the electrochemical curve. To complete the series and fully verify this hypothesis, we had to cycled a $Li_2Fe(SO_4)_2/C_{SP}$ electrode material that had not been prepared by mechanical milling. Simple hand-grinding of carbon with active material was not sufficient for cycling a cell. Therefore, a room-temperature dry carbon deposition **[447–449]** was carried out by Alexandre Ponrouch[*] on the $Li_2Fe(SO_4)_2$ particles to improve their electronic conductivity. This carbon-coated sample could then be cycled in a lithium half-cell at a C/50 rate after being hand-grinded with 30 % of C_{SP} and, as seen in **Figure III.21.a** (electrochemical curve labeled "pristine" at the top of the column) and **Figure III.22.a**, more than 90 % of the 0.55 Li^+ ions extracted from this electrode material occurred on the plateau of the electrochemical curve.

Conclusions on the Li^+ extraction/insertion mechanism in $Li_2Fe(SO_4)_2$

Overall, we have shown here that $Li_2Fe(SO_4)_2$ is altered by the ball-milling step of the electrode preparation. This modification of the active material is reflected in its electrochemical response by a sloping curve, while the oxidation of non-modified $Li_2Fe(SO_4)_2$ material occurs as a plateau centered around 3.83 V *vs.* Li^+/Li^0. X-ray diffraction data suggest that this altered material is not long-range ordered, as supported by its corresponding broad Mössbauer and NMR components (Fe(II+)·B and Li·B) that indicate not well defined iron and lithium environments. Moreover, by comparing the quantitative results obtained from these two spectroscopic techniques, we can infer that the stoichiometric Li:Fe ratio in this altered electrode material is the same as the crystalline *marinite* $Li_2Fe(SO_4)_2$ (providing Fe(II+)·A and Li·A signals), that is 2:1. Therefore, we can imagine for instance that this altered electrode material is simply an amorphous, disordered $Li_2Fe(SO_4)_2$ phase. Another hypothesis could also be that the Fe(II+)·B and Li·B environments correspond in fact to an alteration of the surface of the particles of the active material (although this explanation is less likely since 2D EXSY RMN experiment showed no chemical exchange between the Li·A and Li·B environments).

To test these assumptions, it would have been helpful to be able to distinguish amorphous regions from crystalline ones in samples of $Li_2Fe(SO_4)_2/C_{SP}$ electrode materials by TEM and SAED observations. However, unfortunately, the crystalline *marinite* $Li_2Fe(SO_4)_2$ phase is very sensitive to the electron beam and become amorphous within a few second of exposure, thereby preventing us from any definitive conclusion on the exact nature/location of the Fe(II+)·B and Li·B environments; the only information obtained from these TEM observations is that the particles size of the material is below 100 nm.

---

[*] Institut de Ciència de Materials de Barcelona (ICMAB), CSIC, Barcelona, Spain.

III.4   Other phases Li$_2M$(SO$_4$)$_2$ (M = divalent metal)

In the first part of this chapter, we synthesized and characterized two new phases, namely Li$_2$Co(SO$_4$)$_2$ and Li$_2$Fe(SO$_4$)$_2$. We determined in particular their crystal structure, which is described in a monoclinic unit, and we found attractive electrochemical properties for the *marinite* iron-based phase Li$_2$Fe(SO$_4$)$_2$, which displays an elevated Fe^{III+}/Fe^{II+} redox potential of 3.83 V *vs.* Li$^+$/Li^0.

Knowing the existence of two other compounds having the same general formula (Li$_2$Zn(SO$_4$)$_2$ **[414]** and Li$_2$Ni(SO$_4$)$_2$ **[404,405,425]**), a natural extension of this work was to explore the possibility of preparing other Li$_2M$(SO$_4$)$_2$ analogues with other divalent metals and probe their electrochemical activity. In fact, we placed special interest in synthesizing a manganese-based phase because of the exciting prospect of exploiting the two redox couples Mn^{III+}/Mn^{II+} and Mn^{IV+}/Mn^{III+} to reach a very attractive specific capacity of 204 mAh/g (2 Li$^+$ per formula unit), as compared with the 102 mAh/g theoretical capacity provide by the iron counterpart (1 Li$^+$ per formula unit). On the other hand, the Li$_2$Ni(SO$_4$)$_2$ phase also drew our attention, since this compound was reported to crystallize in an orthorhombic structure **[425]**, different from the monoclinic *marinite* structure that we determined for Li$_2$Co(SO$_4$)$_2$ and Li$_2$Fe(SO$_4$)$_2$. This was indeed somewhat surprising because in many other families of lithium-based polyanionic compounds, the cobalt, iron and nickel analogues had been found to be isostructural (*e.g. olivine* phosphates LiMPO$_4$, *tavorite* fluorosulfates LiMSO$_4$F and fluorophosphates LiMPO$_4$F; *cf.* Chapter I: § I.2.3 Polyanions from page 20). Reminding that the study of such a polymorphism in the fluorosulfate series led to the discovery of the high-potential *triplite* phase LiFeSO$_4$F (3.9 V *vs.* Li$^+$/Li^0, **[323,330,335,427]**), we desired investigating the possibility of stabilizing the Li$_2$Fe(SO$_4$)$_2$ phase into the orthorhombic structure of Li$_2$Ni(SO$_4$)$_2$, in order to probe the effect of this structural modification on the electrochemical response.

We therefore embarked to the synthesis of several Li$_2M$(SO$_4$)$_2$ phases with different divalent cations, as presented below.

III.4.1   Polymorphism of the Li$_2M$(SO$_4$)$_2$ phases (M = Co, Fe, Mn, Mg, Zn, Ni)

Li$_2$Mn(SO$_4$)$_2$

We easily synthesized a white powder sample of Li$_2$Mn(SO$_4$)$_2$ using the same procedure as employed for the preparation of the cobalt counterpart, *i.e.* by annealing under air a stoichiometric mixture of MnSO$_4$ and Li$_2$SO$_4$ at 325°C for 3 days **[442]**. This phase was found to be isostructural with the *marinite* iron and cobalt analogues. This contrasts with other sulfates and fluorosulfates series, in which the manganese phases crystallizes in a structure different from the cobalt one (*e.g. tavorite* LiCoSO$_4$F *vs. triplite* LiMnSO$_4$F, *maxwellite* NaCoSO$_4$F *vs.* undetermined NaMnSO$_4$F, *bloedite* Na$_2$Co(SO$_4$)$_2$·4H$_2$O *vs. kröhnkite* Na$_2$Mn(SO$_4$)$_2$·2H$_2$O; *cf.* Chapter I and Chapter II). **Table III.7** and

Figure III.24 present the results of the Rietveld refinement of the monoclinic *marinite* structure against the XRD pattern of $Li_2Mn(SO_4)_2$.

Table III.7: Crystal structure of $Li_2Mn(SO_4)_2$ resulting from the Rietveld refinement of its XRD powder pattern, measured at room temperature with Cu Kα radiation.

$Li_2Mn(SO_4)_2$						
Space group $P2_1/c$				$\chi^2 = 9.64$	$R_{Bragg} = 8.31\%$	
$a = 4.9920(2)$ Å	$b = 8.3396(2)$ Å		$c = 8.8614(2)$ Å	$\beta = 121.230(5)°$	$V = 315.464(5)$ Å^3	
Atom	**Wyckoff site**	**Occupancy**	**x/a**	**y/b**	**z/c**	**B_{iso} (Å^2)**	**BVS**
Li	4e	1.0	0.021(3)	0.6326(14)	0.1010(16)	1.9(4)	1.08(2)
Mn	2a	1.0	0	0	0	1.32 (4)	1.98 (2)
S	4e	1.0	0.3284 (5)	0.3030 (3)	0.2970 (3)	1.77 (5)	6.29 (4)
O1	4e	1.0	0.1761 (9)	0.4140 (4)	0.1490 (5)	0.84 (10)	2.13 (3)
O2	4e	1.0	0.1954 (9)	0.1405 (5)	0.2460 (5)	1.29 (11)	2.00 (2)
O3	4e	1.0	0.2813 (8)	0.3508 (4)	0.4379 (5)	1.80 (12)	2.12 (3)
O4	4e	1.0	0.6619 (8)	0.2974 (5)	0.3607 (5)	0.61 (10)	2.11 (2)
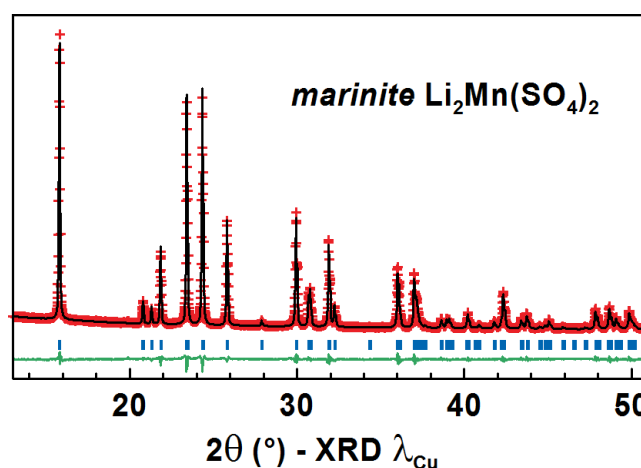
Figure III.24 : Result of the Rietveld refinement of the XRD pattern of $Li_2Mn(SO_4)_2$ using the monoclinic *marinite* structure determined herein.

Regarding the electrochemical properties of this new phase $Li_2Mn(SO_4)_2$, our hopes for a 2-electron electrode material were rapidly dismissed, as we detected no activity up to 4.8 V *vs.* Li^+/Li^0, that is the stability limit of our liquid electrolytes. Recent DFT calculations performed by the group of Islam **[439]** predicted for $Li_2Mn(SO_4)_2$ a voltage of 4.5 V *vs.* Li^+/Li^0, which falls in the electrolyte stability window; however they also anticipated that the delithiated phase $Li_1Mn(SO_4)_2$ would present Jahn-Teller distortion and may thereby be unfavorable to form, which could therefore explain the inactivity of the *marinite* $Li_2Mn(SO_4)_2$ phase.

$Li_2Ni(SO_4)_2$

As expected from what was previously reported [425], we obtained $Li_2Ni(SO_4)_2$ by heating under air a stoichiometric mixture of anhydrous lithium sulfate and nickel sulfate at 500°C for one night [450]. The XRD pattern of the recovered yellow powder was perfectly indexed with the orthorhombic unit cell (space group: *Pbca*) proposed by Isasi *et al.* [425]. The results of the Rietveld refinement of the proposed structure against our XRD data are presented in **Figure III.25** and **Table III.8**.
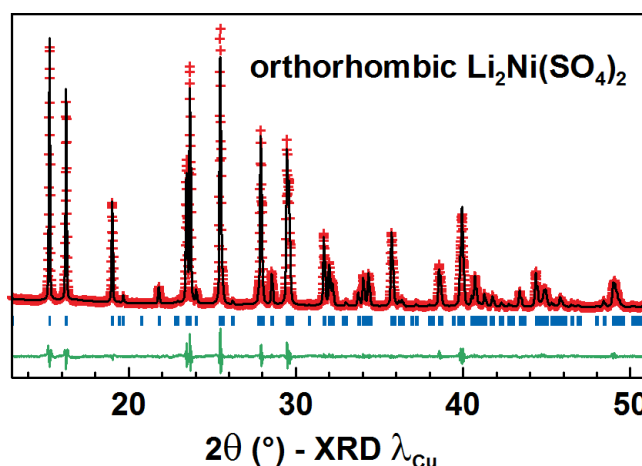
Figure III.25: Result of the Rietveld refinement of the XRD pattern of $Li_2Ni(SO_4)_2$ using the orthorhombic structure proposed by Isasi *et al.* [425].

Table III.8: Crystal structure of $Li_2Ni(SO_4)_2$ resulting from the Rietveld refinement of its XRD powder pattern, measured at room temperature with Cu Kα radiation.

Li₂Ni(SO₄)₂							
Space group *P bca*				χ^2 = 7.39		R_{Bragg} = 2.44 %	
a = 9.1400(2) Å		*b* = 9.0240(2) Å		*c* = 13.5911(2) Å		*V* = 1120.99(3) Å³	
Atom	**Wyckoff site**	**Occupancy**	***x/a***	***y/b***	***z/c***	B_{iso} (Å²)	**BVS**
Li1	8*c*	1.0	0.466(4)	0.718(4)	0.362(4)	0.40(7)	1.04(5)
Li2	8*c*	1.0	0.719(4)	0.538(4)	0.635(4)	0.40(7)	0.97(6)
Ni	8*c*	1.0	0.8617(4)	0.6030(4)	0.3779(3)	0.40(7)	1.90(3)
S1	8*c*	1.0	0.6603(8)	0.8131(7)	0.5089(5)	0.40(7)	5.94(12)
O11	8*c*	1.0	0.5003(13)	0.7967(13)	0.5236(11)	0.40(7)	1.90(3)
O12	8*c*	1.0	0.7050(12)	0.9707(15)	0.4963(12)	0.40(7)	1.92(7)
O13	8*c*	1.0	0.6886(14)	0.7281(14)	0.4187(9)	0.40(7)	2.04(6)
O14	8*c*	1.0	0.7422(10)	0.7561(14)	0.5939(13)	0.40(7)	1.88(7)
S2	8*c*	1.0	0.5755(7)	0.4303(7)	0.2735(5)	0.40(7)	5.87(12)
O21	8*c*	1.0	0.4804(14)	0.4993(12)	0.3405(10)	0.40(7)	2.01(7)
O22	8*c*	1.0	0.5230(13)	0.4617(12)	0.1720(12)	0.40(7)	1.90(6)
O23	8*c*	1.0	0.5725(13)	0.2656(15)	0.2752(11)	0.40(7)	2.01(7)
O24	8*c*	1.0	0.7246(16)	0.4883(15)	0.2750(11)	0.40(7)	2.07(7)

a)   **b)**
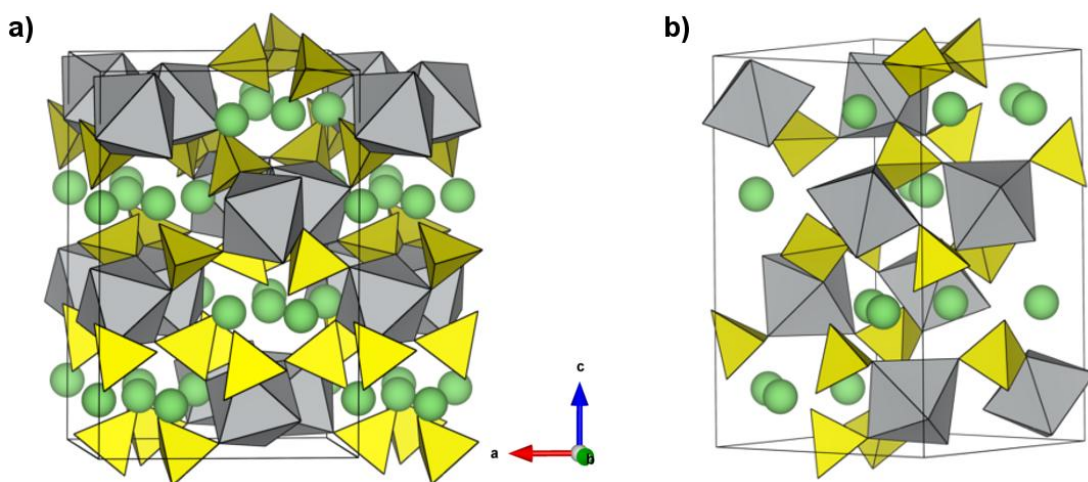
Figure III.26: Representation of the orthorhombic structure of Li$_2$Ni(SO$_4$)$_2$,
viewed along the (a) [010] and (b) [1-10] directions.

Similarly to the *marinite* structure, which was presented at the beginning of this chapter (cf. page 80), the structure of Li$_2$Ni(SO$_4$)$_2$ is based on isolated NiO$_6$ octahedra interconnected through SO$_4$ tetrahedra (**Figure III.26**). Each NiO$_6$ octahedron is linked to six sulfate groups *via* its six corners; each SO$_4$ tetrahedron is connected to three NiO$_6$ octahedra and its fourth corner points to channels that run along the *b*-axis, and in which the lithium cations sit in an octahedral coordination. The difference between the two structures (orthorhombic *vs. marinite* monoclinic) resides in the way MO$_6$ octahedra and SO$_4$ tetrahedra are arranged along the *b*-axis. In the *marinite* structure, the FeO$_6$ octahedra are stacked one behind the other, while in the orthorhombic structure of Li$_2$Ni(SO$_4$)$_2$, the NiO$_6$ octahedra are slightly shifted one with respect to the other, giving rise to sorts of zigzag chains along the *b*-axis. This different stacking leads to shorter *M-M* distances in the orthorhombic structure of Li$_2$Ni(SO$_4$)$_2$ than what is observed in the *marinite* monoclinic phases.

Despite the presence of large open channels containing the lithium cations, which can be viewed as a favorable factor for lithium extraction/insertion, no electrochemical activity could be found for Li$_2$Ni(SO$_4$)$_2$. This is not totally surprising as nickel-based compounds generally display high redox potentials that are hardly reachable with conventional electrolytes, as commented in Chapter 1.

At this stage, we tried to understand the origin of the polymorphism existing in the Li$_2$M(SO$_4$)$_2$ series of compounds. We noticed that Ni^{II+} ions (ionic radii of 0.69 Å, **[111]**) are in fact smaller than Co^{II+} (0.745 Å), Fe^{II+} (0.78 Å) and Mn^{II+} (0.83 Å), whose phases crystallize in the *marinite* structure. To figure out if the cation size was a driving force for stabilizing one polymorph or another, we attempted to synthesized Li$_2$M(SO$_4$)$_2$ phases with other divalent cations having bigger (Cd^{II+}: 0.95 Å and Ca^{II+}: 1.0 Å) or intermediate (Mg^{II+}: 0.95 Å, Cu^{II+}: 0.73 Å, and Zn^{II+}: 0.74 Å) ionic radii. However we

were only successful with the magnesium and zinc counterparts, as presented below and in reference **[450]**; we suppose that too large cations and the Jahn-Taller divalent copper ion may be unfavorable to the formation of the targeted phases.

Li$_2$Mg(SO$_4$)$_2$

Li$_2$Mg(SO$_4$)$_2$ was found much more tricky to obtained than other Li$_2$M(SO$_4$)$_2$ phases. In fact, heating stoichiometric amounts of Li$_2$SO$_4$ and MgSO$_4$ at 300-400°C for several hours resulted in a mixture of Li$_2$Mg$_2$(SO$_4$)$_3$ **[420]** and unreacted lithium sulfate, in agreement with the phase diagrams reported for the binary system Li$_2$SO$_4$–MgSO$_4$ **[405,417,421]**. However, by persevering few days more at 400°C, we observed the growth of a few diffraction peaks that could be compared to the XRD patterns obtained for the *marinite* phases Li$_2$M(SO$_4$)$_2$ (M = Co, Fe, Mn). We eventually obtained a sample presenting Li$_2$Mg(SO$_4$)$_2$ as the main phase with further annealing at 400°C for four weeks **[450]**. The XRD pattern of this white powder sample could be indexed with the monoclinic *marinite* unit cell (**Figure III.27**) with the following unit cell parameters (space group: $P2_1/c$): a = 4.9926(2) Å, b = 8.0853(2) Å, c = 8.7993(2) Å, $β$ = 121.3847(9)° and V = 303.228(9) Å^3.
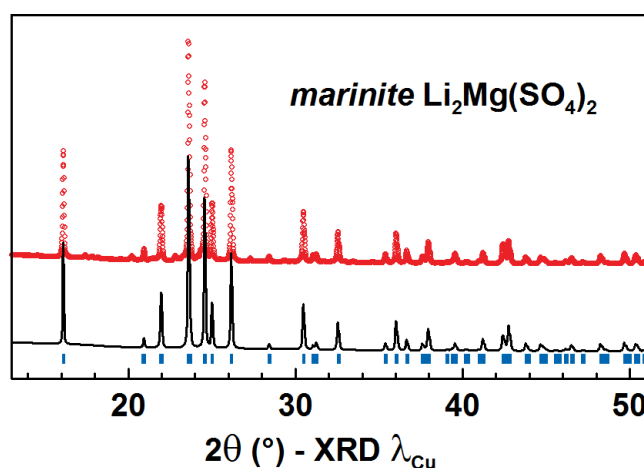
Figure III.27: Comparison of the experimental XRD pattern of the Li$_2$Mg(SO$_4$)$_2$ sample (red circles) and the simulation of this phase from the monoclinic *marinite* structural model of Li$_2$Co(SO$_4$)$_2$ (black line).

Li$_2$Zn(SO$_4$)$_2$

We obtained the zinc phase following a similar procedure to the ones for the other analogues, that is annealing of a stoichiometric mixture of Li$_2$SO$_4$ and ZnSO$_4$ at 400°C for 4 days under air **[450]**. From the XRD pattern of the resulting white powder, we determined that the as-prepared Li$_2$Zn(SO$_4$)$_2$ was isostructural to the nickel counterpart. **Table III.9** and **Figure III.28** show the result of the refinement of the laboratory XRD data starting from the orthorhombic structure proposed by Isasi *et al.* from Li$_2$Ni(SO$_4$)$_2$ **[425]**.

Table III.9: Crystal structure of the orthorhombic form of Li$_2$Zn(SO$_4$)$_2$ resulting from the Rietveld refinement of its XRD powder pattern, measured at room temperature with Co Kα radiation.

Li$_2$Zn(SO$_4$)$_2$							
Space group *P bca*				χ^2 = 11.5		R$_{Bragg}$ = 5.02 %	
a = 9.2178(2) Å		*b* = 9.1065(2) Å		*c* = 13.6492(3) Å		*V* = 1145.74(3) Å^3	
Atom	**Wyckoff site**	**Occupancy**	***x/a***	***y/b***	***z/c***	**B$_{iso}$ (Å^2)**	**BVS**
Li1	8*c*	1.0	0.465(6)	0.737(6)	0.365(5)	0.0	1.01(7)
Li2	8*c*	1.0	0.715(6)	0.531(6)	0.627(6)	0.0	0.94(9)
Zn	8*c*	1.0	0.8606(5)	0.6048(6)	0.3773(3)	0.0	2.04(5)
S1	8*c*	1.0	0.6705(11)	0.8110(10)	0.5100(7)	0.0	5.88(17)
O11	8*c*	1.0	0.5105(18)	0.801(2)	0.5291(16)	0.0	2.03(9)
O12	8*c*	1.0	0.704(2)	0.969(2)	0.4958(17)	0.0	1.99(10)
O13	8*c*	1.0	0.688(2)	0.733(2)	0.4171(13)	0.0	2.13(9)
O14	8*c*	1.0	0.7431(15)	0.749(2)	0.597(2)	0.0	1.91(11)
S2	8*c*	1.0	0.5745(10)	0.4318(11)	0.2745(7)	0.0	5.83(18)
O21	8*c*	1.0	0.487(2)	0.5035(17)	0.3512(15)	0.0	1.94(10)
O22	8*c*	1.0	0.512(2)	0.4621(19)	0.1711(14)	0.0	1.77(7)
O23	8*c*	1.0	0.5680(19)	0.266(2)	0.2707(16)	0.0	1.76(9)
O24	8*c*	1.0	0.7177(3)	0.489(2)	0.2694(16)	0.0	2.18(12)
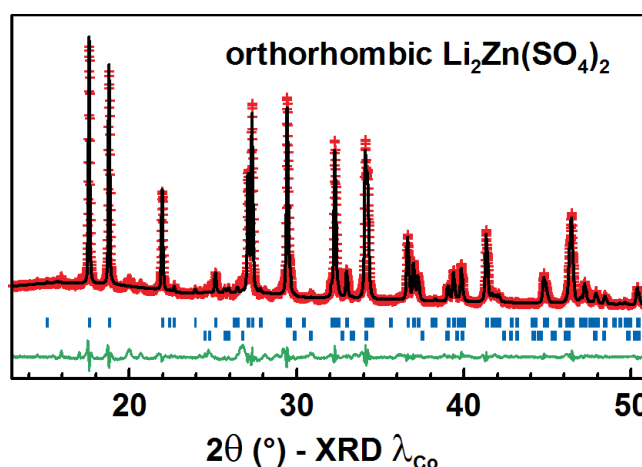
Figure III.28: Results of the Rietveld refinement of the XRD pattern of Li$_2$Zn(SO$_4$)$_2$ prepared at 400°C using the orthorhombic structure proposed by Isasi *et al.* from Li$_2$Ni(SO$_4$)$_2$ [425].

In fact, finding Li$_2$Zn(SO$_4$)$_2$ crystallizing in the orthorhombic structure was somewhat surprising for two reasons: *(i)* given that the ionic radius of Zn^{II+} is very close to the one of Co^{II+} (0.74 Å and 0.745 Å, respectively), we expected the zinc phase to be isostructural to Li$_2$Co(SO$_4$)$_2$, and *(ii)* when they reported the existence of this phase [414], Lundén et al. proposed to index the XRD pattern of Li$_2$Zn(SO$_4$)$_2$ into a monoclinic cell having parameters very close to the ones we determined for the *marinite* structure. This called therefore for further investigation of the zinc compound.
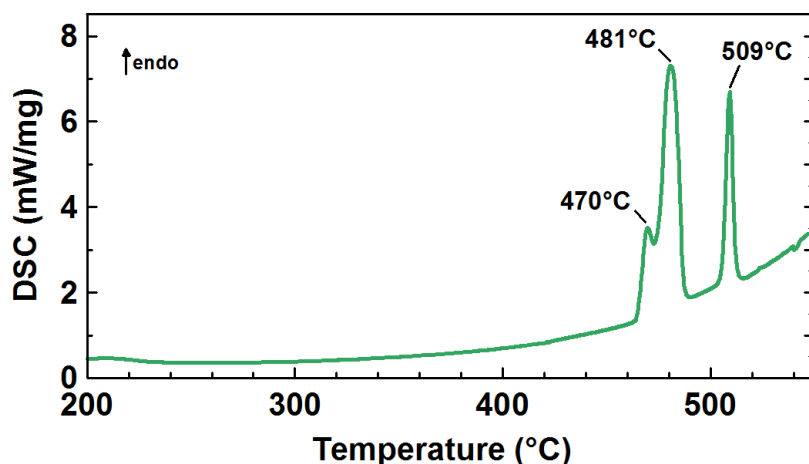
Figure III.29: DSC trace obtained for the orthorhombic form of Li$_2$Zn(SO$_4$)$_2$ measured at a scanning rate of 10K/min under argon flow.

Indeed DSC measurements showed that, before melting at around 510°C, the orthorhombic Li$_2$Zn(SO$_4$)$_2$ undergoes a phase transition between 465 and 480°C (**Figure III.29**). Following this observation, we further heated our sample up to 480°C under air, and the XRD pattern of the recovered powder confirmed that the phase had transformed into the monoclinic *marinite* structure **[450]**. Although the sample contained some impurities, we could simulate the main Bragg reflections of the experimental XRD pattern with the structural model obtained for marinite Li$_2$Co(SO$_4$)$_2$ (**Figure III.30**), using the following unit cell parameters (space group: $P2_1/c$): a = 4.9679(2) Å, b = 8.1281(4) Å, c = 8.7592(4) Å, β = 121.518(3)° and V = 301.51(2) Å^3.
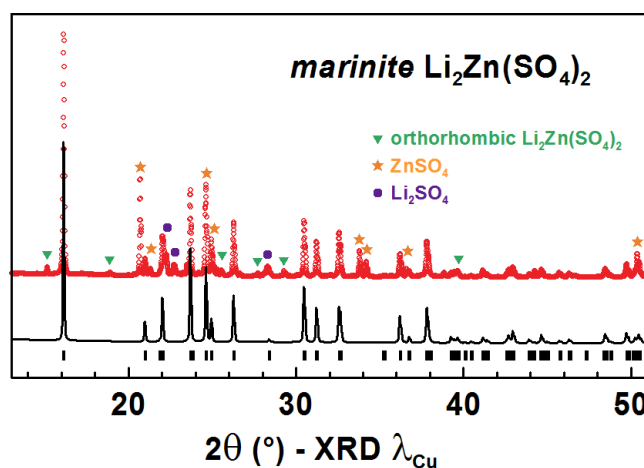
Figure III.30: Comparison of the experimental XRD pattern of the Li$_2$Zn(SO$_4$)$_2$ sample heated up to 480°C (red circles) and the simulation of the Li$_2$Zn(SO$_4$)$_2$ phase from the monoclinic *marinite* structural model of Li$_2$Co(SO$_4$)$_2$ (black line).

Comparison of the different Li$_2$M(SO$_4$)$_2$ phases (M = Co, Fe, Mn, Mg, Zn, Ni)

The aim of this crystal-chemical study was to understand the origin of the polymorphism occurring in the Li$_2$M(SO$_4$)$_2$ series. Overall, we have stabilized five phases crystallizing into the monoclinic *marinite* structure (M = Co, Fe, Mn, Mg, Zn) and two other phases having the orthorhombic structure (M = Ni, Zn). **Figure III.31** clearly shows that the unit cell volume decreases with the ionic radii of the divalent cations M^{II+} in both series, with however the exception of the magnesium counterpart, like in the case of the *bloedite* Na$_2$M(SO$_4$)$_2$.4H$_2$O compounds (*cf.* Chapter I: **Figure II.4** page 48); this may be explained by the different electronic configuration of Mg^{II+} as compared to the 3d transition metals. It is interesting to remark the difference in term of density between the monoclinic *marinite* structure and the orthorhombic one, with the zinc phase crystallizing in the two polymorphs (ρ_{mono} = 2.99 g/cm^3 *vs.* ρ_{ortho} = 3.15 g/cm^3). At this point, DFT calculations could be valuable to have a better insight into the reasons of this polymorphism as well as the difference in terms of stability of these two structures.
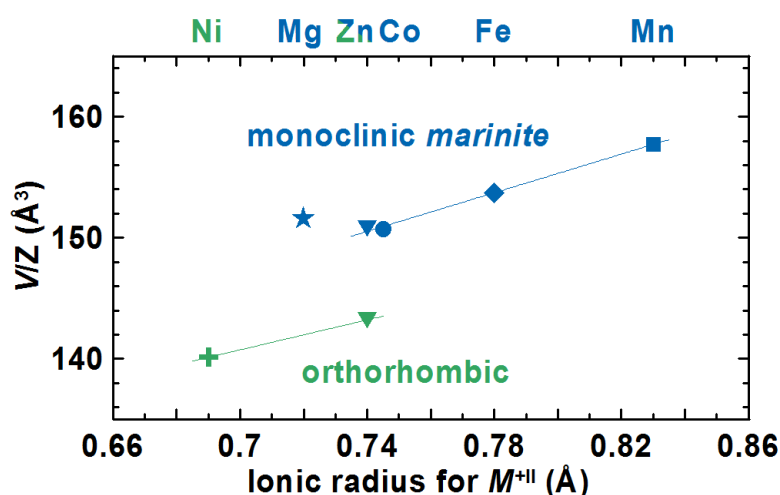
Figure III.31: Evolution of the volume per formula unit as a function of the ionic radii of the divalent cations M^{II+} in the Li$_2$M(SO$_4$)$_2$ series, where M = Ni (green cross), Mg (blue star), Zn (green and blue triangles), Co (blue point), Fe (blue diamond), Mn (blue square).

III.4.2 Study of the solid solutions Li$_2$Fe$_{1-y}$M$_y$(SO$_4$)$_2$

After having synthesized the different end-members of the Li$_2$M(SO$_4$)$_2$ series, we had a look at the solid-solutions Li$_2$Fe$_{1-y}$M$_y$(SO$_4$)$_2$ (M = Mn, Zn, Ni), with the aim of: *(i)* getting more insights about the absence of electrochemical activity for the Li$_2$Mn(SO$_4$)$_2$ phase, and *(ii)* probing the electrochemical properties of an iron-based phase having the orthorhombic structure.

III.4.2.1 Solid solutions Fe/Mn

In order to get more information for the understanding of the absence of electrochemical activity of the Li$_2$Mn(SO$_4$)$_2$ phase, we prepared five phases of the solid-solution Li$_2$Fe$_{1-y}$Mn$_y$(SO$_4$)$_2$ (y = 0.05, 0.25, 0.50, 0.75 and 0.95) by employing the same solid-state synthesis procedure as described for the synthesis of the iron end-member (see § III.2.2 page 76). The XRD patterns obtained for these five samples are presented in **Figure III.32.a**. As expected, refinements of these data showed that the unit cell parameters change linearly with the manganese content (**Figure III.32.a**).
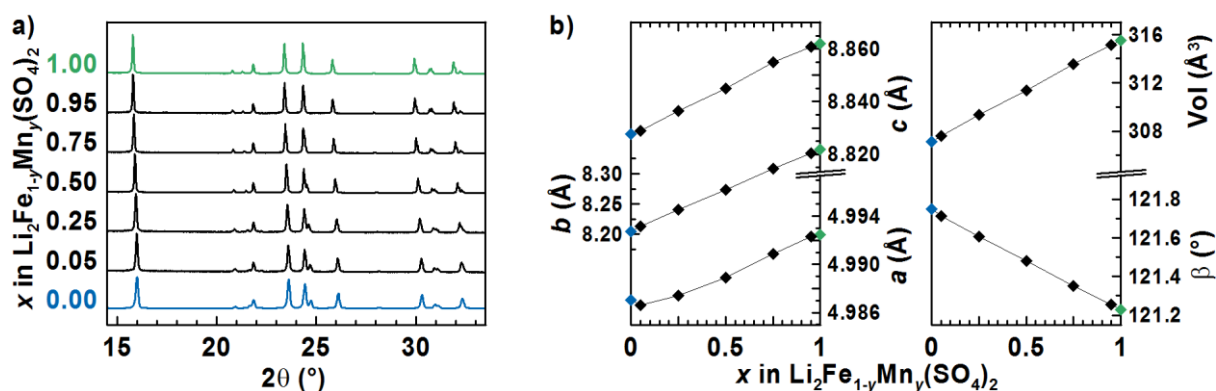
Figure III.32: (a) XRD patterns of the Li$_2$Fe$_{1-y}$Mn$_y$(SO$_4$)$_2$ solid-solution phases, and (b) evolution of the unit cell parameters and volume with the manganese content.

[57]Fe Mössbauer spectroscopy was performed on the same samples. The results of the fitting of these spectra are presented **Figure III.33**. Interestingly, while the isomer shift and line width of the doublet of the main signal of divalent iron remain almost the same for the six spectra, its quadrupole splitting decreases gradually as the manganese content increases, suggesting a modification of the local electronic environment of the iron. Although interpretation of this behavior is difficult without the help of DFT calculations, we can notice that such a decrease of the quadrupole splitting was observed in other manganese-substituted phases such as LiFe$_{1-y}$Mn$_y$PO$_4$ **[451]** and Fe$_{1-y}$Mn$_y$Nb$_2$O$_6$ **[452]**.
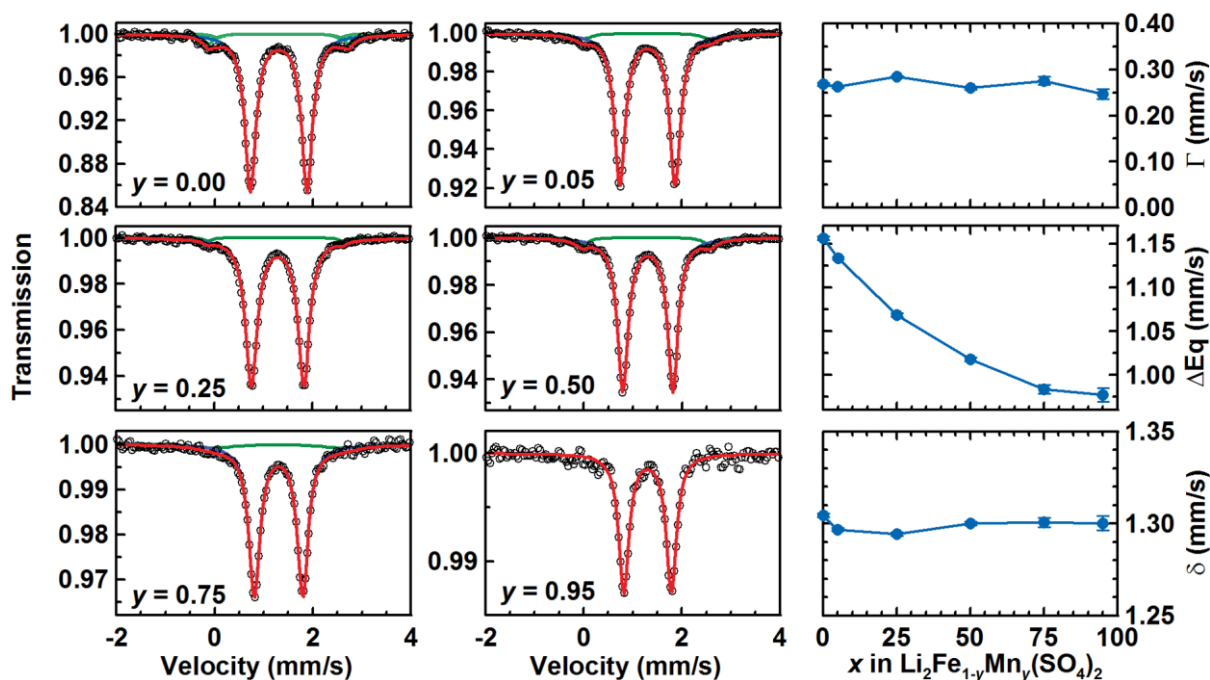
Figure III.33: On the left, ^{57}Fe Mössbauer spectra of the Li$_2$Fe$_{1-y}$Mn$_y$(SO$_4$)$_2$ phases, and on the right, evolution of Mössbauer parameters (δ: isomer shift, ΔE_q: quadrupole splitting and Γ: line width) of the main doublet of the Li$_2$Fe$_{1-y}$Mn$_y$(SO$_4$)$_2$ phases as a function of the manganese content (y).
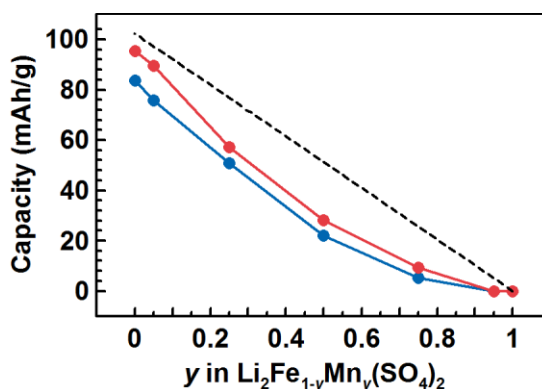
Figure III.34: Evolution, as a function of the manganese content (y) in Li$_2$Fe$_{1-y}$Mn$_y$(SO$_4$)$_2$, of the specific capacities recorded for the first charge (in red) and for the first discharge of these phases, when cycled in lithium half-cells at a C/50 rate. The dotted line represents the theoretical specific capacity expected if all the iron contained in the sample participates is oxidized/reduced during the charge/discharge.

These five samples were probed as positive electrode materials in lithium half-cells. The specific capacities recorded for each sample on the first charge and the first discharge are reported in **Figure III.34** as a red and a blue curve, respectively. These results shows that the specific capacity decrease rapidly as the manganese content (y) in Li$_2$Fe$_{1-y}$Mn$_y$(SO$_4$)$_2$ increases, with almost no activity measured for the samples containing more than 75 % of Mn **[323]**. Besides being inactive, the presence of the manganese in the active material therefore tends to limit the electrochemical response of the Fe^{III+}/Fe^{II+} redox couple, as noticed from the difference between the theoretical curve

(dotted black line in **Figure III.34**) and the experimental ones (blue and red lines in **Figure III.34**). Note that a similar behavior has been observed for other manganese-doped compounds, such as the *triplite* LiFe$_{1-y}$Mn$_y$SO$_4$F **[323]**, the layered LiFe$_{1-y}$Mn$_y$SO$_4$OH **[323]**, the pyrophosphate Li$_2$Fe$_{1-y}$Mn$_y$P$_2$O$_7$ **[453]** and the borate LiFe$_{1-y}$Mn$_y$BO$_3$ **[293]** phases. A plausible reason for such poor capacities is that the structures of the delithiated phases cannot accommodate the local distortion of the octahedra around the Jahn-Teller Mn^{III+} ion, so that delithiation does not occur **[323,439]**, however this still does not fully explain why the iron is not oxidized.

III.4.2.2 Solid solutions Fe/Zn and Fe/Ni

With the aim of stabilizing the an iron-based phase into the orthorhombic structure, we equally attempts to prepare some members of the solid-solutions Li$_2$Fe$_{1-y}$Zn$_y$(SO$_4$)$_2$ and Li$_2$Fe$_{1-y}$Ni$_y$(SO$_4$)$_2$. To synthesize these phases, we also employed the same ceramic route as described for the synthesis of the iron end-member (see § III.2.2 page 76). **Figure III.35** shows the XRD patterns of the phases prepared with 50 and 25 % of iron. The two members of the Fe/Zn solid-solution that we synthesized were obtained as the *marinite* polymorph; however, this is not a really surprising considering that the zinc phase can be obtained on the two forms. We were more successful with the Fe/Ni mixed samples, as the Li$_2$Fe$_{0.25}$Ni$_{0.75}$(SO$_4$)$_2$ phase was stabilized in the orthorhombic structure.
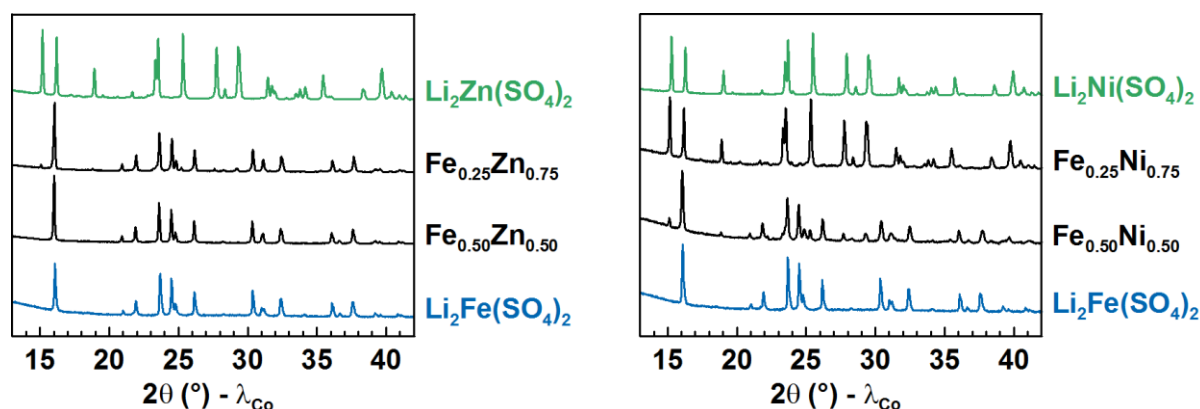
Figure III.35: XRD patterns (black lines) of some members of the solid-solutions Li$_2$Fe$_{1-y}$Zn$_y$(SO$_4$)$_2$ (left) and Li$_2$Fe$_{1-y}$Ni$_y$(SO$_4$)$_2$ (right). There are compared with the pattern of the *marinite* Li$_2$Fe(SO$_4$)$_2$ (in blue) and the ones recorded for the orthorhombic polymorphs of Li$_2$Zn(SO$_4$)$_2$ and Li$_2$Ni(SO$_4$)$_2$ (in green.)

The electrochemical activity of the Li$_2$Fe$_{0.25}$Ni$_{0.75}$(SO$_4$)$_2$ sample was then probed in a lithium half-cell. The voltage-composition trace obtained from this test in presented in the left panel of **Figure III.36**, and shows that almost all the iron contained in the phase can be oxidized, with a potential centered around 3.83 V vs. Li$^+$/Li^0, as better seen in the derivate curve displayed in the right panel of **Figure III.36**.
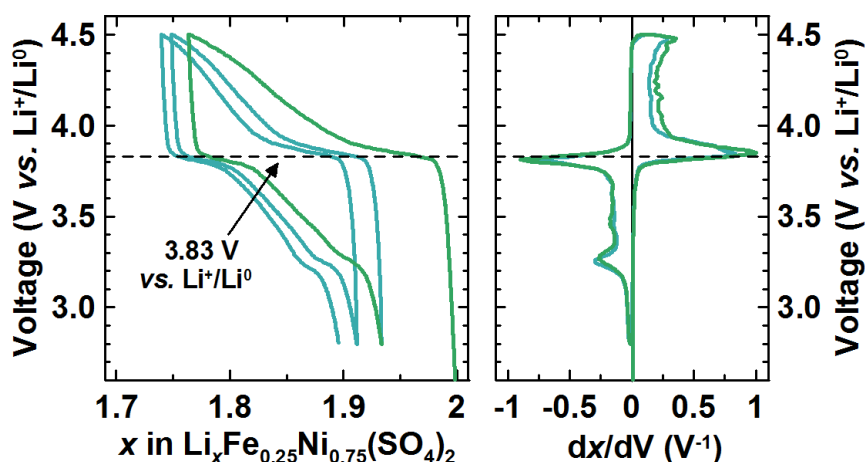
Figure III.36: On the left, voltage-composition trace for the orthorhombic phase $Li_2Fe_{0.25}Ni_{0.75}(SO_4)_2$ cycled in a lithium half-cell. The graph on the right shows the corresponding derivative curve.

Therefore, these preliminary results reveal no obvious change in the redox potential of the Fe^{II+}/Fe^{III+} redox couple when moving from the monoclinic *marinite* structure to the orthorhombic one of the nickel compound. This is certainly explained by the fact that these two structures do not show very important differences in terms of topology and the connectivity between the atoms (contrary to the *tavorite* and *triplite* structures adopted by $LiFeSO_4F$ for instance; see Chapter I: I.2.3.6.1 Lithium-based fluorosulfates, from page 34).

III.5   Conclusion

In this chapter, we have presented a new family of sulfate compounds having the general formula $Li_2M(SO_4)_2$ (M = Co, Fe, Mn, Mg, Zn, Ni), from which only a couple of members had been briefly reported on previously. After having determined the monoclinic structure in which five of these phases crystallize, we have widely studied the electrochemical properties of the iron analogue. Indeed, despite a limited specific capacity (~85 mAh/g) which prevents its consideration for commercial applications, $Li_2Fe(SO_4)_2$ is a very attractive electrode material from a theoretical point of view as it demonstrates a high-operating voltage of 3.83 V *vs.* Li^+/Li^0. This potential is in fact the highest potential ever reported for the Fe^{III+}/Fe^{II+} redox couple in a fluorine-free inorganic compound, and is only exceeded by the *triplite* polymorph of $LiFeSO_4F$ (3.9 V *vs.* Li^+/Li^0).

Besides the attractive electrochemical properties offered by the iron compound, we have also seen that the $Li_2M(SO_4)_2$ series shows an interesting polymorphism, which seems to be nested in the size of the transition metal cations (*i.e.* a monoclinic structure for M = Co, Fe, Mn, Mg, Zn and an orthorhombic one for M = Zn, Ni). Priminary tests showed that the Fe^{III+}/Fe^{II+} redox couple stabilized in the orthorhombic structure would also present a potential at around 3.8 V *vs.* Li^+/Li^0. This is not totally surprising since the monoclinic *marinite* and the orthorhombic structures are not drastically

different and both present MO$_6$ octahedra solely interconnected *via* SO$_4$ tetrahedra; similar redox potentials have been equally obtained for instance with NASICON and anti-NASICON Fe$_2$(SO$_4$)$_3$ (3.6 V *vs.* Li$^+$/Li^0, **[222–224]**) or with *tavorite* and *sillimanite*-like LiFeSO$_4$F (3.6 V *vs.* Li$^+$/Li^0, **[321,332]**), in both cases the two polymophs present similar structural arrangements (see Chapter I: **Figure I.12** page 22 and **Figure I.28** page 36, respectively).

Finally, the two peculiar 3D frameworks of MO$_6$ octahedra and SO$_4$ tetrahedra adopted by these Li$_2$M(SO$_4$)$_2$ phases also make them materials of interest for physical studies, and in particular for magnetism as this will be presented in the next chapter.

Chapter IV. Magnetic study of the Li$_2M$(SO$_4$)$_2$ compounds (M = Co, Fe, Mn, Ni)

IV.1 Introduction

Being based on 3d transition metals, new materials initially designed for battery electrodes are often of interest for magnetic studies. In fact, here electrochemistry can be seen as a tool to synthesize new magnetic materials, with alkali insertion/deinsertion in host compounds permitting to tune the oxidation state of the transition metals while keeping their structural frameworks almost unchanged. Moreover, electrochemical routes can also provide metastable phases, as it has been exemplified for instance in the previous chapter with the case of Li$_1$Fe(SO$_4$)$_2$ (see Chapter I: § III.3.5 page 84).

Beside being interesting from a fundamental point of view, magnetic studies are also of importance for the battery research field, as magnetic structures (experimental ones, or in the absence of, calculated ones) are part of theoretical calculations (*e.g.* DFT) for electrode modelisation **[312,439,440,454–458]**, with in the long term, the goal of being able to design new candidate materials (*e.g.* establish a material genome **[351–354]**) for the next generations of batteries.

Similarly to the potential values of their redox centers, the magnetic properties of polyanionic materials are governed by the way the 3d orbitals of the transition metals overlap with the 2p orbitals of the oxygen atoms (*i.e.* the iono-covalency of the M–O bond). The magnetic interactions within these structures are generally of two types (**Figure IV.1.a**): *(i)* super-exchange interactions, which involve two metals cations connected *via* a single oxygen atom (M–O–M), and *(ii)* super-super-exchange interactions, in which two transition metals are linked *via* two oxygen atoms pertaining to a polyanion group (M–O–O–M). The M–M magnetic couplings implied in these two kinds of interactions are described by the semi-empirical rules of Goodenough-Kanamori-Anderson **[459–464]**, which are shown in **Figure IV.1.b** in the case of 180° super-exchange interactions. Note that these rules have originally been established for super-exchange interactions, but that they also apply for super-super-exchange interactions, although the magnitude of the coupling between the two transition metals is reduced in that case **[464]**.
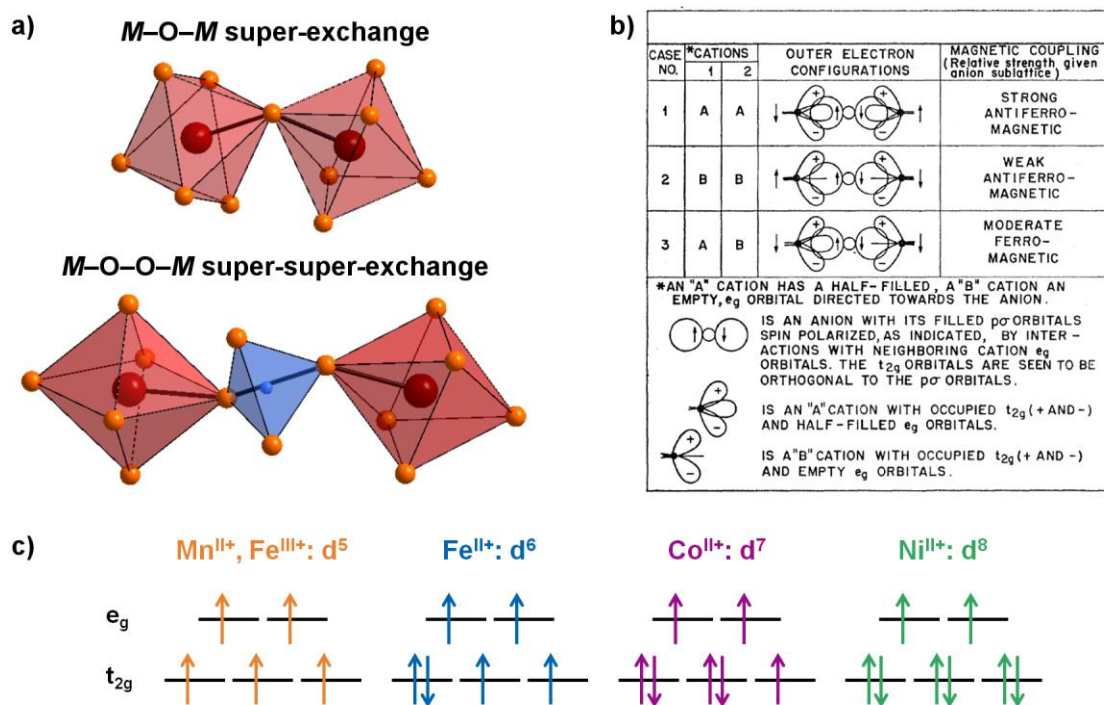
Figure IV.1: (a) Schematic topology of super-exchange and super-super-exchange interactions between two transition metal atoms *M* (shown as red balls). The bold black segments show the interaction paths. Orange balls represent oxygen atoms and the blue tetrahedron is a polyanion group such as PO$_4$, SO$_4$, or AsO$_4$. (b) Goodenough-Kanamori-Anderson rules for 180° super-exchange interactions (from [463]). (c) Electronic configurations of the five transition-metal cations involved in the Li$_2$M(SO$_4$)$_2$ compounds that are studied in this chapter. Note that all of them correspond to case n°1 ("A" cations with a half-filled e$_g$ orbitals) of the Goodenough-Kanamori-Anderson rules as described in (b).

As previously discussed in this thesis, polyanionic compounds provide a great variety of structures and chemistries. They offer thus the possibility of comparing the effect on their magnetic properties when changing the nature of the transition metal (*e.g.* Mn, Fe, Co, Ni), modifying the polyanion group (*e.g.* SO$_4$, PO$_4$, BO$_3$, AsO$_4$), or having different connectivity paths between the magnetic atoms. Here we can mention several works which compare the magnetism of different 3d metals within isostructural sulfate-based compounds, in which both *M*–O–*M* super-exchange interactions and *M*–O–O–*M* super-super-exchange interactions are likely to occur; they include for example the antiferromagnetic anhydrous metal sulfates MSO$_4$ (*M* = Fe, Ni, Co) [465], the antiferromagnetic fluorosulfates AMSO$_4$F (*A* = Li, Na and *M* = Fe, Co) [466–468], the ferrimagnetic hydroxysulfates M_3(OH)$_2$(SO$_4$)$_2$(H$_2$O)$_2$ (*M* = Co, Mn, Ni) [469–471], or also the *jarosite* phases AM_3(SO$_4$)$_2$(OH)$_6$ (*A* = Na, K, Ag, Rb, H, NH$_4$, *etc.* and *M* = Fe, Cr, V) whose *Kagomé* lattice leads to strong frustration and exotic magnetic structures [472–474].

Conversely to the compounds cited above, and as seen in the previous chapter, both the orthorhombic structure of Li$_2$Ni(SO$_4$)$_2$ and the *marinite* monoclinic structure of Li$_x$M(SO$_4$)$_2$ (*x* = 1, 2 and *M* = Co, Fe, Mn) present peculiar arrangements of MO$_6$ octahedra that are only interconnected

through SO$_4$ tetrahedra (**Figure IV.2**), which thereby, solely enable super-super-exchange interactions between the 3d metal cations. In fact, only few iron-based materials present such singular structures in which interactions between magnetic atoms are only possible _via M_-O-O-_M_ pathways. Among these few examples we should cite FePO$_4$ **[475]**, Fe$_2$(SO$_4$)$_3$ **[476,477]**, Fe$_2$(MoO$_4$)$_3$ **[478]**, Li$_3$Fe$_2$(PO$_4$)$_3$ **[479,480]**, LiFeP$_2$O$_7$ **[481]** and _A_Fe(SO$_4$)$_2$ (_A_ = K, Cs, Rb) **[482,483]**; the first ones lead to antiferromagnetic long-range ordering **[475–481]**, whereas the last ones present more complex magnetic structures (_e.g._ helical) due to spin-frustation **[482,483]**.
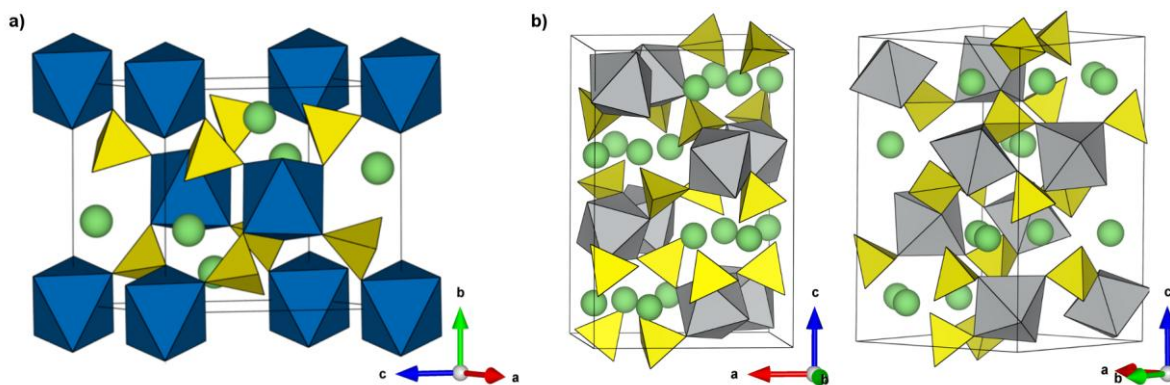
Figure IV.2: Representations of the crystal structures of (a) the monoclinic marinite Li$_2$_M_(SO$_4$)$_2$ phases (_M_ = Fe, Co, Mn) and (b) the orthorhombic Li$_2$Ni(SO$_4$)$_2$ analogue.

In this context, we present in this chapter the results of our magnetic studies of the four _marinite_ compounds Li$_2$Fe^{II}(SO$_4$)$_2$, Li$_1$Fe^{III}(SO$_4$)$_2$, Li$_2$Mn^{II}(SO$_4$)$_2$ and Li$_2$Co^{II}(SO$_4$)$_2$ and the orthorhombic phase Li$_2$Ni^{II}(SO$_4$)$_2$, which were all found to order antiferromagnetically at low temperature **[442,484]**. We also provide models for their ground-state magnetic structures, which were determined from neutron powder diffraction, and we propose an estimation for the relative strengths of the super-super-exchange interaction occurring in these compounds.

IV.2   *Marinites* Li$_2$M(SO$_4$)$_2$ (M = Co, Fe, Mn) and Li$_1$Fe(SO$_4$)$_2$

IV.2.1   Magnetic properties

The macroscopic magnetic properties of the *marinite* compounds Li$_x$M(SO$_4$)$_2$ (x = 2, 1 & M = Co^{II+}, Fe^{II+}, Mn^{II+}, Fe^{III+}) were determined with a SQUID magnetometer (*cf.* Annexes: § A.4.7 Magnetic measurements, page 170) in both zero-field cooled (ZFC) and field cooled (FC) conditions under an applied magnetic field of 10 kOe [442]. The curves of the temperature dependence of the ZFC magnetic susceptibilities (χ = f(T)) are shown in the main panel of **Figure IV.3**. All compounds show cusps of a long-range antiferromagnetic ordering, which occurs at a Néel temperature (T_N) around 7 K for Li$_2$Co^{II}(SO$_4$)$_2$, 6 K for Li$_2$Mn^{II}(SO$_4$)$_2$, 4 K for Li$_2$Fe^{II}(SO$_4$)$_2$ and 35 K for Li$_1$Fe^{III}(SO$_4$)$_2$.

The drastic increase observed in the T_N between the Fe(II+) and the Fe(III+) phase is not a surprise as it has already been reported for other systems upon lithium removal (*e.g. tavorite* (Li)FeSO$_4$F [466], *olivine* (Li)FePO$_4$ [237]). It is due to the fact that d^5–d^5 interactions are stronger than d^6–d^6 ones owing to a greater σ character of the Fe–O bond and a shortening of the Fe–Fe distance. The ordering temperature for the Li$_2$M^{II}(SO$_4$)$_2$ phases (M = Co, Fe, Mn) are nearly the same (within ± 3 K), despite the different electronic configurations of divalent Co^{II+}, Fe^{II+} and Mn^{II+} cations, in agreement with the fact that magnetic interactions are dominated by super-super-exchange interactions. Otherwise, one would have expected the T_N to be higher for Mn^{II+} and decrease as spins are added to the t$_{2g}$ orbitals, as it has been observed for the LiMSO$_4$F series, in which magnetism is governed by super-exchange interactions [466].

The high temperature region (200 to 300 K) of the inverse susceptibility was then fitted to the Curie-Weiss equation (**Figure IV.4.**), in order to check the spin-state of the metal cations and examine the relative strength of the antiferromagnetic interactions. The Curie-Weiss law is given by:

$$\chi = \frac{C}{T - \theta_{CW}}$$

Eq. IV.1

which can be transformed into the linear equation:

$$\frac{1}{\chi} = \frac{T}{C} - \frac{\theta_{CW}}{C}$$

Eq. IV.2

and where χ is the magnetic susceptibility, T is the temperature, θ_{CW} is the Curie-Weiss temperature and and C the Curie constant.
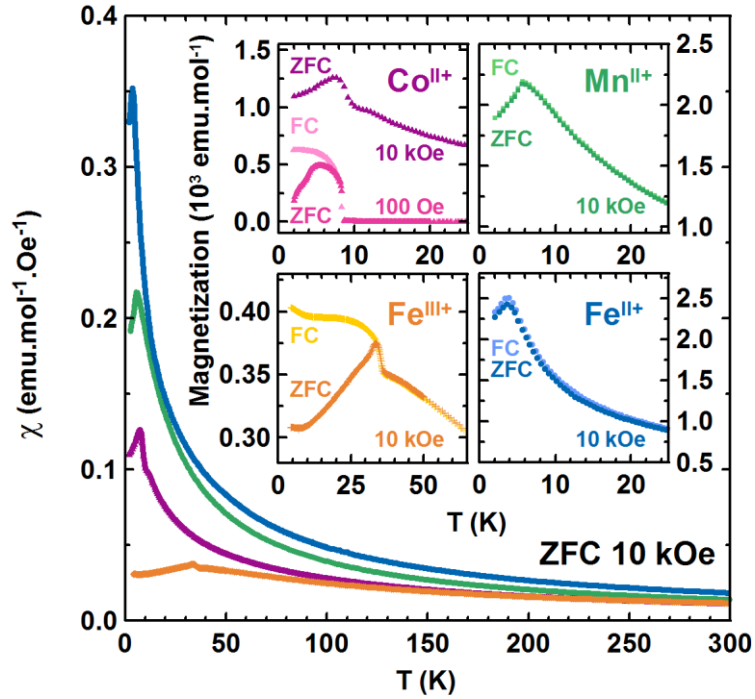
Figure IV.3: Temperature dependence of the magnetic susceptibility χ of the *marinite* compounds Li$_x$M(SO$_4$)$_2$ (*x* = 2, 1 & *M* = Co^{II+}, Fe^{II+}, Mn^{II+}, Fe^{III+}), measured in ZFC conditions with a field of 10 kOe between 300 K and 2 K. Purple triangles, green squares, orange crosses and blue circles are assigned to Li$_2$Co^{II}(SO$_4$)$_2$, Li$_2$Mn^{II}(SO$_4$)$_2$, Li$_1$Fe^{III}(SO$_4$)$_2$ and Li$_2$Fe^{II}(SO$_4$)$_2$, respectively. Insets show enlargement of the ZFC (dark colors) and FC (light colors) magnetization curves at low temperatures. For Li$_2$Co^{II}(SO$_4$)$_2$, only the 10-kOe ZFC curve is shown (purple triangles) and compared to the ZFC (dark pink) and FC (light pink) curves measured with a field of 100 Oe.
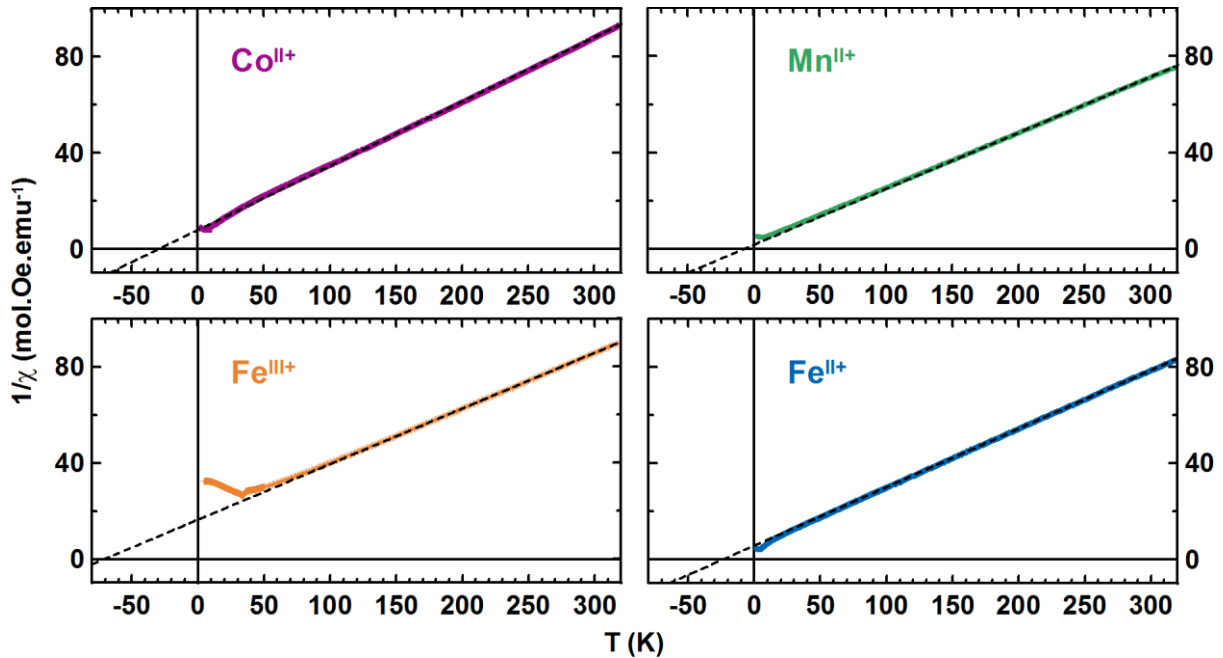
Figure IV.4: Evolution of the inverse of the ZFC magnetic susceptibility 1/χ of the *marinite* compounds Li$_x$M(SO$_4$)$_2$ (*x* = 2, 1 & *M* = Co^{II+}, Fe^{II+}, Mn^{II+}, Fe^{III+}) as a function of the temperature. Experimental curves are fitted with the ideal Curie-Weiss law in the temperature range 200 K ≤ T ≤ 300 K (dashed lines).

From these fittings, we deduced the Curie-Weiss θ_{CW} temperatures of the *marinite* phases to be around −30 K, −8 K, −23 K and −71 K, for Li$_2$Co^{II}(SO$_4$)$_2$, Li$_2$Mn^{II}(SO$_4$)$_2$, Li$_2$Fe^{II}(SO$_4$)$_2$ and Li$_1$Fe^{III}(SO$_4$)$_2$, respectively (**Table IV.1**). We could calculate from these values the frustration parameter $f = |\theta_{CW}|/T_N$ [485,486], which indicated a small degree of frustration in the magnetic structure of the four compounds ($f < 6$), although being slightly more important for Li$_2$Co^{II}(SO$_4$)$_2$ (d^7, $f = 4.29$) and Li$_2$Fe^{II}(SO$_4$)$_2$ (d^6, $f = 5.75$) than for the other two *marinite* phases based on a d^5 transition metals (Mn^{II+} and Fe^{III+}, $f = 1.33$ and 2.03, respectively).

Table IV.1: Magnetic parameters of the *marinite* compounds Li$_x$M(SO$_4$)$_2$ (x = 2, 1 & M = Co^{II+}, Fe^{II+}, Mn^{II+}, Fe^{III+}) deduced from magnetic measurements, and compared to some expected theoretical values.

		Li$_2$Co^{II}(SO$_4$)$_2$	Li$_2$Mn^{II}(SO$_4$)$_2$	Li$_2$Fe^{II}(SO$_4$)$_2$	Li$_1$Fe^{III}(SO$_4$)$_2$
Electronic configuration		d^7: t$_{2g}^5$e$_g^2$	d^5: t$_{2g}^3$e$_g^2$	d^6: t$_{2g}^4$e$_g^2$	d^5: t$_{2g}^3$e$_g^2$
		S = 3/2, L = 3	S = 5/2, L = 0	S = 2, L = 2	S = 5/2, L = 0
Experimental values deduced from magnetic measurements (H = 10 kOe)					
Néel temperature T_N		7 K	6 K	4 K	35 K
Curie-Weiss temperature θ_{CW}		−30 K	−8 K	−23 K	−71 K
Frustration parameter $f = |\theta_{CW}|/T_N$		4.29	1.33	5.75	2.03
Curie Constant C (emu.K.mol^{-1})		3.7	4.3	4.1	4.3
Effective moment μ_{eff}		5.4 μ_B	5.9 μ_B	5.7 μ_B	5.8 μ_B
Expected theoretical values					
Effective moment μ_{eff}	$\mu_{eff}(J) = g \cdot J (J(J+1))^{\frac{1}{2}}$	6.6 μ_B	5.9 μ_B	6.7 μ_B	5.9 μ_B
	$\mu_{eff}(S,L) = (4S(S+1)+L(L+1))^{\frac{1}{2}}$	5.2 μ_B	5.9 μ_B	5.5 μ_B	5.9 μ_B
	$\mu_{eff}(S) = 2 \cdot (S(S+1))^{\frac{1}{2}}$	3.9 μ_B	5.9 μ_B	4.9 μ_B	5.9 μ_B

From the Curie constant (C) deduced from the $1/\chi = f(T)$ fittings (**Eq. IV.2** and **Table IV.1**), we calculated the effective moments ($\mu_{eff} = 2.82 \cdot \sqrt{C}$) to be 5.4 μ_B, 5.9 μ_B, 5.7 μ_B and 5.8 μ_B for Li$_2$Co^{II}(SO$_4$)$_2$, Li$_2$Mn^{II}(SO$_4$)$_2$, Li$_2$Fe^{II}(SO$_4$)$_2$ and Li$_1$Fe^{III}(SO$_4$)$_2$, respectively. These experimental values were then compared to theoretical models to probe the electronic configuration of the four cations Co^{II+}, Mn^{II+}, Fe^{II+} and Fe^{III+}.

Usually, the value of the effective moment of a given cation can be calculated using the following formula:

$$\mu_{eff}(J) = g_J \cdot \sqrt{J(J+1)} \qquad \textbf{Eq. IV.3}$$

where g$_J$ is the Landé gyromagnetic factor and J is the total angular momentum (the sum of the spin angular momentum S and the orbital angular momentum L). However, the effective moment is often affected by the crystal field and thus differs from the expected value for the free ion. Two models are actually used to account for this phenomenon:

(i) the orbital moment L may be fully decoupled from the spin contribution S (*i.e.* the spin-orbit coupling L·S is null), thus leading to an effective moment given by the equation:

$$\mu_{\mathrm{eff}}(S, L) = \sqrt{4S(S + 1) + L(L + 1)} \qquad \textbf{Eq. IV.4}$$

(ii) the orbital contribution L may be completely quenched and the system would then present a spin-only effective moment, which is calculated from the formula:

$$\mu_{\mathrm{eff}}(S) = 2 \cdot \sqrt{S(S + 1)} \qquad \textbf{Eq. IV.5}$$

(or $\mu_{\mathrm{eff}} = \sqrt{n(n + 1)}$, where n is the number of unpaired electrons)

The values of the effective moment expected in these three cases are reported in **Table IV.1** for the four marinite compounds Li$_x$M(SO$_4$)$_2$. They show that the experimental effective moments μ_{eff} deduced from the magnetic measurements of Li$_2$Co$^{\mathrm{II}}$(SO$_4$)$_2$ and Li$_2$Fe$^{\mathrm{II}}$(SO$_4$)$_2$ are consistent with the expected effective moment of a single 3d metal cation in a high-spin octahedral environment with an unquenched orbital moment which is fully decoupled from the spin contribution (**Eq. IV.4**). However one should note that the case of Co$^{\mathrm{II}}$ is always pretty tricky, as high-spin Co$^{\mathrm{II}}$ compounds are known to exhibit significant spin-orbit coupling, and we cannot completely rule out such a possibility without EPR experiments or magnetization measurements on single crystals. In the case of Li$_2$Mn$^{\mathrm{II}}$(SO$_4$)$_2$ and Li$_1$Fe$^{\mathrm{III}}$(SO$_4$)$_2$, the orbital moment is null (L=0) and the experimental values for the effective moment are in good agreement with a spin-only effective moment calculated for a d^5 transition metal (**Eq. IV.5**).

As for the low-temperature region, the insets of **Figure IV.3** (page 119) show enlargements of the magnetization curves of the four *marinite* compounds measured in ZFC and FC conditions under a field of 10 kOe, as well as the ZFC and FC curves for the cobalt-based sample under 100 Oe. Li$_2$Mn$^{\mathrm{II}}$(SO$_4$)$_2$ and Li$_2$Fe$^{\mathrm{II}}$(SO$_4$)$_2$ present a typical antiferromagnetic behavior, with the ZFC and FC curves which superimpose well. Concerning LiFe$^{\mathrm{III}}$(SO$_4$)$_2$, the ZFC and FC curves deviate below T$_N$, which may result from either a ferromagnetic impurity or some ferro/ferrimagnetic contributions. A similar behavior is observed for Li$_2$Co$^{\mathrm{II}}$(SO$_4$)$_2$, with in addition here a non-linearity of the moment versus the applied field, as the curves recorded under a field of 100 Oe lead to magnetization larger than expected from the value obtained at 10 kOe.

To test this point, we recorded the magnetization curves at 2 K for the four samples (**Figure IV.5**). The magnetization curve of Li$_2$Co$^{\mathrm{II}}$(SO$_4$)$_2$ clearly shows a hysteresis loop, which indicates a weak-ferromagnetic behavior with a remnant magnetization (M$_r$) of 0.12 μ_B and a coercive field (H$_c$) of 6.5 kOe. This can explain the discrepancy between the ZFC and FC curves previously mentioned. Close inspection of the data for Li$_2$Mn$^{\mathrm{II}}$(SO$_4$)$_2$ and Li$_1$Fe$^{\mathrm{III}}$(SO$_4$)$_2$ also reveals a tiny

weak-ferromagnetism, with a remnant magnetization is around 0.02 μ_B for the two compounds. Conversely, the absence of any hysteresis loop on the magnetization curve of Li$_2$Fe^{II}(SO$_4$)$_2$ confirms a pure antiferromagnetic ground state that is consistent with the ZFC/FC curves which neatly superimpose.

Switching to higher fields, the evolution of the magnetization of Li$_1$Fe^{III}(SO$_4$)$_2$ is linear with the applied field, while an interesting feature is observed for Li$_2$Fe^{II}(SO$_4$)$_2$ and Li$_2$Co^{II}(SO$_4$)$_2$. In fact, the magnetization curve of Li$_2$Co^{II}(SO$_4$)$_2$ presents an inflexion point around 45 kOe (better seen in the derivative curve in **Figure IV.5**), which may suggest a metamagnetic behavior; this point should however be confirmed by higher field measurements to check the feasibility of saturating the magnetization, and single crystal experiments would also help to confirm this. A similar inflexion point can be seen for the Fe^{II}-based compound, but the field at which it occurs is much lower (about 10 kOe); therefore this could result from a canted magnetic structure that becomes collinear under the effect of the magnetic field. To figure this out, we embarked into a neutron powder diffraction study to determine the magnetic structures of each counterpart.
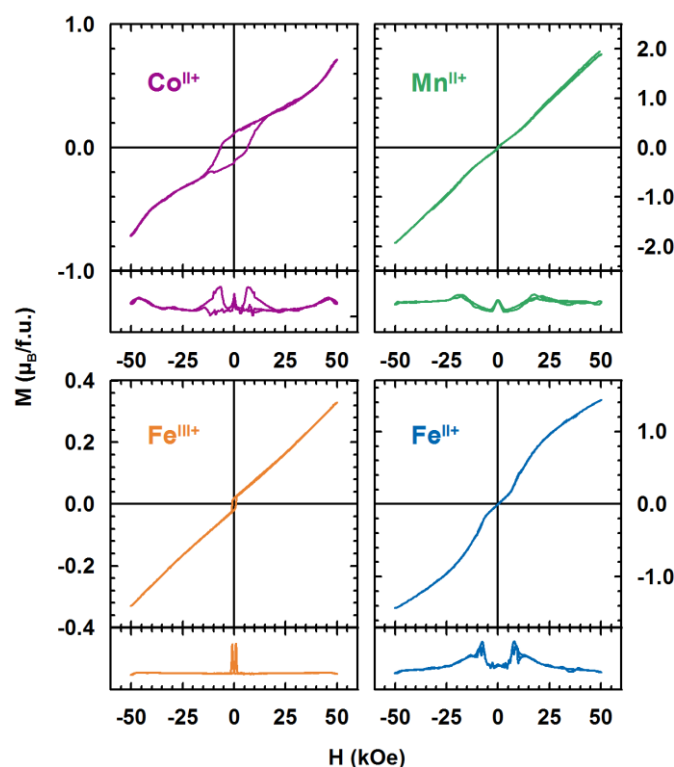
Figure IV.5: Magnetization curves of Li$_2$Co^{II}(SO$_4$)$_2$ (purple), Li$_2$Mn^{II}(SO$_4$)$_2$ (green), Li$_1$Fe^{III}(SO$_4$)$_2$ (orange) and Li$_2$Fe^{II}(SO$_4$)$_2$ (blue) as a function of the applied field measured at 2 K. Derivative curves are displayed in the lower part of each diagram.

IV.2.2 Magnetic structures

Neutron powder diffraction (NPD) measurements were performed on the four title compounds on the D20 diffractometer of the Institut Laue-Langevin (ILL, Grenoble, France; *cf.* Annexes: § A.3.3.2 D20 diffractometer at ILL, page 165). With high resolution at low 2θ angles, the D20 diffractometer is in fact an instrument of choice for magnetic structure determination. NPD patterns of the Li$_2$Co^{II}(SO$_4$)$_2$ and Li$_2$Fe^{II}(SO$_4$)$_2$ samples were acquired in a high-flux configuration using a λ = 2.418 Å wavelength, while the Li$_2$Mn^{II}(SO$_4$)$_2$ and Li$_1$Fe^{III}(SO$_4$)$_2$ phases were measured in a high-resolution mode at two different wavelengths: λ = 1.543 Å and λ = 2.416 Å **[442]**.

First of all, the Rietveld refinements of the NPD patterns acquired above the Néel temperatures of each compound confirmed the accuracy of the monoclinic *marinite* structure that we determined for these phases in the previous chapter. The results of these refinements are presented in **Figure IV.6**, and in **Table IV.2** to **Table IV.5**.
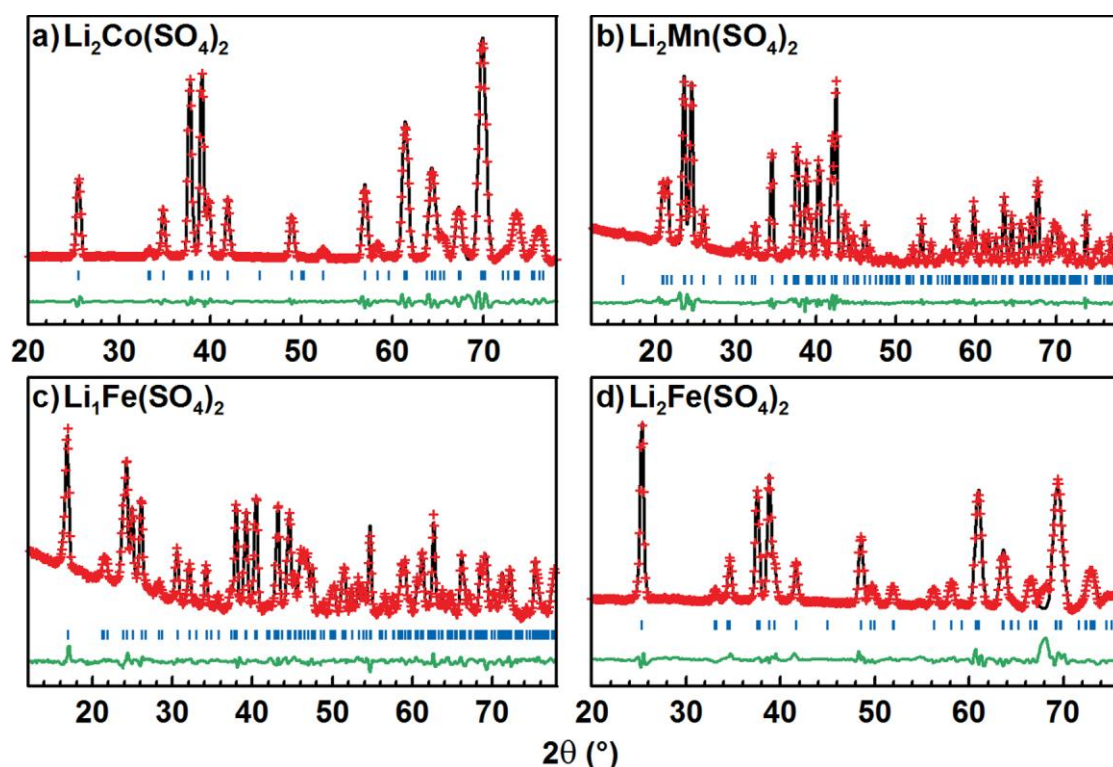
Figure IV.6: Refinements of the nuclear structures of (a) Li$_2$Co(SO$_4$)$_2$ (λ = 2.418 Å), (b) Li$_2$Mn(SO$_4$)$_2$ (λ = 1.543 Å), (c) Li$_1$Fe(SO$_4$)$_2$ (λ = 1.543 Å) and (d) Li$_2$Fe(SO$_4$)$_2$ (λ = 2.418 Å) from their NPD patterns measured above their respective Néel temperatures (*i.e.* 15 K, 15 K, 50 K and 10 K, respectively).

Table IV.2: Crystallographic data and atomic positions of Li$_2$Co^{II}(SO$_4$)$_2$ deduced from the Rietveld refinement of the D20 NPD data recorded for this compound at 15 K (*i.e.* above T$_N$).

		Li$_2$Co^{II}(SO$_4$)$_2$				
Nuclear structure		D20 diffractometer in high-flux mode, λ = 2.418 Å, T = 15 K				
P 2$_1$/*c*		*V* = 299.162 (4) Å^3		R$_{Bragg}$ = 1.86 %	χ^2 = 76.7	
a = 4.9671 (6) Å		*b* = 8.0908 (8) Å		*c* = 8.7639 (9) Å	β = 121.855 (6)°	
Atom	**Wyckoff position**	**Occupancy**	***x/a***	***y/b***	***z/c***	**BVS**
Co	2*a*	1.0	0	0	0	1.94 (3)
Li	4*e*	1.0	0.014 (8)	0.635 (4)	0.101 (6)	1.19 (6)
S	4*e*	1.0	0.339 (6)	0.302 (4)	0.305 (3)	6.0 (3)
O1	4*e*	1.0	0.181 (4)	0.4176 (14)	0.1507 (17)	2.07 (11)
O2	4*e*	1.0	0.200 (3)	0.1342 (18)	0.2463 (14)	1.94 (12)
O3	4*e*	1.0	0.286 (3)	0.3510 (11)	0.4465 (14)	2.06 (15)
O4	4*e*	1.0	0.685 (3)	0.3018 (10)	0.3764 (15)	2.05 (12)

Table IV.3: Crystallographic data and atomic positions of Li$_2$Mn^{II}(SO$_4$)$_2$ deduced from the Rietveld refinement of the D20 NPD data recorded for this compound at 15 K (*i.e.* above T$_N$).

		Li$_2$Mn^{II}(SO$_4$)$_2$					
Nuclear structure		D20 diffractometer in high-resolution mode, λ = 1.543 Å, T = 15 K					
P 2$_1$/*c*		*V* = 312.91 (3) Å^3		R$_{Bragg}$ = 3.38 %	χ^2 = 16.4		
a = 4.9811 (3) Å		*b* = 8.3140 (5) Å		*c* = 8.8382 (5) Å	β = 121.250 (3)°		
Atom	**Wyckoff position**	**Occupancy**	***x/a***	***y/b***	***z/c***	**B$_{iso}$ (Å^2)**	**BVS**
Mn	2*a*	1.0	0	0	0	0.7 (3)	2.12 (18)
Li	4*e*	1.0	0.018 (5)	0.630 (3)	0.104 (3)	0.9 (4)	1.09 (2)
S	4*e*	1.0	0.329 (3)	0.3026 (16)	0.2975 (17)	0.4 (2)	5.97 (13)
O1	4*e*	1.0	0.1756 (17)	0.4145 (8)	0.1497 (8)	0.58 (12)	2.13 (7)
O2	4*e*	1.0	0.1928 (14)	0.1391 (8)	0.2449 (8)	0.51 (12)	2.00 (6)
O3	4*e*	1.0	0.2886 (16)	0.3533 (8)	0.4448 (8)	0.73 (13)	2.00 (8)
O4	4*e*	1.0	0.6711 (17)	0.2980 (8)	0.3630 (9)	0.63 (12)	1.99 (7)

Table IV.4: Crystallographic data and atomic positions of Li$_1$Fe^{III}(SO$_4$)$_2$ deduced from the Rietveld refinement of the D20 NPD data recorded for this compound at 50 K (*i.e.* above T$_N$).

Li$_1$Fe^{III}(SO$_4$)$_2$

Nuclear structure		D20 diffractometer in high resolution mode, λ = 1.543 Å, T = 50 K					
P 2$_1$/c		V = 269.72 (3) Å^3		R$_{Bragg}$ = 2.67 %		χ^2 = 13.5	
a = 4.7974 (3) Å		b = 8.3815 (6) Å		c = 7.8956 (6) Å		β = 121.835 (4)°	
Atom	**Wyckoff position**	**Occupancy**	**x/a**	**y/b**	**z/c**	**B$_{iso}$ (Å^2)**	**BVS**
Fe	2a	1.0	0	0	0	0.31 (17)	2.93 (3)
Li	4e	0.5	0.58 (14)	0.03 (9)	0.52 (12)	1.5 (1.5)	1.06 (14)
S	4e	1.0	0.297 (5)	0.1797 (19)	0.759 (3)	0.1 (4)	6.14 (19)
O1	4e	1.0	0.041 (2)	0.1296 (11)	0.7985 (12)	0.25 (19)	2.03 (12)
O2	4e	1.0	0.260 (3)	0.1067 (12)	0.5871 (13)	0.30 (19)	2.09 (13)
O3	4e	1.0	0.2876 (19)	0.3564 (11)	0.7391 (13)	0.36 (19)	2.07 (8)
O4	4e	1.0	0.378 (2)	0.6428 (12)	0.5594 (14)	0.53 (19)	1.94 (7)

Table IV.5: Crystallographic data and atomic positions of Li$_2$Fe^{II}(SO$_4$)$_2$ deduced from the Rietveld refinement of the D20 NPD data recorded for this compound at 10 K (*i.e.* above T$_N$).

Li$_2$Fe^{II}(SO$_4$)$_2$

Nuclear structure		D20 diffractometer in high flux mode, λ = 2.418 Å, T = 10 K				
P 2$_1$/c		V = 305.3 (2) Å^3		R$_{Bragg}$ = 6.4 %		χ^2 = 87.4
a = 4.9836 (19) Å		b = 8.191 (4) Å		c = 8.811 (3) Å		β = 121.92 (3)°
Atom	**Wyckoff position**	**Occupancy**	**x/a**	**y/b**	**z/c**	**BVS**
Fe	2a	1.0	0	0	0	2.22 (6)
Li	4e	1.0	0.020 (15)	0.645 (8)	0.102 (11)	1.11 (12)
S	4e	1.0	0.344 (12)	0.293 (8)	0.315 (8)	5.8 (5)
O1	4e	1.0	0.185 (8)	0.414 (3)	0.154 (4)	1.7 (2)
O2	4e	1.0	0.194 (6)	0.138 (4)	0.242 (4)	2.2 (3)
O3	4e	1.0	0.284 (5)	0.357 (3)	0.448 (4)	2.3 (4)
O4	4e	1.0	0.688 (6)	0.302 (3)	0.378 (4)	1.9 (3)

Upon cooling the powder samples down to 2 K (**Figure IV.7**), we observed the growth of new peaks, which indicate a long-range ordering of the magnetic moments. These extra peaks are better observed when plotting the difference patterns (green lines in **Figure IV.7**) between a diagram recorded above T$_N$ (red patterns in **Figure IV.7**) and another one recorded below T$_N$ (blue patterns in **Figure IV.7**). Note that, at the opposite, the nuclear Bragg peaks show no changes, suggesting that the structures remain intact at the magnetic transition (*i.e.* no magneto-elastic effect is detected).
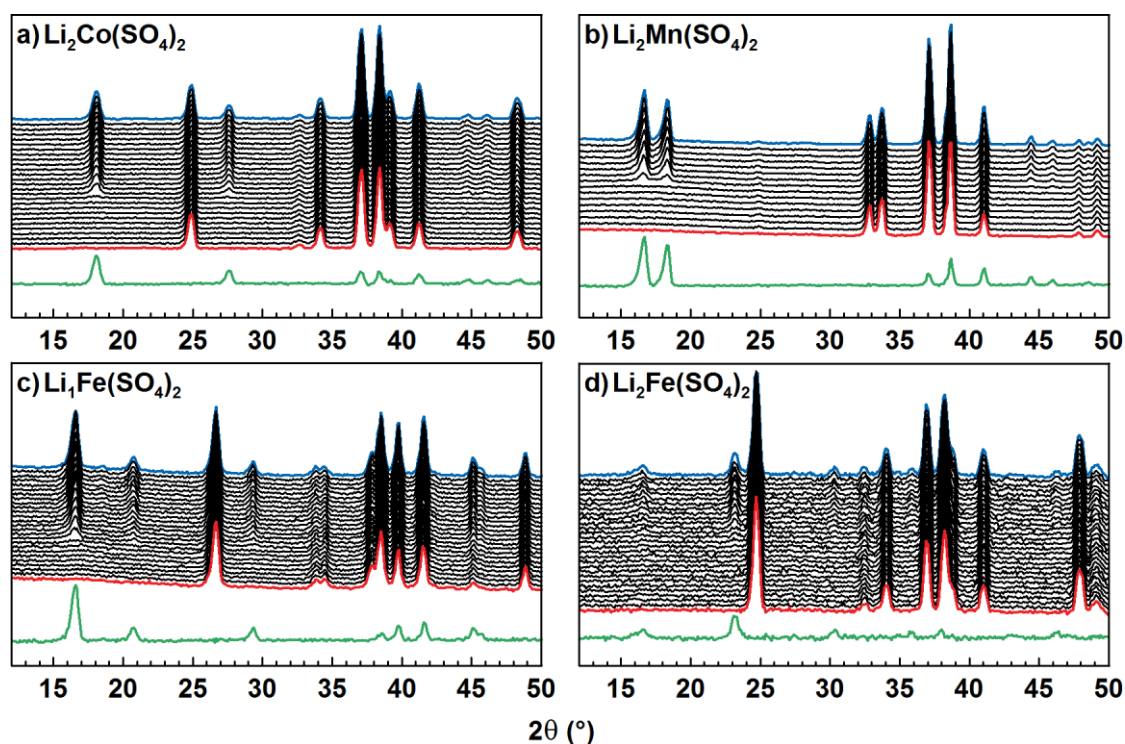
Figure IV.7: Evolution of the neutron powder diffraction patterns of (a) Li$_2$Co(SO$_4$)$_2$, (b) Li$_2$Mn(SO$_4$)$_2$, (c) Li$_1$Fe(SO$_4$)$_2$ and (d) Li$_2$Fe(SO$_4$)$_2$ while cooling the samples down to 2 K (λ = 2.42 Å). Blue patterns are measured at 2 K while the red ones are measured at (a) 12 K, (b) 10 K, (c) 50 K, and (d) 7 K, respectively. Black patterns correspond to intermediate temperatures. The green lines represent the difference curves between the blue and the red patterns for each sample, and thus reveal the magnetic peaks arising from the long-range ordering of their magnetic moments.

High-quality NPD patterns were then recorded at 1.85 K, and we embarked in the determination of the magnetic structure of each compound. We found that the magnetic reflections observed for Li$_2$Co^{II}(SO$_4$)$_2$, Li$_2$Mn^{II}(SO$_4$)$_2$ and Li$_1$Fe^{III}(SO$_4$)$_2$ could be indexed in the same unit cell as its nuclear structure. The propagation vector is the gamma-point of the Brillouin zone: **k** = (0, 0, 0). A symmetry analysis was then performed using Bertaut's method **[487]**, as implemented in the program BasIReps of the FullProf suite of software **[384,443]**, in order to determine all the possible spin configurations compatible with the crystal symmetry of the nuclear structure. The results of this analysis are summed up in **Table IV.6**. Two irreducible representations were found to be associated with the 2a Wyckoff site (0, 0, 0) occupied by the 3d metals: $\Gamma_{magnetic}$ = 3 Γ_1 + 3 Γ_3. These representations are built with three basis vectors **Ψ$_1$**, **Ψ$_2$**, and **Ψ$_3$**, which are collinear to the a, b and c–axes of the unit cell, respectively. In the Γ_1 representation, the magnetic moments of the two metal atoms which are non-related by lattice translations (labeled M_1 in (0, 0, 0) and M_2 in (0, ½, ½)) are constrained to be of the form (u, v, w) and (−u, v, −w) for M_1 and for M_2, respectively. In the Γ_3 representation, the directions of the magnetic moments of the M_1 and M_2 atoms become of the form (u, v, w) and (u, −v, w), respectively. For the three phases Li$_2$Co^{II}(SO$_4$)$_2$, Li$_2$Mn^{II}(SO$_4$)$_2$ and Li$_1$Fe^{III}(SO$_4$)$_2$, we tested all the possibilities given by these two irreducible representations against the NPD patterns recorded at 2 K.

Table IV.6: Results of the symmetry analysis of the $P2_1/c$ unit cell for the propagation vector **k** = (0, 0, 0). The basis vectors **Ψ$_i$** (i = 1, 2, 3) of the two general positions M_1 (x, y, z) and M_2 (−x, y+½, −z+½) are given for each irreducible representation Γ_j (j = 1, 3).

	k = (0, 0, 0)	
Γ$_1$	*x, y, z*	*−x, y+½, −z+½*
Ψ$_1$	1 0 0	-1 0 0
Ψ$_2$	0 1 0	0 1 0
Ψ$_3$	0 0 1	0 0 -1
Γ$_3$	*x, y, z*	*−x, y+½, −z+½*
Ψ$_1$	1 0 0	1 0 0
Ψ$_2$	0 1 0	0 -1 0
Ψ$_3$	0 0 1	0 0 1

First, we found that the best solution to simulate the magnetic reflections of the NPD pattern of Li$_2$Co^{II}(SO$_4$)$_2$ was when the magnetic moments were aligned antiferromagnetically along the b-axis, as allowed by the Γ_3 representation. The symmetry also permitted to add a weak ferromagnetic component in the (ac) plane, in agreement with the SQUID measurements, and without altering the quality of the refinement; however, due to the weakness of these ferromagnetic components, they could not be refined from NPD data and they were then fixed along the a-axis (arbitrarily) to the value of 0.12 μ_B, as deduced from the magnetization measurements (see page 121). The results of the refinement are shown in **Figure IV.8.a** and in **Table IV.7**. The refined value of the magnetic moment of the cobalt is then 3.33(7) μ_B. The magnetic structure of Li$_2$Co^{II}(SO$_4$)$_2$ is illustrated in **Figure IV.9.a**. It shows the alternate orientations (+ −) of the moments along the [011] direction, while the sequence of the moments is (+ +) along the [100] and the [001] directions.

Unlike the cobalt phase, the best agreements with the magnetic reflections observed for Li$_2$Mn^{II}(SO$_4$)$_2$ and Li$_1$Fe^{III}(SO$_4$)$_2$ were obtained using the irreducible representation Γ_1. For the manganese analogue, a magnetic moment aligned along the a-axis provided a rather good fit of the magnetic reflections (hypothesis Mn-H1 in **Figure IV.8.b**). However, adding a small antiferromagnetic component along the c-axis improved the fit of the (1 0 1) and (-1 0 3) reflections (2θ = 46° and 48.5°, respectively) as shown in the panel Mn-H2 of **Figure IV.8.b**. The value of the total magnetic moment was then refined to 4.1(2) μ_B. Regarding Li$_1$Fe^{III}(SO$_4$)$_2$, we determined its moments to be aligned along the c-axis, with a magnitude of 4.33(12) μ_B. Note that a small peak at 2θ = 18.5° remains unindexed and may be attributed to an inhomogeneity of the sample or to a magnetic impurity (**Figure IV.8.c**). Finally, as SQUID measurements suggested a tiny weak-ferromagnetic behavior for both Li$_2$Mn^{II}(SO$_4$)$_2$ and Li$_1$Fe^{III}(SO$_4$)$_2$, a small component of 0.02 μ_B along the b-axis could be added to their magnetic moments without any significant change on the refinement of the NPD data. The results of the refinements relative to the Li$_2$Mn^{II}(SO$_4$)$_2$ and Li$_1$Fe^{III}(SO$_4$)$_2$ compounds are given in **Table IV.8** and **Table IV.9**, and are illustrated in **Figure IV.8.b** and **c**, and **Figure IV.9.b** and **c**, respectively. As the propagation vector of Li$_2$Mn^{II}(SO$_4$)$_2$ and Li$_1$Fe^{III}(SO$_4$)$_2$ is the same as the one of Li$_2$Co^{II}(SO$_4$)$_2$ (**k** = (0, 0, 0)), the spin sequence remains identical in the three compounds: (+ −) along [011] and (+ +) along the a-, b- and c-axes; the only difference lies in the orientation of the moments as discussed above.

Table IV.7: Magnetic structure of Li$_2$Co^{II}(SO$_4$)$_2$ determined from the Rietveld refinement of the D20 NPD data obtained at 1.85 K (*i.e.* below T$_N$).

<div align="center">Li$_2$Co^{II}(SO$_4$)$_2$</div>

Nuclear structure	D20 diffractometer in high-flux mode, λ = 2.418 Å, T = 1.85 K			
P 2$_1$/*c*	*V* = 299.22 (4) Å^3	R$_{Bragg}$ = 3.42 %		χ^2 = 107
a = 4.9675 (6) Å	*b* = 8.0912 (8) Å	*c* = 8.7646 (9) Å		β = 121.855 (6)°
Magnetic structure	D20 diffractometer in high-flux mode, λ = 2.418 Å, T = 1.85 K			
k = (0, 0,0) Γ$_3$				
Atom	M$_x$/*a* (μ$_B$)	M$_y$/*b* (μ$_B$)	M$_z$/*c* (μ$_B$)	M$_{tot}$ (μ$_B$)
Co (0, 0, 0)	0.12	3.33(7)	0	3.33(7)
Co (0, ½, ½)	0.12	-3.33(7)	0	3.33(7)

Table IV.8: Magnetic structure of Li$_2$Mn^{II}(SO$_4$)$_2$ determined from the Rietveld refinement of the D20 NPD data obtained at 1.85 K (*i.e.* below T$_N$).

<div align="center">Li$_2$Mn^{II}(SO$_4$)$_2$</div>

Nuclear structure	D20 diffractometer in high-resolution mode, λ = 1.543 Å, T = 1.85 K			
P 2$_1$/*c*	*V* = 313.76 (3) Å^3	R$_{Bragg}$ = 2.84 %		χ^2 = 16.7
a = 4.9857 (3) Å	*b* = 8.3211 (4) Å	*c* = 8.8462 (5) Å		β = 121.248 (3)°
Magnetic structure	D20 diffractometer in high-resolution mode, λ = 2.416 Å, T = 1.85 K			
k = (0, 0, 0) Γ$_1$				
Atom	M$_x$/*a* (μ$_B$)	M$_y$/*b* (μ$_B$)	M$_z$/*c* (μ$_B$)	M$_{tot}$ (μ$_B$)
Mn (0, 0, 0)	4.0(2)	0.02	-1.0(4)	4.1(2)
Mn (0, ½, ½)	-4.0(2)	0.02	1.0(4)	4.1(2)

Table IV.9: Magnetic structure of Li$_1$Fe^{III}(SO$_4$)$_2$ determined from the Rietveld refinement of the D20 NPD data obtained at 1.85 K (*i.e.* below T$_N$).

<div align="center">Li$_1$Fe^{III}(SO$_4$)$_2$</div>

Nuclear structure	D20 diffractometer in high resolution mode, λ = 1.543 Å, T = 1.85 K			
P 2$_1$/*c*	*V* = 269.74 (4) Å^3	R$_{Bragg}$ = 3.84 %		χ^2 = 21.8
a = 4.7972 (4) Å	*b* = 8.3808 (8) Å	*c* = 7.8943 (7) Å		β = 121.801 (5)°
Magnetic structure	D20 diffractometer in high resolution mode, λ = 2.416 Å, T = 1.85 K			
k = (0, 0, 0) Γ$_1$				
Atom	M$_x$/*a* (μ$_B$)	M$_y$/*b* (μ$_B$)	M$_z$/*c* (μ$_B$)	M$_{tot}$ (μ$_B$)
Fe (0, 0, 0)	0	0.02	4.33(12)	4.33(12)
Fe (0, ½, ½)	0	0.02	-4.33(12)	4.33(12)
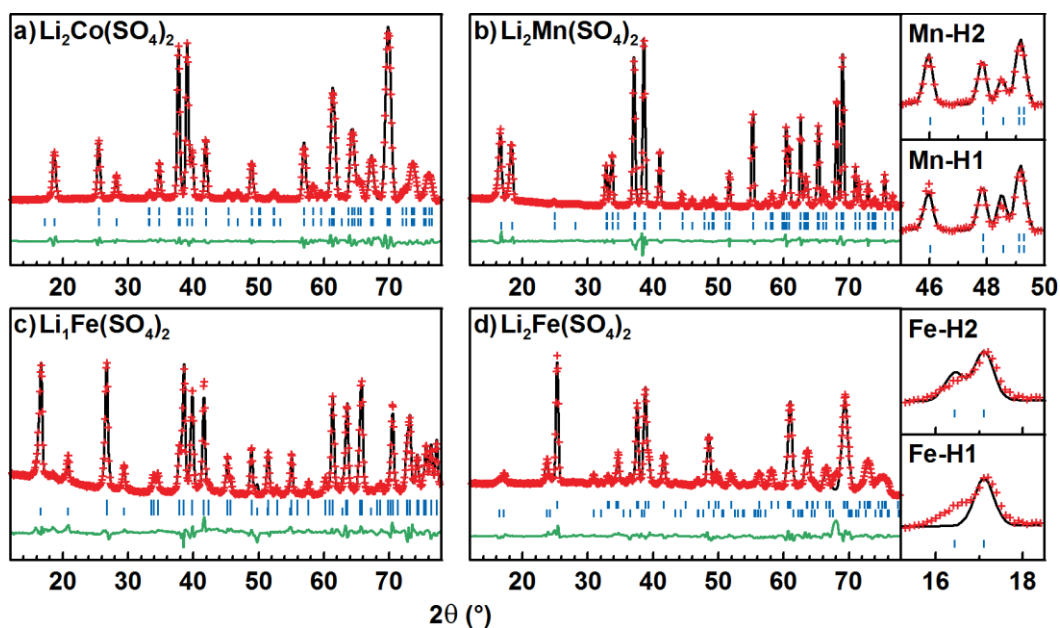
Figure IV.8: Refinements of the nuclear and magnetic parts of the NPD patterns measured at 1.85K for (a) Li$_2$Co(SO$_4$)$_2$ (λ = 2.418 Å), (b) Li$_2$Mn(SO$_4$)$_2$ (λ = 2.416 Å), (c) Li$_1$Fe(SO$_4$)$_2$ (λ = 2.416 Å) and (d) Li$_2$Fe(SO$_4$)$_2$ (λ = 2.418 Å). For each phase, the first line of blue sticks corresponds to the Bragg positions of the nuclear part while the second line of blue sticks shows the positions of the expected reflections of the magnetic part. The boxes H1 and H2 on the right of the diagrams (b) and (d) highlight the difference of fitting of the patterns depending on the model chosen as described in the text.
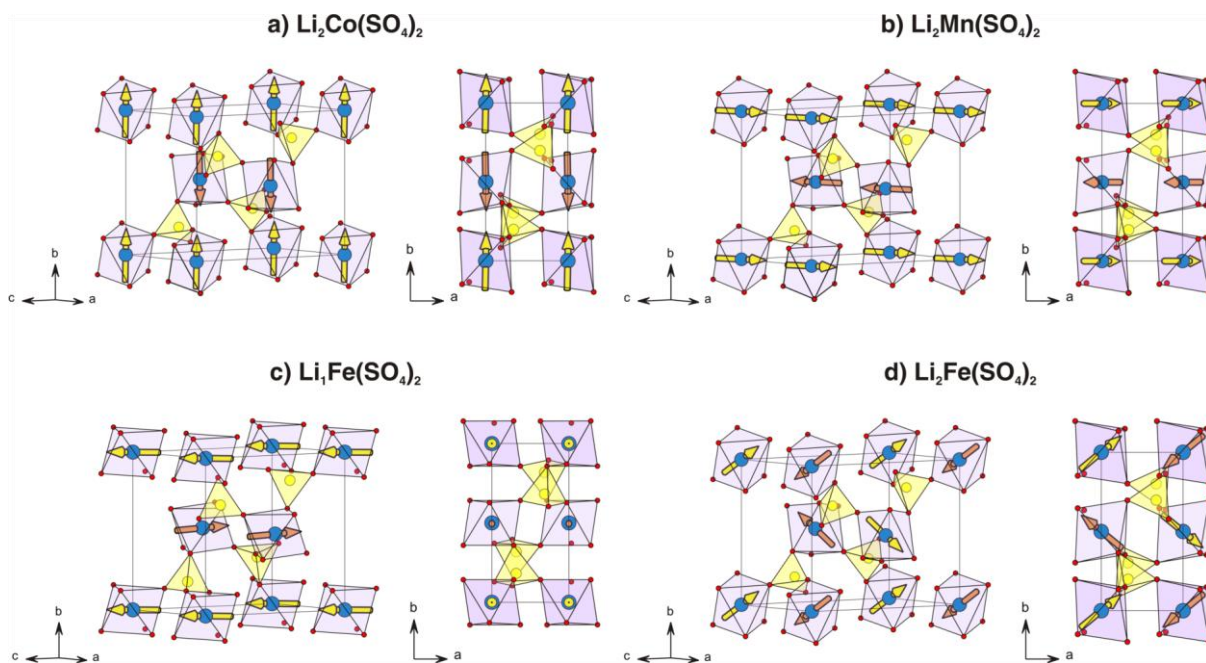
Figure IV.9: Nuclear and magnetic structures of (a) Li$_2$Co^{II}(SO$_4$)$_2$, (b) Li$_2$Mn^{II}(SO$_4$)$_2$, (c) Li$_1$Fe^{III}(SO$_4$)$_2$ and (d) Li$_2$Fe(SO$_4$)$_2$. Magnetic moments are represented by a vector through the 3d metal atoms. Yellow vectors stand for positive moments, while the orange ones stand for negative moments. For clarity, Li atoms are omitted.

The same procedure was employed for the determination of the magnetic structure of Li$_2$Fe^{II}(SO$_4$)$_2$. However, although it crystallizes in the same crystal structure as the previous compounds, its magnetic reflections could not be indexed in the nuclear unit cell. Therefore, in this case the propagation vector **k** was not (0, 0, 0) as for the other *marinite* compounds but it was found to be (½, 0, 0), which results in a magnetic unit cell 2$a \times b \times c$, where a, b and c are the unit cell parameters of the nuclear structure. A symmetry analysis was then performed for **k** = (½, 0, 0), and led to the two irreducible representations Γ$_1$ and Γ$_3$, as described in **Table IV.10**. The representation Γ$_1$, with the basis vectors {(1, 0, 0), (0, 1, 0), (0, 0, 1)} for Fe1 and {(-1, 0, 0), (0, 1, 0), (0, 0, -1)} for Fe2, was found to give the best agreement with the observed magnetic peaks. A first magnetic model was determined with all the magnetic moments being aligned along the a-axis. However the refinement of this model did not result in a good fitting of all the magnetic peaks, as the intensity of the first satellite reflection at 2θ = 16.4° was not reproduced by this model (see hypothesis Fe-H1 in **Figure IV.8.d**). Adding a magnetic component along the b-axis was finally found to fit well the neutron data, leading to a non-collinear magnetic structure (panel Fe-H2 in **Figure IV.8.d**). The refined value of the magnetic moment of the iron is then 3.2(4) μ$_B$. The results of the refinement are summarized in **Table IV.11**, and are displayed in **Figure IV.8.d** and **Figure IV.9.d**. Thus, the propagation vector **k** = (½, 0, 0) for Li$_2$Fe^{II}(SO$_4$)$_2$ results in a different spin sequence from the ones observed for the other *marinite* Li$_x$M(SO$_4$)$_2$ compounds. In Li$_2$Fe^{II}(SO$_4$)$_2$, the spin sequence is (+ −) along [011] and [100], and (+ +) along the b- and c-axes. Moreover, the spins direction presents both a component along the a-axis and another component along the b-axis, so that the magnetic moments are not collinear. Therefore, we can retrospectively try to interpret the inflexion point at 10 kOe observed in the magnetization curve of Li$_2$Fe^{II}(SO$_4$)$_2$ (**Figure IV.5**, page 122): it is likely that this field is strong enough to align the magnetic moments and the magnetic structure becomes collinear at higher field.

Table IV.10: Results of the symmetry analysis of the $P2_1/c$ unit cell for the propagation vector **k** = (½, 0, 0). The basis vectors Ψ$_i$ (i = 1, 2, 3) of the two general positions M_1 (x, y, z) and M_2 ($-x, y+½, -z+½$) are given for each irreducible representation Γ$_j$ (j = 1, 3).

	k = (½, 0, 0)	
Γ$_1$	**x, y, z**	**−x, y+½, −z+½**
Ψ$_1$	1 0 0	-1 0 0
Ψ$_2$	0 1 0	0 1 0
Ψ$_3$	0 0 1	0 0 -1
Γ$_3$	**x, y, z**	**−x, y+½, −z+½**
Ψ$_1$	1 0 0	1 0 0
Ψ$_2$	0 1 0	0 -1 0
Ψ$_3$	0 0 1	0 0 1

Table IV.11: Magnetic structure of Li$_2$Fe^{II}(SO$_4$)$_2$ determined from the Rietveld refinement of the D20 NPD data obtained at 1.85 K (*i.e.* below T$_N$).

Li$_2$Fe^{II}(SO$_4$)$_2$				
Nuclear structure	D20 diffractometer in high flux mode, λ = 2.418 Å, T = 1.85 K			
$P\,2_1/c$	V = 305.4 (3) Å^3	R$_{Bragg}$ = 14.4 %	χ^2 = 124	
a = 4.984 (3) Å	b = 8.190 (5) Å	c = 8.813 (5) Å	β = 121.91 (3)°	
Magnetic structure	D20 diffractometer in high flux mode, λ = 2.418 Å, T = 1.85 K			
k = (½, 0, 0) Γ$_1$				
Atom	**M$_x$/a (μ$_B$)**	**M$_y$/b (μ$_B$)**	**M$_z$/c (μ$_B$)**	**M$_{tot}$ (μ$_B$)**
Fe (0, 0, 0)	2.97(18)	1.3(3)	0	3.2(4)
Fe (0, ½, ½)	-2.97(18)	1.3(3)	0	3.2(4)

Overall, **Table IV.12** summarizes the values of the magnetic moments obtained from the refinements of the magnetic structures of the four *marinite* compounds studied here. This table shows that the magnetic moments refined for the manganese and the two iron phases are below the expected spin-only value (m$_{th}$ = g·S = 5 μ$_B$ and 4 μ$_B$ for the d^5 and d^6 ions, respectively). The reduction of the magnetic moment may be due to one (or more) of the following reasons: *(i)* the moments are not fully saturated at 1.85 K as these compounds present relatively low Néel temperatures, *(ii)* zero-point fluctuations of the antiferromagnetic ground state. Conversely, the experimental magnetic moment for the cobalt compound (Co^{II+}: d^7) is slightly larger than the theoretical value of 3 μ$_B$, which indicates a small contribution of the orbital moment, as often observed for Co^{II+} **[467,468]**.

Table IV.12: Magnetic parameters of the *marinite* compounds Li$_x M$(SO$_4$)$_2$ (x = 2, 1 & M = Co^{II+}, Fe^{II+}, Mn^{II+}, Fe^{III+}) deduced from neutron diffraction measurements, compared to some expected theoretical values.

	Li$_2$Co^{II}(SO$_4$)$_2$	Li$_2$Mn^{II}(SO$_4$)$_2$	Li$_2$Fe^{II}(SO$_4$)$_2$	Li$_1$Fe^{III}(SO$_4$)$_2$
Electronic configuration	d^7: t$_{2g}^5$e$_g^2$	d^5: t$_{2g}^3$e$_g^2$	d^6: t$_{2g}^4$e$_g^2$	d^5: t$_{2g}^3$e$_g^2$
	S = 3/2, L = 3	S = 5/2, L = 0	S = 2, L = 2	S = 5/2, L = 0
Experimental values deduced from neutron diffraction				
Néel temperature T$_N$	8 K	6 K	5 K	39 K
Magnetic moment at 1.85 K	3.3 μ$_B$	4.1 μ$_B$	3.2 μ$_B$	4.3 μ$_B$
Expected theoretical values				
Magnetic moment m = g·S	3 μ$_B$	5 μ$_B$	4 μ$_B$	5 μ$_B$

Finally, neutron diffraction patterns were recorded for each sample at small intervals of temperature from 2 K until the magnetic peaks vanished. Sequential refinements against these data were performed using the FullProf program **[384,443]** in order to follow the evolution of the magnitude of the magnetic moment with the temperature. The results of these refinements are presented in **Figure IV.10**. The Néel temperatures deduced from these measurements (**Table IV.12**) are in good agreement with the ones obtained from the SQUID data (**Table IV.1**, page 120).
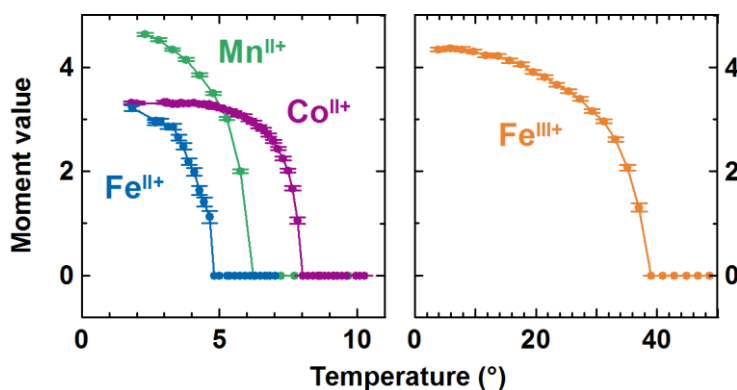
Figure IV.10: Temperature dependence of the moment value deduced from the sequential refinement of the magnetic structures against the D20 neutron powder diffraction data between 2 K and 50 K for the *marinite* compounds Li$_2$Co^{II}(SO$_4$)$_2$ (purple), Li$_2$Mn^{II}(SO$_4$)$_2$ (green), Li$_1$Fe^{III}(SO$_4$)$_2$ (orange) and Li$_2$Fe^{II}(SO$_4$)$_2$ (blue).

IV.2.3   Analysis of the exchange paths of the *marinite* compounds

To understand why Li$_2$Fe(SO$_4$)$_2$ (Fe^{II+}: d^6) presents a magnetic structure whose spin sequence is completely different from the other three *marinite* Li$_x$M(SO$_4$)$_2$ compounds (*M* = Fe^{III+}, Mn^{II+}, Co^{II+} and *x* = 1, 2), we have performed an analysis of the topology of the super-super-exchange interactions which govern the nature of the long-range magnetic ordering.

Inspection of the NPD patterns as a function of the temperature showed that whatever the transition metal, no additional magnetic reflections develop below the onset of long-range order, so that the magnetic structures that we determined in the previous section can be seen as the ground states. An analysis of the relative strengths and signs of the different super-super-exchange interactions that are required to produce the observed magnetic structure was performed by using the two programs SIMBO and ENERMAG **[488]**, which are delivered with the FullProf suite **[384,443]**. These programs are described in details by Khayati *et al*. in reference **[489]**. We followed here a procedure which was successfully applied to other iron phosphates and sulfates **[237,466,467,480,481]**.

Three interactions J$_n$ (*n* = 1, 2, 3) are to be considered between the transition metal atoms in the *marinite* structure (**Figure IV.11**). J$_1$ is the shortest one (less than 5Å for the *M*–*M* direct distance), and links two transition metals (*M*) along [100] *via* two SO$_4$ tetrahedra, so that J$_1$ has a double exchange path. J$_2$ and J$_3$ link two *M* atoms *via* a single SO$_4$ tetrahedron, the former along [211] and

the latter along [011]. J$_2$ and J$_3$ both show more linear M−O−O−M configurations than J$_1$ and therefore their M−M direct distances are between 6.0 and 6.2 Å, respectively. The geometric characteristics of these three exchange paths are reported for each compound in **Table IV.13**, and the topology of these exchange paths within the monoclinic *marinite* unit cell is shown **Figure IV.12**. Here, it appears clearly that J$_1$, J$_2$ and J$_3$ form triangular networks which may lead to frustration, if being of the same sign and strength. Therefore, we embarked in a study of their relative values, so as to obtain the observed magnetic structures as the ground state. Note that our analysis only deals with the spin sequence of the magnetic moments carried by the transition metal atoms; it does not consider their spatial orientation. This is a consequence of the fact that this analysis neglects the magnetocrystalline anisotropy which may play a role in these compounds, mostly for the cases in which L≠0.
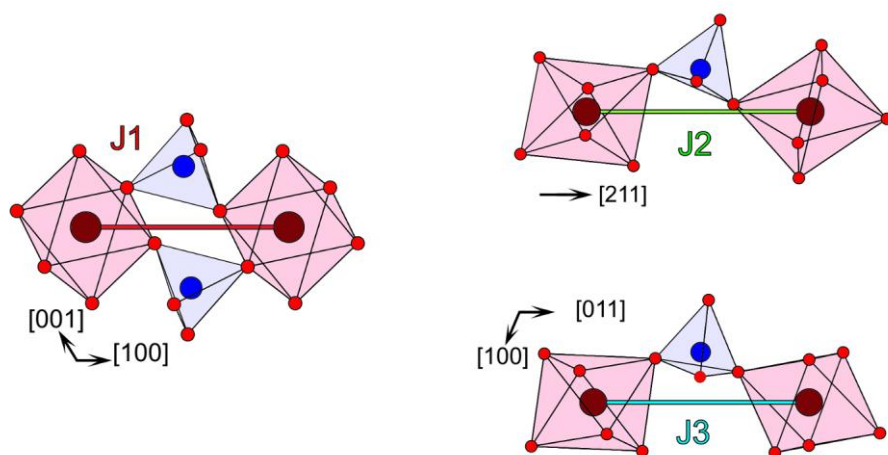
Figure IV.11: Geometrical characteristics of the three super-super-exchange paths J$_1$, J$_2$ and J$_3$.
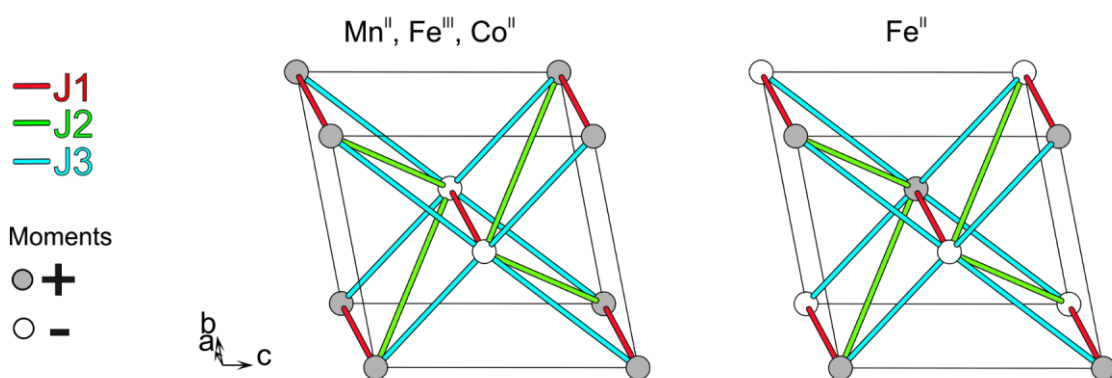
Figure IV.12: Topology of the super-super-exchange paths J$_1$, J$_2$ and J$_3$ within the *marinite* unit cell (*i.e.* how these three paths connect the transition metal atoms). For sake of clarity, only the magnetic atoms M are displayed; they are in colored in grey or white depending on the sign of their magnetic moment (as determined from our NPD experiment). Remark that J$_1$, J$_2$ and J$_3$ form triangular paths in the (011) and (01-1) planes.

Table IV.13: Super-super-exchange paths of the four *marinite* compounds and their geometrical characteristics: distances M–O, O–O and O–M (expressed in Å), and angles M–O–O, O–O–M and dihedral angles M–O–O–M (expressed in °).

		Distances (Å)			Angles (°)		
Li$_2$Co^{II}(SO$_4$)$_2$	**M–M**	**M–O**	**O–O**	**O–M**	**M–O–O**	**O–O–M**	**M–O–O–M**
Exchange interaction J$_1$	4.9787						
Path 1		2.0745	2.4193	2.1168	153.58	103.59	-35.43
Path 2		2.1168	2.4193	2.0745	103.59	153.58	35.43
Exchange interaction J$_2$	6.1214						
Path 1		2.1518	2.4188	2.1168	125.65	161.24	136.24
Exchange interaction J$_3$	5.9778						
Path 1		2.1518	2.3714	2.0745	159.71	136.59	40.17
Li$_2$Mn^{II}(SO$_4$)$_2$	**M–M**	**M–O**	**O–O**	**O–M**	**M–O–O**	**O–O–M**	**M–O–O–M**
Exchange interaction J$_1$	4.9811						
Path 1		2.126	2.4069	2.2164	155.97	99.62	-37.95
Path 2		2.2164	2.4069	2.126	99.62	155.97	37.95
Exchange interaction J$_2$	6.2275						
Path 1		2.1881	2.4353	2.2164	122.71	157.93	145.56
Exchange interaction J$_3$	6.0671						
Path 1		2.1881	2.3761	2.126	161.34	134.57	53.17
Li$_2$Fe^{II}(SO$_4$)$_2$	**M–M**	**M–O**	**O–O**	**O–M**	**M–O–O**	**O–O–M**	**M–O–O–M**
Exchange interaction J$_1$	4.9849						
Path 1		2.1192	2.3787	2.116	154.82	103.59	-31.19
Path 2		2.116	2.3787	2.1192	103.59	154.82	31.19
Exchange interaction J$_2$	6.1490						
Path 1		2.2007	2.4349	2.116	124.22	161	137.15
Exchange interaction J$_3$	6.0156						
Path 1		2.2007	2.3376	2.1192	157.51	136.42	51.31
Li$_1$Fe^{III}(SO$_4$)$_2$	**M–M**	**M–O**	**O–O**	**O–M**	**M–O–O**	**O–O–M**	**M–O–O–M**
Exchange interaction J$_1$	4.7974						
Path 1		2.0206	2.3943	2.0113	103.23	139.9	68.71
Path 2		2.0113	2.3943	2.0206	139.9	103.23	-68.71
Exchange interaction J$_2$	6.0152						
Path 1		2.0417	2.3699	2.0113	162.56	144.47	-44.86
Exchange interaction J$_3$	5.7574						
Path 1		2.0417	2.4113	2.0206	118.89	146.99	135.59

The first ordered magnetic state is obtained by a calculation as a function of the exchange integrals and of the propagation vector **k** (on the surface or inside the Brillouin zone). It is given by the eigenvector corresponding to the highest eigenvalue of the Fourier transform of the following matrix of exchange integrals:

$$\xi_{ij}(\boldsymbol{k}) = \sum_l J_{ij}(\boldsymbol{R}_l) \cdot e^{-2\pi i \boldsymbol{k}\cdot\boldsymbol{R}_l} \qquad \textbf{Eq. IV.6}$$

where i and j refer to the magnetic atoms in a primitive cell, and $J_{ij}(\boldsymbol{R}_l)$ is the isotropic exchange interaction between the spins of the atoms i and j in unit cells separated by the lattice vector $\boldsymbol{R}_l$. Our convention is that a negative value of J_{ij} means an antiparallel coupling (pair interaction energy: $E_{ij} = -J_{ij} \cdot \boldsymbol{S}_i \cdot \boldsymbol{S}_j$).

The ξ_{ij}(**k**, J$_1$, J$_2$, J$_3$) matrices contain many terms and eigenvalues, and are therefore cumbersome to obtain by hand; the phase diagram is therefore more easily obtained using the program ENERMAG **[488]**. The values of the three J$_n$ (n = 1, 2, 3) were allowed to vary between −100 and +100, so as to map all possibilities for the relative values of exchange integrals. The resulting phase diagram is shown **Figure IV.13**, as cuts in the J$_2$–J$_3$ planes given for different values of J$_1$. This diagram of first-ordered state indicate the magnetic structure (propagation vector and sign sequence) for a given set of (J$_1$, J$_2$, J$_3$) values, which presents the lowest energy and therefore can be considered as the ground state if there is no further magnetic phase transition below the Néel temperature.

First of all, we can notice wide domains in the phase diagram for which we got incommensurate or disordered magnetic phases (light blue regions in **Figure IV.13**), especially when J$_1$ is negative and J$_2$ and J$_3$ are of same relative values and signs, and when J$_1$ is positive and J$_2$ and J$_3$ are of opposite signs but have the same absolute values. This comes as no surprise considering the possible geometric frustration present in these systems (**Figure IV.12**, page 134). Apart from these domains, the system adopts more likely two propagation vectors (**k** = (0, 0, 0) and **k** = (½, 0, 0)), each of them giving two different spin sequences between the magnetic moments located in M_1 (0, 0, 0) and in M_2 (0, ½, ½). Therefore four ordered magnetic structures are seen as ground states, depending on the relative values of J$_1$, J$_2$, and J$_3$: **k** = (0, 0, 0) with (+ +) and (+ −), and **k** = (½, 0, 0) with (+ +) and (+ −). For example, the ferromagnetic structure, characterized by **k** = (0, 0, 0) and (+ +) is observed in the region for which all J$_n$ (n = 1, 2, 3) are positive (yellow domain in **Figure IV.13**).
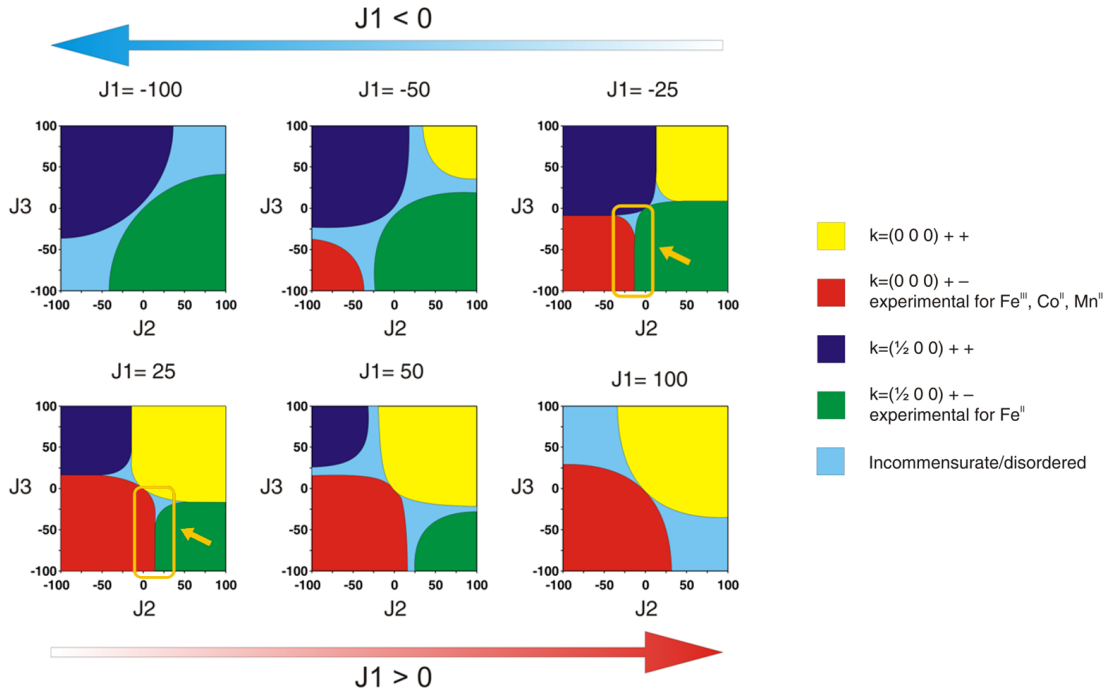
Figure IV.13: Phase diagram showing the influence of the values of the super-super-exchange integrals J_n (n = 1, 2 and 3) on the ground-state magnetic structures. The diagram is shown as cuts in the J_2–J_3 planes, for different values of J_1, all varying between −100 and +100. The orange arrows highly the domain which most probably corresponds to the experimental magnetic structures of the *marinite* compounds Li$_x$M(SO₄)₂ (x = 2, 1 & M = Co^{II+}, Fe^{II+}, Mn^{II+}, Fe^{III+}).

First of all, the experimentally deduced magnetic structures for Li$_x$M(SO₄)₂ (M = Fe^{III+}, Co^{II+}, Mn^{II+}) (**k** = (0, 0, 0) and (+ −); red domain in **Figure IV.13**) and for Li₂Fe^{II}(SO₄)₂ (**k** = (½, 0, 0) and (+ −); green domain in **Figure IV.13**) are mainly observed as the ground state when J_3<0. This is in good agreement with the elongated M−O−O−M configuration of the J_3 path (**Figure IV.11** and **Table IV.13**), for which the Goodenough−Kanamori−Anderson rules **[459–464]** would predict an antiferromagnetic super-super-exchange interaction. Next, a closer inspection indicates that both structures can be obtained as a result of a slight change in intensity of J_1 or J_2, when J_1 and J_2 are of the same sign and strength, and smaller than J_3 (this region in highlighted in **Figure IV.13** with the orange arrows). Thus only a small variation of the exchange integral J_1 or J_2 can explain the change from the structure **k** = (0, 0, 0) (+ −) to the **k** = (½, 0, 0) (+ −) one. However this analysis can not figure out what would be the sign of the two integrals J_1 and J_2. Therefore, more detailed theoretical and numerical approaches (*e.g.* DFT calculations) would be needed to determine the exact nature of these two interactions (*i.e.* ferro- *vs.* antiferro-magnetic), as well as to understand the peculiar magnetic behavior of Li₂Fe^{II}(SO₄)₂ in the *marinite* series.

At this stage, we decided to undertake a similar magnetic study for the Li$_2$Ni(SO$_4$)$_2$ phase, in order to probe whether its orthorhombic structure, which equally enables only super-super-exchange interactions, also results in a long-range antiferromagnetic ordering as observed for the monoclinic *marinite* compounds.

IV.3   The orthorhombic phase Li$_2$Ni(SO$_4$)$_2$

IV.3.1   Magnetic properties

As we previously did for the *marinite* compounds, we recorded the magnetic susceptibility of Li$_2$Ni^{II}(SO$_4$)$_2$ as a function of the temperature between 2 K and 300 K, and in both zero-field cooled (ZFC) and field cooled (FC) conditions with an applied field of 10 kOe, using a SQUID magnetometer [484]. Both ZFC and FC curves overlap on the whole range of temperature and show a cusp around T$_N$ = 28 K, as it is characteristic of a pure antiferromagnetic behavior (**Figure IV.14.a**).

The high-temperature region (200 to 300 K) of the inverse susceptibility was then fitted to the Curie-Weiss equation (see **Eq. IV.1** and **Eq. IV.2**, page 118), as shown in **Figure IV.14.b**. The characteristic values for Li$_2$Ni^{II}(SO$_4$)$_2$ deduced from this fit are summed up in **Table IV.14**. The Curie-Weiss temperature was determined to be θ_{CW} = −45 K, which gives a frustration parameter $f = |\Theta_{CW}/T_N| \approx 1.6$, indicating a small degree of frustration in the magnetic structure [485,486]. Moreover, an effective moment μ_{eff} of ~3.3 μ_B per nickel atom was deduced from the Curie constant. This traduces a partial contribution of the orbital moment as it falls in-between the expected value for a spin-only effective moment (μ_{eff}(S) = 2.8 μ_B, **Eq. IV.5** page 121) and the one calculated for an unquenched orbital moment which is decoupled from the spin contribution (m$_{eff}$(S+L) = 4.5 μ_B, **Eq. IV.4** page 121).

Finally, to probe the field dependence of the magnetism of Li$_2$Ni^{II}(SO$_4$)$_2$, a magnetization curve M = f(H) was recorded at 2 K. The resulting curve is presented in **Figure IV.15** and shows the linear response that is expected for a perfect collinear antiferromagnetic ground state.
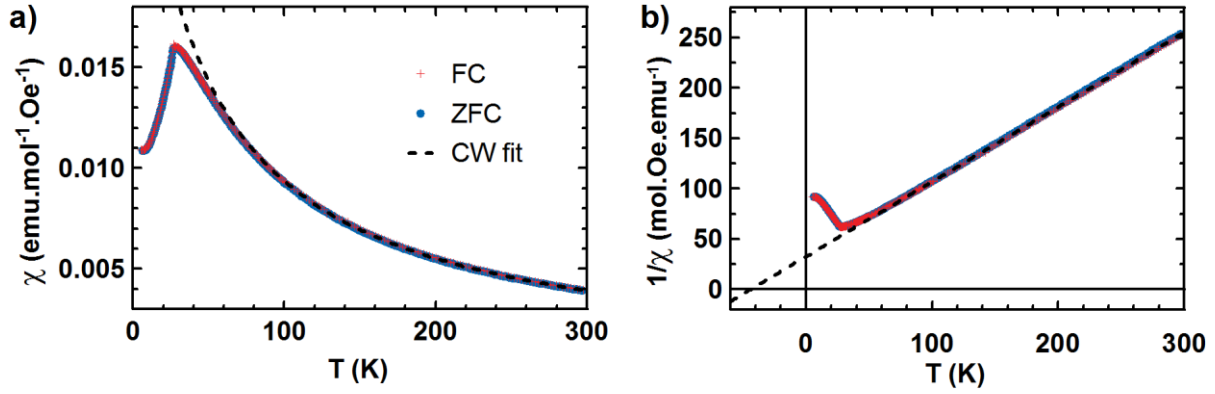
Figure IV.14: Temperature dependence of (a) the magnetic susceptibility χ and (b) the inverse of the magnetic susceptibility 1/χ of Li$_2$Ni(SO$_4$)$_2$, measured in ZFC (blue points) and FC (red crosses) conditions with a magnetic field of 10 kOe. The ideal Curie-Weiss behavior is represented by the dashed line (CW fit).

Table IV.14: Magnetic parameters of the orthorhombic Li$_2$Ni(SO$_4$)$_2$ deduced from magnetic measurements, and compared to some expected theoretical values.

Li$_2$Ni^{II}(SO$_4$)$_2$		
Electronic configuration		d^8: t$_{2g}$^{6}e$_g$^{2} S=1, L=3
Experimental values deduced from magnetic measurements (H = 10 kOe)		
Néel temperature T$_N$		28 K
Curie Weiss temperature θ$_{CW}$		-45 K
Frustration parameter f = |θ$_{CW}$|/T$_N$		1.6
Curie Constant C (emu.K.mol^{-1}.Oe^{-1})		1.35
Effective moment μ$_{eff}$		3.3 μ$_B$
Expected theoretical values		
Effective moment μ$_{eff}$	μ$_{eff}$(J) = g$_J$·(J(J+1))$^{\frac{1}{2}}$	5.6 μ$_B$
	μ$_{eff}$(S,L) = (4S(S+1)+L(L+1))$^{\frac{1}{2}}$	4.5 μ$_B$
	μ$_{eff}$(S) = 2·(S(S+1))$^{\frac{1}{2}}$	2.8 μ$_B$

Figure IV.15: Magnetization curve of Li$_2$Ni^{II}(SO$_4$)$_2$ as a function of the applied field, measured at 2 K. The inset shows an enlargement of the low-field domain.

IV.3.2   Magnetic structures

To better understand the magnetic ground state of Li$_2$Ni^{II}(SO$_4$)$_2$, neutron powder diffraction experiments (NPD) were performed on the high-intensity D20 diffractometer at the Institut Laue Langevin (ILL, Grenoble, France, *cf.* Annexes: § A.3.3.2 D20 diffractometer at ILL, page 165). We started by acquiring a NPD pattern of Li$_2$Ni^{II}(SO$_4$)$_2$ above the Néel temperature that we had determined from magnetic measurements. The Rietveld refinement of the latter confirmed the orthorhombic structure proposed by Isasi *et al.* **[425]** that we had used to refined our XRD data in the previous chapter (see Chapter I: **Figure III.25** page 103). The results of this refinement are presented in **Table IV.17** and **Figure IV.16**.
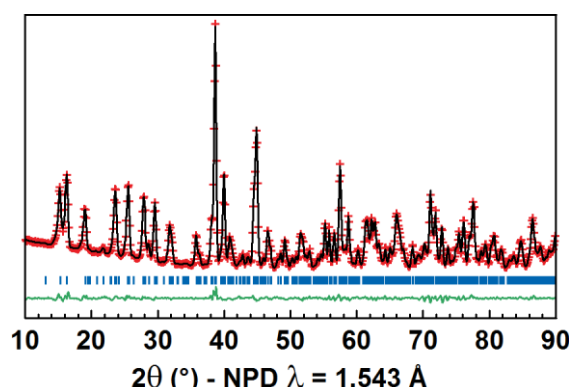
Figure IV.16: Result of the Rietveld refinement of the orthorhombic nuclear structure of Li$_2$Ni^{II}(SO$_4$)$_2$ against its NPD pattern measured at 35 K.

Table IV.15: Crystallographic data and atomic positions of Li$_2$Ni^{II}(SO$_4$)$_2$ deduced from the Rietveld refinement of the D20 NPD data recorded for this compound at 35 K (*i.e.* above T$_N$).

<table>
<tr><td colspan="8" align="center">**Li$_2$Ni^{II}(SO$_4$)$_2$**</td></tr>
<tr><td>**Nuclear structure**</td><td colspan="7" align="center">D20 diffractometer in high resolution mode λ = 1.543 Å T = 35 K</td></tr>
<tr><td>*P b c a*</td><td colspan="4" align="center">R$_{Bragg}$ = 1.93 %</td><td colspan="3">χ^2 = 11.6</td></tr>
<tr><td>*a* = 9.1236 (6) Å</td><td colspan="2" align="center">*b* = 9.0096 (4) Å</td><td colspan="2" align="center">*c* = 13.5593 (10) Å</td><td colspan="3">*V* = 1114.58 (11) Å^3</td></tr>
</table>

Atom	Wyckoff position	Occupancy	x/a	y/b	z/c	B$_{iso}$ (Å^2)	BVS
Ni	8*c*	1.0	0.8615 (11)	0.6029 (11)	0.3780 (7)	0.13 (17)	2.02 (5)
Li1	8*c*	1.0	0.467 (6)	0.719 (5)	0.375 (5)	0.6 (9)	0.99 (6)
Li2	8*c*	1.0	0.724 (6)	0.540 (6)	0.626 (4)	0.4 (9)	0.99 (7)
S1	8*c*	1.0	0.660 (4)	0.812 (4)	0.508 (3)	0.1 (3)	6.0 (3)
O11	8*c*	1.0	0.5010 (18)	0.8000 (15)	0.5233 (12)	0.3 (4)	2.02 (15)
O12	8*c*	1.0	0.7040 (16)	0.9690 (17)	0.4940 (13)	0.5 (4)	2.03 (14)
O13	8*c*	1.0	0.6882 (17)	0.7284 (18)	0.4169 (12)	0.2 (3)	2.08 (16)
O14	8*c*	1.0	0.7426 (17)	0.756 (2)	0.5946 (13)	0.3 (3)	1.87 (15)
S2	8*c*	1.0	0.576 (4)	0.431 (4)	0.274 (3)	0.1 (3)	6.0 (3)
O21	8*c*	1.0	0.4824 (18)	0.4965 (18)	0.3476 (13)	0.3 (3)	2.11 (18)
O22	8*c*	1.0	0.524 (2)	0.4639 (16)	0.1713 (12)	0.2 (3)	1.94 (16)
O23	8*c*	1.0	0.5736 (17)	0.2647 (18)	0.2779 (13)	0.3 (3)	1.88 (14)
O24	8*c*	1.0	0.7279 (19)	0.488 (2)	0.2793 (12)	0.3 (3)	1.95 (15)

As with the *marinite* compounds, upon cooling the Li$_2$Ni^{II}(SO$_4$)$_2$ sample down to 2 K, we observed the growth of new peaks at low angles, indicating a long-range ordering of the magnetic moments (**Figure IV.17**). Here also, the nuclear Bragg peaks show no changes, suggesting that the structure remains intact at the magnetic transition (no magneto-elastic effect).
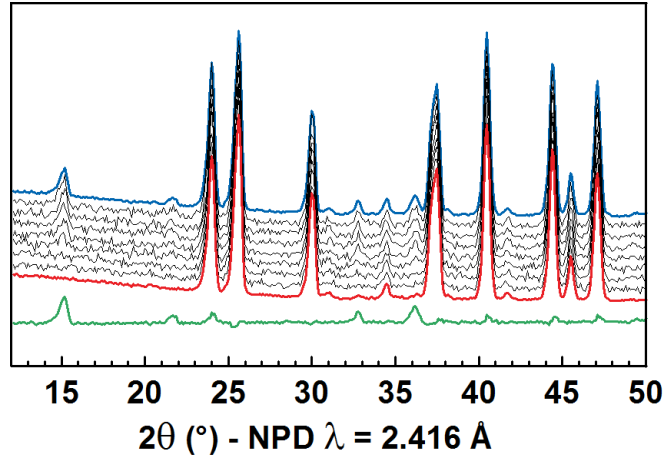
Figure IV.17: Evolution of the NPD patterns of Li$_2$Ni(SO$_4$)$_2$ while cooling the sample from 35 K (red pattern) to 2 K (blue pattern). Patterns recorded at intermediate temperatures are displayed in black. The green line is the difference curve between the blue and the red patterns.

High-quality NPD patterns were then recorded at 1.85 K using the two wavelengths 2.416 Å and 1.543 Å in order to determine the magnetic structure of Li$_2$Ni^{II}(SO$_4$)$_2$. The magnetic reflections, which are better observed on the former pattern, could be indexed in the same unit cell as the nuclear structure, *i.e.* using a propagation vector **k** = (0, 0, 0).

A symmetry analysis was then performed using Bertaut's method **[487]** with the BasIReps program **[384,443]**, in order to determine all of the possible spin configurations which are compatible with the crystal symmetry of Li$_2$Ni^{II}(SO$_4$)$_2$. Eight irreducible representations associated with the general Wyckoff site 8c (x, y, z) occupied by the Ni atoms: $\Gamma_{mag} = \Gamma_1 + \Gamma_2 + \Gamma_3 + \Gamma_4 + \Gamma_5 + \Gamma_6 + \Gamma_7 + \Gamma_8$. These representations are built with three basis vectors Ψ_i (i = 1, 2, 3) which are collinear to the a, b and c unit cell directions, respectively. **Table IV.16** describes for each irreducible representation Γ_j (1 ≤ j ≤ 8) the orientation of magnetic moments carried by each of the eight Ni atoms of the unit cell.

Table IV.16: Results of the symmetry analysis of the *Pbca* unit cell for the propagation vector **k** = (0, 0, 0). The basis vectors **Ψ**$_i$ (*i* = 1, 2, 3) of the eight general positions generated for the Wyckoff site 8*c* (*x*, *y*, *z*) are given for each irreducible representation Γ$_j$ (1 ≤ *j* ≤ 8). Note that the eight general positions are given according to the order recommended in the International Tables for Crystallography **[490]**.

				k = (0, 0, 0)				
Γ₁	*x, y, z*	*-x+½, -y, z+½*	*-x, y+½, -z+½*	*x+½, -y+½, -z*	*-x, -y, -z*	*x+½, y, -z+½*	*x, -y+½, z+½*	*-x+½, y+½, z*
Ψ₁	1, 0, 0	$\bar{1}$, 0, 0	$\bar{1}$, 0, 0	1, 0, 0	1, 0, 0	$\bar{1}$, 0, 0	$\bar{1}$, 0, 0	1, 0, 0
Ψ₂	0, 1, 0	0, $\bar{1}$, 0	0, 1, 0	0, $\bar{1}$, 0	0, 1, 0	0, $\bar{1}$, 0	0, 1, 0	0, $\bar{1}$, 0
Ψ₃	0, 0, 1	0, 0, 1	0, 0, $\bar{1}$	0, 0, $\bar{1}$	0, 0, 1	0, 0, 1	0, 0, $\bar{1}$	0, 0, $\bar{1}$
Γ₂	*x, y, z*	*-x+½, -y, z+½*	*-x, y+½, -z+½*	*x+½, -y+½, -z*	*-x, -y, -z*	*x+½, y, -z+½*	*x, -y+½, z+½*	*-x+½, y+½, z*
Ψ₁	1, 0, 0	$\bar{1}$, 0, 0	$\bar{1}$, 0, 0	1, 0, 0	$\bar{1}$, 0, 0	1, 0, 0	1, 0, 0	$\bar{1}$, 0, 0
Ψ₂	0, 1, 0	0, $\bar{1}$, 0	0, 1, 0	0, $\bar{1}$, 0	0, $\bar{1}$, 0	0, 1, 0	0, $\bar{1}$, 0	0, 1, 0
Ψ₃	0, 0, 1	0, 0, 1	0, 0, $\bar{1}$	0, 0, $\bar{1}$	0, 0, $\bar{1}$	0, 0, $\bar{1}$	0, 0, 1	0, 0, 1
Γ₃	*x, y, z*	*-x+½, -y, z+½*	*-x, y+½, -z+½*	*x+½, -y+½, -z*	*-x, -y, -z*	*x+½, y, -z+½*	*x, -y+½, z+½*	*-x+½, y+½, z*
Ψ₁	1, 0, 0	$\bar{1}$, 0, 0	1, 0, 0	$\bar{1}$, 0, 0	1, 0, 0	$\bar{1}$, 0, 0	1, 0, 0	$\bar{1}$, 0, 0
Ψ₂	0, 1, 0	0, $\bar{1}$, 0	0, $\bar{1}$, 0	0, 1, 0	0, 1, 0	0, $\bar{1}$, 0	0, $\bar{1}$, 0	0, 1, 0
Ψ₃	0, 0, 1	0, 0, 1	0, 0, 1	0, 0, 1	0, 0, 1	0, 0, 1	0, 0, 1	0, 0, 1
Γ₄	*x, y, z*	*-x+½, -y, z+½*	*-x, y+½, -z+½*	*x+½, -y+½, -z*	*-x, -y, -z*	*x+½, y, -z+½*	*x, -y+½, z+½*	*-x+½, y+½, z*
Ψ₁	1, 0, 0	$\bar{1}$, 0, 0	1, 0, 0	$\bar{1}$, 0, 0	$\bar{1}$, 0, 0	1, 0, 0	$\bar{1}$, 0, 0	1, 0, 0
Ψ₂	0, 1, 0	0, $\bar{1}$, 0	0, $\bar{1}$, 0	0, 1, 0	0, $\bar{1}$, 0	0, 1, 0	0, 1, 0	0, $\bar{1}$, 0
Ψ₃	0, 0, 1	0, 0, 1	0, 0, 1	0, 0, 1	0, 0, $\bar{1}$	0, 0, $\bar{1}$	0, 0, $\bar{1}$	0, 0, $\bar{1}$
Γ₅	*x, y, z*	*-x+½, -y, z+½*	*-x, y+½, -z+½*	*x+½, -y+½, -z*	*-x, -y, -z*	*x+½, y, -z+½*	*x, -y+½, z+½*	*-x+½, y+½, z*
Ψ₁	1, 0, 0	1, 0, 0	$\bar{1}$, 0, 0	$\bar{1}$, 0, 0	1, 0, 0	1, 0, 0	$\bar{1}$, 0, 0	$\bar{1}$, 0, 0
Ψ₂	0, 1, 0	0, 1, 0	0, 1, 0	0, 1, 0	0, 1, 0	0, 1, 0	0, 1, 0	0, 1, 0
Ψ₃	0, 0, 1	0, 0, $\bar{1}$	0, 0, $\bar{1}$	0, 0, 1	0, 0, 1	0, 0, $\bar{1}$	0, 0, $\bar{1}$	0, 0, 1
Γ₆	*x, y, z*	*-x+½, -y, z+½*	*-x, y+½, -z+½*	*x+½, -y+½, -z*	*-x, -y, -z*	*x+½, y, -z+½*	*x, -y+½, z+½*	*-x+½, y+½, z*
Ψ₁	1, 0, 0	1, 0, 0	$\bar{1}$, 0, 0	$\bar{1}$, 0, 0	$\bar{1}$, 0, 0	$\bar{1}$, 0, 0	1, 0, 0	1, 0, 0
Ψ₂	0, 1, 0	0, 1, 0	0, 1, 0	0, 1, 0	0, $\bar{1}$, 0	0, $\bar{1}$, 0	0, $\bar{1}$, 0	0, $\bar{1}$, 0
Ψ₃	0, 0, 1	0, 0, $\bar{1}$	0, 0, $\bar{1}$	0, 0, 1	0, 0, $\bar{1}$	0, 0, 1	0, 0, 1	0, 0, $\bar{1}$
Γ₇	*x, y, z*	*-x+½, -y, z+½*	*-x, y+½, -z+½*	*x+½, -y+½, -z*	*-x, -y, -z*	*x+½, y, -z+½*	*x, -y+½, z+½*	*-x+½, y+½, z*
Ψ₁	1, 0, 0	1, 0, 0	1, 0, 0	1, 0, 0	1, 0, 0	1, 0, 0	1, 0, 0	1, 0, 0
Ψ₂	0, 1, 0	0, 1, 0	0, $\bar{1}$, 0	0, $\bar{1}$, 0	0, 1, 0	0, 1, 0	0, $\bar{1}$, 0	0, $\bar{1}$, 0
Ψ₃	0, 0, 1	0, 0, $\bar{1}$	0, 0, 1	0, 0, $\bar{1}$	0, 0, 1	0, 0, $\bar{1}$	0, 0, 1	0, 0, $\bar{1}$
Γ₈	*x, y, z*	*-x+½, -y, z+½*	*-x, y+½, -z+½*	*x+½, -y+½, -z*	*-x, -y, -z*	*x+½, y, -z+½*	*x, -y+½, z+½*	*-x+½, y+½, z*
Ψ₁	1, 0, 0	1, 0, 0	1, 0, 0	1, 0, 0	$\bar{1}$, 0, 0	$\bar{1}$, 0, 0	$\bar{1}$, 0, 0	$\bar{1}$, 0, 0
Ψ₂	0, 1, 0	0, 1, 0	0, $\bar{1}$, 0	0, $\bar{1}$, 0	0, $\bar{1}$, 0	0, $\bar{1}$, 0	0, 1, 0	0, 1, 0
Ψ₃	0, 0, 1	0, 0, $\bar{1}$	0, 0, 1	0, 0, $\bar{1}$	0, 0, $\bar{1}$	0, 0, 1	0, 0, $\bar{1}$	0, 0, 1

After testing all the possibilities given by this symmetry analysis against the NPD pattern recorded at 1.85 K with the 2.416 Å wavelength, we found that the best agreement with the observed magnetic reflections was obtained using Γ_2. Coefficients that multiply the three basis vectors were first freely refined, and this led to a main component on Ψ_3 and tiny values for Ψ_1 and Ψ_2, which included the zero value considering the standard deviations. A refinement was therefore undertaken with constraining the magnetic moments to be collinear to the c-axis only (*i.e.* by refining Ψ_3 only, Ψ_1 and Ψ_2 being null). This latter refinement, which is shown in **Figure IV.18**, did not led to worse reliability values, and these results were then kept a the final model for the magnetic structure of Li$_2$Ni^{II}(SO$_4$)$_2$ (**Table IV.17**). Finally, this final magnetic structure was used for a Rietveld refinement of the NPD pattern recorded at 1.85 K with the shorter wavelength of 1.543 Å. The results of this refinement indicates, as initially assumed, that no structural distortion accompanies the magnetic transition (**Table IV.17**).
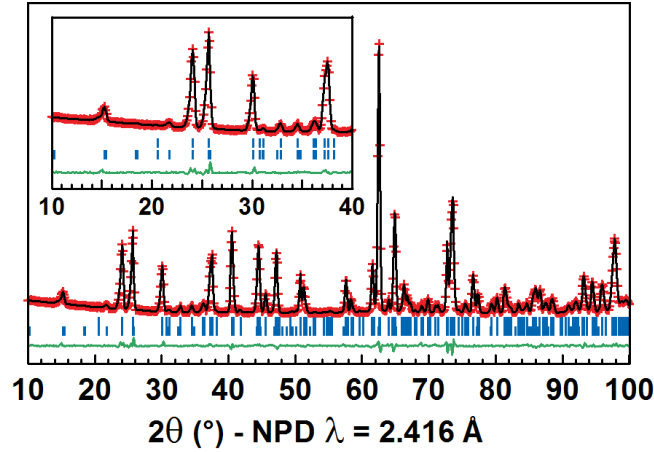
Figure IV.18: Rietveld refinement of the NPD pattern of Li$_2$Ni^{II}(SO$_4$)$_2$ measured at 1.85 K. The first line of blue sticks corresponds to the Bragg positions of the nuclear part while the second line of blue sticks shows the positions of the expected reflections of the magnetic part.

Table IV.17: Magnetic structure of Li$_2$Ni^{II}(SO$_4$)$_2$ determined from the Rietveld refinement of the NPD data recorded at 1.85K (*i.e.* below T$_N$). The eight general positions of Ni are given according to the order recommended in the International Tables for Crystallography **[490]**.

Li$_2$Ni^{II}(SO$_4$)$_2$			
Nuclear structure	D20 diffractometer in high resolution mode, λ = 1.543 Å, T = 1.85 K		
P b c a		R$_{Bragg}$ = 2.07 %	χ^2 = 12.2
a = 9.1260 (5) Å	b = 9.0117 (5) Å	c = 13.5611 (7) Å	V = 1115.28 (10) Å^3
Magnetic structure	D20 diffractometer in high resolution mode, λ = 2.416 Å, T = 1.85 K		
k = (0 0 0)	Γ_2		
Atom	**M$_z$/c (µ$_B$)**	**Atom**	**M$_z$/c (µ$_B$)**
Ni$_1$ (0.861, 0.603, 0.378)	+ 2.15(12)	Ni$_5$ (0.139, 0.397, 0.622)	− 2.15(12)
Ni$_2$ (0.639, 0.397, 0.878)	+ 2.15(12)	Ni$_6$ (0.361, 0.603, 0.122)	− 2.15(12)
Ni$_3$ (0.139, 0.103, 0.122)	− 2.15(12)	Ni$_7$ (0.861, 0.897, 0.878)	+ 2.15(12)
Ni$_4$ (0.361, 0.897, 0.622)	− 2.15(12)	Ni$_8$ (0.639, 0.103, 0.378)	+ 2.15(12)

The magnetic structure of Li$_2$Ni^{II}(SO$_4$)$_2$ deduced from these analyses is shown in **Figure IV.19**. The magnetic moments of Li$_2$Ni^{II}(SO$_4$)$_2$ are aligned antiferromagnetically along the c-axis, with a spin sequence (+ + − − − − + +), as seen in **Table IV.17** (from Ni$_1$ to Ni$_8$). Remark that this magnetic structure can also be described as an antiferromagnetic stacking of ferromagnetic layers along the c-axis.
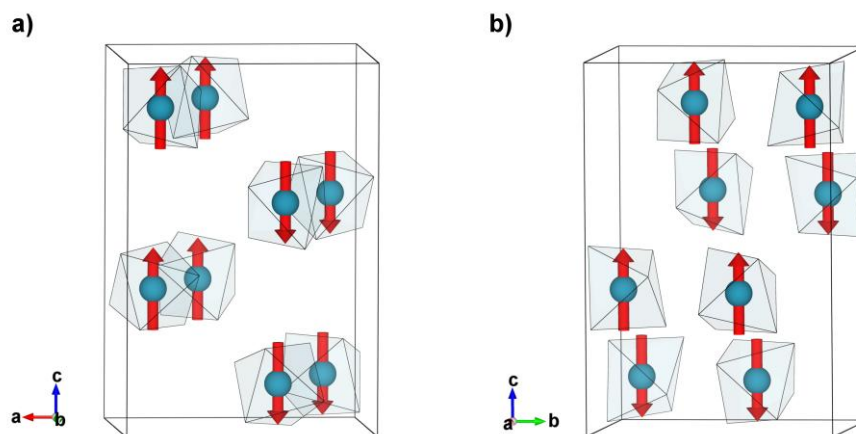
Figure IV.19: Magnetic structure of Li$_2$Ni(SO$_4$)$_2$. The blue balls shown the position of the Ni atoms within the unit cell, and red vectors represent their magnetic moments.
For the sake of clarity, all other atoms (Li, S, O) are omitted.

Finally, the refined value of the magnetic moments carried by each Ni^{II+} is 2.15(12) μ_B at 1.85 K. This is in good agreement with the spin-only magnetic moment m = g·S = 2 μ_B expected for a d^8 cation in low-spin configuration (t$_{2g}^6$e$_g^2$: S = 1). On heating, the magnetic peaks decrease in intensity, resulting from a decrease in the magnetic moment that reaches zero at T$_N$ = 28 K (**Figure IV.20**), in perfect agreement with the Néel temperature deduced from the SQUID data (see **Table IV.14** page 139).
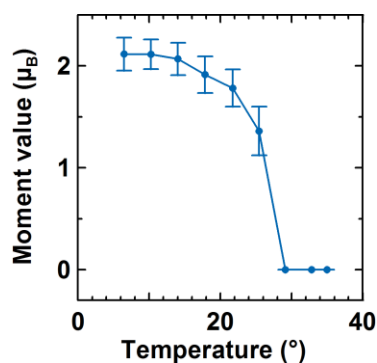
Figure IV.20: Temperature dependence of the moment value deduced from the refinement of the magnetic structure of Li$_2$Ni^{II}(SO$_4$)$_2$ against the NPD patterns recorded between 2 and 35 K.

At this stage, we undertook a similar analysis of the super-super-echange interactions governing the long-range ordering in the orthorhombic structure of Li$_2$Ni^{II}(SO$_4$)$_2$, as we previously did for the *marinite* compounds.

IV.3.3 Analysis of the exchange paths in the orthorhombic structure of Li$_2$Ni(SO$_4$)$_2$

The orthorhombic structure of Li$_2$Ni^{II}(SO$_4$)$_2$ indicates that only super-super-exchange interactions occur in this material. Considering the eight Ni atoms present in the unit cell, we identified five geometrically distinct Ni−O−O−Ni interactions, all of them going through the edge of one or two SO$_4$ tetrahedra, and giving the following direct Ni−Ni distances: 4.55 Å (J$_1$), 4.94 Å (J$_2$), 5.73 Å (J$_3$) and 6.22 Å (J$_4$ and J$_5$). If we considered only the shortest paths J$_1$ and J$_2$, the magnetic structure would not be long-range ordered because some parts of the structure would be disconnected from the others along the c-axis. Therefore, we had to consider the three first paths J$_1$, J$_2$ and J$_3$ in order to obtain a 3D connectivity. We neglected the last two paths (J$_4$ and J$_5$), because of the large distance gap between them and J$_3$. The detailed geometrical characteristics of the J$_1$, J$_2$ and J$_3$ paths are reported in **Table IV.18** and are shown in **Figure IV.21**.

Table IV.18: Super-super-exchange paths of the orthorhombic structure of Li$_2$Ni^{II}(SO$_4$)$_2$ and their geometrical characteristics: distances Ni−O, O−O and O−Ni (expressed in Å), and angles Ni−O−O, O−O−Ni and dihedral angle Ni−O−O−Ni (expressed in °).

	Distances (Å)				Angles (°)		
	Ni−Ni	Ni−O	O−O	O−Ni	Ni−O−O	O−O−Ni	Ni−O−O−Ni
Exchange interaction J$_1$	4.5554						
Path 1		2.0429	2.4290	2.0694	108.28	105.60	89.02
Path 2		2.0694	2.4290	2.0429	105.60	108.28	89.02
Exchange interaction J$_2$	4.9401						
Path 1		2.0694	2.4092	2.0132	100.19	124.85	108.32
Path 2		2.0849	2.4525	2.0774	138.35	113.96	27.16
Exchange interaction J$_3$	5.7296						
Path 1		2.0849	2.3774	2.0509	153.84	135.25	3.18
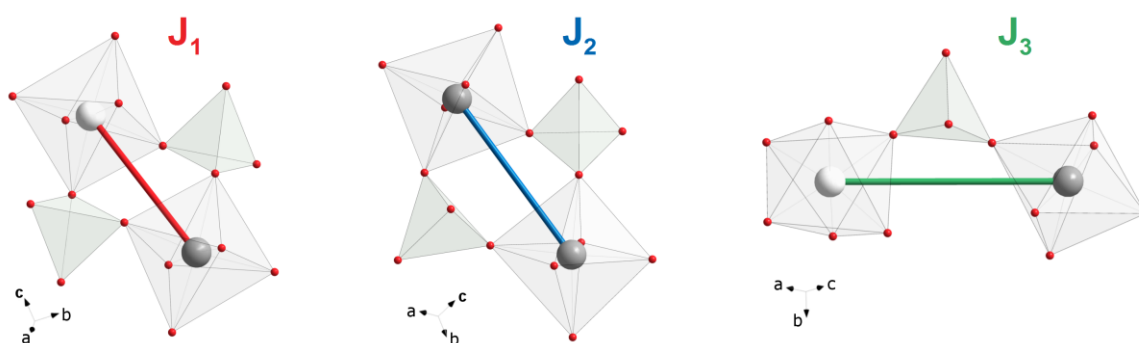
Figure IV.21: Geometrical characteristics of the three super-super-exchange paths J$_1$ (red segment), J$_2$ (blue segment) and J$_3$ (green segment). Grey and white balls represent the Ni atoms that carry a positive and a negative magnetic moment, respectively. Light grey octahedra and light green tetrahedra show the connectivity of the NiO$_6$ and SO$_4$ groups around these three super-super-exchange paths.

The connectivity of these three exchange paths is shown in **Figure IV.22**. Conversely to the case of the *marinite* structure, this figure reveals no triangular paths, suggesting that Li$_2$Ni(SO$_4$)$_2$ is not subject to geometrical frustration, in complete agreement with the frustration parameter value deduced from the susceptibility measurements (*f* = 1.6, see **Table IV.14** page 139).
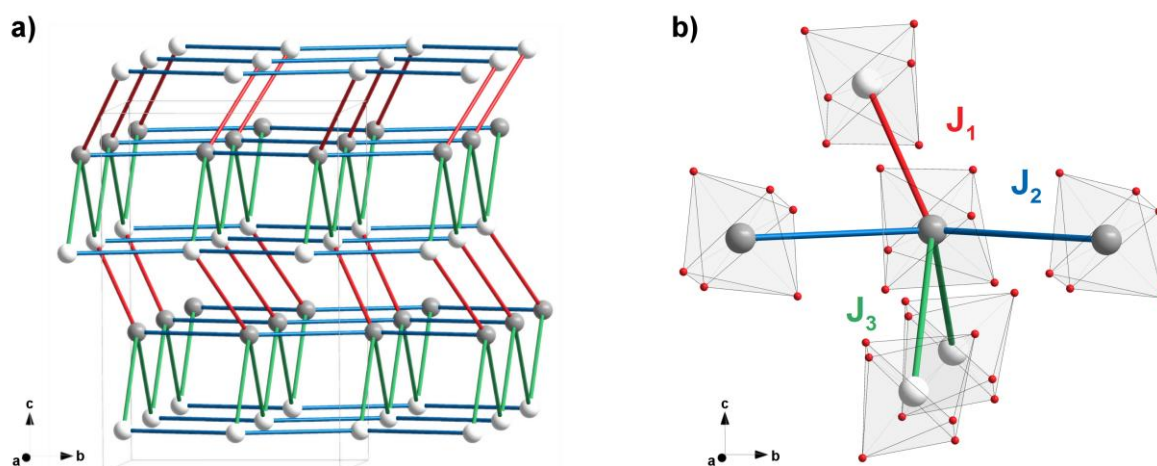
Figure IV.22: (a) Topology of the three super-super-exchange paths J$_1$ (red), J$_2$ (blue) and J$_3$ (green) connecting the nickel atoms in the Li$_2$Ni^{II}(SO$_4$)$_2$ structure. (b) Enlargement showing the distribution of the five super-super-exchange paths surrounding a Ni atom. Small red small are the oxygen atoms pertaining to the NiO$_6$ octahedra; other atoms are omitted.

To establish the relative signs and strengths of the three exchange integrals J$_1$, J$_2$ and J$_3$ required to produce the observed magnetic structure, we used the same procedure as employed for the *marinite* compounds and described in the first part of this chapter (see page 136). With the help of the ENERMAG program **[488]**, we calculated the ξ(**k**, J$_1$, J$_2$, J$_3$) matrices for different values of J$_1$, J$_2$ and J$_3$ varying between −100 and +100, and we kept for each given set of (J$_1$, J$_2$, J$_3$) values, the magnetic structure (*i.e.* the propagation vector + the spin sequence) corresponding to the lowest energy to built the phase diagram shown in **Figure IV.23**. This phase diagram displays eight regions delimited by the sign of the three exchange integrals J$_n$ (*n* = 1, 2, 3). Whatever the relative values of J$_1$, J$_2$ and J$_3$, the propagation vector **k =** (0, 0, 0) were found to give the lowest energy. Thus, the eight regions differs solely by the spin sequence of the eight magnetic moments.
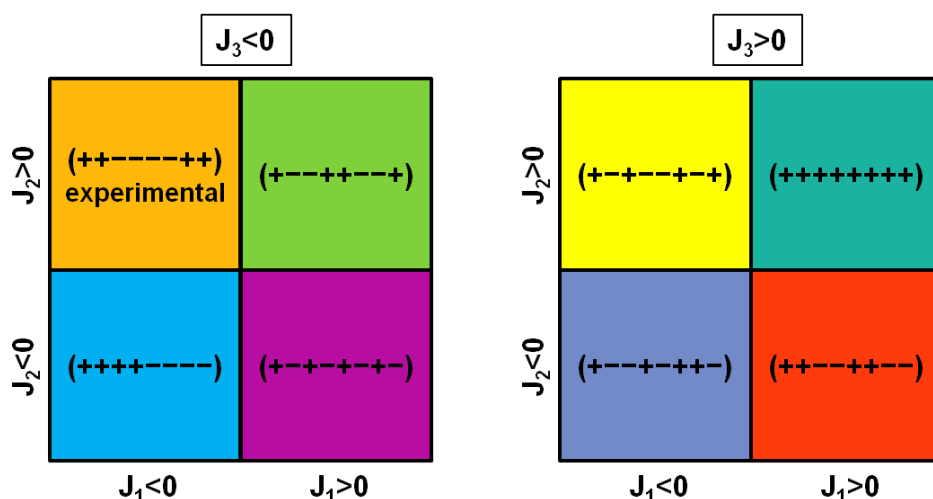
Figure IV.23: Phase diagram showing the influence of the sign of the super-super-exchange integrals J$_1$, J$_2$ and J$_3$ on the spin sequence of the ground-state magnetic structure of Li$_2$Ni^{II}(SO$_4$)$_2$. The domain corresponding to the experimental results is colored in orange.

The spin sequence (+ + − − − − + +) deduced experimentally is then observed as the ground state for J$_1$<0, J$_2$>0 and J$_3$<0 (orange region in **Figure IV.23**). As in the case of the *marinite* compounds, the negative sign of J$_3$ (i.e. antiferromagnetic interaction) is in good agreement with the Goodenough−Kanamori−Anderson rules **[459–464]**, given that the elongated geometry of this exchange pathway (see **Figure IV.21** and **Table IV.18**). However, having J$_1$ and J$_2$ of opposite signs was rather surprising at a first sight as these two exchange paths look similar from **Figure IV.21**: they both enlist a double exchange through two distinct SO$_4$ groups. Nevertheless, when observing carefully the angles between the bonds involved in the exchange interaction J$_2$ (see **Table IV.18**), one can remark that the two corresponding paths present indeed very different dihedral angles (108.32° *vs.* 27.16°), *i.e.* they are very distorted as compared with the paths J$_1$ and J$_3$. In any case, among the five interactions surrounding a Ni^{II+} atom in the orthorhombic structure of Li$_2$Ni(SO$_4$)$_2$ (see **Figure IV.22.b**), three of them are antiferromagnetic (J$_1$ and 2 x J$_3$) and two are ferromagnetic (2 x J$_2$). Here, it is interesting to mention that a similar situation had been observed in the nickel-based oxides PrNiO$_3$ and SmNiO$_3$, in which an equal number of ferromagnetic and antiferromagnetic interactions between the nearest Ni atoms was reported **[491–493]**. Note that although the nickel is formally in the oxidation state III+ in these latter compounds, the proximity of their 3d levels with the 2p levels of the oxygen induces ligan-hole effects, so that the ground state can also be seen as Ni^{II+}/O$^-$.

IV.4   Conclusion

In this chapter we have reported on the magnetic structures and properties of the four members of the *marinite* series Li$_x$M(SO$_4$)$_2$ (x = 1,2 and M = Fe, Co, Mn), as well as those of the orthorhombic phase Li$_2$Ni^{II}(SO$_4$)$_2$ **[442,484]**. A careful study of their magnetic properties revealed that these five compounds present a Curie-Weiss antiferromagnetism, with the Co^{II+}, Mn^{II+} and Fe^{III+}-based analogues presenting a weak ferromagnetism and Li$_2$Co^{II}(SO$_4$)$_2$ showing indications of a possible meta-magnetic behavior.

Moreover, the magnetic structures of these compounds have been determined from low-temperature neutron powder diffraction. Both the monoclinic *marinite* and the orthorhombic structures present particular arrangements of MO$_6$ octahedra and SO$_4$ tetrahedra that solely allows super-super-exchange interactions, so that these compounds can be seen as model cases to probe the Goodenough-Kanamori-Anderson rules **[459–464]**. First analyses of the sign and relative strength of exchange interactions for the five compounds showed no inconsistency with these semi-empirical rules. However they remind us the possibility of a coexistence of both negative (antiferromagnetic) and positive (ferromagnetic) super-super-exchange integrals to obtain the observed ground-state magnetic structures. Therefore, this study recalls that caution should be exercised when trying to predict the nature of the magnetic interactions within a structure by looking at the geometrical paths only.

Indeed, in the case of electrode materials, determining the experimental magnetic ground-state among the other possibilities offered by the nuclear structure of the compound is of high importance to make reliable voltage predictions using DFT calculations. The results provided in this chapter have indeed been already employed for preliminary theoretical investigations of the *marinites* phases Li$_2$M^{II}(SO$_4$)$_2$ (M = Fe, Co, Mn) and Li$_1$Fe^{III}(SO$_4$)$_2$, which provided good estimations of the open circuit voltages for these compounds **[439]**.

Finally, although magnetic ordering occurs at very low temperature (typically < 150 K) while electrochemical properties are generally tested at ambient temperature, both the strength of the magnetic exchange interactions between 3d metals and the positioning of their redox potentials in polyanionic compounds are in part nested in the iono-covalency of the M-O bonds. Thus, noticing that Li$_2$Fe^{II}(SO$_4$)$_2$ presented a very low Néel temperature (T$_N$ = 5 K) while this compound displayed in the meantime one of the highest redox potential (3.83 V *vs.* Li$^+$/Li^0) among the iron-based polyanionic electrode materials encouraged our group to relate magnetic parameters with redox potential values **[323,494]**. Indeed, the connection was straight: the better the covering between the 3d orbitals of the transition metal with the 2p orbitals of the oxygen, the more covalent the M-O bonds, the lower

the potential of the $M^{n+}/M^{(n-1)+}$ redox couple, but the highest the magnetic temperature ordering T$_N$ (*i.e.* facil magnetic ordering). This trend was verified for a series of several Fe(II+)-based polyanionic electrode materials, as seen in **Figure IV.24**, although more examples are still needed to fully demonstrate the validity of this correlation.
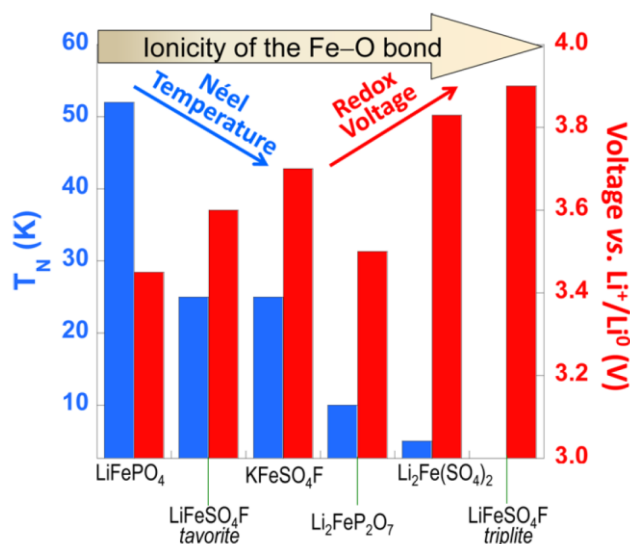
Figure IV.24: Correlation between antiferromagnetic Néel temperature (in blue) and redox voltage (in red) for various Fe^{II+}-containing sulfate and phosphate compounds, showing that T$_N$ decreases as the redox potential increases (from **[323]**).

In fact, relating structural features to magnetic properties has been a key topic over the last 50 years and physicists are still not able to elaborate tailor-made magnetic materials. Neither chemists can presently design electrode materials with the proper redox potential on demand. Nevertheless, we are fully convinced that bridging both the magnetism and the battery communities could provide supplementary clues in the search of the universal indicators that we are all looking for to correlate structures with magnetic and electrochemical properties.

General conclusion

This thesis work was aimed at searching for new positive electrode materials for Li- and Na-ion batteries made of sustainable, low-cost and environmentally benign elements and displaying high operating voltages. Guided by our previous work on iron fluorosulfates, which demonstrate attractive potentials of 3.6-3.9 V *vs.* Li$^+$/Li^0 **[318,320,321,325,331,335,345,495]**, but with the desire to avoid safety concerns associated with the use of fluorine, we decided to focus on sulfate-based compounds.

In the search for new materials, we noticed that the nature provides numerous examples of sulfate compounds phases among minerals. We rapidly realized the advantages of using mineral species as a source of inspiration because: *(i)* most of mineral compounds have been well characterized by mineralogists, and they constitute thus a precious database in which the chemists can spot structures displaying the best features for the targeted application, *(ii)* these natural phases are most probably thermodynamically stable (or at least metastable), and knowing the conditions of their formation in nature can provide a first approach for their syntheses in the laboratory, and *(iii)* once the model mineral compound chosen, the chemist can play with its composition or use structural considerations to modify the phase so as to obtain the desired physicochemical properties.

In the work presented herein, we have successfully employed this strategy to prepare several compounds Na$_2$$M$(SO$_4$)$_2$·4H$_2$O ($M$ = Mg, Zn, Ni, Co, Fe), which are all isostructural to the *bloedite* mineral, and from which we identified the iron phase to be electrochemically active *versus* both sodium and lithium **[363]**. More importantly, we showed that this new electrode material displays elevated potentials of 3.3 V *vs.* Na$^+$/Na^0 and 3.6 V *vs.* Li$^+$/Li^0, which compete with the ones reported for other sulfate-based electrode materials (*e.g.* NASICON Fe(SO$_4$)$_3$, *tavorite* LiFeSO$_4$F, layered LiFeSO$_4$OH, *maxwellite* NaFeSO$_4$F). Consequently, we prepared the dehydrated derivates α-Na$_2$$M$(SO$_4$)$_2$ (M = Fe, Co), for which we determined a monoclinic super-structure arising from a complex ordering of the SO$_4$ groups, and we equally obtained high potentials of 3.4 V *vs.* Na$^+$/Na^0 and 3.6 V *vs.* Li$^+$/Li^0 for the iron counterpart **[364]**. Finally, we also evaluated the redox potential of three other mineral phases, namely NaFe(SO$_4$)$_2$, KFe(SO$_4$)$_2$ and Na$_3$Fe(SO$_4$)$_3$, which although presenting limited reversible capacities, demonstrate as well Fe^{III+}/Fe^{II+} redox potentials centered around 3.5 V *vs.* Li$^+$/Li^0.

Next, in the search for lithium analogues to these compounds, we successfully synthesized the Li$_2$$M$(SO$_4$)$_2$ (M = Co, Fe) phases **[337,426,428]**. After having determined the monoclinic *marinite*

structure of these compounds, we established that the iron analogue displays an outstanding voltage of 3.83 V *vs.* Li^+/Li^0, which is in fact the highest potential ever reported for the Fe^{III+}/Fe^{II+} redox couple in an inorganic material free of fluorine, and is only matched by the *triplite* polymorph of $LiFeSO_4F$ (3.9 V *vs.* Li^+/Li^0). Besides these attractive electrochemical properties, we identified several other members of the $Li_2M(SO_4)_2$ series (*M* = Mn, Mg, Ni, Zn), which crystallize into two different structures (*i.e.* the aforementioned monoclinic *marinite* one and the orthorhombic structure previously reported for the nickel phase) **[442,484]**. Now a remaining question regards the existence of polymorphism as observed for the *tavorite* and *triplite* phases of $LiFeSO_4F$.

At this stage, we realized that these $Li_2M(SO_4)_2$ phases could also be of interest beyond the field of electrochemistry, and in particular for magnetic studies. Indeed, their peculiar structural frameworks of MO_6 octahedra and SO_4 tetrahedra solely allow super-super-exchange interactions, and these phases can thus serve as model compounds to test the Goodenough-Kanamori-Anderson rules for this kind of interactions. Therefore, we found from magnetic measurements that the five phases $Li_2Mn^{II+}(SO_4)_2$, $Li_1Fe^{III+}(SO_4)_2$, $Li_2Fe^{II+}(SO_4)_2$, $Li_2Co^{II+}(SO_4)_2$ and $Li_2Ni^{II+}(SO_4)_2$ show antiferromagnetic behavior at low temperatures (below 35 K), and we determined their magnetic structures at 2 K from neutron powder diffraction **[442,484]**. A first analysis of the super-super-exchange interactions within these structures was also provided.

Overall, in this thesis work, we have prepared several new alkali iron sulfates which present elevated redox potentials versus both lithium and sodium metal anodes. Therefore, we have demonstrated, as it was also achieved in the meantime with the layered hydroxysulfate $LiFeSO_4OH$ **[342]**, that the presence of fluorine in sulfate-based electrode materials is not necessary to reach high operating voltages. **Figure G.C.1** shows indeed that these new sulfate compounds, in particular $Li_2Fe(SO_4)_2$, rank at the top of the scale of potentials for the iron-based polyanionic materials studied up to now as positive electrodes for Li-ion and Na-ion batteries. However, this figure also illustrates well the main drawback of our bimetallic disulfates $A_xFe(SO_4)_2 \cdot nH_2O$ (*A* = Li, Na, *x* = 1, 2 and *n* = 0, 4), which is nested in their low intrinsic specific capacities (*i.e.* below 100 mAh/g) due to the fact that they contain two heavy sulfate groups per iron atom. Therefore, this reminds us that searching for new electrode materials does not systematically lead to compounds with outstanding performances in terms of both operating voltage and energy density.
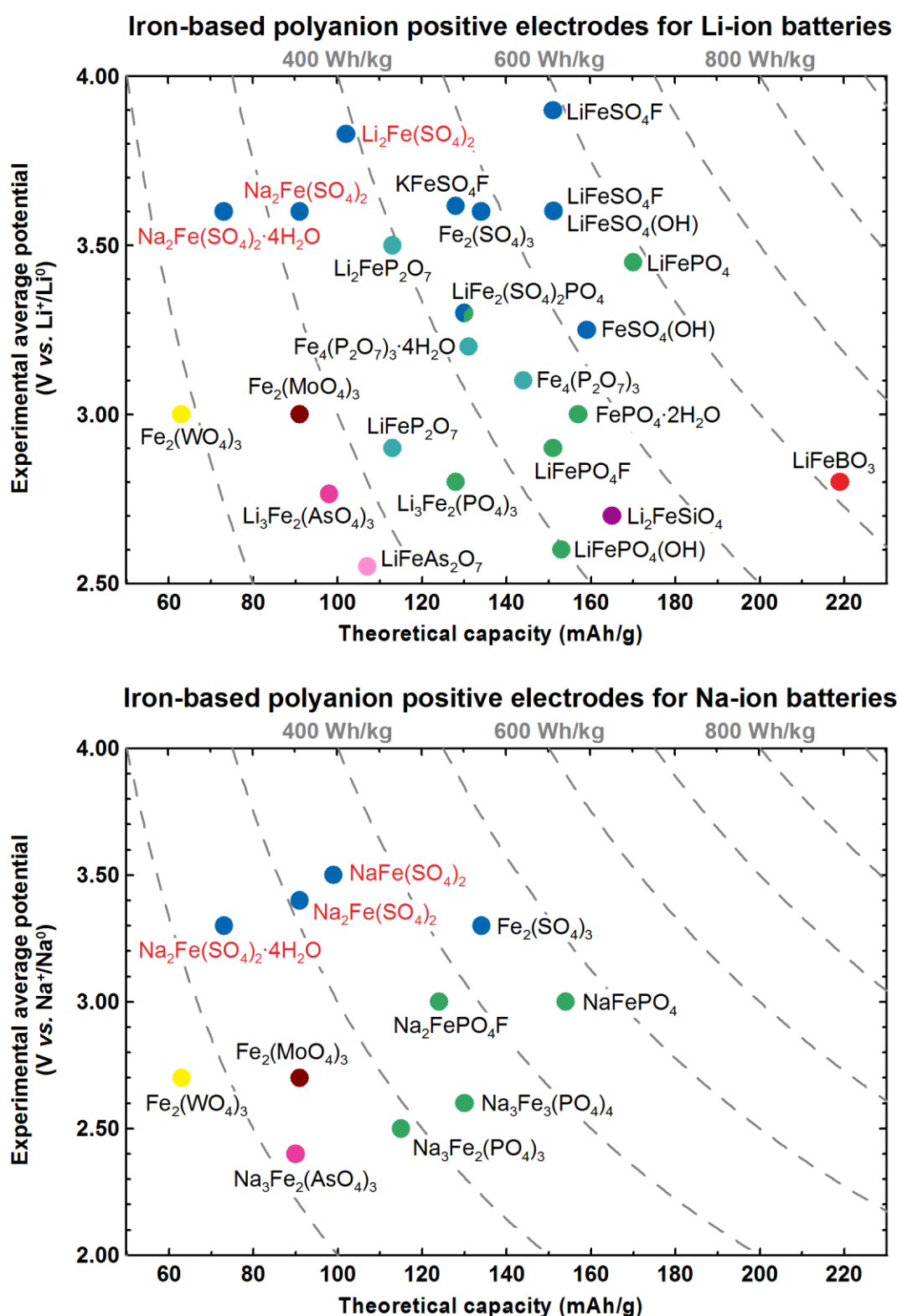
Figure G.C.1: Performances, in terms of operating voltage and theoretical specific capacity, of iron-based polyanion compounds studied as positive electrodes for Li-ion (top) and Na-ion (bottom) batteries (data from **[105]**). The different families of compounds are gathered in different colors: blue for sulfates, green for phosphates, cyan for pyrophosphates, red for borates, purple for silicates, pink for arseniates, brown for molybdates, yellow for tungstates. New electrodes materials which were presented in this work are labeled in red.

However, we believe that these new sulfate compounds are certainly valuable materials, in particular to enhance our basic understanding of the chemical and structural factors influencing the redox potentials of the polyanionic electrode materials. As we have started to discuss in Chapter I, the potential of the redox couple $M^{n+}/M^{(n+1)+}$ in an inorganic compound is highly related to the iono-covalency of the M–O bond. The difference observed in the voltage of a given redox couple between oxides and polyanionic compounds is explained by the strong covalent bonding within the polyanionic units (*i.e.* the X-O bond), which weakens the M–O bond and stabilizes the anti-bonding orbitals of the redox center **[222,232,233]**. This inductive effect has been widely described since the early works of Goodenough on NASICON compounds **[222,232,233,496]**. It is a strong indicator, which justifies well the overall general trends in voltage differences between the polyanionic compounds: sulfates present higher redox potentials than phosphates, which usually have enhanced potential as compared with silicates, borates or arsenates (**Figure G.C.1**). However, a closer inspection of this figure reveals that these general rules have their own limitations as they cannot be applied blindly to any compounds. In fact the inductive effect applies well when comparing compounds having the same structure (*e.g.* potential variations within the NASICON compounds, the *tavorite* structure, *etc.*), but it becomes less efficient to account for differencies observed between compounds having different structures, in particular when having the same polyanion **[234]**, and completely fails in comparing two polymorphs having the same exact composition (*e.g. tavorite vs. triplite* LiFeSO$_4$F). This clearly shows that other structural factors play an important role in tuning the redox potentials.

Besides the iono-covalent character of the M-O bonding, the crystal field experienced by the cation M^{n+} would also affect the energy positioning of its anti-bonding orbitals **[349,350]**. Indeed, the presence of various cations surrounding the redox center (*i.e.* other transition metals M^{n+}, the cations X^{x+} of the polyanionic groups, but also the alkali cation A^+) and more importantly the connectivity of the redox center polyhedron with the neighboring polyhedra MO_6, XO_4 and AO_z (*i.e.* corner-, edge- or face-sharing) will influence the strength of the Madelung electric field felt by the cation. Hence, shorter distances M–M, M–X or M–A (*e.g.* due to edge- or face-sharing polyhedra) result in more cationic repulsions and lower Madelung electric field, which in turn yields in a higher redox potential **[349,350]**.

At this stage, the difficulty resides in the fact that all these parameters (*i.e.* ionocovalency, Madelung electric field, inductive effect, electronegativity, interatomic distances, *etc.*) are highly correlated. Researchers are still actively seeking to identify new descriptors (*e.g. M*–O bond lengths, number of polyanion per transition metal, number of coordination, density) to rationalize the potential differences experimentally observed between different polyanionic electrode materials

[115,234,323,349,350]. In our quest for such indicators, our group has recently proposed to correlate redox potentials of the electrode materials with their magnetic ordering temperature T_N **[323,494]**, since these two properties are partly nested in the iono-covalency of the M–O bonds; $Li_2Fe(SO_4)_2$ illustrates well this trend, displaying both a very low Néel temperature ($T_N = 5$ K) and one of the highest redox potentials (3.83 V *vs.* Li^+/Li^0) observed in Fe(II+)-based polyanionic compounds.

However, there is not presently an ideal framework that permits the evaluation of each parameter influencing redox potential. In analogy to French grammar, when a new indicator that describes well the voltage trend in a series of model compounds is identified, one often faces one or two exceptions that rapidly limit the universality of the rule. Nonetheless, the search for new polyanion-based electrode materials is a pursuit of great importance; even if new compounds fail to compete performance-wise with today's electrode materials, they expand the database available for identifying relevant indicators, as this thesis work has demonstrated with *marinite* $Li_2Fe(SO_4)_2$. This is essential for better understanding the existing relationships, if any, between composition, structure and redox potential, which will facilitate the design of high-performance polyanionic cathode materials for the next generations of batteries.

Annexes

A.1   Samples preparation

A.1.1   Quartz tubes sealed under vacuum

Ceramic syntheses of samples containing divalent iron require to work under inert or reducing conditions in order to prevent the oxidation of the Fe(II+) into Fe(III+). One solution is to seal under vaccum a pelletized powder sample into a quart tube **[426]**. To do so, the powder reactants are first thouroughly mixed together (usually by ball-milling), and then pressed into a pellet with an unixial press at 10 tons for one minute. The pellet is then introduced into a quartz tube, which is pumped under primary vacuum (~10^{-2} bar) for 20 minutes. While maintaining a dynamical vacuum, the quartz tube is melted using an oxygen/butane torch to close the tube under vacuum. The pellet inside the tube under vacuum can then be annealed in any furnace.

A.1.2   SPS

Spark Plasma Sintering (SPS), also named Flash Sintering, is a synthesis route, in which a high pressure and an electric current are concurrently applied to a powder sample so that the rate and mass transfer is significantly increased to allow rapid diffusion of atoms **[497,498]**. Compared with classical ceramic or hot pressing approaches, SPS has the advantage of providing heating in a quick and homogeneous way in order to significantly reduce the reaction time.
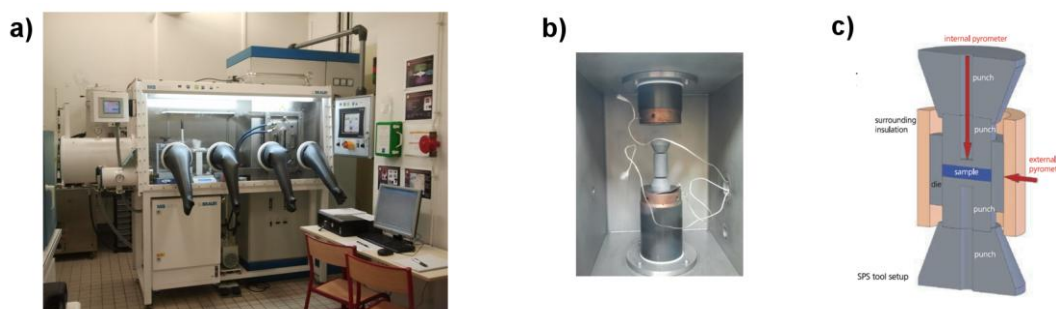
Figure A.1: (a) SPS machine connected to the argon-filled glove box. (b) Carbon matrix containing the powder sample, and placed in the SPS machine. (c) Drawing of the synthesis principle.

$Li_2M(SO_4)_2$ (M = Co, Fe) could also synthesized *via* Spark Plasma Sintering with an *HPD 10 FCT* SPS machine connected to an argon dry box (**Figure A.1**) **[337]**. This apparatus was handled by Sylvain Boulineau (Laboratoire de Réactivité et de Chimie des Solides – LRCS, CNRS UMR 7314, UPJV, Amiens, France). For these syntheses, a powder mixture of Li_2SO_4 and MSO_4, previously ball-milled under argon for 45 minutes, was placed between two carbon paper disks (*Papyex®*) and introduced

in a 10-mm inner-diameter carbon matrix (*Mersen 2333®*). The powder was then pressed into the carbon matrix at 50 MPa and annealed under vacuum of under argon at 320°C (heating ramp: 75°C/min, *via* a sequence of 1 pulse of 1 ms of DC polarization) for 15 minutes in the SPS machine.

A.1.3   Mechanical-milling

Mechanical-milling (or ball-milling) enable is an energetic milling, which was used to thouroughly mix powder reactants for a synthesis, or a pristine material with carbon for electrode preparation. Note that this milling also induces a reduction of the particle size.

To do so, the powders to be mixed were introduced with a stainless steal ball (of 7 g or 4 g) into cylindrical cells (inner volume of 40 cm^3 for reactant mixing or 10 cm^3 for electrode preparation). The mechanical-milling were carried out using a *SPEX 8000®* miller for 15 to 60 minutes. During this process, the cell is moved with a complex movement in the three directions at a high rotation speed of 1400 rpm. For samples containing Fe(II+), which is prone to be oxidized during the milling due to the high temperature that can be generated locally, special care was taken in closing the ball-milling cell under argon, and divide the milling time into 15-min milling steps separated by at least 10-min pauses into order to prevent overheating of the cell.

A.2   Electrochemical characterizations

To characterize the electrochemical properties of our materials, all electrochemical tests were performed in *half cells*, which consist in using a single electrode material (the material to test) as the working electrode (WE) and pure lithium or sodium metal as the counter electrode (CE), which is also used as the reference electrode (RE) since its potential does not change during the charge/discharge cycles (Li^+/Li^0: –3.045 V *vs.* SHE and Na^+/Na^0: –2.714 V *vs.* SHE) and can then be set to be zero.

A.2.1   Electrode preparation

As discussed in Chapter I, polyanionic compounds present low electronic conductivities, which constitute an important limitant factor for their electrochemical activity. To enhance the electronic conductivity of a material for priliminary evaluation of its electrochemical performances, the particles of the pristine compound can be reduced in size and mixed with a conductive additive using mechanical milling (*cf.* § A.1.3 Mechanical-milling, page 158). In our case, we usually ball-milled for (unless otherwise specified) 20 minutes the pristine materials with carbon Super P (also named carbon SP), taken in a mass ratio 80:20 or 70:30, in a 10-cm^3 ball-milling cell closed under argon.

A.2.2 Electrochemical cells

A.2.2.1 Swagelok cells

Most of the electrochemical tests *versus* lithium (or sodium) were carried out in Swagelok®-type cells (**Figure A.2**). The cells were assembled in an argon-filled glove box, using the as-prepared working electrode materials as the positive electrodes and lithium (or sodium) metal disc as the negative electrodes. These two electrodes were separated by two *Whatman® GF/D* borosilicate glass fibre sheets saturated with an electrolyte of (unless otherwise specified) 1M $LiClO_4$ (or $NaClO_4$) in propylene carbonate (PC). Usual cathode loading was 9-13 mg.cm^{-2} per cell.

1. Current collectors
2. Stainless steel disc
3. Lithium or sodium metal anode
4. Separator
5. Positive electrode
6. Spring
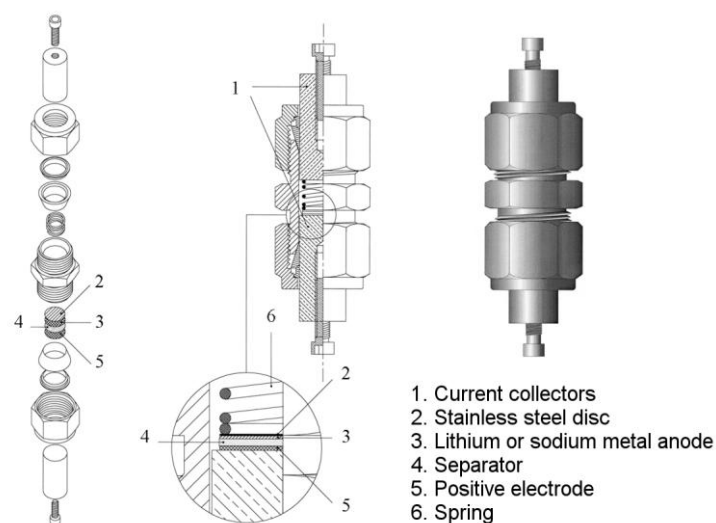
Figure A.2: Technical drawing of a Sawgelok® cell.

A.2.2.2 Special cell for in operando experiments

For *in operando* experiments, we used a special cell (**Figure A.3**) designed in house by Jean-Bernard Leriche (Laboratoire de Réactivité et de Chimie des Solides – LRCS, CNRS UMR 7314, UPJV, Amiens, France). Its special shape is adapted to the sample holder of the *Bruker D8* diffractometers (*cf.* § A.3.1 Laboratory XRD measurements, page 162). It is equipped beryllium window, which is almost transparent to X-ray and also acts as a current collector, and on which is desposited the electrode material to be studied **[499,500]**. In our case, a thin sheet of aluminum foil (thckiness: 3 µm, from *Goodfellow*) was placed between the beryllium window and the positive electrode material to prevent the oxidation of the beryllium during the high-voltage stage. The rest of the cell was assembled as usual (cathode material // separator + electrolyte // anode material) in an argon-filled glove-box. Note that Be and Al give diffraction peaks at (λ_{Co}) 2θ = 53.8° and 59.9°, and 2θ = 45.2°, respectively.

This special cell being bigger than the Swagelok® cells, is was also used to prepare larger quantity of cycled electrode materials for *ex situ* experiments. In this case, the beryllium window was replaced by a stainless steel current collector, and the cathode loading was up to 30 mg per cell (*i.e.* still 9-13 mg.cm^{-2}).
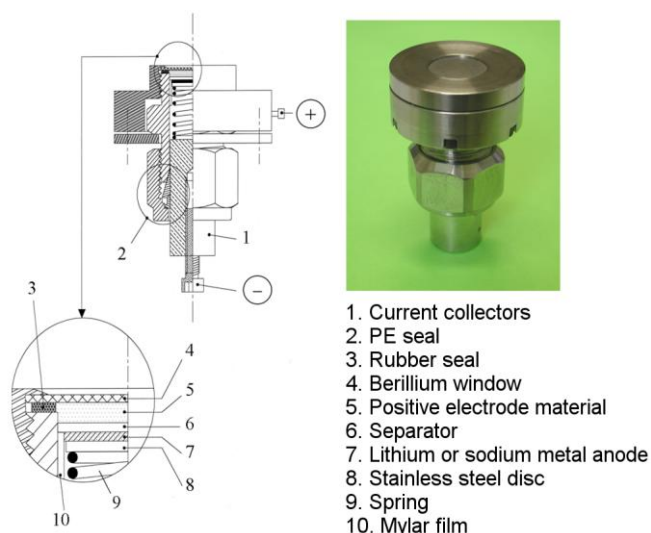
Figure A.3: Technical drawing and picture of the special cell designed at the LRCS for *in operando* XRD experiments.

A.2.3 Electrochemical cycling tests

Electrochemical tests were conducted at 20°C using a *Mac-Pile* system (BioLogic S.A.) or more occasionally a *VMP3* unit (BioLogic S.A.). Unless otherwise specified, the cells were typically cycled between 3.2 and 4.5 V *vs.* Li$^+$/Li^0 (or between 2.5 and 4.2 V *vs.* Na$^+$/Na^0) at a rate of 1 Li$^+$ (Na$^+$) exchanged per 20 hours (noted C/20).

A.2.3.1 Galvanostatic tests

Most of the electrochemical tests presented in this thesis were performed in galvanostatic mode, *i.e.* by imposing a constant current density to the cell and following the evolution of the cell voltage, which is recorded regularly. The charge (or discharge) rate is generally given using the nomenclature C/n, which means that the intensity of the current is imposed so that the complete charge (or discharge) is reached in n hours. Note that, in this thesis, a complete charge (or discharge) corresponds to the removal (or uptake) of 1 Li$^+$ or 1 Na$^+$ per transition metal.

These galvanostatic measurements enable to trace the voltage-composition curves V = f(x) presented throughout the thesis. These curves provide first information on the charge/discharge mechanism, as they generally present either a S-shape for a single-phase (solid solution) process or a plateau (L-shape) for a two-phase mechanism. Moreover, calculating the derivative -δx/δV of the voltage-composition traces and plotting the curves -δx/δV = f(V) (*i.e.* ~simulation of a cyclic

voltammetry) often enable to determine more precisely the average working potential of the electrode material.

A.2.3.2 Galvanostatic Intermittent Titration Technique (GITT) tests

When cycling a cell in a classical galvanostatic mode, the system is generally not at equilibrium, and there is thus a shift of the experimental potential as compared to the theoretical one. This polarization is usually dependent of the charge/discharge rate. Indeed to reach the potential at the thermodynamical equilibrium, the system must be maintained in open circuit for an extended period of time.

The principle of these GITT measurements consist in alternating short times of galvanostatic charge/discharge and longer stages of open circuit voltage relaxation (no current), so that to obtain a curve whose values at the end of the open circuit periods is close to the thermodynamic potential **[501]**. For this work, GITT tests have been performed at room temperature with a charge/discharge rate equivalent to C/20 for steps of 30 minutes alternated with open circuit stages of 15 hours.

A.2.3.3 Potentiostatic Titration Technique (PITT) tests

A PITT experiment consists in increasing the potential applied to the cell by small steps of a few mV and following the evolution of the current response until it reaches a limit value (i_{lim}) **[502]**. Such an experiment provides some information about the charge/discharge mechanism. Indeed in the case of a single-phase process, the kinetics of Li^+ de/intercalation is controlled by the diffusion of the ions through the host compound and the current variations are governed by a Cottrell equation ($i \propto \sqrt{1/t}$); on the other hand, for a two-phase mechanism, there are two cases: either the limitant step is the kinetics of phase transformation or the ionic or electronic diffusion within one of the two phases, so that the current decays does not necessarily follow a Cottrel equation.

For the PITT experiements presented in this thesis, the voltage was incremented by 10 mV between 2.5 and 4.5 V, letting the current decay until a limit corresponding to a fixed rate of C/100.

A.3   Structural characterizations

A.3.1   Laboratory XRD measurements

Laboratory X-ray diffraction (XRD) was used for this thesis work as a routine characterization method for verifying the purity of the samples. High-quality laboratory X-ray patterns were also acquired on the best samples in order to perform Rietveld refinement of the structural models proposed in the literature, or to determine the structure of novel phases.

A.3.1.1   Facilities

Three different XRD diffractometers were used to record the laboratory XRD patterns presented in this thesis:

- a *Bruker D8* diffractometer equipped with a Vantec detector and a Co-Kα source ($\lambda_{K\alpha1}$ = 1.78897 Å, $\lambda_{K\alpha2}$ = 1.79285 Å), operating at 40 kV and 40 mA, in reflection mode with a θ/θ Bragg-Brentano geometry,

- a *Bruker D8* diffractometer equipped with a LynxEye detector and a Cu-Kα source ($\lambda_{K\alpha1}$ = 1,54056 Å et $\lambda_{K\alpha2}$ = 1.54439 Å), operating at 40 kV and 40 mA, in reflection mode with a θ/θ Bragg-Brentano geometry,

- a *Bruker D4 ENDEAVOR* diffractometer equipped with a LynxEye detector and a Cu-Kα source ($\lambda_{K\alpha1}$ = 1,54056 Å et $\lambda_{K\alpha2}$ = 1.54439 Å), operating at 40 kV and 40 mA, in reflection mode with a θ/2θ Bragg-Brentano geometry,

A.3.1.2   Air sensitive samples

To record XRD patterns of the air sensitive samples, the sample was prepared in an argon-filled glove-box and closed either in a special sample "dome" holder or below the X-ray transparent beryllium window of the electrochemical cell originally designed for *in operando* experiments and described above (see § A.2.2.2 page 159).

A.3.1.3   In operando *XRD experiments*

For *in operando* experiments, we used the special electrochemical cell equipped with a X-ray transparent beryllium window described above (see § A.2.2.2 page 159). The cell was placed in the *Bruker D8* diffractometer (λ_{Co}) in place of the standard sample holder, and connected to a MacPile unit to control the electrochemical experiment. XRD patterns were continuously recorded in the range 10 ≤ 2θ ≤ 50° (approximately two-hour scans) while performing a classical galvanostatic cycling of the cell at a C/40 rate.

A.3.1.4 High-temperature XRD measurements

Temperature-controlled XRD experiments were carried out with the *Bruker D8* diffractometer having the Co source (see above), which was equipped with an *Anton Paar HTK1200* furnace chamber (**Figure A.4**). For these experiments, the powder samples were placed on an alumina sample holder, and heated under air or under nitrogen flow, from room temperature and up to 600°C with a ramp of 12°C/min. A delay of five minutes was observed before recording each pattern in the range $10 \leq 2\theta \leq 50°$ for approximately one hour at constant temperature.
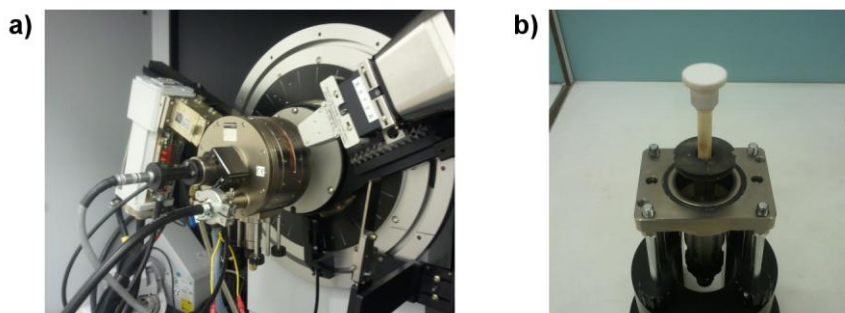
Figure A.4: (a) *Anton Paar HTK1200* furnace chamber monted on the the *Bruker D8* diffractometer. (b) Alumina sample holder for high-temperature XRD experiments.

A.3.2 Synchrotron XRD measurements

Additional high-resolution Synchrotron X-ray powder diffraction data were also recorded for some samples in order to confirm or determine their structural models.

A.3.2.1 11-BM mail-in service of the Advanced Photon Source at Argonne National Laboratory

Samples of $Li_xM(SO_4)_2$ (x = 1, 2 and M = Co, Fe) were measured with Synchrotron X-ray radiation (wavelengths of λ = 0.4131 Å or λ = 0.4139 Å) through the mail-in service of the 11-BM beamline of the Advanced Photon Source (APS) at Argonne National Laboratory (ANL, Argonne, USA). For these measurements, the samples $Li_2M(SO_4)_2$ (M = Co, Fe) were sealed under argon in 0.7-mm diameter quartz capillaries, the latter being fitted in the kapton tube of the sample bases provided by the 11-BM mail-in service. In the case of $Li_1Fe(SO_4)_2$, the sample was directly filled into the kapton tube of the sample base and sealed with a drop of epoxy glue in an argon-filled glove-box.
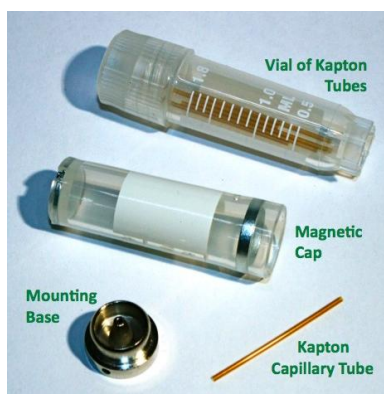
Figure A.5: Sample base kit of the 11-BM mail-in service.

A.3.2.2 CRISTAL beamline at SOLEIL Synchrotron

For the $Na_2M(SO_4)_2 \cdot nH_2O$ (M = Co, Zn and n = 4, 0) compounds, temperature-controlled high-resolution Synchrotron X-ray diffraction was performed on the 2-circle diffractometer of the CRISTAL beamline at SOLEIL Synchrotron (Saint-Aubin, France), with a wavelength of λ = 0.6681 Å. $Na_2M(SO_4)_2 \cdot 4H_2O$ (M = Co, Zn) powder samples were filled in 0.7-mm diameter quartz capillaries, which were let open at one end in order to permit the departure of water. After having acquired a pattern of hydrated compound at room temperature, the formation of the corresponding dehydrated phase $Na_2M(SO_4)_2$ was followed by recording X-ray patterns while heating the capillary using a Cyberstar hot-gas blower.

These measurements were performed with the assistance of Erik Elkaim, who is kindly acknowledged.
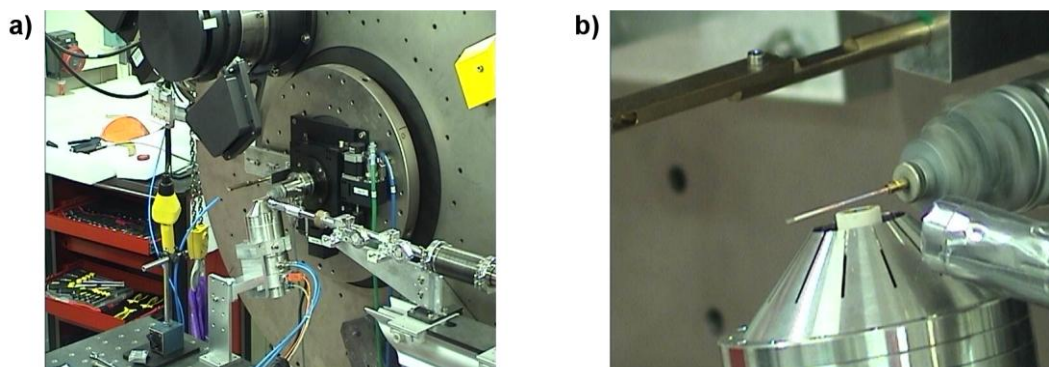
Figure A.6: (a) Large view of the 2-circle diffractometer of the CRISTAL beamline, with the gas blower installed for high-temperature experiments. (b) Enlargement on the sample capillary during the high-temperature experiment performed on the $Na_2Co(SO_4) \cdot 4H_2O$ sample. Note the difference in the color of the sample between the extremities of the capillary (pink: $Na_2Co(SO_4) \cdot 4H_2O$) and the middle of the capillary above the gas blower (purple: dehydrated phase $Na_2Co(SO_4)_2$).

A.3.3 Neutron powder diffraction

Neutron diffraction is a complementary technique to X-ray diffraction, since the former enables to localize light elements (in our case the lithium atoms) which are barely visible with the latter. This is due to the fact that X-rays interfere with electrons, and are thus more scattered by heavier atoms. Conversely, neutrons interfere with nuclei.

Moreover when a compound presents antiferromagnetic interactions, neutron powder diffraction enables to determine the long range ordering of the magnetic moments. The spatial orientation and the magnitude of the magnetic moments carried by the transition metals can indeed be unambiguously determined.

In both cases, a large quantity of powder sample is necessary for NPD experiments as compared to XRD experiments (*i.e.* about one gram for the former *vs.* few milligrams for the latter).

For this thesis work, Neutron Powder Diffraction (NPD) has been performed with the assistance of Thomas Hansen on the two diffractometers D2B and D20 at the Institut Laue Langevin (ILL, Grenoble, France). Both diffractometers are in Debye-Scherrer geometry. Powder samples were filled into vanadium cylindrical sample holders (vanadium is transparent to neutrons).

A.3.3.1 *D2B diffractometer at ILL*

The high resolution D2B diffractometer was used to recorded NPD patterns at room temperature with a wavelength of $\lambda = 1.594$ Å, in order to precisely refine the nuclear structures. It was in particular employed to localize the lithium into the $Li_1Fe(SO_4)_2$ phase, and also to confirm the super-structure of the $\alpha\text{-}Na_2Co(SO_4)_2$ phase thanks to better contrast between the atoms obtained with neutrons.

A.3.3.2 *D20 diffractometer at ILL*

The high-intensity D20 diffractometer was mainly used for the determination of magnetic structures. For these measurements, the sample holder was placed in a helium cryostat, which enables to reach temperatures as low as 1.8 K. NPD patterns were acquired in two different configurations: *(i)* either in high-flux mode with a wavelength of $\lambda = 2.418$ Å, *(ii)* or in high-resolution mode with two different wavelengths $\lambda = 1.543$ Å and $\lambda = 2.416$ Å. In the second case, patterns recorded with the first wavelength on a wide 2θ angle range were used to refine the nuclear structures at low temperature, while patterns obtained with the large second wavelength were of good resolution at low 2θ angles and were used to determine the magnetic structure of the compounds.

A.3.4 Diffraction data treatment

A.3.4.1 Refinement of the structures from XRD and NPD patterns

Crystal structures were refined against our experimental XRD and NPD patterns using the Rietveld method [385], as implemented in the FullProf suite of software [383,384].

Results of these refinements are presented in different tables within this thesis. All the values are given with standard deviations corresponding to 3 sigmas (*i.e.* three times the value reported in the output file of FullProf).

In most cases, a bond valence sum (BVS) analysis was also performed during the Rieveld refinement, using the b_0 parameters from Brown and Altermatt [402].

A.3.4.2 Crystal structure determination

Powder patterns were indexed using the *Dicvol* program [429,430], which is distributed with the *FullProf* suite software [383,384]. From the angular positions of the main diffraction peaks observed in the XRD powder pattern, this program proposes one or several solutions of crystalline systems and unit cell parameters that could index the pattern. Each proposition is associated with two figures of merit (M_N and F_N) which account for its validity. The XRD pattern is then refined using the Le Bail method (Profile Matching) with the FullProf program in order to determine more precisely the unit cell parameters.

The structure determinations were then carried out with both the *EXPO* software, using the direct method [433–435], and the *FOX* program [432,431], using global optimization (*ab initio* calculations). The as-determined cristal structures were then refined using the Rietveld method [385], as implemented in the FullProf suite of software [383,384].

A.3.4.3 Magnetic structure determination

Magnetic structures were determined from a symmetry analysis, using the method of Bertaut [487] as implemented in the BasIreps program of the FullProf suite of software [383,384]. This analysis enable to impose constraints to the magnetic moment carried by each magnetic atoms in the unit cell according to the symmetry of the unit cell, and permit to reduce the number of possible magnetic configurations, as some of them are forbidden by symmetry.

A.3.4.4 Visualisation, drawing and analyses of the structures

The structures were standardized using the *STRUCTURE TIDY* program [436]. They were drawn and examined with the help of three programs: *(i)* the *FullProf Studio* program of the *FullProf* suite [383,384], *(ii)* the *VESTA* visualization program [503] and *(iii)* the *DIAMOND* software.

Data of the structures that were not determined from our diffraction data were obtained from the ICSD database.

A.4   Other physical-chemical characterizations

A.4.1 ^{57}Fe Mössbauer Spectrosocopy

The ^{57}Fe Mössbauer Spectrosocopy is a nuclear resonant technique, which permit to obtain information about the oxidation state of the iron, the symmetry of its environment and its magnetic properties, if any, in the material studied **[504]**. It implies transitions between the nuclear ground state of the ^{57}Fe and its first nuclear excited states, which are the consequences of the absorption of a photon.

If the material does not present magnetic interactions (which is the cases of the materials studied at room temperature in this thesis), the Mössbauer spectrum of a nucleus of ^{57}Fe is generally a doublet, as seen in **Figure A.7**. The difference between the two maxima of the doublet is named *quadrupole splitting* (noted ΔEq), while their barycentre with respect to the origin of the velocities is named *isomeric shift* (noted δ). These two hyperfine parameters are influenced by the electric field generated by the electrons of the iron atoms and the ones of the neighboring atoms. Thus the Mössbauer doublet of an iron in the oxidation state II+ typically presents an isomer shift around 1.0 mm/s and a quadripole splitting ranging from 0.2 to 3.5 mm/s, while the doublet of an iron III+ has an isomer shift close to 0.3-0.4 mm/s and a quadripole splitting smaller than 2 mm/s **[505]**.
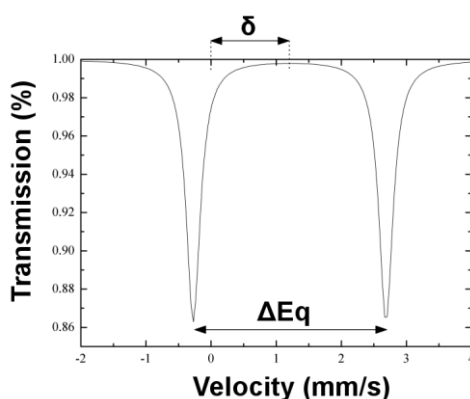
Figure A.7: Schematic Mössbauer spectra showing the isomer shift (δ) and the quadripole splitting (ΔEq) of a typical doublet of Fe(II+).

For this thesis, Mössbauer experiments were performed at the Institut Charles Gerhadt (UMR 5253, Université de Montpellier 2, Montpellier, France) in close collaboration with Dr. Moulay Tahar Sougrati. ^{57}Fe Mössbauer spectra were recorded in transmission geometry (**Figure A.8**) in constant acceleration mode and with a ^{57}Co(Rh) source with normal activity of 925 MBq. The velocity scale

($\pm$ 4 mm/s^{-1}) was calibrated at room temperature with a α-Fe foil. The absorbers were typically prepared from 20 to 50 mg of powder samples (**Figure A.8**). For *in operando* experiments, we used a special cell similar to the one designed for *in operando* experiments, but having two beryllium windows: one at the positive and one at the negative electrodes.

The hyperfine parameters δ (isomer shift, giving with respect to that of α-Fe) and ΔE_q (quadrupole splitting) were determined by fitting Lorentzian lines to the experimental data using *MOSFIT* program and were then refined using the program *FullHam* of Dr. R. P. Hermann.
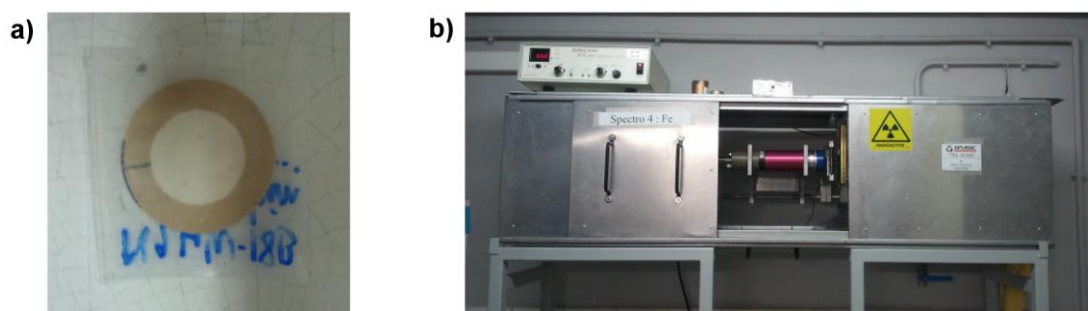
Figure A.8: (a) Iron-base sample prepared in a 1-cm diameter absorber probe scealed under argon for Mössbauer spectroscopy measurement. (b) In-house built Mössbauer spectrometer at the AIME laboratory (Montpellier, France).

A.4.2 ^{7}Li solid-state NMR

^{7}Li solid-state Nuclear Magnetic Resonance (NMR) was used to probe the local environment of the lithium within the $Li_2Fe(SO_4)_2$ samples. These experiments were carried out by Dr. Robert Messinger at the Laboratory "Conditions Extrêmes et Matériaux: Haute Température et Irradiation" (CEMHTI, Site Haute Température, CNRS UPR 3079, Orléans, France).

All spectra were acquired on a 300 MHz *Bruker AVANCE II 300 NMR* spectrometer with a 7.05 Tesla wide-bore superconducting magnet operating at 116.6 MHz for ^{7}Li nuclei. Measurements were conducted with a *Bruker* 1.3-mm magic-angle-spinning (MAS) probehead, where samples were rotated in zirconia rotors at ultra-fast MAS rates of 62.5 kHz with pure N_2 gas at ambient temperature. ^{7}Li spin-echo MAS spectra were acquired with half-echo delays (τ/2) of one rotor period (16 μs), and with a recycle delay of 100 ms (so that all paramagnetic and diamagnetic ^{7}Li species have fully relaxed). ^{7}Li shifts were referenced to a 1 M aqueous solution of LiCl.

2D ^{7}Li{^{7}Li} EXSY (EXchange SpectroscopY) experiments were performed with a micing time of 1 ms and were spin-echo detected with half-echo delays of one rotor period.

A.4.3 Thermal analyses

Thermal analyses enable to follow the physical and chemical changes of a material with the temperature. ThermoGravimetric Analyses (TGA) detect mass variations (mass loss or mass gain) while heating the sample in a given atmosphere (*e.g.* inert gas, air, reducing conditions). Their can be coupled to Mass Spectroscopy (MS), in order to analyse the gas associated with a mass loss. Differential Scanning Calorimetry (DSC) enable to observe changes of state, phase transitions and chemical reactions by measuring the difference in the amount of heat required to increase the temperature of the sample as compared to a reference.

In our case, these experiments were performed by Matthieu Courty (Laboratoire de Réactivité et de Chimie des Solides – LRCS, CNRS UMR 7314, UPJV, Amiens, France) Unless otherwise specified, TGA-MS analyses were carried out on ~20 mg of powder samples placed in an alumina or a platinum crucible, in the temperature range 20-800°C (heating rate: 10°C/min) under argon flow (50 cm^3/min) using a *STA-449C Jupiter* unit (*Netzsch*) coupled to a quadrupole mass spectrometer *QMS 403 Aëlos* equipped with a stainless-steel capillary and a secondary-electron multiplier detector (*Channeltron*). DSC measurements were performed under the same conditions using a *204F1 Netzsch* unit, with the samples sealed in aluminium crucibles.

A.4.4 Elemental analyses using atomic absorption spectroscopy

Atomic absorption spectroscopy was used to quantify alkali to transition metals ratio in the samples. These measurements were performed on a *Perkin Elmer AAnalyst 300* spectrometer equipped with a 10-cm single slot burner head for a C_2H_2-air combustion flame. Samples were solubilized in water to get solutions at around 2 ppm in metal to be titrated. Solutions were continuously aspirated through a mounted stainless steel nebulizer that was mounted to a plastic coated mixing chamber with an end cap with a drain interlock assembly. Gas flow rates recommended by a spectrometer manufacturer were used to maintain oxidizing flame conditions. The smallest slit widths were selected to lessen any spectral interferences.

A.4.5 Electronic microscopy and elemental analyses

SEM images were recorded on a *FEI Quanta 200F* Scanning Electron Microscope operating at 20 kV. Elemental analyses were performed with an EDAX EDS (X-ray Energy Dispersive Spectroscopy) in order to check the sulfur to transition metals ratio of the samples; these measurements were repeated on at least 10 different spots, on different particules of the samples.

Transmission Electron Microscopy (TEM) on the $Li_2M(SO_4)_2$ samples was performed by Pr. Loic Dupont (Laboratoire de Réactivité et de Chimie des Solides – LRCS, CNRS UMR 7314, UPJV, Amiens,

France) on a *Tecnai F20 S-Twin* microscope, operating at 200 keV and fitted with an EDAX EDS (X-ray Energy Dispersive Spectroscopy).

On the other hand, the α-$Na_2Co(SO_4)_2$ sample was studied by Transmission Electron Microscopy by Artem M. Abakumov and Gustaaf Van Tendeloo (Laboratory "Electron Microscopy for Materials Science", University of Antwerp, Antwerp, Belgium). Selected Area Electron Diffraction (SAED) patterns and EDX spectra were obtained with a *Tecnai G2* electron microscope operated at 200 kV equipped with an EDAX attachment. SAED patterns of α-$Na_2Co(SO_4)_2$ were taken with a very weak and widely spread electron beam. In these conditions the material almost did not suffer from the electron beam damage and allowed obtaining tilt series of the SAED patterns, which could be used for a reconstruction of the 3D reciprocal lattice.

A.4.6   Infra-red spectroscopy

Fourier Transform Infrared Spectroscopy (FTIR) was used to probe the presence of water in the samples. To do so, the samples were mixed with KBr powder using a mortar in an argon filled glove-box. This mixture was pressed at 10 tons for one minute to form a 13-mm diameter pellet, which was transferred in a FTIR sample holder close under argon, so that to prevent the pellet to be contaminated by moisture. Spectar were collected in the 4000-500 cm^{-1} wavenumber range using a *Nicolet Avatar 370 DTGS* spectrometer in transmission mode.

A.4.7   Magnetic measurements

Macroscopic magnetic properties of the $Li_xM(SO_4)_2$ samples (x = 1, 2 and M = Fe, Co, Mn, Ni) were probed on about 20 mg of the powder samples filled into gel caps, using either a *SQUID 5S* or a *SQUID XL* magnetometers (*Quantum design*). Susceptibility measurements (χ = f(T)) were carried out in zero-field-cooled (ZFC) and field-cooled (FC) conditions, in the temperature range 2 K-300 K, under applied magnetic fields (H) of 10 kOe and 100 Oe. Magnetization curves (M = f(H)) were recorded at 2 K by varying the applied field between -50 kOe and 50 kOe.

A.5 Useful data tables

A.5.1 Shannon ionic radii of a selection of cations

Cation	Electronic configuration	Coordination number	Spin state	Ionic radius (Å) [111]
Fe(III+)	[Ar] $3d^5$	6	HS	0.645
Ni(II+)	[Ar] $3d^8$	6		0.69
Mg(II+)	[Ne] $3s^0$	6		0.72
Cu(II+)	[Ar] $3d^9$	6		0.73
Zn(II+)	[Ar] $3d^{10}$	6		0.74
Co(II+)	[Ar] $3d^7$	6	HS	0.745
Li(I+)	[He] $2s^0$	6		0.76
Fe(II+)	[Ar] $3d^6$	6	HS	0.78
Mn(II+)	[Ar] $3d^5$	6	HS	0.83
Ag(II+)	[Kr] $4d^9$	6		0.94
Cd(II+)	[Kr] $4d^{10}$	6		0.95
Ca(II+)	[Ar] $4s^0$	6		1.00
Na(I+)	[Ne] $3s^0$	6		1.02
K(I+)	[Ar] $4s^0$	6		1.38

A.5.2 Hyperfine parameters obtained from the Mössbauer spectra of several sulfate-based compounds

Phase	Oxidation state of Fe	δ (mm/s)	ΔEq (mm/s)
$FeSO_4.7H_2O$	+II	1.26	3.20
$FeSO_4.H_2O$	+II	1.26	2.72
α-$FeSO_4$	+II	1.28	3.11
β-$FeSO_4$	+II	1.28	2.8-2.9
Monoclinic *marinite* $Li_2Fe(SO_4)_2$	+II	1.30	1.16
Amorphous $Li_2Fe(SO_4)_2$	+II	1.26	2.44-2.99
$Na_2Fe(SO_4)_2.4H_2O$	+II	1.25	3.25
$Na_6Fe(SO_4)_4$	+II	1.30	1.47
$K_2Fe(SO_4)_2.4H_2O$	+II	1.26	3.55
	+II	1.3	1.83
$K_2Fe_2(SO_4)_3$	+II	1.31	0.28
	+II	1.32	0.85
Amorphous $Fe_2(SO_4)_3.5H_2O$	+III	0.45	0.36
Rhombohedral $Fe_2(SO_4)_3$	+III	0.46	0
Monoclinic $Fe_2(SO_4)_3$	+III	0.5	0.28
$FeSO_4OH$	+III	0.42	1.39
Monoclinic *marinite* $Li_1Fe(SO_4)_2$	+III	0.46	0.33
$Na_1Fe(SO_4)_2.4H_2O$	+III	0.45	0.41
$NaFe(SO_4)_2$	+III	0.47	0.46
$Na_3Fe(SO_4)_3$	+III	0.46	0.12
$KFe(SO_4)_2$	+III	0.47	0.29

A.5.3 Tables of selected interatomic distances and bond angles

A.5.3.1 $Na_2Co(SO_4)_2.4H_2O$

Distances (Å)			
Co-Co	5.5356(4)	Na-O1	2.391(12)
Co-Co	6.9124(3)	Na-O2	2.424(12)
Co-Co	8.2436(5)	Na-O2	2.375(9)
Co-O3	2.089(9)	Na-O4	2.388(12)
Co-O5	2.074(9)	Na-O5	2.421(9)
Co-O6	2.136(9)	Na-O6	2.610(12)
S-O1	1.496(12)	S-O3	1.473(9)
S-O2	1.467(9)	S-O4	1.478(12)
O5-H1	1.00(4)	O6-H3	0.94(4)
O5-H2	0.96(4)	O6-H4	0.98(4)
Angles (°)			
H1-O5-H2	109(1)	H3-O6-H4	103(1)

A.5.3.2 $Na_2Fe(SO_4)_2.4H_2O$

Distances (Å)			
Fe-Fe	5.5581(2)	Na-O1	2.391(11)
Fe-Fe	6.9491(1)	Na-O2	2.470(10)
Fe-Fe	8.2622(2)	Na-O2	2.291(9)
Fe-O3	2.270(8)	Na-O4	2.370(10)
Fe-O5	2.153(8)	Na-O5	2.302(9)
Fe-O6	2.162(8)	Na-O6	2.615(10)
S-O1	1.451(11)	S-O3	1.368(10)
S-O2	1.498(9)	S-O4	1.537(11)
O5-H1	1.024(8)	O6-H3	0.896(7)
O5-H2	1.040(7)	O6-H4	1.049(8)
Angles (°)			
H1-O5-H2	101(1)	H3-O6-H4	102(1)

A.5.3.3 α-Na₂Co(SO₄)₂

Distances (Å)

Co1-Co1	4.71(2)	Co1-Co3	4.76(3)	Co2-Co3	4.66(2)
Co1-Co2	4.83(3)	Co1-Co3	5.32(2)	Co2-Co3	5.04(2)
Co1-Co2	5.40(2)	Co2-Co2	4.84(3)	Co3-Co3	4.99(3)
Co1-O1a	2.08(3)	Co2-O2a	2.03(3)	Co3-O3b	2.09(4)
Co1-O1b	2.09(4)	Co2-O4a	2.04(4)	Co3-O4b	2.09(4)
Co1-O4c	2.20(4)	Co2-O3c	2.08(4)	Co3-O1c	2.02(4)
Co1-O1e	2.41(4)	Co2-O3d	2.22(4)	Co3-O1d	2.16(3)
Co1-O2e	2.28(4)	Co2-O1f	2.15(4)	Co3-O2d	2.14(4)
Co1-O3e	1.99(4)	Co2-O3f	2.25(4)	Co3-O4f	2.11(4)
Na1-O4a	2.73(6)	Na2-O2b	2.53(5)	Na3-O2b	2.36(6)
Na1-O4e	2.32(4)	Na2-O4c	2.68(5)	Na3-O2c	2.61(5)
Na1-O3f	2.71(4)	Na2-O2d	2.66(6)	Na3-O3c	2.59(5)
Na6-O1a	2.58(4)	Na2-O4d	2.30(5)	Na3-O3d	2.48(5)
Na6-O3c	2.41(4)	Na2-O2e	2.76(6)	Na3-O1e	2.49(6)
Na6-O1e	2.41(4)	Na2-O2f	2.24(5)	Na3-O2e	2.49(5)
Na4-O2a	2.46(5)	Na5-O3b	2.37(5)	Na7-O3a	2.61(6)
Na4-O3a	2.26(5)	Na5-O2c	2.35(5)	Na7-O1b	2.72(5)
Na4-O1d	2.44(5)	Na5-O2d	2.42(5)	Na7-O4b	2.46(5)
Na4-O3e	2.48(5)	Na5-O1f	2.33(5)	Na7-O1d	2.62(6)
Na4-O4e	2.54(5)	Na5-O4f	2.39(5)	Na7-O1f	2.49(6)
Na4-O3f	2.49(5)	Na5-O1c	2.92(5)	Na7-O4d	2.86(6)
S1-O11	1.46(3)	S2-O21	1.47(4)	S3-O31	1.47(4)
S1-O12	1.45(3)	S2-O22	1.46(4)	S3-O32	1.49(4)
S1-O13	1.45(4)	S2-O23	1.49(4)	S3-O33	1.48(4)
S1-O14	1.47(4)	S2-O24	1.49(4)	S3-O34	1.49(4)
S4-O41	1.46(4)	S5-O51	1.49(4)	S6-O61	1.48(3)
S4-O42	1.46(4)	S5-O52	1.46(4)	S6-O62	1.47(4)
S4-O43	1.49(4)	S5-O53	1.50(4)	S6-O63	1.45(4)
S4-O44	1.47(4)	S5-O54	1.45(4)	S6-O64	1.47()

A.5.3.4 Li₂Co(SO₄)₂

Distances (Å)

Co-Co	4.9786(2)	S-O1	1.4502(17)
Co-Co	5.9777(2)	S-O2	1.4834(18)
Co-Co	6.1213(2)	S-O3	1.4976(19)
Co-O2	2.1472(16)	S-O4	1.4767(19)
Co-O2	2.1472(16)	Li-O1	1.871(6)
Co-O3	2.0759(21)	Li-O1	1.977(6)
Co-O3	2.0759(21)	Li-O2	2.079(8)
Co-O4	2.1151(16)	Li-O3	2.254(7)
Co-O4	2.1151(16)	Li-O4	1.994(7)

A.5.3.5 Li₂Fe(SO₄)₂

Distances (Å)			
Fe-Fe	4.9886(2)	S-O1	1.4751(17)
Fe-Fe	6.0270(2)	S-O2	1.4824(18)
Fe-Fe	6.1671(2)	S-O3	1.4726(19)
Fe-O2	2.1843(16)	S-O4	1.4808(19)
Fe-O2	2.1843(16)	Li-O1	1.871(6)
Fe-O3	2.1142(20)	Li-O1	1.977(6)
Fe-O3	2.1142(20)	Li-O2	2.079(8)
Fe-O4	2.1586(16)	Li-O3	2.254(7)
Fe-O4	2.1586(16)	Li-O4	1.994(7)

A.5.3.6 Li₁Fe(SO₄)₂

Distances (Å)			
Fe-Fe	4.7975(2)	S-O1	1.4880(19)
Fe-Fe	5.7540(2)	S-O2	1.4413(19)
Fe-Fe	6.0256(2)	S-O3	1.5041(18)
Fe-O1	2.0133(2)	S-O4	1.4767(13)
Fe-O1	2.0133(2)	Li-O1	2.367(11)
Fe-O3	2.0335(2)	Li-O2	1.842(17)
Fe-O3	2.0335(2)	Li-O2	1.843(17)
Fe-O4	1.9997(2)	Li-O3	2.128(13)
Fe-O4	1.9997(2)	Li-O3	2.188(12)

A.5.3.7 Li₂Mn(SO₄)₂

Distances (Å)			
Mn-Mn	4.9925(4)	S-O1	1.451(4)
Mn-Mn	6.0847(3)	S-O2	1.483(4)
Mn-Mn	6.2458(4)	S-O3	1.452(5)
Mn-O1	2.190(4)	S-O4	1.456(4)
Mn-O1	2.190(4)	Li-O1	1.970(11)
Mn-O3	2.135(4)	Li-O2	2.005(12)
Mn-O3	2.135(4)	Li-O2	2.106(15)
Mn-O4	2.239(3)	Li-O3	2.265(11)
Mn-O4	2.239(3)	Li-O3	1.972(11)

Résumé étendu

F.1.   Introduction générale

Depuis la domestication du feu il y a environ 400 000 ans, l'histoire des énergie a été intimement liée à celle des changements technologiques, économiques et politiques [1,2]. L'énergie musculaire et le bois étaient les seules sources d'énergie durant la Préhistoire. Pendant l'Antiquité, les Grecs et les Romains commencèrent à utiliser la force du vent pour le transport, et au Moyen-Age les moulins à vent et moulins à eau se multiplièrent pour le meulage et le sciage. Plus tard, l'utilisation massive du bois pour les constructions et les premières industries (métallurgie, verrerie, *etc*.) conduit à la déforestation rapide de l'Europe aux XVIIème et XVIIIème siècles, ce qui encouragea ensuite l'exploitation des mines de charbon. Le charbon et l'invention de la machine à vapeur à la fin du XVIIème siècle marqueront d'ailleurs le début de la Révolution Industrielle en Occident. La fin du XIXème siècle sera le témoin à son tour d'une accélération considérable du développement industriel, avec d'une part le début du raffinage du pétrole et l'invention du moteur à combustion, et d'autre part le début de la production et de la distribution d'électricité à grande échelle ainsi que de la conception du moteur électrique. Le développement de ces deux technologies conduira à la Seconde Révolution Industrielle et à la naissance d'un nouveau moyen de transport individuel, la voiture.

Aujourd'hui, nous sommes certainement à notre tour à l'aube d'une nouvelle révolution dans le domaine de l'énergie. La majorité de l'énergie consommée dans le monde est d'origine fossile (*i.e.* pétrole, charbon et gaz) [3]. L'utilisation massive de ces sources d'énergie entraine de plus en plus de tensions politiques et économiques, car ces ressources sont limitées et sont sur la voie de l'épuisement. En effet, le monde fait face à une augmentation rapide de la demande d'énergie (**Figure F.1**), principalement dû à l'explosion des échanges mondiaux, à la croissance rapide de la population (depuis 1950, la population mondiale a augmenté de 13 à 22% tous les 10 ans, et les prévisions des Nations Unies ne suggèrent pas de ralentissement de cette tendance pour le XXIème siècle [4]), ainsi qu'au développement rapide des pays émergeants, qui prétendent au même niveau de vie que les pays développés. La demande croissante d'énergie combinée aux craintes d'un possible épuisement a inévitablement conduit à une montée régulière des prix des combustibles fossiles depuis la première crise du pétrole au début des années 1970.

Par ailleurs, l'utilisation massive des énergies fossiles est également à l'origine de problèmes environnementaux, puisque leur combustion génère de grandes quantités de gaz à effet de serre (**Figure F.1**). Depuis les années 1950, la communauté scientifique a remarqué un impact non

négligeable de ces gaz sur le climat, avec nombreux changements sans précédent : l'atmosphère et les océans se sont réchauffés, les quantités de neige et de glace ont diminué, le niveau de la mer s'est élevé, *etc.* **[5]**. Les conséquences exactes de ces changements climatiques sont encore en débat, mais elles vont sans aucun doute affecter l'écosystème mondial (**Figure F.1**) et sont susceptibles de provoquer de plus en plus régulièrement des évènements climatiques extrêmes (par exemple : tempêtes, inondations, sècheresses), des migrations massives de populations (en conséquence de l'érosion des côtes, de la submersion des littoraux, des perturbations des productions agricoles), *etc*. Limiter ces changements climatiques ne sera possible que si nous parvenons à réduire de façon considérable nos émissions de gaz à effet de serre.
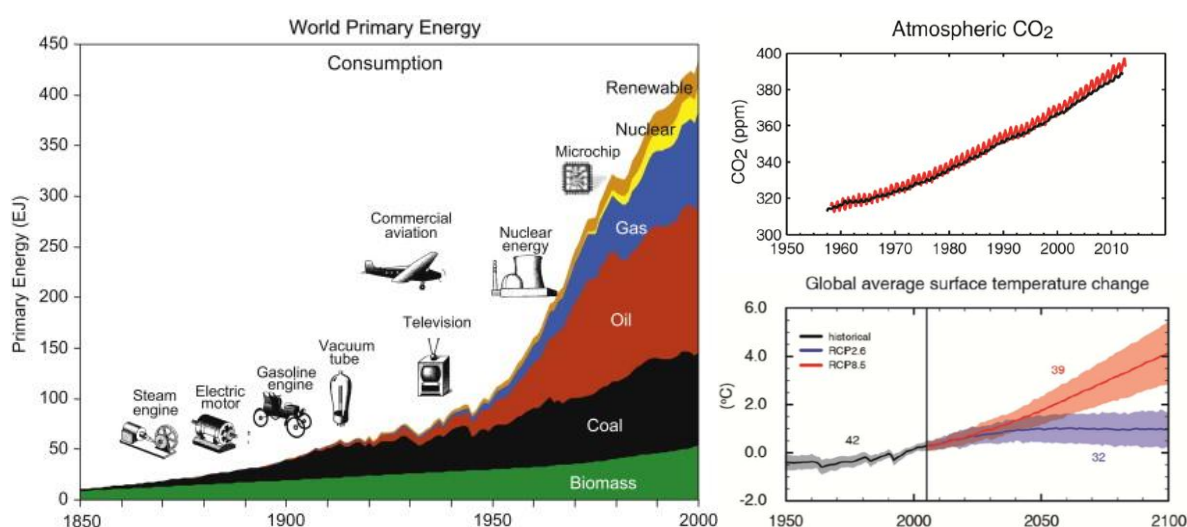
Figure F.1 : A gauche : consommation mondiale d'énergie en fonction du type de ressource pendant la période 1850-2000, avec en parallèle les inventions technologiques majeures de cette période (d'après **[3]**). A droite : évolution des changements de la température moyenne à l'échelle mondiale (les prédictions optimistes et pessimistes sont respectivement représentées en bleu et en rouge) et évolution de la concentration atmosphérique en CO_2 depuis 1950 (d'après **[5]**).

Ainsi, il est devenu urgent de développer des sources d'énergies plus abondantes, renouvelables et moins polluantes, telles que le sont les énergies hydraulique, solaire et éolienne, la biomasse et la géothermie. Cependant, certaines d'entre elles ne fournissent pas de l'énergie en continu (*i.e.* énergies intermittentes), et doivent donc être couplées à des solutions de stockage afin d'équilibrer production et demande d'énergie. Parmi les différentes options existantes, lesquelles sont discutées en détails dans la référence **[6]**, les systèmes de stockage électrochimique (piles à combustible, batteries, supercondensateurs, *etc.* **[7]**), et en particulier les batteries, apparaissent comme les solutions les plus prometteuses. Les batteries convertissent l'énergie électrique en énergie chimique quand elles sont chargées, et inversement, fournissent de l'énergie électrique quand elles sont déchargées ; cela avec un rendement de conversion élevé et sans émission de gaz à effet de serre. De plus, la forme et la taille de ces dispositifs peuvent être adaptées (*e.g.* de quelques

mm^3 à plusieurs dizaines de m^3), et ils peuvent donc être utilisés tout autant pour des applications de stockage stationnaire (unités d'alimentation permanentes, écrêtage de pointe) que pour des applications mobiles (dispositifs électroniques portables, véhicules électriques et hybrides).

Plusieurs technologies de batteries existent, les plus courantes sont les batteries au *plomb*, les batteries *nickel-cadmium* (Ni-Cd), les batteries *nickel-hydrure métallique* (Ni-MH), et les batteries au *lithium*. Grâce à leur densité d'énergie élevée par rapport aux autres technologies, les batteries Li-ion ont rapidement envahi le marché de l'électronique portable depuis le début des années 1990, et elles sont maintenant sur le point de conquérir les véhicules électriques et le stockage de masse. Cependant, malgré 30 ans de recherche académique et de développement industriel consacrés à cette technologie, des améliorations sont encore possibles et nécessaires. Nous pouvons considérer que les challenges actuels sont doubles. D'un côté, les besoins pour les dispositifs électroniques portables et les véhicules électriques stimulent la recherche vers des systèmes Li-ion présentant de plus grandes capacités d'énergie et de plus haut potentiels ; d'un autre côté, le développement du stockage de masse requiert des batteries moins chères, et dont la solution pourrait se trouver dans une technologie soeur : les batteries Na-ion. Dans les deux cas, la conception et l'optimisation de nouveaux matériaux de batteries est requis.

Contrairement à d'autres technologies, les batteries Li-ion reposent sur une chimie riche, où une grande variété de matériaux peuvent être employés en tant qu'électrodes positives et négatives. Cependant, les matériaux d'électrodes positives actuels présentent encore de trop faibles capacités spécifiques, et sont ainsi le principal facteur pénalisant les batteries en termes de densité d'énergie [9]. C'est pourquoi ces 30 dernières années d'importants efforts ont été dédiés à la recherche de nouveaux matériaux de cathode présentant de meilleures performances.

Le matériau d'électrode positive idéal reposerait sur un couple redox possédant un haut potentiel, mais compatible avec la fenêtre de stabilité des électrolytes actuels (*i.e.* < 4.8 V *vs.* Li$^+$/Li^0). Il présenterait également une grande capacité spécifique, laquelle est proportionnelle au nombre d'électrons échangés par formule unitaire et inversement proportionnelle à la masse molaire du composé. Cependant ces deux propriétés ne sont pas les uniques critères qu'un bon matériau d'électrode positive doit remplir. Il doit également réagir avec le lithium selon un mécanisme d'insertion/désinsertion parfaitement réversible, de façon à présenter une bonne rétention de capacité. Cette réversibilité est principalement liée aux modifications structurales et morphologiques subies par le matériau d'électrode lors de l'extraction et de la réinsertion des cations alcalins dans le matériau actif. Une électrode positive doit également être un bon conducteur ionique et

électronique, puisque ces deux propriétés sont les principaux facteurs limitant la cinétique de la réaction redox (plus que le transfert de masse) et qu'ils déterminent ainsi les performances en puissance de l'électrode. Enfin, elle doit contenir du lithium pour être facilement implémentée dans les batteries Li-ion, et, pour des raisons de durabilité et de sécurité, les autres constituants doivent être préférablement choisis parmi les éléments abondants, peu chers et non toxiques.

Les principaux matériaux d'électrode positive étudiés jusqu'à présent peuvent être classés en deux groupes : les oxydes et les composés polyanioniques. Les oxydes, qui sont à l'origine du premier succès commercial des batteries Li-ion, fournissent de hauts potentiels et de hautes densités d'énergie. Cependant, pour des raisons environnementales et économiques, ces matériaux d'électrodes à base de cobalt et de nickel sont maintenant appelés à être remplacés par des éléments plus durables tels que le fer ou le manganèse. Les oxydes de fer présentant des performances médiocres en tant que matériaux d'électrode positive, les recherches se sont tournées à la fin des années 1990 vers les matériaux polyanioniques à base de fer, qui offrent des charpentes structurelles robustes permettant de meilleures performances en cyclage, et avec lesquelles il est possible d'ajuster le potentiel redox du couple Fe^{III+}/Fe^{II+} en jouant sur la composition et la structure du composé.

Bien qu'il n'existe pas d'indicateur universel permettant de prévoir les performances électrochimiques d'un composé donné avant de l'avoir synthétisé, plusieurs paramètres importants ont été identifiés à travers des différentes familles de matériaux d'électrode étudiés ces 25 dernières années **[348]**. Tout d'abord, une première caractéristique rencontrée dans la plupart des bons matériaux d'électrode est leur charpente structurale ouverte, favorisant la diffusion des cations alcalins et permettant des cyclages à hauts régimes. En ce qui concerne le potentiel du couple redox $M^{n+}/M^{(n+1)+}$, celui-ci est fortement corrélé au caractère ionocovalent de la liaison M–O, qui lui-même dépend de différents paramètres chimiques et structurels interdépendants: la compacité de la structure (polyèdres MO_x isolés ou partageant des sommets, des arêtes ou des faces **[234,349]**), la présence et la connectivité d'éléments électronégatifs et de groupements polyanioniques autour du centre redox (effet inductif **[222,232,233]**), la position du cation hôte dans la structure **[113,115,349,350]**, *etc*. Ces différents paramètres sont utilisés pour expliquer les tendances générales observées dans les différentes familles de matériaux d'électrode. Toutefois, ils doivent être employés avec précautions pour prédire le potentiel d'un nouveau composé, puisque aucun d'entre eux n'est parfaitement fiable pris individuellement, et que le potentiel redox d'un matériau donné est souvent le résultat d'une combinaison de ces différents paramètres.

En tenant compte de ces observations, plusieurs stratégies peuvent être adoptées pour concevoir de nouveaux matériaux d'électrode. L'une d'entre elles s'appuie sur des calculs théoriques combinatoires, avec lesquels on va tenter de prédire les structures de milliers de matériaux avec des compositions chimiques aléatoires et de calculer leurs propriétés physico-chimiques, dans le but d'identifier la « composition magique » présentant à la fois un haut potentiel et une grande capacité spécifique **[351–354]**. Les premiers résultats de telles études théoriques ont été rapportées ces dernières années **[288,355–357]**, mais leur succès reste encore limité. Une autre approche, suivie par le chimiste expérimental, consiste à repérer parmi les structures de composés connus (par exemple, des phases précédemment synthétisées, des minéraux, *etc.*) les familles de matériaux qui présentent des aspects structuraux favorables au transport ionique. Pour les travaux présentés dans ce manuscrit, nous avons choisi de nous inspirer des quelques 4000 espèces minérales rapportées par nos confrères minéralogistes pour concevoir de nouveaux matériaux d'électrode. En plus du fait que les structures des minéraux sont généralement connues avec précision, la compréhension des conditions de leur formation dans la nature peut suggérer un bon point de départ pour leur synthèse artificielle, laquelle pourra ensuite être généralisée à la préparation de leurs dérivés structuraux. Il est par ailleurs intéressant de remarquer que de nombreux composés polyanioniques précédemment étudiés en tant que matériaux d'électrode cristallisent en fait dans des structures de minéraux.

Inspirés par les minéraux, nous avons donc exploré dans ce travail de thèse une nouvelle famille de composés à base de sulfates de formule générale $A_2M(SO_4)_2 \cdot nH_2O$ (A = alcalin, M = métal de transition 3d, et n = 0, 4). Ce manuscrit décrit les principaux résultats obtenus au cours de cette étude.

F.2. Elaboration de nouveaux matériaux d'électrode à partir de minéraux à base de sulfates

Parmi tous les matériaux d'électrode contenant des groupements polyanioniques, les sulfates sont ceux qui présentent les potentiels redox les plus élevés ; ceci est expliqué par le fait que le soufre est plus électronégatif que les autres éléments centraux de groupements polyanioniques (phosphore, bore, silicium, *etc.*). Les fluorosulfates, qui combinent l'effet inductif des groupements sulfates et l'électronégativité du fluor, affichent en fait les plus hauts potentiels jamais rapportés pour le couple redox Fe^{III+}/Fe^{II+} (3,9 V *vs.* Li^+/Li^0 pour la *triplite* $LiFeSO_4F$ **[330,335]** et 3,5 V *vs.* Na^+/Na^0 pour la *maxwellite* $NaFeSO_4F$ **[331]**). Cependant, connaissant les réticences des industriels à utiliser des composés d'électrode fluorés, nous avons entrepris la recherche d'autres matériaux à base de sulfates mais dépourvus de fluor. Dans ce but, nous avons choisi d'explorer les minéraux, parmi

lesquels sont rapportés de nombreux sulfates **[358]**. Nous nous sommes en particuliers focalisés sur les sulfates minéraux contenant à la fois des métaux alcalins (Na ou K) et des métaux de transition 3d ou des cations magnésium, et nous avons choisi de travailler sur des composés dérivés du minéral *bloedite* Na$_2$Mg(SO$_4$)$_2\cdot$4H$_2$O.

F.2.1.   Les composés de type *bloedite* Na$_2$*M*(SO$_4$)$_2\cdot$4H$_2$O (*M* = Mg, Zn, Co, Fe, Ni)

Les composés de type *bloedite* Na$_2$*M*(SO$_4$)$_2\cdot$4H$_2$O (*M* = Mg, Zn, Ni, Co, Fe) ont été très largement étudiés depuis les années 1940 **[365–382]**. Pour la synthèse de ces composés, nous avons commencé par imiter le processus d'évaporation des saumures naturelles, en évaporant lentement une solution équimolaire de sulfate de sodium Na$_2$SO$_4$ et du sulfate de métal correspondant *M*SO$_4\cdot$7H$_2$O à des températures allant de 20°C à 90°C. Nous avons ensuite obtenu les mêmes phases par précipitation de cette même solution dans l'éthanol. Enfin, nous avons également pu préparer les cinq composés Na$_2$*M*(SO$_4$)$_2\cdot$4H$_2$O par broyage mécanique (Spex 8000M®) d'un mélange équimolaire des sulfates précurseurs pendant 20 minutes, sous air ou sous argon. Quelque soit la voie de synthèse utilisée, les phases hydratées se forment selon la réaction suivante:

$$\text{Na}_2\text{SO}_4 + M^{\text{II}}\text{SO}_4\cdot7\text{H}_2\text{O} \rightarrow \text{Na}_2M^{\text{II}}(\text{SO}_4)_2\cdot4\text{H}_2\text{O} + 3\text{H}_2\text{O}$$
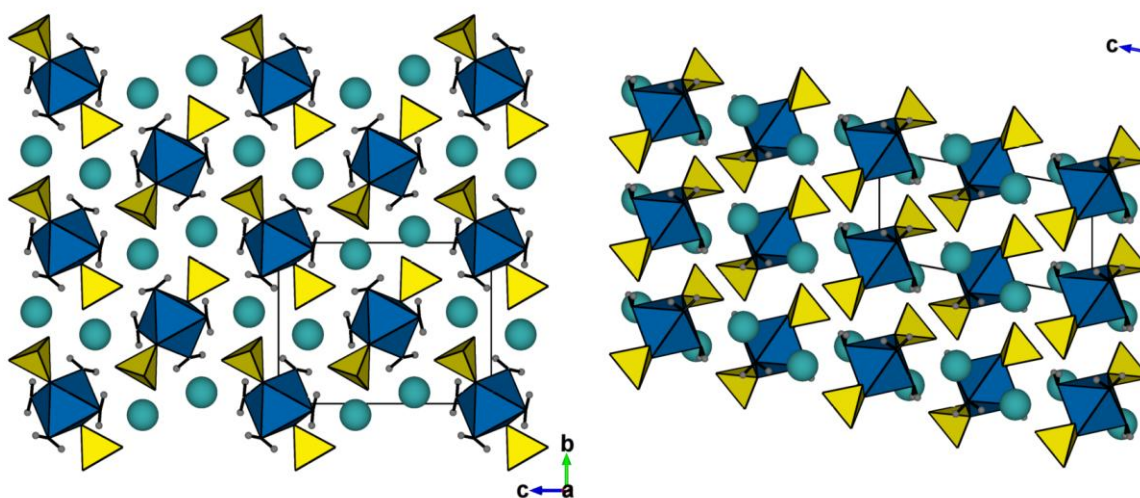
Figure F.2 : Représentation de la structure *bloedite*, selon les axes *a* (à gauche) et *b* (à droite).

La structure *bloedite* est constituée d'unités isolées, faites d'un octaèdre *M*O$_6$ entouré de quatre molécules d'eau placées dans le plan équatorial de l'octaèdre et de deux tétraèdres SO$_4$ en positions axiales. Ces unités *M*(SO$_4$)$_2$(H$_2$O)$_4$ sont alignées selon l'axe *a* (**Figure F.2**), et les ions sodium sont rangés deux par deux dans de larges tunnels parallèles à cette même direction. Chaque atome de sodium est coordiné à six atomes d'oxygène, formant ainsi des octaèdres NaO$_6$ distordus, qui partagent deux à deux leurs faces pour former des groupements isolés Na$_2$O$_{10}$.

Afin de vérifier la possibilité d'extraire le sodium de ces larges tunnels, nous avons testé les propriétés électrochimiques des cinq phases $Na_2M(SO_4)_2 \cdot 4H_2O$ (M = Mg, Zn, Ni, Co, Fe) face au lithium et au sodium ; seul le composé à base de fer s'est révélé être électrochimiquement actif, comme le montrent les courbes présentées dans la **Figure F.3 [363,364]**. Le potentiel redox du couple Fe^{III+}/Fe^{II+} est centré autour de 3,6 V *versus* Li^+/Li^0 et 3,3 V *versus* Na^+/Na^0. Ces potentiels sont plus élevés que celui de $LiFePO_4$ (3,45 V *vs.* Li^+/Li^0 **[233]**) et sont du même ordre de grandeur que d'autres composés à base de sulfates, tels que les NASICON $Fe_2(SO_4)_3$ (3,6 V *vs.* Li^+/Li^0 **[222,223]**), les *tavorites* $LiFeSO_4F$ (3,6 V *vs.* Li^+/Li^0 **[321]**) et $FeSO_4OH$ (3,2 V *vs.* Li^+/Li^0 **[340]**), le composé lamellaire $LiFeSO_4OH$ (3,6 V *vs.* Li^+/Li^0 **[342]**), et la *maxwellite* $NaFeSO_4F$ (~3,5 V *vs.* Na^+/Na^0 **[331]**).
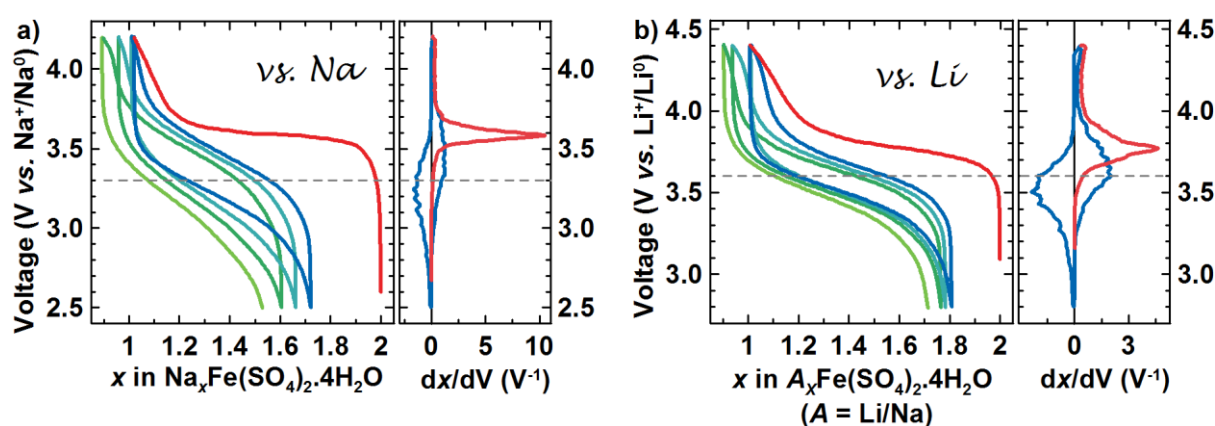
Figure F.3 : Courbes électrochimiques de $Na_2Fe(SO_4)_2 \cdot 4H_2O$ cyclé face (a) au sodium et (b) au lithium, en utilisant respectivement des électrolytes à base de $NaClO_4$ dans PC et $LiClO_4$ dans PC, et un régime de C/50. Les cadres de gauche montrent les courbes potentiels-composition, avec une première charge relativement plate (en rouge) et les décharges et charges suivantes plus pentues (de bleu à vert). Dans les cadres de droite sont représentées les courbes dérivées correspondantes (dx/dV).

Des mesures de diffraction des rayons X (DRX), de spectrométrie Mössbauer du ^{57}Fe et de spectroscopie infrarouge réalisées sur des matériaux d'électrodes à différents états de charge (expériences *ex situ*) ont permis de mettre en évidence que, lors de la première charge (en rouge sur la **Figure F.3**), l'extraction d'un sodium est associée à l'amorphisation du matériau actif et à la perte des quatre molécules d'eau présentes dans sa structure.

Sachant que $Na_2Fe(SO_4)_2 \cdot 4H_2O$ pouvait perdre son eau structurelle, une prolongation évidente de ce travail était d'essayer de préparer une phase anhydre $Na_2Fe(SO_4)_2$ (capacité spécifique théorique de ~91 mAh/g contre ~73 mAh/g pour la phase hydratée), afin d'étudier son comportement électrochimique.

F.2.2.   Les dérivés anhydres des phases *bloedite* α-$Na_2M(SO_4)_2$ (M = Co, Fe)

Les analyses thermogravimétriques des phases $Na_2M(SO_4)_2 \cdot 4H_2O$ (M = Mg, Zn, Ni, Co, Fe) ont montré que leurs quatre molécules d'eau étaient libérées entre 100 et 300°C, suivant deux mécanismes

différents selon la nature du métal divalent. Pour cette raison, nous avons décidé de nous focaliser pour cette étude sur les systèmes au cobalt et au fer, qui présentaient des comportements similaires.

Pour mieux comprendre le procédé de déshydratation des deux phases $Na_2M(SO_4)_2 \cdot 4H_2O$ ($M =$ Co, Fe), nous avons suivi l'évolution de leurs diagrammes de DRX en fonction de la température (**Figure F.4**). A la fin de la déshydratation, nous avons observé la cristallisation d'une nouvelle phase dont le diagramme de DRX (en rouge dans la **Figure F.4**) correspondait au diagramme de Debye-Scherrer rapporté par Cot pour la phase α-$Na_2Co(SO_4)_2$ **[376,381]**.
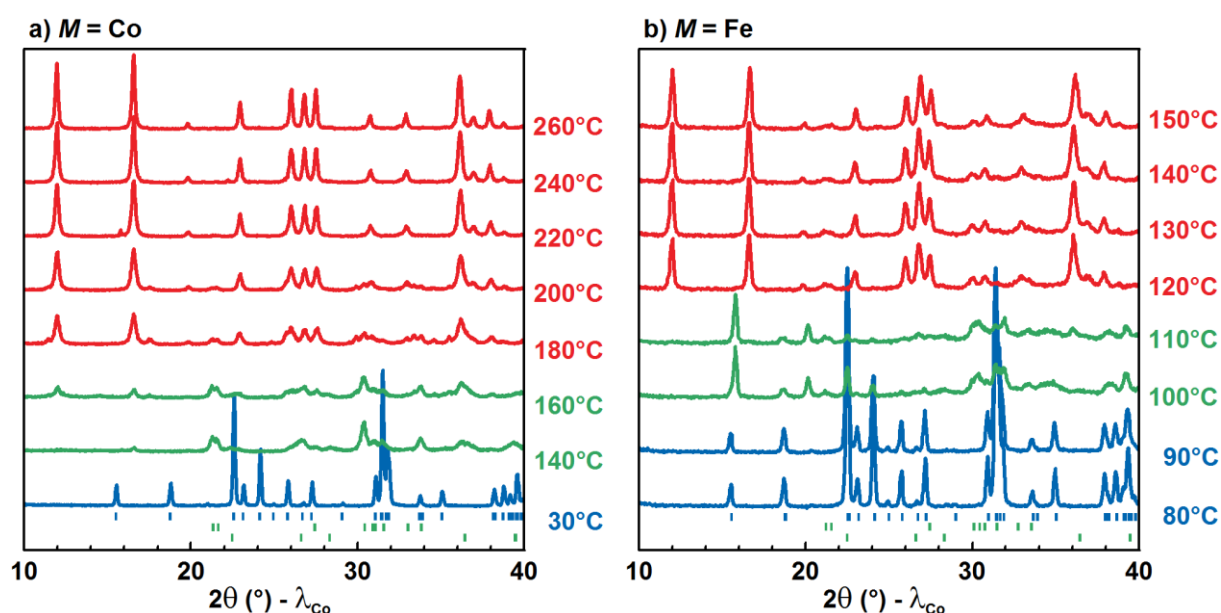
Figure F.4 : Evolution des digrammes de DRX pendant le processus de déshydratation de (a) $Na_2Co(SO_4)_2 \cdot 4H_2O$ et (b) $Na_2Fe(SO_4)_2 \cdot 4H_2O$. Les diagrammes bleus correspondent aux phases $Na_2M(SO_4)_2 \cdot 4H_2O$, les verts à une étape intermédiaire dans laquelle on peut identifier les composés Na_2SO_4 et $MSO_4 \cdot H_2O$ parmi d'autres phases, et les diagrammes rouges sont ceux des phases α-$Na_2M(SO_4)_2$.

Nous avons déterminé la structure des phases α-$Na_2M(SO_4)_2$ ($M =$ Co, Fe) **[364]** en combinant des mesures de diffraction des rayons X avec un rayonnement Synchrotron, de diffraction des neutrons sur poudre (NPD) et de diffraction électronique (SAED). Nous avons ainsi déterminé que ces phases cristallisent dans une super-maille monoclinique (groupe d'espace : $C2/c$), avec les paramètres suivants pour la phase au cobalt : $a = 23.262(2)$ Å, $b = 10.3057(9)$ Å, $c = 17.4047(15)$ Å, $\beta = 98.972(6)°$, $V = 4121.4(6)$ Å^3. Leur structure consiste en un arrangement compliqué d'octaèdres de MO_6 et de tétraèdres de SO_4, qui sont alternativement connectés soit par des sommets et des arêtes, soit par des sommets uniquement, et forment ainsi de courtes chaines comme illustrées dans la **Figure F.5**. Les atomes de sodium se trouvent dans des petits tunnels parallèles à la direction [101].
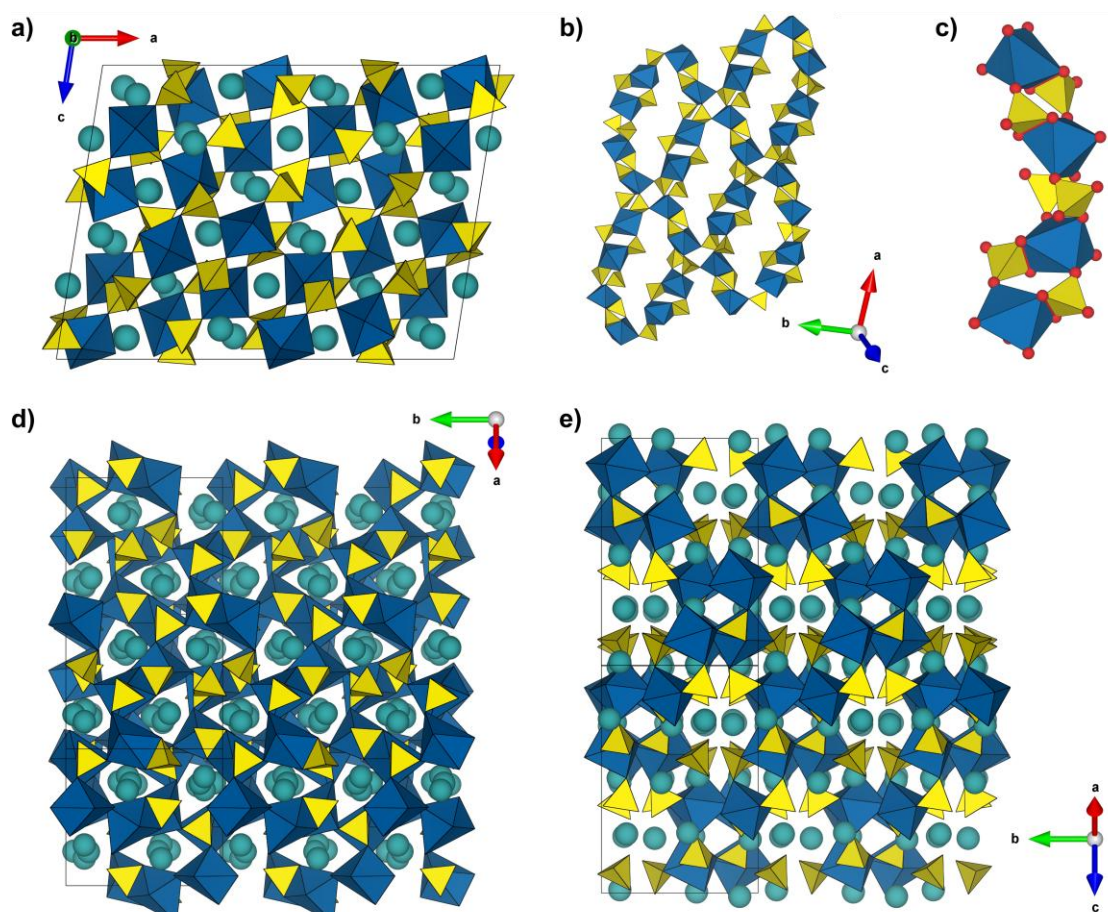
Figure F.5 : Structure de α-Na$_2$Co(SO$_4$)$_2$ représentée avec la super-maille monoclinique décrite dans le texte. (a), (d) and (e) Projections selon l'axe *b* et les directions [1 0 -2] et [1 0 1], respectivement. Les groupes CoO$_6$ et SO$_4$ sont respectivement représentés par des octaèdres bleus et des tétraèdres jaunes. Les boules cyan correspondent aux atomes de sodium. (b) Chaines d'octaèdres CoO$_6$ et de tétraèdres SO$_4$, qui sont alternativement connectés par des sommets et des arêtes. Les atomes de sodium ne sont pas représentés pour plus de clarté. (c) Détails d'une chaine, où les atomes d'oxygènes sont représentés en rouge. Les arêtes partagées par les octaèdres de CoO$_6$ et les tétraèdres de SO$_4$ sont mis en évidence par des traits rouges.

Les phases α-Na$_2$*M*(SO$_4$)$_2$ (*M* = Co, Fe) ont ensuite été testées face au sodium et au lithium, mais comme pour les composés hydratés, seul le matériau à base de fer s'est révélé électroactif dans la fenêtre de potentiel accessible avec les électrolytes utilisés **[364]**. Les courbes potentiel-composition (**Figure F.6**) montrent que le potentiel du couple Fe^{III+}/Fe^{II+} est une nouvelle fois élevé: 3,6 V *vs.* Li$^+$/Li^0 et 3,4 V *vs.* Na$^+$/Na^0. Le profil des courbes galvanostatiques de α-Na$_2$Fe(SO$_4$)$_2$ diffère de celui de la phase hydratée Na$_2$Fe(SO$_4$)$_2$·4H$_2$O : elles présentent une forme en S dès la première charge. De plus, des mesures préliminaires de diffraction des rayons X sur les matériaux d'électrode semblent montrer que α-Na$_2$Fe(SO$_4$)$_2$ ne s'amorphise pas pendant le cyclage, bien que la mauvaise cristallinité du matériau d'électrode ne permette pas à ce stade de déterminer la nature du mécanisme de charge-décharge.
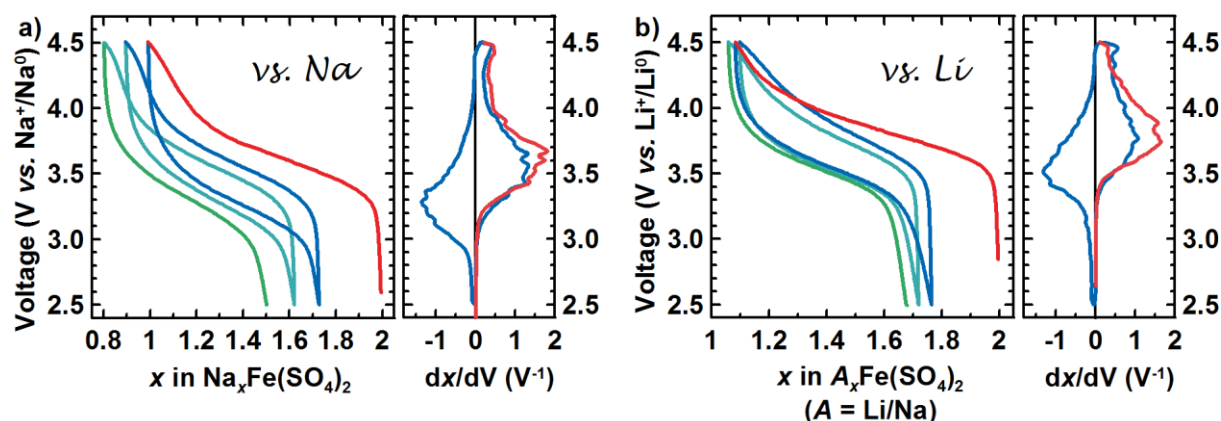
Figure F.6 : Caractérisation électrochimique de α-Na$_2$Fe(SO$_4$)$_2$ (a) *versus* sodium et (b) *versus* lithium. La première charge est tracée en rouge, et les décharges et charges suivantes sont représentées en bleu et vert. Les courbes dérivées correspondantes dx/dV sont montrées à la droite de chaque courbe galvanostatique.

F.2.3. Conclusion

Dans cette étude, nous avons prouvé la faisabilité de préparer de nouveaux matériaux d'électrode à base d'éléments abondants et durables (sodium, fer, soufre et oxygène) en s'inspirant d'espèces minérales, et nous avons ainsi montré que les composés minéraux constituent une riche base de données dans laquelle les chercheurs peuvent choisir des structures modèles à partir desquelles concevoir de nouveaux matériaux fonctionnels.

Nous avons rapporté la synthèse des composés de types *bloedite* Na$_2$$M$(SO$_4$)$_2$·4H$_2$O ($M$ = Mg, Zn, Ni, Co, Fe) et de leur dérivés déshydratés Na$_2$$M$(SO$_4$)$_2$ (M = Co et Fe), pour lesquels nous avons résolu la structure cristalline. Ces matériaux d'électrodes sont relativement limités en terme de capacité (< 80 mAh/g) du fait de leur grande masse moléculaire, mais ils présentent toutefois des potentiels élevés pour le couple redox Fe^{III+}/Fe^{II+} (3,5-3,6 V *vs.* Li$^+$/Li^0 et 3,3-3,4 V *vs.* Na$^+$/Na^0), pour lesquels ces nouveaux matériaux d'électrode restent intéressants d'un point de vue fondamental.

Ces potentiels redox excèdent en effet les valeurs de références obtenues avec des composés à base de phosphates (LiFePO$_4$: 3,45 V *vs.* Li$^+$/Li^0, NaFePO$_4$ et Na$_2$FePO$_4$F : ~3,0 V *vs.* Na$^+$/Na^0) et sont proches des potentiels rapportés pour d'autres matériaux à base de sulfates (type NASICON Fe$_2$(SO$_4$)$_3$, lamellaire LiFeSO$_4$OH et *tavorite* LiFeSO$_4$F : 3,6 V *vs.* Li$^+$/Li^0, *maxwellite* NaFeSO$_4$F : ~3,5 V *vs.* Na$^+$/Na^0). Par conséquent, ces résultats corroborent les précédentes observations qui suggéraient que l'utilisation de sulfates dans les matériaux d'électrode permettait d'atteindre de hautes valeurs de potentiels. De plus, ils confirment une fois de plus que l'incorporation de fluor dans des matériaux d'électrode n'est pas indispensable pour obtenir de hauts potentiels.

Poursuivant notre quête de nouveaux matériaux d'électrode à haut potentiel, nous avons ensuite essayé de préparer des analogues aux phases *bloedite* à base de lithium.

F.3. Une nouvelle famille de composés Li₂*M*(SO₄)₂ (*M* = Co, Fe, Mn, Ni, Zn, Mg)

Pour la synthèse de nouveaux sulfates bimétalliques à base de lithium, nous avons commencé par utiliser les mêmes voies de synthèse que celles utilisées pour la préparation des phases de type *bloedite*, mais toutes les tentatives sont restées infructueuses. Nous avons également essayé de procéder à des échanges ioniques Li ↔ Na sur les composés au sodium (phases hydratées et anhydres), mais bien que ces phases aient été cyclées dans des batteries au lithium, tous nos essais ont conduit à la décomposition partielle des composés, avec en particulier la formation de sulfate de lithium. Toutefois, en chauffant à 200°C des pastilles de α-Na₂Co(SO₄)₂ mélangé avec du chlorure de lithium ou du nitrate de lithium, nous avons remarqué qu'après décomposition du sulfate de sodium et de cobalt, de nouveaux pics de diffraction apparaissaient dans les diagrammes de DRX du mélange. Les positions de ces nouveaux pics de diffraction étaient en fait très similaires à ceux d'un diagramme de DRX rapporté par Touboul *et al.* pour une phase Li₂Co(SO₄)₂ **[404,405]**, et nous avons alors entrepris d'explorer cette nouvelle famille de composés.

F.3.1. Synthèse des phases Li₂*M*(SO₄)₂ (*M* = Co, Fe, Mn, Ni, Zn, Mg)

A notre connaissance, seuls trois composés répondant à la formule générale Li₂*M*(SO₄)₂ avaient été jusqu'alors rapportés dans la littérature (*M* = Co **[404,405]**, Ni **[404,405,425]** et Zn **[414]**), et seule la structure de Li₂Ni(SO₄)₂ avait été déterminée **[425]**. Nous avons obtenu ces phases pures par voie solide et avons ensuite étendu leur synthèse à d'autres métaux divalents (*M* = Fe, Mn, Mg). Les diagrammes de rayons X des composés au cobalt, fer, manganèse et magnésium ont montré que ces quatre phases sont isostructurales et cristallisent dans une maille différente de celle de la structure orthorhombique de Li₂Ni(SO₄)₂ (**Figure F.7**). En ce qui concerne le composé à base de zinc, nous avons pu le stabiliser dans les deux structures.

Nous avons résolu la structure des phases Li₂*M*(SO₄)₂ (*M* = Co, Fe, Mn, Mg, Zn) à partir de nos diagrammes de rayons X **[426]**. L'ensemble des pics de diffraction ont pu être indexés dans une maille monoclinique avec les paramètres de mailles suivants : $P2_1/n$, $a = 4.9787(2)$ Å, $b = 8.1113(2)$ Å, $c = 8.7831(2)$ Å, $\beta = 121.811(2)°$, $V = 301.416(2)$ Å^3 pour la phase au cobalt.
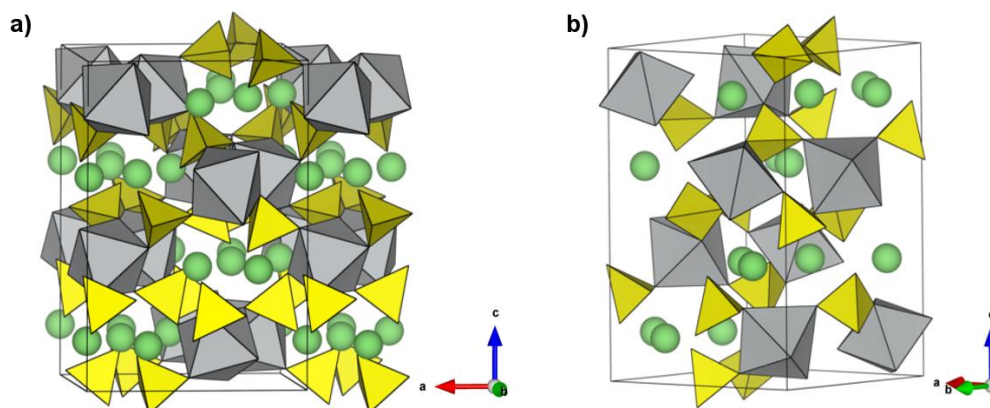
Figure F.7 : Représentation de la structure orthorhombique de Li$_2$Ni(SO$_4$)$_2$, vue selon les directions (a) [010] et (b) [1-10].

Tout comme celle de la phase Li$_2$Ni(SO$_4$)$_2$ (**Figure F.7**), la structure des phases monocliniques (**Figure F.8**) est constituée d'octaèdres de MO$_6$ isolés les uns des autres et reliés par le biais de tétraèdres de SO$_4$. Cette charpente tridimensionnelle donne naissance à de larges tunnels le long de la direction [100], dans lesquels se trouvent les cations Li$^+$. Chaque octaèdre de MO$_6$ partage ses six sommets avec un groupement sulfate, tandis que chaque tétraèdre SO$_4$ est lié à trois octaèdres MO$_6$ et que son quatrième sommet pointe dans les tunnels occupés par les ions lithium. Cet arrangement particulier donne une structure très ouverte, comme reflété par la faible densité de ces composés ($\rho \approx 2.8$ g/cm^3). La principale différence entre les structures orthorhombique (**Figure F.7**) et monoclinique (**Figure F.8**) réside en fait dans la façon dont les polyèdres de MO$_6$ et SO$_4$ sont interconnectés le long des chaines d'octaèdres et de tétraèdres.
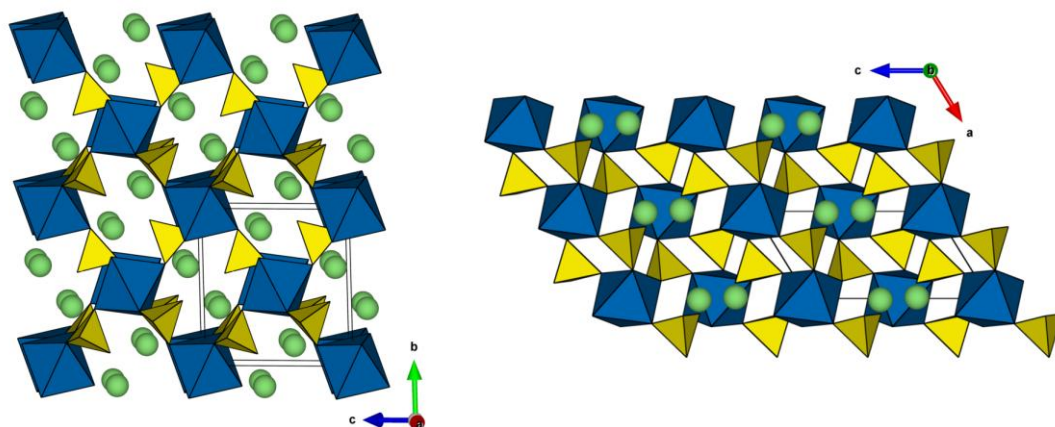
Figure F.8 : Représentation de la structure monoclinique *marinite* de Li$_2$$M$(SO$_4$)$_2$ (M = Co, Fe, Mn, Zn, Mg), vue selon les axes a et b.

F.3.2. Propriétés électrochimiques de Li$_2$Fe(SO$_4$)$_2$

Comme observé pour les phases à base de sodium, parmi les six composés Li$_2$$M$(SO$_4$)$_2$ (M = Co, Fe, Mn, Mg, Zn), seule la phase à base de fer est électrochimiquement active face au lithium métallique

(**Figure F.9**). Pendant la première charge, environ un lithium est extrait de la structure, et 0,86 lithium sont ensuite réinsérés en décharge ; ce qui donne une capacité réversible d'environ 88 mAh/g (capacité spécifique théorique de 102 mAh/g). L'activité électrochimique $Li_2Fe(SO_4)_2$ est centrée autour de 3,83 V *vs.* Li^+/Li^0 **[426,428]**, comme confirmé par la courbe dérivée dx/dV (**Figure F.9**) et les mesures en mode GITT. Il est important de remarquer que ce potentiel de 3,83 V est en fait le plus haut potentiel jamais rapporté pour le couple redox Fe^{III+}/Fe^{II+} dans un composé inorganique dépourvu de fluor **[105,323,426,428]**, et qu'il est seulement dépassé par la forme *triplite* de $LiFeSO_4F$ (3,9 V *vs.* Li^+/Li^0, **[330,335]**). De plus, nous avons également testé les performances en puissance de $Li_2Fe(SO_4)_2$ (**Figure F.9**). Compte tenu du fait que le matériau d'électrode ne contient que 20% de carbone et que la composition de l'électrode n'a pas été optimisé, la rétention de 85% de la capacité initiale à un régime de 1C reflète une bonne cinétique d'insertion du lithium.
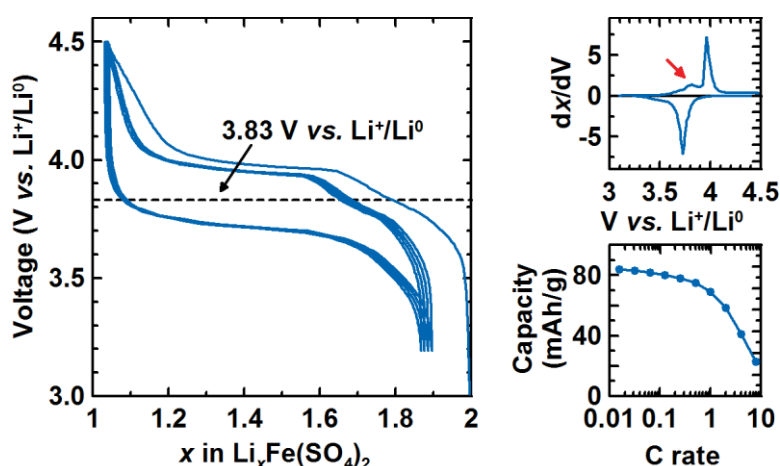
Figure F.9 : Caratérisations électrochimiques de la phase *marinite* $Li_2Fe(SO_4)_2$.
A gauche : Courbe galvanostatique de $Li_2Fe(SO_4)_2$ cyclé face au lithium métallique à un régime de C/20.
En haut à droite : courbe dérivée dx/dV correspondante. La flèche rouge indique l'accident discuté dans le texte. En bas à droite : capacité en décharge en function du régime de cyclage.

Concernant le mécanisme d'extraction/insertion du lithium, le plateau observé en charge et en décharge dans la courbe potentiel-composition (**Figure F.9**) suggère un processus biphasique, comme également corroboré par les mesures en mode PITT. Cependant, on peut également observer une région plus pentue au début de chaque charge ($2 \le x \le 1.7$), qui n'est pas visible en décharge. Cet "accident" est davantage visible sur la courbe dérivée dx/dV, comme indiqué avec la flèche rouge dans la **Figure F.9**. Pour comprendre ces observations, nous avons entrepris une étude détaillée du mécanisme de charge/décharge de notre nouveau matériau d'électrode.

Des expériences *in operando* de diffraction des rayons X ont confirmé le caractére biphasique du processus électrochimique au niveau du plateau observé en charge et en décharge (**Figure F.10**). Toutefois, nous n'avons observé aucun changement dans le diagramme de diffraction (ni dans la

position des pics, ni dans leur intensité) au début de la charge entre $x = 2$ et $x \approx 1,7$. Ces résultats semblaient donc suggérer que l'activité électrochimique en début de charge pouvait être associée avec une partie amorphe du matériau d'électrode. Pour confirmer cette hypothèse, nous avons effectué une expérience complémentaire de spectrométrie Mössbauer *in operando* afin de sonder l'environnement du fer dans le matériau d'électrode et de suivre son état d'oxydation pendant le cyclage (**Figure F.11**).
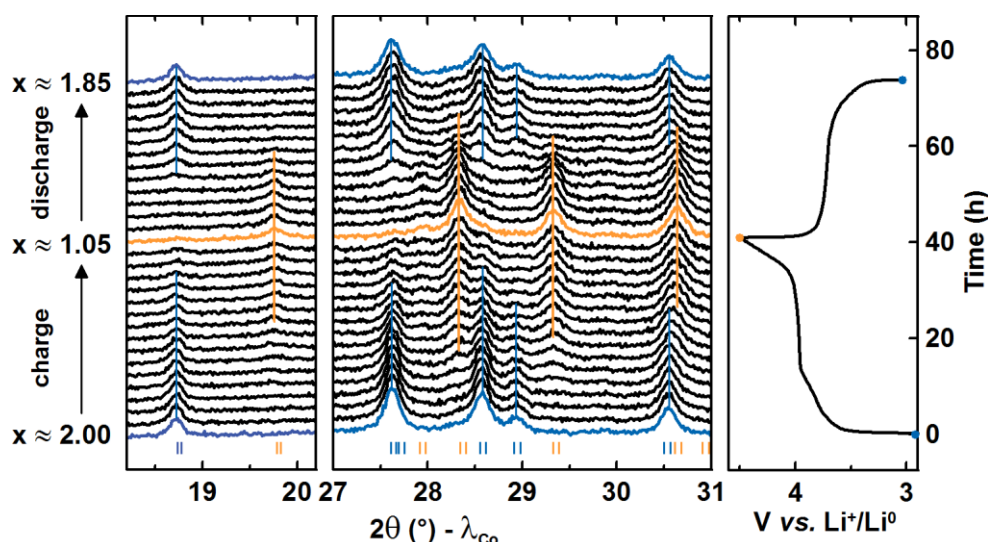
Figure F.10 : Diagrammes de DRX du materiau d'électrode $Li_2Fe(SO_4)_2/C_{SP}$ enregistrés i*n operando*. Les barres bleues et jaunes indiquent la position des reflections de Bragg pour les phases $Li_2Fe(SO_4)_2$ et $Li_1Fe(SO_4)_2$.

Nous avons tout d'abord remarqué que le spectre Mössbauer du matériau d'électrode ($Li_2Fe(SO_4)_2$ mélangé à 20% de C_{SP} par broyage mécanique) était distinct de celui du matériau actif seul. Alors que notre spectre de référence de $Li_2Fe(SO_4)_2$ présentait un doublet majoritaire de Fe(II+) (noté Fe(II+)·A) ayant les paramètres hyperfins suivants : $\delta = 1,30(1)$ mm/s, $\Delta Eq = 1,16(1)$ mm/s, $\Gamma = 0.27(1)$ mm/s et représentant plus de 92% du fer de l'échantillon, nous avons eu besoin de quatre doublets de Fe(II+) (environnements notés Fe(II+)·A1, Fe(II+)·A2, Fe(II+)·B1 et Fe(II+)·B2) pour simuler le spectre du matériau d'électrode avant cyclage (**Figure F.11**.**a**). Pendant la première partie de la charge ($2 \geq x \geq 1,6$, *i.e.* la partie pentue de la courbe électrochimique), nous observons que la contribution relative des sous-spectres Fe(II+)·B1 et Fe(II+)·B2 (en vert) diminue au profit de l'apparition d'un nouveau doublet de Fe(III+) (**Figure F.11**.**a** à **c**); puis lorsque les signaux Fe(II+)·B1 et Fe(II+)·B2 ont totalement disparu et que la courbe électrochimique aborde le plateau, le fer de type Fe(II+)·A1 et Fe(II+)·A2 (en bleu) commence a être oxydé (**Figure F.11**.**c** à **g**). A la fin de la charge, la totalité du fer est à l'état d'oxydation III+ (**Figure F.11**.**g**). En décharge, en revanche, les quatre environnements de fer divalent apparaissent simultanément au fur et à mesure que le fer trivalent est réduit et jusqu'à la fin du premier cycle, où l'on retrouve un spectre très similaire à celui du matériau d'électrode initial (**Figure F.11**.**h** à **k**).
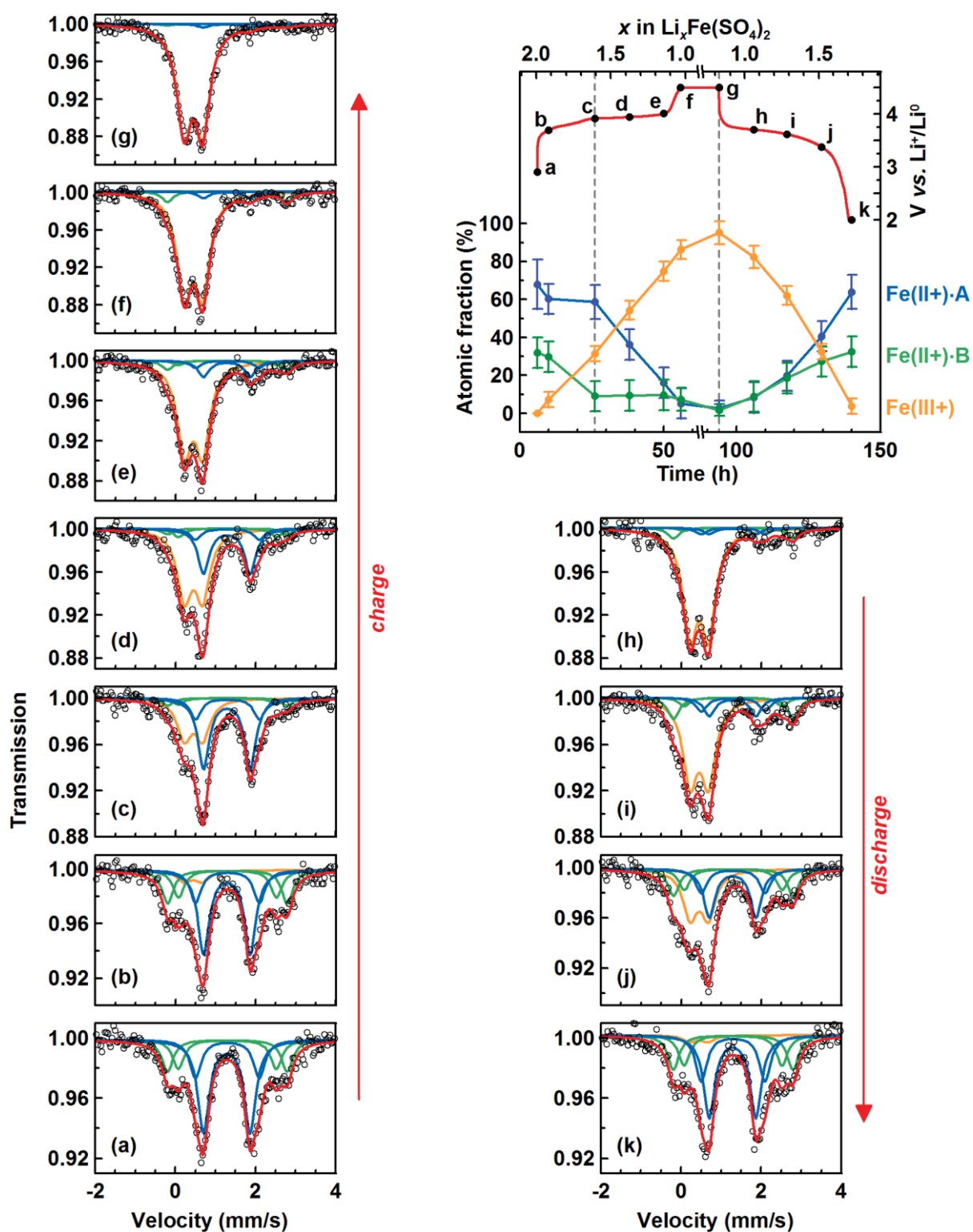
Figure F.11 : Spectres Mössbauer du [57]Fe enregistrés *in operando* pendant le cyclage du matériau d'électrode Li$_2$Fe(SO$_4$)$_2$/C$_{SP}$ face au lithium métallique. Les cercles noirs et les lignes rouges représentent respectivement les spectres expérimentaux et simulés. Les sous-spectres bleus correspondent aux contributions notées Fe(II)·A1 et A2, les sous-spectres verts représentent celles notées Fe(II)·B1 et B2. Dans le graphique en haut à droite, l'état de charge/décharge de l'électrode est indiqué par des points noirs sur la courbe électrochimique en rouge. L'évolution pendant le cyclage des contributions relatives des environnements Fe(II)·A, Fe(II)·B et Fe(III+) est représentée sur le même graphique par les courbes bleue, verte et jaune, respectivement.

Ainsi, nous avons montré grâce à cette expérience Mössbauer *in operando* que la phase $Li_2Fe(SO_4)_2$ était altérée pendant la préparation du matériau d'électrode par broyage mécanique. Le nouvel environnement de fer ainsi généré (Fe(+II)·B) s'oxyde au début de la charge (partie pentue de la courbe électrochimique) alors que le fer de la phase cristalline $Li_2Fe(SO_4)_2$ (Fe(+II)·A) ne rentre en jeu qu'à partir du plateau centré à 3.83 V.
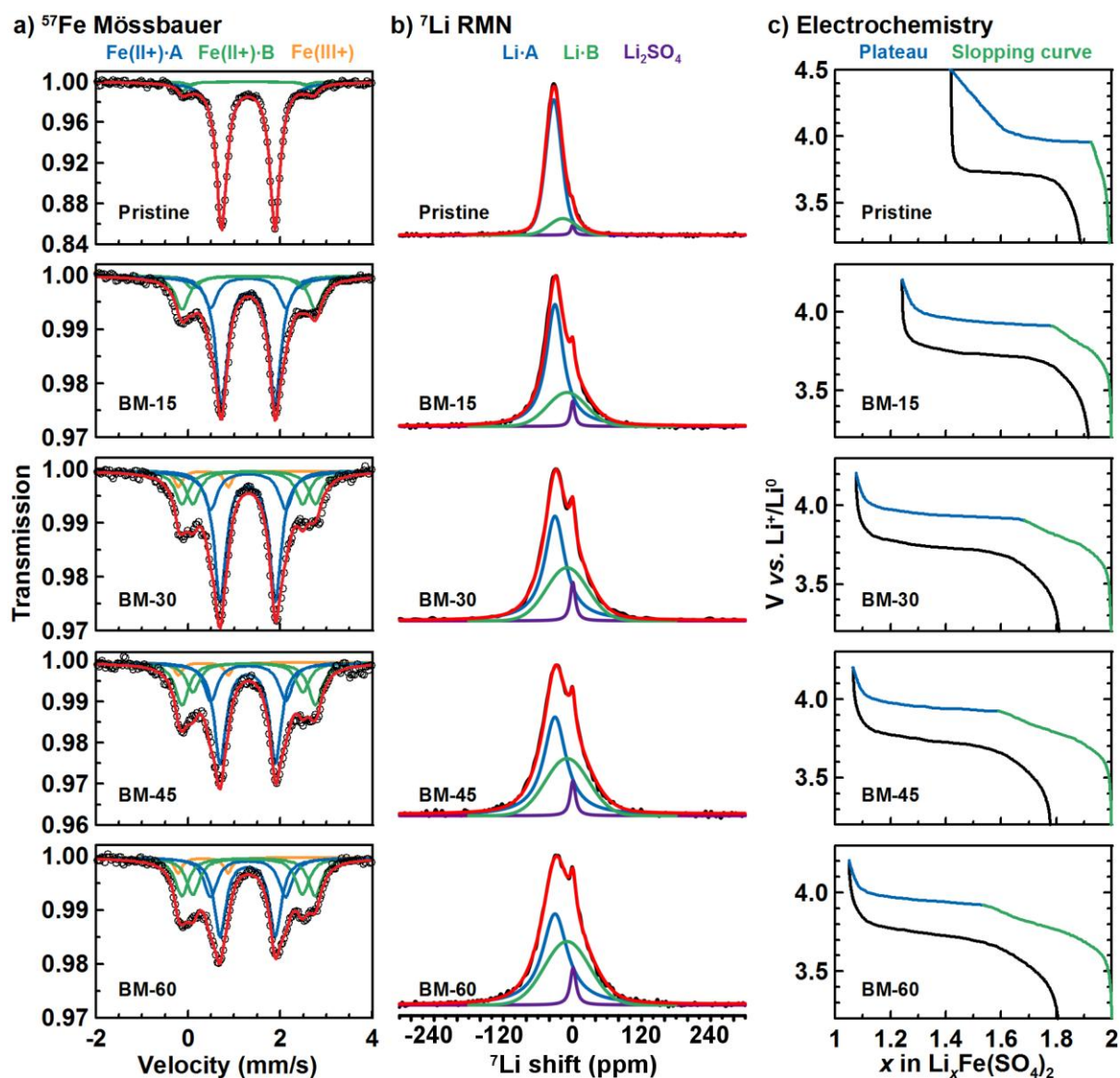
Figure F.12 : Influence du temps de broyage sur les propriétés du matériau d'électrode $Li_2Fe(SO_4)_2/C_{SP}$. (a) Spectres Mössbauer du ^{57}Fe, (b) spectres RMN du ^{7}Li à l'état solide et (c) courbes électrochimiques de la phase $Li_2Fe(SO_4)_2$ et des matériaux d'électrode broyés pendant 15, 30, 45 et 60 minutes (de haut en bas). La première courbe électrochimique a été obtenue avec un matériau d'électrode de $Li_2Fe(SO_4)_2$ coaté avec du carbone et non broyé.

Pour complètement confirmer cette hypothèse, nous avons combiné des mesures de diffraction des rayons X, spectrométrie Mössbauer, RMN du ^{7}Li à l'état solide et cyclages galvanostatiques sur plusieurs matériaux d'électrodes préparés avec différents temps de broyage (**Figure F.12**). Ces

caractérisations ont permis de montrer que la modification du matériau d'électrode par broyage mécanique est directement corrélée à la longueur de la partie pentue de la courbe électrochimique. Le matériau d'électrode ainsi altéré est vraisemblablement très mal cristallisé puisque non visible par diffraction des rayons X. L'analyse quantitative des résultats Mössbauer et RMN a par ailleurs permis d'établir que le ratio Li:Fe dans le matériau altéré est identique à celui de la phase *marinite* $Li_2Fe(SO_4)_2$, ce qui pourrait suggère qu'il puisse être simplement une phase $Li_2Fe(SO_4)_2$ amorphe, très désordonnée.

F.3.3.   Conclusion

Nous avons présenté une nouvelle famille de composés ayant la formule générale $Li_2M(SO_4)_2$ (*M* = Co, Fe, Mn, Mg, Zn, Ni), parmi lesquels seuls trois de ces phases avaient été précédemment rapportées [404,405,425]. Après avoir déterminé la structure monoclinique dans laquelle cinq de ces phases cristallisent, nous avons étudié les propriétés électrochimiques de l'analogue au fer. Malgré une capacité spécifique relativement faible (~85 mAh/g), $Li_2Fe(SO_4)_2$ est un matériau d'électrode très intéressant d'un point de vue fondamental car il possède un potentiel redox élevé de 3,83 V *vs.* Li^+/Li^0 ; ce potentiel étant en fait le plus haut potentiel jamais rapporté pour le couple redox Fe^{III+}/Fe^{II+} dans un composé inorganique dépourvu de fluor.

Outre les propriétés électrochimiques présentées par le composé au fer, nous avons par la suite montré que les composés $Li_2M(SO_4)_2$ (*M* = Co, Fe, Mn, Ni) sont également intéressants du point de vue de leurs propriétés magnétiques.

F.4.   Etude magnétique des composés $Li_2M(SO_4)_2$ (*M* = Co, Fe, Mn, Ni)

Etant basés sur des métaux de transition 3d, les nouveaux matériaux d'électrodes sont souvent intéressants à étudier pour leurs propriétés magnétiques. De manière similaire aux potentiels de leurs couples redox, les propriétes magnétiques des matériaux polyanioniques sont gouvernées par la façon dont les orbitales 3d des métaux de transition se recouvrent avec les orbitales 2p des atomes d'oxygène (*i.e.* l'ionocovalence de la liaison *M*–O). Les interactions magnétiques dans ces structures sont généralement de deux types : *(i)* des interactions de super-échange, qui impliquent deux cations métalliques connectés *via* un seul atome d'oxygène (*M*–O–*M*), et *(ii)* des interactions de super-super-échange, dans lesquelles deux métaux de transition sont liés *via* deux atomes d'oxygène appartenant à un groupement polyanionique (*M*–O–O–*M*). Les couplages magnétiques *M*–*M* impliqués dans ces deux types d'interactions sont décrits par les règles semi-empiriques de Goodenough-Kanamori-Anderson [459–464]. Remarquons que ces règles ont été initialement établies pour des interactions de super-échange, mais qu'elles s'appliquent aussi pour les

interactions de super-super-échange, bien que la force de ce couplage entre deux métaux de transition est plus faible que dans le cas du super-échange **[464]**.
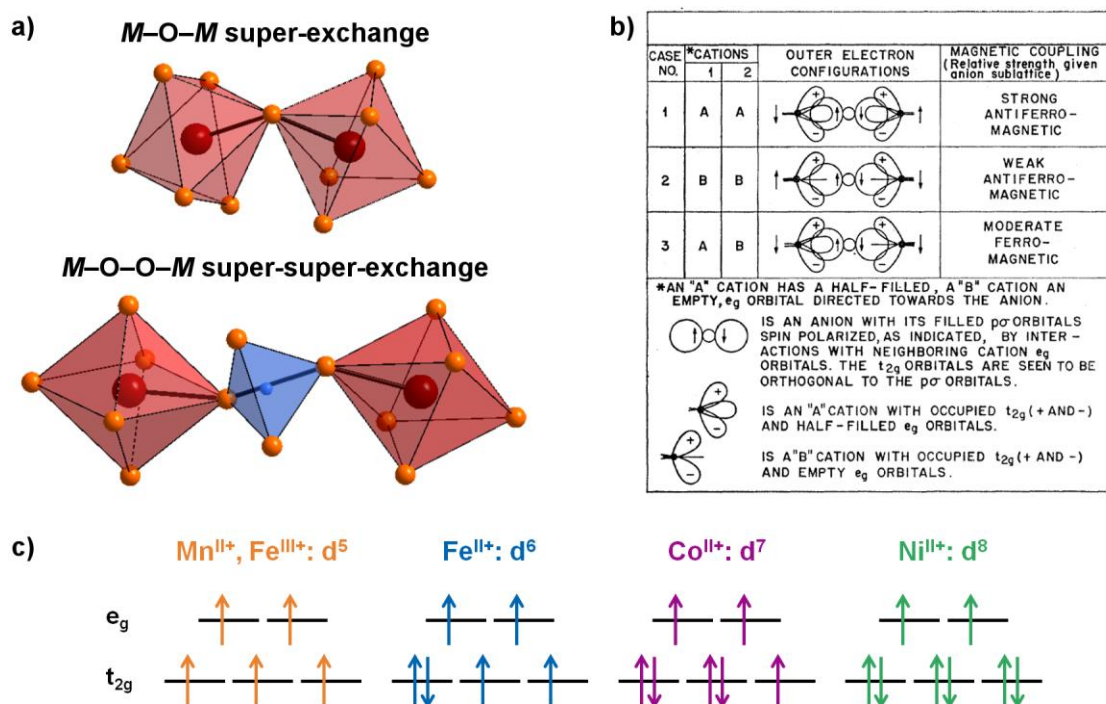
Figure F.13 : (a) Topologie des interactions de super-échange et de super-super-échange entre deux métaux de transition M (représentés par des boules rouges). Les segments noirs indiquent les chemins d'interaction. Les boules orange sont les atomes d'oxygène et les tétraèdres bleus représentent un groupement polyanionique tel que PO_4, SO_4 ou AsO_4. (b) Règles de Goodenough-Kanamori-Anderson pour des interactions de super-échange à 180° (d'après **[463]**). (c) Configurations électroniques des cinq métaux de transition présents dans les composés $Li_2M(SO_4)_2$ étudiés ici. Remarquons que tous correspondent au cas n°1 (cations "A" avec des orbitales e_g à moitié remplies) des règles de Goodenough-Kanamori-Anderson décrites dans (b).

La structure orthorhombique de $Li_2Ni^{II}(SO_4)_2$ et la structure monoclinique des phases $Li_2Fe^{II}(SO_4)_2$, $Li_1Fe^{III}(SO_4)_2$, $Li_2Mn^{II}(SO_4)_2$ et $Li_2Co^{II}(SO_4)_2$ présentent toutes deux des arrangements singuliers d'octaèdres MO_6 qui sont interconnectés au travers de tétraèdres SO_4. Les seules interactions magnétiques possibles dans ces cinq phases sont donc de type super-super-échange.

Dans cette étude, nous avons montré que tous ces composés s'ordonnent antiferromagnétiquement à basse température **[442,484]**. L'évolution de leurs courbes de susceptibilité magnétique en fonction de la température (**Figure F.14**) a pu être modélisée avec des modèles de type Curie-Weiss. De plus, les courbes d'aimantation enregistrées à 2K ont montré que les composés à base de Co^{II+}, Mn^{II+} et Fe^{III+} présentent un ferromagnétisme faible et que $Li_2Co^{II}(SO_4)_2$ pourrait avoir un comportement méta-magnétique.
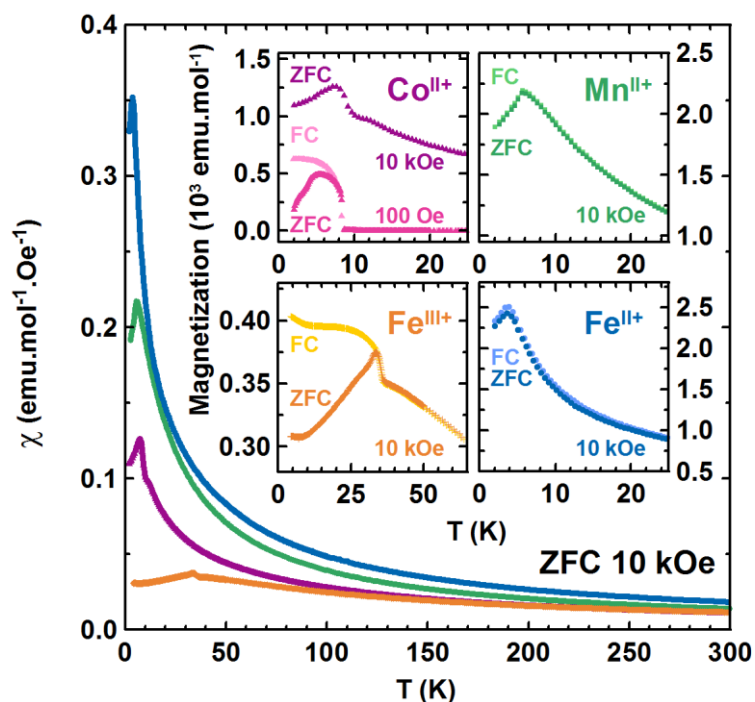
Figure F.14 : Evolution de la susceptibilité magnétique des composés *marinite* $Li_xM(SO_4)_2$ (*x* = 2, 1 & *M* = Co^{II+}, Fe^{II+}, Mn^{II+}, Fe^{III+}) en fonction de la température, refroidis sous champ nul (conditions ZFC) et mesurés avec un champ de 10 kOe entre 2 K et 300 K. Les inserts montrent des agrandissements des courbes d'aimantation des quatre phases refroidies sous champ nul (ZFC, couleurs vives) et sous champ (FC, couleurs pâles).

Nous avons observé par des mesures de diffraction des neutrons sur poudre (NPD) que les moments magnétiques de ces cinq phases s'ordonnaient à basse température (**Figure F.15** et **Figure F.17** gauche), et nous en avons résolu les structures magnétiques à 2 K (**Figure F.16** et **Figure F.17** droite) **[442,484]**. Pour les phases $Li_1Fe^{III}(SO_4)_2$, $Li_2Mn^{II}(SO_4)_2$ et $Li_2Co^{II}(SO_4)_2$, nous avons déterminé un vecteur de propagation nul et un couplage antiferromagnétique le long de la direction [011] ; les trois structures présentent des moments colinéaires et ne diffèrent que par l'orientation de leurs moments. Dans le cas de $Li_2Fe^{II}(SO_4)_2$, la structure magnétique est un peu plus complexe, puisque le vecteur de propagation est **k** = (½, 0, 0) et que les moments magnétiques ne sont alors plus colinéaires. Enfin, dans la phase orthorhombique $Li_2Ni^{II}(SO_4)_2$, les moments sont alignés antiferromagnétiquement selon l'axe *c* et la structure magnétique peut être décrite comme un empilement antiferromagnétique de couches ferromagnétiques selon ce même axe.

Enfin, les premières analyses du signe et de la force relative des interactions d'échange pour ces cinq composés ont montré que les règles semi-empiriques de Goodenough-Kanamori-Anderson **[459–464]** sont respectées dans ces matériaux où seules des interactions de super-super-échange gouvernent la mise en ordre magnétique.
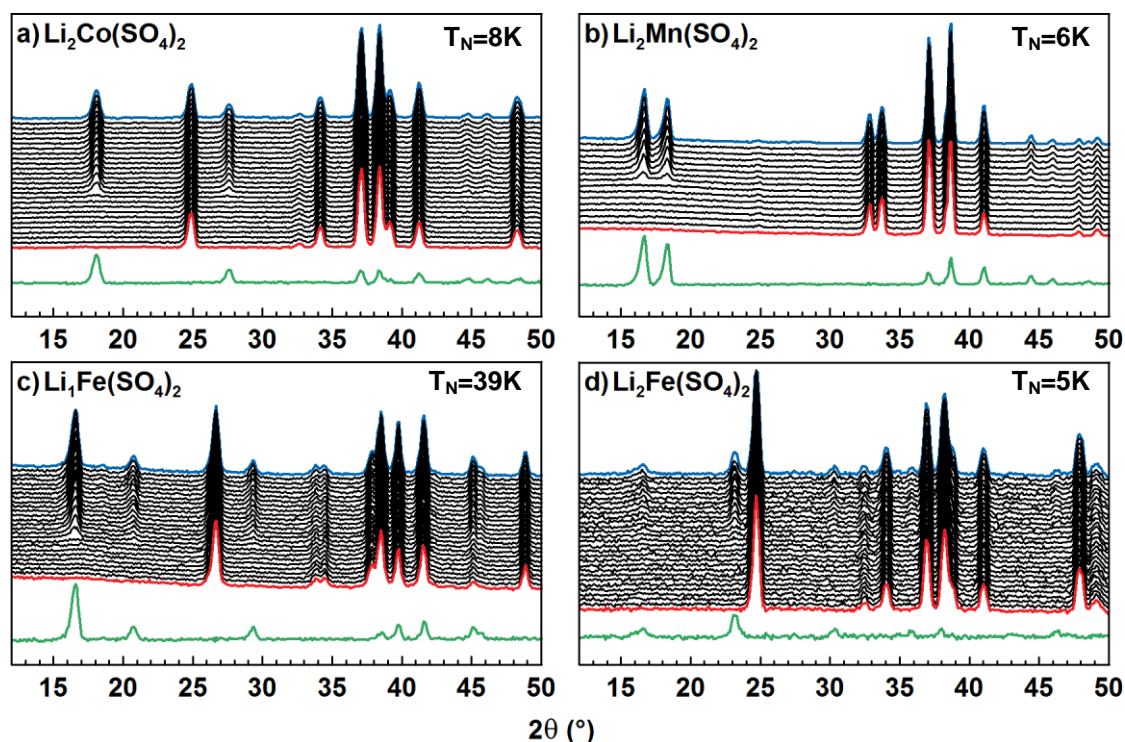
Figure F.15 : Evolution des diagrammes de diffraction des neutrons sur poudre de (a) $Li_2Co(SO_4)_2$, (b) $Li_2Mn(SO_4)_2$, (c) $Li_1Fe(SO_4)_2$ et (d) $Li_2Fe(SO_4)_2$ pendant le refroidissement des échantillons à 2 K (λ = 2.42 Å). Les diagrammes bleus correspondent à la température de 2 K tandis que les rouges ont été mesurés à (a) 12 K, (b) 10 K, (c) 50 K et (d) 7 K. Les diagrammes noirs correspondent aux températures intermédiaires. Les lignes vertes sont les courbes de différence entre les diagrammes bleu et rouge, et montrent ainsi les pics magnétiques apparaissant lors de la mise en ordre des moments magnétiques à basse température.
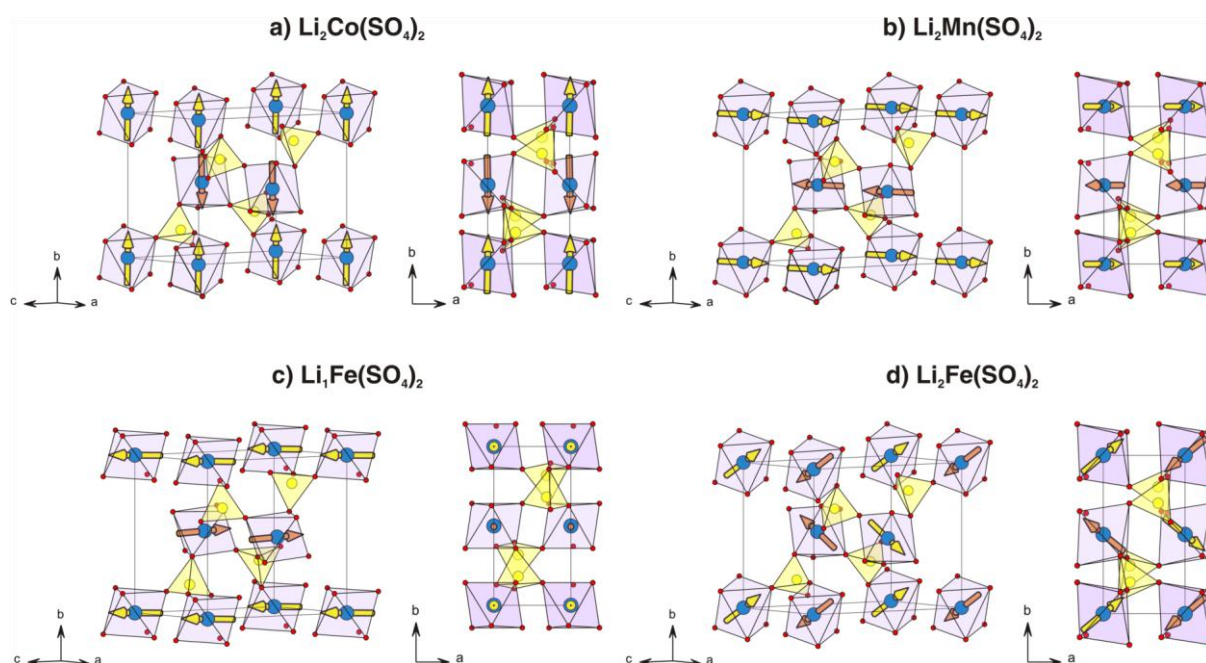
Figure F.16 : Structures nucléaires et magnétiques de (a) $Li_2Co^{II}(SO_4)_2$, (b) $Li_2Mn^{II}(SO_4)_2$, (c) $Li_1Fe^{III}(SO_4)_2$ et (d) $Li_2Fe(SO_4)_2$. Les moments magnétiques sont représentés par un vecteur traversant les atomes de métaux de transition. Les atomes de lithium ont été omis pour plus de clarté.
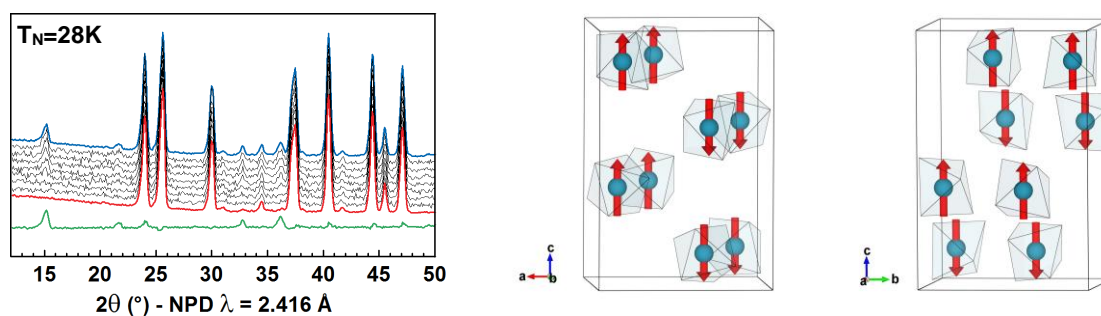
Figure F.17 : A gauche : évolution des diagrammes de NPD de $Li_2Ni(SO_4)_2$ entre 35 K (diagramme rouge) et 2 K (diagramme bleu). Les diagrammes enregistrés aux températures intermédiaires sont tracés en noir. La ligne verte est la différence entre les diagrammes bleu et rouge. A droite : Structure magnétique de $Li_2Ni(SO_4)_2$. Les boules bleues indiquent la position des atomes de Ni dans la maille, et les vecteurs rouges représentent leurs moments magnétiques. Les autres atomes (Li, S, O) sont omis pour plus de clarté.

En conclusion, nous avons montré au cours de cette étude que les cinq phases $Li_2M(SO_4)_2$ (M = Co, Fe, Mn, Ni) s'ordonnent antiferromagnétiquement à basse température. De plus, nous pouvons remarquer que $Li_2Fe^{II}(SO_4)_2$, qui présente l'un des plus hauts potentiels redox (3,83 V *vs*. Li^+/Li^0) rapporté pour un matériau d'électrode polyanionique à base de fer, possède également l'une des plus basses températures de Néel (T_N = 5 K). La **Figure F.18** suggère en fait que les valeurs de potentiels du couple Fe^{III+}/Fe^{II+} pourraient être corrélées aux valeurs de températures de Néel dans les matériaux polyanioniques **[323,494]**. La force des interactions magnétiques entre les métaux 3d et le positionnement de leurs potentiels redox sont tous deux gouvernés par l'ionocovalence des liaisons M-O dans les composés polyanioniques. En effet, plus le recouvrement entre les orbitales 3d du métal de transition et les orbitales 2p de l'oxygène est important, plus la liaison M-O est covalente, plus le potentiel du couple redox $M^{n+}/M^{(n-1)+}$ sera faible, mais plus la température de mise en ordre magnétique T_N sera élevée (*i.e.* la mise en ordre sera plus facile).
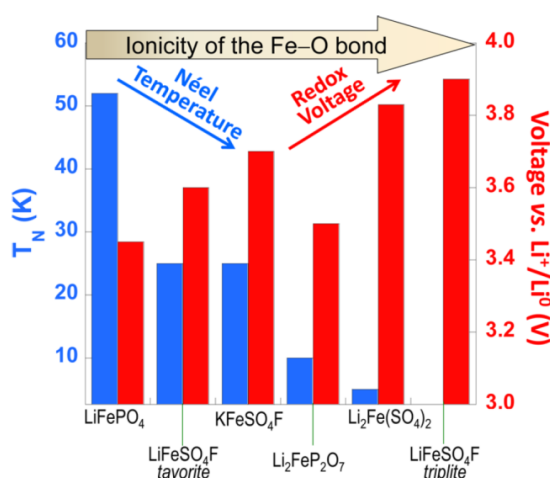
Figure F.18 : Corrélation entre la température de Néel (en bleu) et le potentiel redox (en rouge) pour plusieurs phosphates et sulfates de Fe(II+), montrant que la T_N diminue quand le potentiel redox augmente **[323]**.

F.5.   Conclusion générale

L'objectif de ce travail de thèse était de concevoir de nouveaux matériaux d'électrode positive pour les batteries Li-ion et Na-ion, constitués d'éléments peu chers, durables et inoffensifs pour l'environnement, et présentant des potentiels redox élevés. Guidés par notre précédent travail sur les fluorosulfates à base de fer, qui montraient des potentiels intéressants de 3,6-3,9 V *vs.* Li$^+$/Li^0 **[318,320,321,325,331,335,345,495]**, mais souhaitant s'affranchir des éventuels problèmes de sécurité associés à l'utilisation de fluor, nous avons décidé de concentrer nos efforts sur des composés à base de sulfate. Nous avons alors remarqué que la nature fourni de nombreux exemples de sulfates parmi les minéraux, et nous avons rapidement compris les avantages d'utiliser les espèces minérales comme source d'inspiration : *(i)* la plupart des minéraux ont été bien caractérisés par les minéralogistes et ils contituent ainsi une précieuse banque de données dans laquelle les chimistes peuvent identifier les structures ayant les meilleures caractéristiques pour l'application visée, *(ii)* ces phases minérales sont très probablement thermodynamiquement stables (ou au moins métastables) et la connaissance des conditions de leur formation dans la nature peut fournir une première approche pour leur synthèse en laboratoire, *(iii)* une fois le composé minéral modèle choisi, le chimiste peut modifier la phase de façon à obtenir les propriétés physico-chimiques désirées.

Dans le travail présenté ici, nous avons employé avec succès cette stratégie pour préparer plusieurs composés Na$_2$$M$(SO$_4$)$_2$·4H$_2$O ($M$ = Mg, Zn, Ni, Co, Fe), tous isostructuraux au minéral *bloedite*, et parmi lesquels nous avons montré que la phase à base de fer était électrochimiquement active face au sodium et au lithium **[363]**. Nous avons en fait montré que ce nouveau matériau d'électrode affiche des potentiels élevés de 3,3 V *vs.* Na$^+$/Na^0 et 3,6 V *vs.* Li$^+$/Li^0, qui rivalisent avec ceux rapportés pour d'autres matériaux d'électrode à base de sulfate (par exemple, le NASICON Fe(SO$_4$)$_3$, la *tavorite* LiFeSO$_4$F, la phase lamellaire LiFeSO$_4$OH, la *maxwellite* NaFeSO$_4$F). Nous avons ensuite préparé les dérivés déshydratés α-Na$_2$$M$(SO$_4$)$_2$ (M = Fe, Co) pour lesquels nous avons déterminé une super-structure monoclinique, et nous avons également obtenu de hauts potentiels de 3,4 V *vs.* Na$^+$/Na^0 et 3,6 V *vs.* Li$^+$/Li^0 avec le composé à base de fer **[364]**.

Ensuite, en recherchant des analogues à base de lithium à ces composés, nous avons synthétisé avec succès les phases Li$_2$$M$(SO$_4$)$_2$ (M = Co, Fe, Mn, Mg, Ni, Zn) **[337,426,428,442,484,450]**. Après avoir déterminé la structure monoclinique *marinite* de ces composés, nous avons établi que le composé à base de fer présente un potentiel exceptionnel de 3.83 V *vs.* Li$^+$/Li^0, lequel est en fait le plus haut potentiel jamais rapporté pour le couple redox Fe^{III+}/Fe^{II+} dans un composé inorganique à base de fluor et est seulement dépassé par le polymorphe *triplite* de LiFeSO$_4$F (3,9 V *vs.* Li$^+$/Li^0). Le mécanisme

d'insertion/désinsertion du lithium dans $Li_2Fe(SO_4)_2$ a été étudié par diffraction des rayons X et spectroscopie Mössbauer, et des résultats préliminaires pourraient suggérer l'existence d'un polymorphisme pour $Li_2Fe(SO_4)_2$, comme cela a été précédemment observé pour les phases *tavorite* et *triplite* de $LiFeSO_4F$.

Enfin, nous avons étudié les propriétés magnétiques des phases $Li_2Mn^{II+}(SO_4)_2$, $Li_1Fe^{III+}(SO_4)_2$, $Li_2Fe^{II+}(SO_4)_2$, $Li_2Co^{II+}(SO_4)_2$ et $Li_2Ni^{II+}(SO_4)_2$ et en avons déterminé les strcutures magnétiques à basse température **[442,484]**. Les structures particulières de ces composés permettent uniquement des interactions de super-super-échange, et nous avons donc utilisé ces phases pour tester les règles de Goodenough-Kanamori-Anderson pour ce type d'interactions.

Pour résumer, dans ce travail de thèse, nous avons préparé plusieurs nouveaux sulfates à base de fer et d'ions alcalins, qui présentent des potentiels redox élevés face à des anodes de lithium et de sodium. Nous avons ainsi démontré, et cela a été également confirmé avec les résultats récemment publiés pour l'hydroxysulfate lamellaire $LiFeSO_4OH$ **[342]**, que la présence de fluor dans des matériaux d'électrode à base de sulfate n'est pas indispensable pour atteindre de hauts potentiels. La **Figure F.19** montre en effet que les nouveaux sulfates présentés dans ce manuscrit, et en particulier $Li_2Fe(SO_4)_2$, offrent des potentiels qui sont parmi les plus hauts sur l'échelle de potentiel des matériaux polyanioniques à base de fer étudiés en tant qu'électrode positive pour les batteries Li-ion et Na-ion. Cependant, la **Figure F.19** illustre également bien le principal défaut de nos disulfates bimétalliques $A_xFe(SO_4)_2 \cdot nH_2O$ (A = Li, Na, x = 1, 2 and n = 0, 4) : leurs faibles capacités spécifiques intrinsèques (*i.e.* inférieures à 100 mAh/g) dues au fait qu'ils contiennent deux lourds groupements sulfates par atome de fer. Ceci nous rappelle que concevoir de nouveaux matériaux d'électrode présentant des performances exceptionnelles à la fois en termes de potentiel et de densité d'énergie n'est pas une tâche facile.
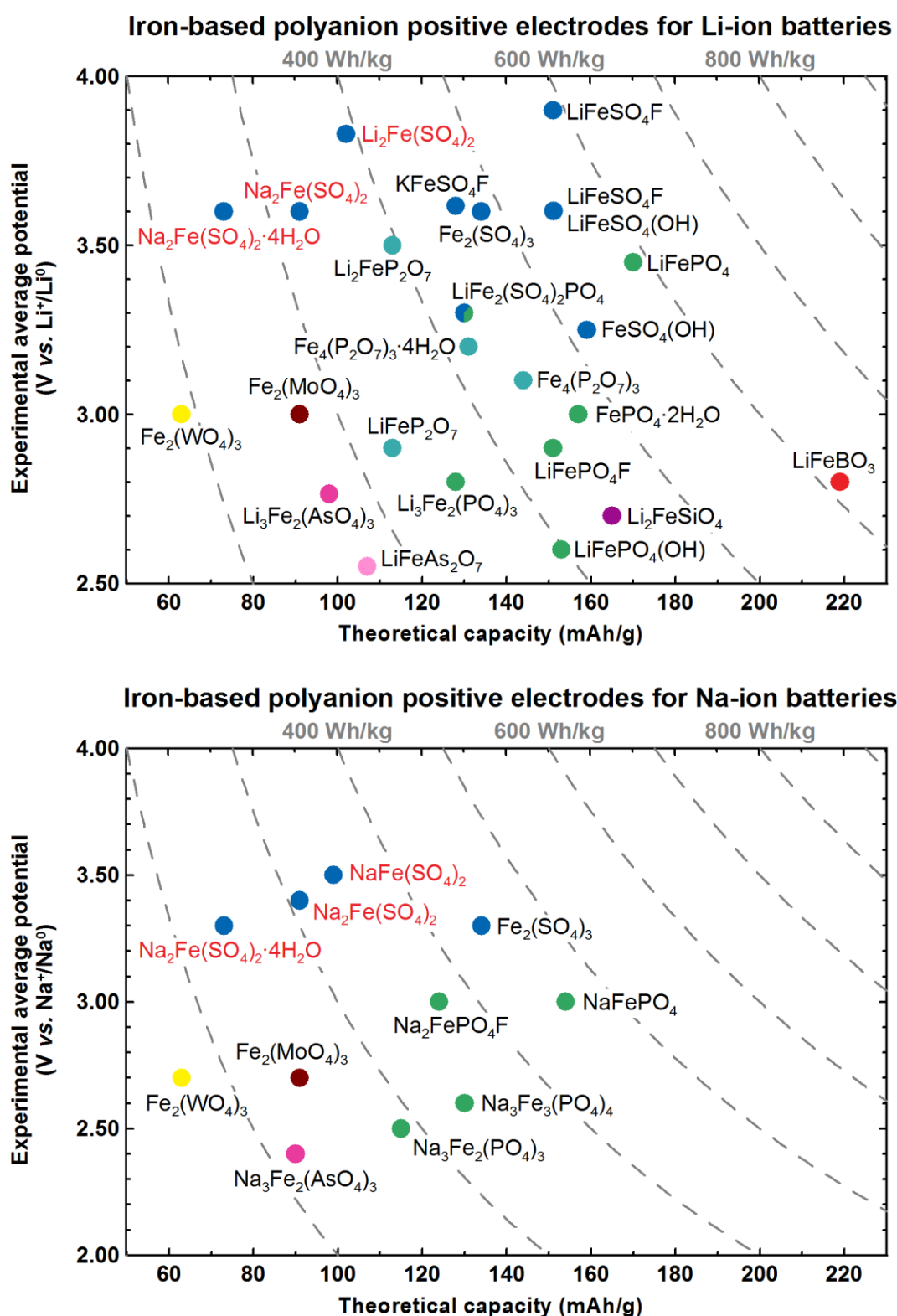
Figure F.19 : Performances, en termes de potentiel expérimental et de capacité spécifique théorique, de différents composés polyanioniques à base de fer étudiés en tant qu'électrode positive pour les batteries Li-ion (en haut) et Na-ion (en bas) (données de la référence [105]). Les différentes familles de composés sont regroupées par couleurs : bleu pour les sulfates, vert pour les phosphates, cyan pour les pyrophosphates, rouge pour les borates, violet pour les silicates, rose pour les arséniates, marron pour les molybdates, jaunes pour les tungstates. Les nouveaux matériaux présentés dans ce manuscrit sont indiqués en rouge.

Nous croyons que les nouveaux sulfates présentés ici restent toutefois des matériaux intéressants, en particulier pour améliorer notre compréhension des facteurs chimiques et structurels qui influencent les potentiels redox des matériaux d'électrode polyanioniques.

Le potentiel d'un couple redox $M^{n+}/M^{(n+1)+}$ dans un composé inorganique est intimement lié à l'iono-covalence de la liaison M–O. La différence observée dans le potentiel d'un couple redox donné entre oxydes et composés polyanioniques est en fait expliquée par le fort caractère covalent des liaisons au sein des groupements polyanioniques (*i.e.* les liaisons X-O), qui affaiblissent la liaison M–O et stabilisent les orbitales anti-liantes du centre redox **[222,232,233]**. Cet effet inductif a été largement décrit depuis les premiers travaux de Goodenough sur les composés NASICON **[222,232,233,496]**. Il explique ainsi très bien les tendances générales observées entre les composés contenant différents groupements polyanioniques : les sulfates présentent de plus haut potentiels redox que les phosphates, lesquels ont généralement de meilleurs potentiels que les silicates, borates ou arsenates (**Figure F.19**). Cependant, la **Figure F.19** montre également des exceptions à cette tendance ; l'effet inductif ne peut en fait être utilisé rigoureusement que lorsque l'on compare des composés isostructuraux (par exemple, pour expliquer les variations de potentiel au sein des composés NASICON ou des phases de structure *tavorite*), mais il est moins évident de l'utiliser pour expliquer les différences observées entre des composés ayant des structures différentes, d'autant plus si elles contiennent le même polyanion **[234]**, et il est même totalement impossible de comparer deux polymorphes ayant la même composition (*e.g. tavorite vs. triplite* $LiFeSO_4F$) avec le seul effet inductif. Au vu de ces observations, il est évident que d'autres facteurs structurels jouent un rôle important dans la stabilisation des couples redox.

Hormis le caractère iono-covalent de la liaison M-O, le champ crystallin autour du cation M^{n+} affecte également le positionnement de l'énergie de ses orbitales anti-liantes **[349,350]**. En fait, la présence de plusieurs cations autour du centre redox (*i.e.* autres métaux de transition M^{n+}, les cations X^{x+} des groupements polyanioniques, mais aussi les cations alcalins A^+) et, plus important encore, la connectivité du polyèdre MO_6 avec les polyèdres voisins MO_6, XO_4 et AO_z (*i.e.* partage de sommets, arêtes ou faces) influencent la force du champ électrique de Madelung ressenti par le cation M^{n+}. Ainsi, de plus courtes distances M–M, M–X ou M–A (par exemple dues à des polyèdres partageant des arêtes ou des faces) conduisent à plus de répulsions cationiques et à un potentiel de Madelung plus faible, ce qui à son tour engendre un potentiel redox plus élevé **[349,350]**.

La principale difficulté réside dans le fait que tous ces paramètres (*i.e.* ionocovalence, champ électrique de Madelung, effet inductif, électronégativité, distances interatomiques, *etc.*) sont intimement corrélés. Les chercheurs essaient donc d'identifier de nouveaux descripteurs (*e.g.,* les

longueurs de liaison M–O, le nombre de polyanions par métal de transition, la coordinence des centres redox, la compacité de la structure, *etc.*) qui permettraient de rationaliser les différences de potentiel observées expérimentalement entre tous les matériaux d'électrode polyanioniques **[115,234,323,349,350]**. Notre groupe a ainsi récemment proposé de corréler les potentiels redox des matériaux d'électrode avec leurs températures de mise en ordre magnétique T_N **[323,494]**, puisque ces deux propriétés dépendent en partie de l'ionocovalence des liaisons M–O ; $Li_2Fe(SO_4)_2$ illustre bien cette correlation, puisqu'il présente à la fois une température de Néel très basse (T_N = 5 K) et l'un des plus hauts potentiels redox (3.83 V *vs.* Li^+/Li^0) observés parmi les composés polyanioniques à base de Fe(II+).

Malheureusement, l''évaluation de ces indicateurs est difficile puisqu'il n'existe pas de structure idéale qui permette de modifier indépendemment chacun paramètre influençant le potentiel redox. Comme dans la grammaire française, quand un nouvel indicateur est proposé pour expliquer l'évolution de potentiel dans une série de composés modèles, on trouve souvent une ou deux exceptions qui limitent rapidement l'universalité de cette règle. Quoi qu'il en soit, la recherche de nouveaux matériaux d'électrode à base de polyanions est une quête de grande importante. Même si ces nouveaux composés ne permettent pas toujours de rivaliser en termes de performances avec les matériaux d'électrodes actuels, ils peuvent, comme l'a démontré ce travail de thèse avec la *marinite* $Li_2Fe(SO_4)_2$, contribuer à une meilleure compréhension des relations existant entre composition, structure et potentiel redox, ce qui facilitera certainement la conception de matériaux de cathodes à base de polyanions présentant de hautes performances pour les prochaines générations de batteries.

References

1. M. Weissenbacher. *Sources of Power: How Energy Forges Human History*. (ABC-CLIO, 2009).

2. Energies - Exposition permanente de la Cité des Sciences (Paris). .

3. International Energy Outlook 2013. *U.S. Energy Information Administration (EIA)*. Available at http://www.eia.gov/forecasts/ieo/index.cfm.

4. World Population Prospects, the 2012 Revision. *United Nations, Department of Economic and Social Affairs*. Available at http://esa.un.org/wpp/Excel-Data/population.htm.

5. *Fourth and fifth Assessment Reports of the Intergovernmental Panel on Climate Change (IPCC)*. (2013) Available at http://www.ipcc.ch.

6. H. Ibrahim, A. Ilinca and J. Perron. Energy storage systems—Characteristics and comparisons. *Renewable and Sustainable Energy Reviews*. Vol. 12, pages 1221–1250 (2008).

7. M. Winter and R. J. Brodd. What Are Batteries, Fuel Cells, and Supercapacitors? *Chemical Reviews*. Vol. 104, pages 4245–4270 (2004).

8. M. R. Palacín. Recent advances in rechargeable battery materials: a chemist's perspective. *Chemical Society Reviews*. Vol. 38, pages 2565–2575 (2009).

9. J.-M. Tarascon and M. Armand. Issues and challenges facing rechargeable lithium batteries. *Nature*. Vol. 414, pages 359–367 (2001).

10. G. Planté. Nouvelle pile secondaire d'une grande puissance. *Comptes rendus hebdomadaires des séances de l'Académie des sciences*. Vol. 50, pages 640–642 (1860).

11. G. Planté. *The Storage Of Electrical Energy*. (1859) Available at http://archive.org/details/storageofelectri031249mbp.

12. A. Volta. On the Electricity excited by the mere Contact of conducting Substances of different kind. *Philosophical transactions of the Royal Society of London*. Vol. 1, pages 403–431 (1800).

13. E. W. Jungner. Method of producing electrodes for electric accumulators. Patent US 731308. Issued June 16, 1903. Available at http://www.google.com/patents?id=M7JlAAAAEBAJ.

14. G. Neumann. Hermetically sealed storage battery. Patent US 2651669. Issued September 8, 1953. Available at http://www.google.com/patents?id=wc5gAAAAEBAJ.

15. Case note - World's Largest Battery Energy Storage System - Fairbanks, Alaska, USA. *ABB Inc. Power Electronics*. Available at http://www05.abb.com/global/scot/scot232.nsf/veritydisplay/3c4e15816e4a7bf1c12578d100500565/$file/case_note_bess_gvea_fairbanks-web.pdf.

16. B. J. R. G. C. M. Van and G. Frens. Electrochemical cell. Patent EP 0301647.–Patent B1. Issued January 18, 1995.

17. C. Déportes, M. Duclot, P. Fabry, J. Fouletier, A. Hammou, M. Kleitz, E. Siebert and J. L. Souquet. *Electrochimie des solides*. (Presses Universitaires de Grenoble, 1994).

18. N. Weber and J. T. Kummer. Sodium-sulfur secondary battery. *Annual Power Sources Conference*. Vol. 21, pages 37–39 (1967).

19. J. T. Kummer and W. Neill. Secondary battery employing molten alkali metal reactant. Patent US 3404035A. Issued October 1, 1968.

20. Energy Storage Case Study - Rokkasho-Futamata Wind Farm: Wind Power + Solar PV Generation + Sodium-Sulfur (NaS) Battery Energy Storage: 85 MW. *CleanEnergy - Action Project*. Available at http://www.cleanenergyactionproject.com/CleanEnergyActionProject/CS.Rokkasho-Futamata_Wind_Farm___Energy_Storage_Case_Study.html.

21. J. Coetzer and M. Nolte. Electrochemical cell. Patent US 4592969. Issued June 3, 1986. Available at http://www.google.com/patents?id=bLE6AAAAEBAJ.

22. C.-H. Dustmann. Advances in ZEBRA batteries. *Journal of Power Sources*. Vol. 127, pages 85–92 (2004).

23. F.Z. Sonick Plans to Manufacture Molten Salt Sodium Nickel Chloride Batteries for Mobile and Stationary Electricity Storage Applications. *Energy Storage News*. (2011) Available at http://www.energystoragenews.com/FZ%20Sonick%20Plans%20to%20Manufacture%20Molten%20Salt%20Sodium%20Nickel%20Choride%20Batteries%20for%20Mobile%20and%20Stationary%20Electricity%20Storage%20Applications.htm.

24. D. R. Vissers, Z. Tomczuk and R. K. Steunenberg. A Preliminary Investigation of High Temperature Lithium/Iron Sulfide Secondary Cells. *Journal of The Electrochemical Society*. Vol. 121, pages 665–667 (1974).

25. E. C. Gay, D. R. Vissers, F. J. Martino and K. E. Anderson. Performance Characteristics of Solid Lithium-Aluminum Alloy Electrodes. *Journal of The Electrochemical Society*. Vol. 123, pages 1591–1596 (1976).

26. T. D. Kaun, P. A. Nelson, L. Redey, D. R. Vissers and G. L. Henriksen. High temperature lithium/sulfide batteries. *Electrochimica Acta*. Vol. 38, pages 1269–1287 (1993).

27. B. C. H. Steele. in *Fast ion Transport in Solids: Solid State Batteries and Devices. Proceedings of the NATO sponsored Advanced Study Institute on Fast ion Transport in Solids, Belgirate, Italy, 5-15 September 1972*. (W. van Gool) pages 103–109 (1973).

28. M. Armand. in *Fast ion Transport in Solids: Solid State Batteries and Devices. Proceedings of the NATO sponsored Advanced Study Institute on Fast ion Transport in Solids, Belgirate, Italy, 5-15 September 1972*. (W. van Gool) pages 665–673 (1973).

29. M. S. Whittingham and F. R. Gamble Jr. The lithium intercalates of the transition metal dichalcogenides. *Materials Research Bulletin*. Vol. 10, pages 363–371 (1975).

30. M. S. Whittingham. Electrical Energy Storage and Intercalation Chemistry. *Science*. Vol. 192, pages 1126–1127 (1976).

31. M. S. Whittingham. The Role of Ternary Phases in Cathode Reactions. *Journal of The Electrochemical Society*. Vol. 123, pages 315–320 (1976).

32. M. S. Whittingham. Preparation of stoichiometric titanium disulfide. Patent US 4007055. Issued February 8, 1977.

33. M. S. Whittingham. Rechargeable electrochemical cell with cathode of stoichiometric titanium disulfide. Patent US 4084046 (division of patent US 4007055). Issued April 11, 1978.

34. M. S. Whittingham. Chalcogenide battery. Patent US 4009052.-Patent A. Issued February 22, 1977.

35. D. W. Murphy and F. A. Trumbore. Metal chalcogenides as reversible electrodes in nonaqueous lithium batteries. *Journal of Crystal Growth*. Vol. 39, pages 185–199 (1977).

36. M. S. Whittingham. Chemistry of intercalation compounds: metal guests in chalcogenide hosts. *Progress in Solid State Chemistry*. Vol. 21, pages 41–99 (1978).

37. M. S. Whittingham. Intercalation chemistry and energy storage. *Journal of Solid State Chemistry*. Vol. 29, pages 303–310 (1979).

38. R. Brec, A. Dugast and A. Le Mehauté. Chemical and electrochemical study of the Li_xFeS_2 cathodic system ($0 < x \leqslant 2$). *Materials Research Bulletin*. Vol. 15, pages 619–625 (1980).

39. R. R. Haering, J. A. R. Stiles and K. Brandt. Lithium molybdenum disulphide battery cathode. Patent US 4224390. Issued September 23, 1980. Available at http://www.google.com/patents?id=MLI3AAAAEBAJ.

40. J. A. R. Stiles, K. Brandt, D. S. Wainwright and K. C. Lee. Constant volume lithium battery cell and process. Patent US 4587182. Issued May 6, 1986.

41. A. H. Thompson and M. S. Whittingham. Intercalated transition metal phosphorus trisulfides. Patent 4049879. Issued September 20, 1977. Available at http://www.google.com/patents?id=MVk6AAAAEBAJ.

42. A. H. Thompson and M. S. Whittingham. Transition metal phosphorus trisulfides as battery cathodes. *Materials Research Bulletin*. Vol. 12, pages 741–744 (1977).

43. A. Le Méhauté, G. Ouvrard, R. Brec and J. Rouxel. Insertion de lithium la structure lamellaire $NiPS_3$. *Materials Research Bulletin*. Vol. 12, pages 1191–1197 (1977).

44. J. S. Gore and C. R. Walk. Rechargeable Power Source. Patent US 3929504. Issued December 30, 1975. Available at http://www.google.com/patents/US3929504.

45. D. W. Murphy, P. A. Christian, F. J. Di Salvo and J. V. Waszczak. Lithium incorporation by vanadium pentoxide. *Inorganic Chemistry*. Vol. 18, pages 2800–2803 (1979).

46. D. W. Murphy and P. A. Christian. Solid State Electrodes for High Energy Batteries. *Science*. Vol. 205, pages 651–656 (1979).

47. J. O. Besenhard and R. Schöllhorn. The discharge reaction mechanism of the MoO_3 electrode in organic electrolytes. *Journal of Power Sources*. Vol. 1, pages 267–276 (1976).

References

48. K. Mizushima, P. C. Jones, P. J. Wiseman and J. B. Goodenough. Li_xCoO_2 (0<x<-1): A new cathode material for batteries of high energy density. *Materials Research Bulletin*. Vol. 15, pages 783–789 (1980).

49. K. Mizushima, P. C. Jones, P. J. Wiseman and J. B. Goodenough. Li_xCoO_2 (0<x≤1): A new cathode material for batteries of high energy density. *Solid State Ionics*. Vol. 3–4, pages 171–174 (1981).

50. J. B. Goodenough and K. Mizuchima. Electrochemical cell with new fast ion conductors. Patent US 4302518.-Patent A. Issued November 24, 1981.

51. J. B. Goodenough and K. Mizushima. Fast ion conductors. Patent US 4357215.-Patent A. Issued November 2, 1982.

52. A. N. Dey. Electrochemical Alloying of Lithium in Organic Electrolytes. *Journal of The Electrochemical Society*. Vol. 118, pages 1547–1549 (1971).

53. B. M. L. Rao, R. W. Francis and H. A. Christopher. Lithium-Aluminum Electrode. *Journal of The Electrochemical Society*. Vol. 124, pages 1490–1492 (1977).

54. I. Epelboin, M. Froment, M. Garreau, J. Thevenin and D. Warin. Behavior of Secondary Lithium and Aluminum-Lithium Electrodes in Propylene Carbonate. *Journal of The Electrochemical Society*. Vol. 127, pages 2100–2104 (1980).

55. J. Wang, I. D. Raistrick and R. A. Huggins. Behavior of Some Binary Lithium Alloys as Negative Electrodes in Organic Solvent-Based Electrolytes. *Journal of The Electrochemical Society*. Vol. 133, pages 457–460 (1986).

56. Y. Matsuda. International Power Sources Symposium, 32nd, Cherry Hill, NJ, June 9-12, 1986, Proceedings. in *32nd International Power Sources Symposium*. Vol. 1, page 124 (1986).

57. M. B. Armand. in *Materials for Advanced Batteries*. (Murphy, D. W., Broadhead, J. & Steele, B. C. H.) pages 145–161 (Springer US, 1980) Available at http://link.springer.com/chapter/10.1007/978-1-4684-3851-2_7.

58. D. W. Murphy, F. J. Di Salvo, J. N. Carides and J. V. Waszczak. Topochemical reactions of rutile related structures with lithium. *Materials Research Bulletin*. Vol. 13, pages 1395–1402 (1978).

59. M. Lazzari and B. Scrosati. A Cyclable Lithium Organic Electrolyte Cell Based on Two Intercalation Electrodes. *Journal of The Electrochemical Society*. Vol. 127, pages 773–774 (1980).

60. B. Di Pietro, M. Patriarca and B. Scrosati. On the use of rocking chair configurations for cyclable lithium organic electrolyte batteries. *Journal of Power Sources*. Vol. 8, pages 289–299 (1982).

61. M. Lazzari and B. Scrosati. Rechargeable lithium batteries with non-metal electrodes. Patent US 4464447. Issued October 7, 1984.

62. N. Watanabe and M. Fukuba. Primary Cell for Electric Batteries. Patent US 3536532. Issued October 27, 1970. Available at http://www.google.com/patents?id=pCRqAAAAEBAJ.

63. B. K. Brown. *Transactions of the American Electrochemical Society*. Vol. 53, page 113 (1928).

64. K. Braeuer, L. Branch and K. R. Moyes. High Energy Density Battery. Patent US 3514337. Issued May 26, 1970. Available at http://www.google.com/patents/US3514337.

65. J. S. Dunning, W. H. Tiedemann, L. Hsueh and D. N. Bennion. A Secondary, Nonaqueous Solvent Battery. *Journal of The Electrochemical Society*. Vol. 118, pages 1886–1890 (1971).

66. H. F. Hunger and G. J. Heymach. Cathodic Discharge of Graphite Intercalation Compounds in Organic Electrolytes. *Journal of The Electrochemical Society*. Vol. 120, pages 1161–1168 (1973).

67. M. Armand and P. Touzain. Graphite intercalation compounds as cathode materials. *Materials Science and Engineering*. Vol. 31, pages 319–329 (1977).

68. M. Zanini, S. Basu and J. E. Fischer. Alternate synthesis and reflectivity spectrum of stage 1 lithium—graphite intercalation compound. *Carbon*. Vol. 16, pages 211–212 (1978).

69. S. Basu, C. Zeller, P. J. Flanders, C. D. Fuerst, W. D. Johnson and J. E. Fischer. Synthesis and properties of lithium-graphite intercalation compounds. *Materials Science and Engineering*. Vol. 38, pages 275–283 (1979).

70. T. Nakajima, K. Sanechika and A. Yoshino. Secondary battery. Patent US 4668595.-Patent A. Issued May 26, 1987.

71. Y. Nishi, H. Azuma and A. Omaru. Non aqueous electrolyte cell. Patent US 4959281. Issued September 25, 1990.

72. T. Nagaura and K. Tozawa. Lithium ion rechargeable battery. *Prog. Batteries Solar Cells*. Vol. 9, page 209 (1990).

73. Y. Nishi. The development of lithium ion secondary batteries. *The Chemical Record*. Vol. 1, pages 406–413 (2001).

74. K. Ozawa. Lithium-ion rechargeable batteries with $LiCoO_2$ and carbon electrodes: the $LiCoO_2$/C system. *Solid State Ionics*. Vol. 69, pages 212–221 (1994).

75. The Lithium-ion Battery - R&D - Asahi Kasei. *Asahi KASEI*. Available at http://www.asahi-kasei.co.jp/asahi/en/r_and_d/interview/yoshino/.

76. M. Yoshio, R. J. Brodd and A. Kozawa. *Lithium-Ion Batteries - Sciences and Technologies*. (2009).

77. M. Armand, J. M. Chabagno and M. J. Duclot. in *Fast ion Transport in Solids: Electrodes and Electrolytes. Proceedings of the International Conference on Fast ion Transport in Solids, Lake Geneva, Wisconsin, U.S.A., 21-25 May 1979*. (Vashishta, P., Mundy, J.-N. & Shenoy, G. K.) pages 131–136 (1979).

78. M. Armand and M. Duclot. Nouveaux matériaux élastomères à conduction ionique. Patent FR 2442512. Issued June 20, 1980.

79. M. Armand and M. Duclot. Electrochemical generators for producing current and new materials for their manufacture. Patent US 4303748.-Patent A. & Patent CA 1165814.–Patent A1. Issued December 1, 1981.

80. Batscap - la batterie lithium métal polymère. *Batscap*. Available at www.batscap.com/la-batterie-lithium-metal-polymere/technologie.php.

References

81. Bluecar. *Bluecar*. Available at www.bluecar.fr/fr.

82. G. Feuillade and P. Perche. Ion-conductive macromolecular gels and membranes for solid lithium cells. *Journal of Applied Electrochemistry*. Vol. 5, pages 63–69 (1975).

83. I. Kelly, J. R. Owen and B. C. H. Steele. Mixed polyether lithium-ion conductors. *Journal of Electroanalytical Chemistry and Interfacial Electrochemistry*. Vol. 168, pages 467–478 (1984).

84. I. E. Kelly, J. R. Owen and B. C. H. Steele. Poly(ethylene oxide) electrolytes for operation at near room temperature. *Journal of Power Sources*. Vol. 14, pages 13–21 (1985).

85. A. S. Gozdz, C. Schmutz and J.-M. Tarascon. Rechargeable lithium intercalation battery with hybrid polymeric electrolyte. Patent US 5296318. Issued March 22, 1994.

86. A. S. Gozdz, C. Schmutz, J.-M. Tarascon and P. C. Warren. Method of making an electrolyte activatable lithium-ion rechargeable battery cell. Patent US 5456000. Issued October 10, 1995.

87. A. S. Gozdz, C. Schmutz, J.-M. Tarascon and P. C. Warren. Polymeric electrolytic cell separator membrane. Patent US 5418091. Issued May 23, 1995.

88. J.-M. Tarascon, A. S. Gozdz, C. Schmutz, F. Shokoohi and P. C. Warren. Performance of Bellcore's plastic rechargeable Li-ion batteries. *Solid State Ionics*. Vol. 86–88, Part 1, pages 49–54 (1996).

89. History - Valence Technology. *Valence Technology*. Available at http://www.valence.com/about/history.

90. A. S. Nagelberg and W. L. Worrell. A thermodynamic study of sodium-intercalated TaS_2 and TiS_2. *Journal of Solid State Chemistry*. Vol. 29, pages 345–354 (1979).

91. C. Delmas, J.-J. Braconnier, C. Fouassier and P. Hagenmuller. Electrochemical intercalation of sodium in Na_xCoO_2 bronzes. *Solid State Ionics*. Vol. 3-4, pages 165–169 (1981).

92. J. J. Braconnier, C. Delmas and P. Hagenmuller. Etude par desintercalation electrochimique des systemes Na_xCrO_2 et Na_xNiO_2. *Materials Research Bulletin*. Vol. 17, pages 993–1000 (1982).

93. J. Molenda, C. Delmas and P. Hagenmuller. Electronic and electrochemical properties of Na_xCoO_{2-y} cathode. *Solid State Ionics*. Vol. 9–10, pages 431–435 (1983).

94. J.-M. Tarascon and G. W. Hull. Sodium intercalation into the layer oxides $Na_xMo_2O_4$. *Solid State Ionics*. Vol. 22, pages 85–96 (1986).

95. C. Delmas, F. Cherkaoui, A. Nadiri and P. Hagenmuller. A nasicon-type phase as intercalation electrode: $NaTi_2(PO_4)_3$. *Materials Research Bulletin*. Vol. 22, pages 631–639 (1987).

96. Y. Ma, M. M. Doeff, S. J. Visco and L. C. D. Jonghe. Rechargeable Na / Na_xCoO_2 and $Na_{15}Pb_4$ / Na_xCoO_2 Polymer Electrolyte Cells. *Journal of The Electrochemical Society*. Vol. 140, pages 2726–2733 (1993).

97. M. M. Doeff, Y. Ma, S. J. Visco and L. C. D. Jonghe. Electrochemical Insertion of Sodium into Carbon. *Journal of The Electrochemical Society*. Vol. 140, pages L169–L170 (1993).

98. M. M. Doeff, M. Y. Peng, Y. Ma and L. C. D. Jonghe. Orthorhombic Na_xMnO_2 as a Cathode Material for Secondary Sodium and Lithium Polymer Batteries. *Journal of The Electrochemical Society*. Vol. 141, pages L145–L147 (1994).

99. M. M. Doeff, S. J. Visco, M. Yanping, M. Peng, D. Lei and L. C. De Jonghe. Thin film solid state sodium batteries for electric vehicles. *Electrochimica Acta*. Vol. 40, pages 2205–2210 (1995).

100. J. Morales, J. Santos and J. L. Tirado. Electrochemical studies of lithium and sodium intercalation in $MoSe_2$. *Solid State Ionics*. Vol. 83, pages 57–64 (1996).

101. B. L. Ellis and L. F. Nazar. Sodium and sodium-ion energy storage batteries. *Current Opinion in Solid State and Materials Science*. Vol. 16, pages 168–177 (2012).

102. S.-W. Kim, D.-H. Seo, X. Ma, G. Ceder and K. Kang. Electrode Materials for Rechargeable Sodium-Ion Batteries: Potential Alternatives to Current Lithium-Ion Batteries. *Advance Energy Materials*. Vol. 2, pages 710–721 (2012).

103. V. Palomares, P. Serras, I. Villaluenga, K. B. Hueso, J. Carretero-González and T. Rojo. Na-ion batteries, recent advances and present challenges to become low cost energy storage systems. *Energy Environ. Sci.* Vol. 5, pages 5884–5901 (2012).

104. V. Palomares, M. Casas-Cabanas, E. Castillo-Martínez, M. H. Han and T. Rojo. Update on Na-Based Battery Materials. A Growing Research Path. *Energy & Environmental Science*. Vol. 6, pages 2312–2337 (2013).

105. C. Masquelier and L. Croguennec. Polyanionic (Phosphates, Silicates, Sulfates) Frameworks as Electrode Materials for Rechargeable Li (or Na) Batteries. *Chemical Reviews*. Vol. 113, pages 6552–6591 (2013).

106. La pénurie de lithium n'est pas pour demain. *L'Usine Nouvelle*. (2009) Available at http://www.usinenouvelle.com/article/la-penurie-de-lithium-n-est-pas-pour-demain.N118353.

107. Lithium Market Becoming More Reliant on Batteries for Continued Strong Demand Growth. *PR Newswire*. (2013) Available at http://www.prnewswire.com/news-releases/lithium-market-becoming-more-reliant-on-batteries-for-continued-strong-demand-growth-207723401.html.

108. S. Romero. Bolivia has lithium, and the president intends to make world pay for it. *The New York Times*. (2009) Available at http://www.nytimes.com/2009/02/02/world/americas/02iht-lithium.4.19877751.html?pagewanted=all&_r=0.

109. Commodities & statistics. *MineralsUK - British Geological Survey Centre for Sustainable Mineral Development - Natural Environment Research Council*. Available at http://www.bgs.ac.uk/mineralsuk/statistics/home.html.

110. Periodic Table of Elements. *EnvironmentalChemistry.com*. Available at http://environmentalchemistry.com/yogi/periodic.

111. R. D. Shannon. Revised effective ionic radii and systematic studies of interatomic distances in halides and chalcogenides. *Acta Crystallographica Section A*. Vol. 32, pages 751–767 (1976).

112. M. Armand and J.-M. Tarascon. Building better batteries. *Nature*. Vol. 451, pages 652–657 (2008).

113. J. B. Goodenough. Design considerations. *Solid State Ionics*. Vol. 69, pages 184–198 (1994).

114. M. S. Whittingham. Lithium Batteries and Cathode Materials. *Chemical Reviews*. Vol. 104, pages 4271–4302 (2004).

115. J. B. Goodenough and Y. Kim. Challenges for Rechargeable Li Batteries. *Chemistry of Materials*. Vol. 22, pages 587–603 (2010).

116. B. L. Ellis, K. T. Lee and L. F. Nazar. Positive Electrode Materials for Li-Ion and Li-Batteries. *Chem. Mater.* Vol. 22, pages 691–714 (2010).

117. Z. Gong and Y. Yang. Recent advances in the research of polyanion-type cathode materials for Li-ion batteries. *Energy & Environmental Science*. Vol. 4, pages 3223–3242 (2011).

118. Commodity and Metal Prices. *InvestmentMine - Mining Markets & Investment*. Available at http://www.infomine.com/investment/metal-prices.

119. NIOSH Pocket Guide to Chemical Hazards. *Centers for Disease Control and Prevention (CDC) - U.S. National Institute for Occupational Safety and Health (NIOSH)*. Available at http://www.cdc.gov/niosh/npg/pgintrod.html.

120. S. P. Ong, V. L. Chevrier, G. Hautier, A. Jain, C. Moore, S. Kim, X. Ma and G. Ceder. Voltage, stability and diffusion barrier differences between sodium-ion and lithium-ion intercalation materials. *Energy & Environmental Science*. Vol. 4, pages 3680–3688 (2011).

121. P. Ge and M. Fouletier. Electrochemical intercalation of sodium in graphite. *Solid State Ionics*. Vol. 28–30, Part 2, pages 1172–1175 (1988).

122. D. A. Winn, J. M. Shemilt and B. C. H. Steele. Titanium disulphide: A solid solution electrode for sodium and lithium. *Materials Research Bulletin*. Vol. 11, pages 559–566 (1976).

123. G. H. Newman and L. P. Klemann. Ambient Temperature Cycling of an Na - TiS_2 Cell. *Journal of The Electrochemical Society*. Vol. 127, pages 2097–2099 (1980).

124. J. N. Reimers and J. R. Dahn. Electrochemical and In Situ X-Ray Diffraction Studies of Lithium Intercalation in Li_xCoO_2. *Journal of The Electrochemical Society*. Vol. 139, pages 2091–2097 (1992).

125. E. Rossen, J. N. Reimers and J. R. Dahn. Synthesis and electrochemistry of spinel LT-$LiCoO_2$. *Solid State Ionics*. Vol. 62, pages 53–60 (1993).

126. G. G. Amatucci, J.-M. Tarascon and L. C. Klein. CoO_2, The End Member of the Li_xCoO_2 Solid Solution. *Journal of The Electrochemical Society*. Vol. 143, pages 1114–1123 (1996).

127. M. G. S. R. Thomas, W. I. F. David, J. B. Goodenough and P. Groves. Synthesis and structural characterization of the normal spinel $Li[Ni_2]O_4$. *Materials Research Bulletin*. Vol. 20, pages 1137–1146 (1985).

128. J. R. Dahn, U. von Sacken and C. A. Michal. Structure and electrochemistry of $Li_{1\pm y}NiO_2$ and a new Li_2NiO_2 phase with the $Ni(OH)_2$ structure. *Solid State Ionics*. Vol. 44, pages 87–97 (1990).

129. J. R. Dahn, U. von Sacken, M. W. Juzkow and H. Al-Janaby. Rechargeable $LiNiO_2$ / Carbon Cells. *Journal of The Electrochemical Society*. Vol. 138, pages 2207–2211 (1991).

130. R. Kanno, T. Shirane, Y. Kawamoto, Y. Takeda, M. Takano, M. Ohashi and Y. Yamaguchi. Synthesis, Structure, and Electrochemical Properties of a New Lithium Iron Oxide, $LiFeO_2$, with a Corrugated Layer Structure. *Journal of The Electrochemical Society*. Vol. 143, pages 2435–2442 (1996).

131. R. Kanno, T. Shirane, Y. Inaba and Y. Kawamoto. Synthesis and electrochemical properties of lithium iron oxides with layer-related structures. *Journal of Power Sources*. Vol. 68, pages 145–152 (1997).

132. Y. Sakurai, H. Arai, S. Okada and J. Yamaki. Low temperature synthesis and electrochemical characteristics of $LiFeO_2$ cathodes. *Journal of Power Sources*. Vol. 68, pages 711–715 (1997).

133. K. Ado, M. Tabuchi, H. Kobayashi, H. Kageyama, O. Nakamura, Y. Inaba, R. Kanno, M. Takagi and Y. Takeda. Preparation of $LiFeO_2$ with Alpha- $NaFeO_2$-Type Structure Using a Mixed-Alkaline Hydrothermal Method. *Journal of The Electrochemical Society*. Vol. 144, pages L177–L180 (1997).

134. Y. Sakurai, H. Arai and J. Yamaki. Preparation of electrochemically active α-$LiFeO_2$ at low temperature. *Solid State Ionics*. Vol. 113–115, pages 29–34 (1998).

135. T. Matsumura, R. Kanno, Y. Inaba, Y. Kawamoto and M. Takano. Synthesis, Structure, and Electrochemical Properties of a New Cathode Material, $LiFeO_2$, with a Tunnel Structure. *Journal of The Electrochemical Society*. Vol. 149, pages A1509–A1513 (2002).

136. S. Okada and J. Yamaki. Iron-based cathodes/anodes for Li-ion and post Li-ion batteries. Vol. 10, pages 1104–113 (2004).

137. J. Morales and J. Santos-Peña. Highly electroactive nanosized α-$LiFeO_2$. *Electrochemistry Communications*. Vol. 9, pages 2116–2120 (2007).

138. J. Li, J. Li, J. Luo, L. Wang and X. He. Recent Advances in the $LiFeO_2$-based Materials for Li-ion Batteries. *International Journal of Electrochemical Science*. Vol. 6, pages 1550–1561 (2011).

139. A. R. Armstrong and P. G. Bruce. Synthesis of layered $LiMnO_2$ as an electrode for rechargeable lithium batteries. *Nature*. Vol. 381, pages 499–500 (1996).

140. F. Capitaine, P. Gravereau and C. Delmas. A new variety of $LiMnO_2$ with a layered structure. *Solid State Ionics*. Vol. 89, pages 197–202 (1996).

141. R. Chen and M. S. Whittingham. Cathodic Behavior of Alkali Manganese Oxides from Permanganate. *Journal of The Electrochemical Society*. Vol. 144, pages L64–L67 (1997).

142. Y. Gao, M. V. Yakovleva and W. B. Ebner. Novel $LiNi_{1-x}Ti_{x/2}Mg_{x/2}O_2$ Compounds as Cathode Materials for Safer Lithium-Ion Batteries. *Electrochemical and Solid-State Letters*. Vol. 1, pages 117–119 (1998).

143. C. Pouillerie, L. Croguennec and C. Delmas. The $Li_xNi_{1-y}Mg_yO_2$ (y=0.05, 0.10) system: structural modifications observed upon cycling. *Solid State Ionics*. Vol. 132, pages 15–29 (2000).

144. C. Pouillerie, F. Perton, P. Biensan, J. . Pérès, M. Broussely and C. Delmas. Effect of magnesium substitution on the cycling behavior of lithium nickel cobalt oxide. *Journal of Power Sources*. Vol. 96, pages 293–302 (2001).

145. C. Delmas and I. Saadoune. Electrochemical and physical properties of the $Li_xNi_{1-y}Co_yO_2$ phases. *Solid State Ionics*. Vol. 53–56, pages 370–375 (1992).

146. E. Zhecheva and R. Stoyanova. Stabilization of the layered crystal structure of $LiNiO_2$ by Co-substitution. *Solid State Ionics*. Vol. 66, pages 143–149 (1993).

147. A. Rougier, I. Saadoune, P. Gravereau, P. Willmann and C. Delmas. Effect of cobalt substitution on cationic distribution in $LiNi_{1-y}Co_yO_2$ electrode materials. *Solid State Ionics*. Vol. 90, pages 83–90 (1996).

148. I. Saadoune and C. Delmas. $LiNi_{1-y}Co_yO_2$ positive electrode materials: relationships between the structure, physical properties and electrochemical behaviour. *Journal of Materials Chemistry*. Vol. 6, pages 193–199 (1996).

149. I. Saadoune, M. Ménétrier and C. Delmas. Redox processes in $Li_xNi_{1-y}Co_yO_2$ cobalt-rich phases. *Journal of Materials Chemistry*. Vol. 7, pages 2505–2511 (1997).

150. I. Saadoune and C. Delmas. On the $Li_xNi_{0.8}Co_{0.2}O_2$ System. *Journal of Solid State Chemistry*. Vol. 136, pages 8–15 (1998).

151. J. S. Weaving, F. Coowar, D. A. Teagle, J. Cullen, V. Dass, P. Bindin, R. Green and W. J. Macklin. Development of high energy density Li-ion batteries based on $LiNi_{1-x-y}Co_xAl_yO_2$. *Journal of Power Sources*. Vol. 97–98, pages 733–735 (2001).

152. S. Madhavi, G. V. Subba Rao, B. V. R. Chowdari and S. F. Y. Li. Effect of aluminium doping on cathodic behaviour of $LiNi_{0.7}Co_{0.3}O_2$. *Journal of Power Sources*. Vol. 93, pages 156–162 (2001).

153. K. K. Lee, W. S. Yoon, K. B. Kim, K. Y. Lee and S. T. Hong. Characterization of $LiNi_{0.85}Co_{0.10}M_{0.05}O_2$ (M = Al, Fe) as a cathode material for lithium secondary batteries. *Journal of Power Sources*. Vol. 97–98, pages 308–312 (2001).

154. J. Shim, R. Kostecki, T. Richardson, X. Song and K. A. Striebel. Electrochemical analysis for cycle performance and capacity fading of a lithium-ion battery cycled at elevated temperature. *Journal of Power Sources*. Vol. 112, pages 222–230 (2002).

155. J. Shim and K. A. Striebel. Characterization of high-power lithium-ion cells during constant current cycling: Part I. Cycle performance and electrochemical diagnostics. *Journal of Power Sources*. Vol. 122, pages 188–194 (2003).

156. M. Guilmard, C. Pouillerie, L. Croguennec and C. Delmas. Structural and electrochemical properties of $LiNi_{0.70}Co_{0.15}Al_{0.15}O_2$. *Solid State Ionics*. Vol. 160, pages 39–50 (2003).

157. T. Ohzuku and Y. Makimura. Layered Lithium Insertion Material of $LiCo_{1/3}Ni_{1/3}Mn_{1/3}O_2$ for Lithium-Ion Batteries. *Chemistry Letters*. Vol. 30, pages 642–643 (2001).

158. Z. Lu, D. D. MacNeil and J. R. Dahn. Layered $Li[Ni_xCo_{1-2x}Mn_x]O_2$ Cathode Materials for Lithium-Ion Batteries. *Electrochemical and Solid-State Letters*. Vol. 4, pages A200–A203 (2001).

159. N. Yabuuchi and T. Ohzuku. Novel lithium insertion material of $LiCo_{1/3}Ni_{1/3}Mn_{1/3}O_2$ for advanced lithium-ion batteries. *Journal of Power Sources*. Vol. 119–121, pages 171–174 (2003).

160. B. J. Hwang, Y. W. Tsai, D. Carlier and G. Ceder. A Combined Computational/Experimental Study on $LiNi_{1/3}Co_{1/3}Mn_{1/3}O_2$. *Chemistry of Materials*. Vol. 15, pages 3676–3682 (2003).

161. J.-M. Kim and H.-T. Chung. Role of transition metals in layered Li[Ni,Co,Mn]O$_2$ under electrochemical operation. *Electrochimica Acta*. Vol. 49, pages 3573–3580 (2004).

162. N. Yabuuchi and T. Ohzuku. Electrochemical behaviors of LiCo$_{1/3}$Ni$_{1/3}$Mn$_{1/3}$O$_2$ in lithium batteries at elevated temperatures. *Journal of Power Sources*. Vol. 146, pages 636–639 (2005).

163. C. Delmas, C. Fouassier and P. Hagenmuller. Structural classification and properties of the layered oxides. *Physica B+C*. Vol. 99, pages 81–85 (1980).

164. A. Mendiboure, C. Delmas and P. Hagenmuller. New layered structure obtained by electrochemical deintercalation of the metastable LiCoO$_2$ (O$_2$) variety. *Materials Research Bulletin*. Vol. 19, pages 1383–1392 (1984).

165. Y. Takeda, K. Nakahara, M. Nishijima, N. Imanishi, O. Yamamoto, M. Takano and R. Kanno. Sodium deintercalation from sodium iron oxide. *Materials Research Bulletin*. Vol. 29, pages 659–666 (1994).

166. R. J. Balsys and R. Lindsay Davis. Refinement of the structure of Na$_{0.74}$CoO$_2$ using neutron powder diffraction. *Solid State Ionics*. Vol. 93, pages 279–282 (1997).

167. H. W. Zandbergen, M. Foo, Q. Xu, V. Kumar and R. J. Cava. Sodium ion ordering in Na$_x$CoO$_2$: Electron diffraction study. *Physical Review B*. Vol. 70, page 024101 (2004).

168. G. J. Shu and F. C. Chou. Sodium-ion diffusion and ordering in single-crystal P2-Na$_x$CoO$_2$. *Physical Review B*. Vol. 78, page 052101 (2008).

169. S. Komaba, C. Takei, T. Nakayama, A. Ogata and N. Yabuuchi. Electrochemical intercalation activity of layered NaCrO$_2$ vs. LiCrO$_2$. *Electrochemistry Communications*. Vol. 12, pages 355–358 (2010).

170. C. Didier, M. Guignard, C. Denage, O. Szajwaj, S. Ito, I. Saadoune, J. Darriet and C. Delmas. Electrochemical Na-Deintercalation from NaVO$_2$. *Electrochemical and Solid-State Letters*. Vol. 14, pages A75–A78 (2011).

171. R. Berthelot, D. Carlier and C. Delmas. Electrochemical investigation of the P2–Na$_x$CoO$_2$ phase diagram. *Nature Materials*. Vol. 10, pages 74–80 (2011).

172. D. Carlier, J. H. Cheng, R. Berthelot, M. Guignard, M. Yoncheva, R. Stoyanova, B. J. Hwang and C. Delmas. The P2-Na$_{2/3}$Co$_{2/3}$Mn$_{1/3}$O$_2$ phase: structure, physical properties and electrochemical behavior as positive electrode in sodium battery. *Dalton Transactions*. Vol. 40, page 9306 (2011).

173. M. Guignard, C. Didier, J. Darriet, P. Bordet, E. Elkaïm and C. Delmas. P2-Na$_x$VO$_2$ system as electrodes for batteries and electron-correlated materials. *Nature Materials*. Vol. 12, pages 74–80 (2013).

174. E. J. Wu, P. D. Tepesch and G. Ceder. Size and charge effects on the structural stability of LiMO$_2$ (M = transition metal) compounds. *Philosophical Magazine Part B*. Vol. 77, pages 1039–1047 (1998).

175. M. M. Thackeray, W. I. F. David and J. B. Goodenough. Structural characterization of the lithiated iron oxides Li$_x$Fe$_3$O$_4$ and Li$_x$Fe$_2$O$_3$ (0<x<2). *Materials Research Bulletin*. Vol. 17, pages 785–793 (1982).

176. M. M. Thackeray, W. I. F. David, P. G. Bruce and J. B. Goodenough. Lithium insertion into manganese spinels. *Materials Research Bulletin*. Vol. 18, pages 461–472 (1983).

177. M. M. Thackeray, P. J. Johnson, L. A. de Picciotto, P. G. Bruce and J. B. Goodenough. Electrochemical extraction of lithium from $LiMn_2O_4$. *Materials Research Bulletin*. Vol. 19, pages 179–187 (1984).

178. J. M. Tarascon, E. Wang, F. K. Shokoohi, W. R. McKinnon and S. Colson. The Spinel Phase of $LiMn_2O_4$ as a Cathode in Secondary Lithium Cells. *Journal of The Electrochemical Society*. Vol. 138, pages 2859–2864 (1991).

179. J.-M. Tarascon and D. Guyomard. Li Metal-Free Rechargeable Batteries Based on $Li_{1+x}Mn_2O_4$ Cathodes ($0 \leq x \leq 1$) and Carbon Anodes. *Journal of The Electrochemical Society*. Vol. 138, pages 2864–2868 (1991).

180. M. M. Thackeray. Manganese oxides for lithium batteries. *Progress in Solid State Chemistry*. Vol. 25, pages 1–71 (1997).

181. P. Arora, R. E. White and M. Doyle. Capacity Fade Mechanisms and Side Reactions in Lithium-Ion Batteries. *Journal of The Electrochemical Society*. Vol. 145, pages 3647–3667 (1998).

182. G. Amatucci and J.-M. Tarascon. Optimization of Insertion Compounds Such as $LiMn_2O_4$ for Li-Ion Batteries. *Journal of The Electrochemical Society*. Vol. 149, pages K31–K46 (2002).

183. J. Vetter, P. Novák, M. R. Wagner, C. Veit, K.-C. Möller, J. O. Besenhard, M. Winter, M. Wohlfahrt-Mehrens, C. Vogler and A. Hammouche. Ageing mechanisms in lithium-ion batteries. *Journal of Power Sources*. Vol. 147, pages 269–281 (2005).

184. J.-M. Tarascon, W. R. McKinnon, F. Coowar, T. N. Bowmer, G. Amatucci and D. Guyomard. Synthesis Conditions and Oxygen Stoichiometry Effects on Li Insertion into the Spinel $LiMn_2O_4$. *Journal of The Electrochemical Society*. Vol. 141, pages 1421–1431 (1994).

185. R. Bittihn, R. Herr and D. Hoge. The SWING system, a nonaqueous rechargeable carbon/metal oxide cell. *Journal of Power Sources*. Vol. 43, pages 223–231 (1993).

186. G. G. Amatucci, N. Pereira, T. Zheng, I. Plitz and J.-M. Tarascon. Enhancement of the electrochemical properties of $Li_1Mn_2O_4$ through chemical substitution. *Journal of Power Sources*. Vol. 81–82, pages 39–43 (1999).

187. G. G. Amatucci, N. Pereira, T. Zheng and J.-M. Tarascon. Failure Mechanism and Improvement of the Elevated Temperature Cycling of $LiMn_2O_4$ Compounds Through the Use of the $LiAl_xMn_{2-x}O_{4-z}F_z$ Solid Solution. *Journal of The Electrochemical Society*. Vol. 148, pages A171–A182 (2001).

188. Y. Shin and A. Manthiram. Factors Influencing the Capacity Fade of Spinel Lithium Manganese Oxides. *Journal of The Electrochemical Society*. Vol. 151, pages A204–A208 (2004).

189. T. Numata, C. Amemiya, T. Kumeuchi, M. Shirakata and M. Yonezawa. Advantages of blending $LiNi_{0.8}Co_{0.2}O_2$ into $Li_{1+x}Mn_{2-x}O_4$ cathodes. *Journal of Power Sources*. Vol. 97–98, pages 358–360 (2001).

190. J. Liu, K. Xu, T. R. Jow and K. Amine. Improved Spinel Lithium Manganese Oxide as Cathode for High Power Battery for HEV Application. Vol. MA2002-02, page C2.135 (2002).

191. K. Amine, J. Liu, S. Kang, I. Belharouak, Y. Hyung, D. Vissers and G. Henriksen. Improved lithium manganese oxide spinel/graphite Li-ion cells for high-power applications. *Journal of Power Sources*. Vol. 129, pages 14–19 (2004).

192. P. Strobel and B. Lambert-Andron. Crystallographic and magnetic structure of Li_2MnO_3. *Journal of Solid State Chemistry*. Vol. 75, pages 90–98 (1988).

193. A. Boulineau, L. Croguennec, C. Delmas and F. Weill. Reinvestigation of Li_2MnO_3 Structure: Electron Diffraction and High Resolution TEM. *Chemistry of Materials*. Vol. 21, pages 4216–4222 (2009).

194. A. Boulineau, L. Croguennec, C. Delmas and F. Weill. Structure of Li_2MnO_3 with different degrees of defects. *Solid State Ionics*. Vol. 180, pages 1652–1659 (2010).

195. M. Rossouw and M. Thackeray. Lithium manganese oxides from Li_2MnO_3 for rechargeable lithium battery applications. *Materials Research Bulletin*. Vol. 26, pages 463–473 (1991).

196. C. S. Johnson, S. D. Korte, J. T. Vaughey, M. M. Thackeray, T. E. Bofinger, Y. Shao-Horn and S. A. Hackney. Structural and electrochemical analysis of layered compounds from Li_2MnO_3. *Journal of Power Sources*. Vol. 81–82, pages 491–495 (1999).

197. Y. Paik, C. P. Grey, C. S. Johnson, J.-S. Kim and M. M. Thackeray. Lithium and Deuterium NMR Studies of Acid-Leached Layered Lithium Manganese Oxides. *Chemistry of Materials*. Vol. 14, pages 5109–5115 (2002).

198. P. Kalyani, S. Chitra, T. Mohan and S. Gopukumar. Lithium metal rechargeable cells using Li_2MnO_3 as the positive electrode. *Journal of Power Sources*. Vol. 80, pages 103–106 (1999).

199. A. D. Robertson and P. G. Bruce. Mechanism of Electrochemical Activity in Li_2MnO_3. *Chemistry of Materials*. Vol. 15, pages 1984–1992 (2003).

200. K. Numata, C. Sakaki and S. Yamanaka. Synthesis and characterization of layer structured solid solutions in the system of $LiCoO_2$–Li_2MnO_3. *Solid State Ionics*. Vol. 117, pages 257–263 (1999).

201. K. Numata and S. Yamanaka. Preparation and electrochemical properties of layered lithium–cobalt–manganese oxides. *Solid State Ionics*. Vol. 118, pages 117–120 (1999).

202. B. Ammundsen, J. Paulsen, I. Davidson, R.-S. Liu, C.-H. Shen, J.-M. Chen, L.-Y. Jang and J.-F. Lee. Local Structure and First Cycle Redox Mechanism of Layered $Li_{1.2}Cr_{0.4}Mn_{0.4}O_2$ Cathode Material. *Journal of The Electrochemical Society*. Vol. 149, pages A431–A436 (2002).

203. Z. Lu, D. D. MacNeil and J. R. Dahn. Layered Cathode Materials $Li[Ni_xLi_{(1/3-2x/3)}Mn_{(2/3-x/3)}]O_2$ for Lithium-Ion Batteries. *Electrochemical and Solid-State Letters*. Vol. 4, pages A191–A194 (2001).

204. Z. Lu, L. Y. Beaulieu, R. A. Donaberger, C. L. Thomas and J. R. Dahn. Synthesis, Structure, and Electrochemical Behavior of $Li[Ni_xLi_{1/3-2x/3}Mn_{2/3-x/3}]O_2$. *Journal of The Electrochemical Society*. Vol. 149, pages A778–A791 (2002).

205. J.-S. Kim, C. S. Johnson and M. M. Thackeray. Layered $xLiMO_{2(1-x)}Li_2M'O_3$ electrodes for lithium batteries: a study of $0.95LiMn_{0.5}Ni_{0.5}O_2 \cdot 0.05Li_2TiO_3$. *Electrochemistry Communications*. Vol. 4, pages 205–209 (2002).

206. J.-S. Kim, C. S. Johnson, J. T. Vaughey, M. M. Thackeray, S. A. Hackney, W. Yoon and C. P. Grey. Electrochemical and Structural Properties of $xLi_2M'O_3 \cdot (1-x)LiMn_{0.5}Ni_{0.5}O_2$ Electrodes for Lithium Batteries (M' = Ti, Mn, Zr; $0 \leq x \leqslant 0.3$). *Chemistry of Materials*. Vol. 16, pages 1996–2006 (2004).

207. C. S. Johnson, J.-S. Kim, C. Lefief, N. Li, J. T. Vaughey and M. M. Thackeray. The significance of the Li_2MnO_3 component in "composite" $xLi_2MnO_3 \cdot (1-x)LiMn_{0.5}Ni_{0.5}O_2$ electrodes. *Electrochemistry Communications*. Vol. 6, pages 1085–1091 (2004).

208. M. M. Thackeray, C. S. Johnson, J. T. Vaughey, N. Li and S. A. Hackney. Advances in manganese-oxide "composite" electrodes for lithium-ion batteries. *Journal of Materials Chemistry*. Vol. 15, pages 2257–2267 (2005).

209. M. M. Thackeray, S.-H. Kang, C. S. Johnson, J. T. Vaughey and S. A. Hackney. Comments on the structural complexity of lithium-rich $Li_{1+x}M_{1-x}O_2$ electrodes (M = Mn, Ni, Co) for lithium batteries. *Electrochemistry Communications*. Vol. 8, pages 1531–1538 (2006).

210. C. S. Johnson, N. Li, C. Lefief, J. T. Vaughey and M. M. Thackeray. Synthesis, Characterization and Electrochemistry of Lithium Battery Electrodes: $xLi_2MnO_3 \cdot (1-x)LiMn_{0.333}Ni_{0.333}Co_{0.333}O_2$ ($0 \leq x \leq 0.7$). *Chemistry of Materials*. Vol. 20, pages 6095–6106 (2008).

211. C. S. Johnson, N. Li, J. T. Vaughey, S. A. Hackney and M. M. Thackeray. Lithium–manganese oxide electrodes with layered–spinel composite structures $xLi_2MnO_3 \cdot (1-x)Li_{1+y}Mn_{2-y}O_4$ ($0 < x < 1$, $0 \leqslant y \leqslant 0.33$) for lithium batteries. *Electrochemistry Communications*. Vol. 7, pages 528–536 (2005).

212. Z. Lu, Z. Chen and J. R. Dahn. Lack of Cation Clustering in $Li[Ni_xLi_{1/3-2x/3}Mn_{2/3-x/3}]O_2$ ($0 < x \leq 1/2$) and $Li[Cr_xLi_{(1-x)/3}Mn_{(2-2x)/3}]O_2$ ($0 < x < 1$). *Chemistry of Materials*. Vol. 15, pages 3214–3220 (2003).

213. R. Xiao, H. Li and L. Chen. Density Functional Investigation on Li_2MnO_3. *Chemistry of Materials*. Vol. 24, pages 4242–4251 (2012).

214. H. Koga, L. Croguennec, M. Ménétrier, K. Douhil, S. Belin, L. Bourgeois, E. Suard, F. Weill and C. Delmas. Reversible Oxygen Participation to the Redox Processes Revealed for $Li_{1.20}Mn_{0.54}Co_{0.13}Ni_{0.13}O_2$. *Journal of The Electrochemical Society*. Vol. 160, pages A786–A792 (2013).

215. H. Koga, L. Croguennec, M. Ménétrier, P. Mannessiez, F. Weill and C. Delmas. Different oxygen redox participation for bulk and surface: A possible global explanation for the cycling mechanism of $Li_{1.20}Mn_{0.54}Co_{0.13}Ni_{0.13}O_2$. *Journal of Power Sources*. Vol. 236, pages 250–258 (2013).

216. M. Sathiya, K. Ramesha, G. Rousse, D. Foix, D. Gonbeau, A. S. Prakash, M. L. Doublet, K. Hemalatha and J.-M. Tarascon. High Performance $Li_2Ru_{1-y}Mn_yO_3$ ($0.2 \leq y \leq 0.8$) Cathode Materials for Rechargeable Lithium-Ion Batteries: Their Understanding. *Chemistry of Materials*. Vol. 25, pages 1121–1131 (2013).

217. M. Sathiya, G. Rousse, K. Ramesha, C. P. Laisa, H. Vezin, M. T. Sougrati, M.-L. Doublet, D. Foix, D. Gonbeau, W. Walker, A. S. Prakash, M. Ben Hassine, L. Dupont and J.-M. Tarascon. Reversible

anionic redox chemistry in high-capacity layered-oxide electrodes. *Nature Materials*. Vol. 12, pages 827–835 (2013).

218. A. Nadiri, C. Delmas, R. Salmon and P. Hagenmuller. Chemical and electrochemical alkali metal intercalation in the 3D-framework of $Fe_2(MoO_4)_3$. *Revue de chimie minérale*. Vol. 21, pages 537–544 (1984).

219. W. M. Reiff, J. H. Zhang and C. C. Torardi. Topochemical lithium insertion into $Fe_2(MoO_4)_3$: Structure and magnetism of $Li_2Fe_2(MoO_4)_3$. *Journal of Solid State Chemistry*. Vol. 62, pages 231–240 (1986).

220. C. Delmas, A. Nadiri and J. L. Soubeyroux. The nasicon-type titanium phosphates $ATi_2(PO_4)_3$ (A=Li, Na) as electrode materials. *Solid State Ionics*. Vol. 28–30, pages 419–423 (1988).

221. A. Manthiram and J. B. Goodenough. Lithium insertion into $Fe_2(MO_4)_3$ frameworks: Comparison of M = W with M = Mo. *Journal of Solid State Chemistry*. Vol. 71, pages 349–360 (1987).

222. A. Manthiram and J. B. Goodenough. Lithium insertion into $Fe_2(SO_4)_3$ frameworks. *Journal of Power Sources*. Vol. 26, pages 403–408 (1989).

223. S. Okada, K. S. Nanjundaswamy, A. Manthiram, J. B. Goodenough, H. Ohtsuka, H. Arai and J. Yamaki. $Fe_2(SO_4)_3$ as a cathode material for rechargeable lithium batteries. in *Proceedings of the 36th International Power Sources Symposium*. pages 110–113 (IEEE, 1994).

224. K. S. Nanjundaswamy, A. K. Padhi, J. B. Goodenough, S. Okada, H. Ohtsuka, H. Arai and J. Yamaki. Synthesis, redox potential evaluation and electrochemical characteristics of NASICON-related-3D framework compounds. *Solid State Ionics*. Vol. 92, pages 1–10 (1996).

225. B. Bensaude-Vincent and A. Hessenbruch. Sciences: histoire orale. Entretien avec John B. Goodenough. (2001) Available at http://www.sho.espci.fr/spip.php?article28.

226. H. Y.-P. Hong. Crystal structures and crystal chemistry in the system $Na_{1+x}Zr_2Si_xP_{3-x}O_{12}$. *Materials Research Bulletin*. Vol. 11, pages 173–182 (1976).

227. J. B. Goodenough, H. Y.-P. Hong and J. A. Kafalas. Fast Na^+-ion transport in skeleton structures. *Materials Research Bulletin*. Vol. 11, pages 203–220 (1976).

228. P. C. Christidis and P. J. Rentzeperis. The crystal structure of rhombohedral $Fe_2(SO_4)_3$. *Zeitschrift für Kristallographie*. Vol. 144, pages 341–352 (1976).

229. P. C. Christidis and P. J. Rentzeperis. The crystal structure of the monoclinic $Fe_2(SO_4)_3$. *Zeitschrift für Kristallographie*. Vol. 141, pages 233–245 (1975).

230. S. Patoux. Matériaux d'électrode positive à charpente polyanionique pour batteries au lithium: Approches cristallochimiques et électroniques. Ph.D. dissertation, Amiens (France), September 9, 2003.

231. A. K. Padhi, K. S. Nanjundaswamy, C. Masquelier and J. B. Goodenough. Mapping of transition metal redox energies in phosphates with NASICON structure by lithium intercalation. *Journal of the Electrochemical Society*. Vol. 144, pages 2581–2586 (1997).

232. A. K. Padhi, V. Manivannan and J. B. Goodenough. Tuning the position of the redox couples in materials with NASICON structure by anionic substitution. *Journal of the Electrochemical Society*. Vol. 145, pages 1518–1520 (1998).

233. A. K. Padhi, K. S. Nanjundaswamy and J. B. Goodenough. Phospho-olivines as positive-electrode materials for rechargeable lithium batteries. *Journal of the Electrochemical Society*. Vol. 144, pages 1188–1194 (1997).

234. A. K. Padhi, K. S. Nanjundaswamy, C. Masquelier, S. Okada and J. B. Goodenough. Effect of Structure on the Fe^{3+}/Fe^{2+} Redox Couple in Iron Phosphates. *Journal of The Electrochemical Society*. Vol. 144, pages 1609–1613 (1997).

235. J. B. Goodenough, A. K. Padhi, K. S. Nanjundaswamy and C. Masquelier. Cathode materials for secondary (rechargeable) lithium batteries. Patent US 5910382. Issued June 8, 1999. Available at http://www.google.com/patents?id=RYEZAAAAEBAJ.

236. A. Losey, J. Rakovan, J. M. Hughes, C. A. Francis and M. D. Dyar. Structural Variation in the Lithiophilite–Triphylite Series and Other Olivine-Group Structures. *The Canadian Mineralogist*. Vol. 42, pages 1105–1115 (2004).

237. G. Rousse, J. Rodríguez-Carvajal, S. Patoux and C. Masquelier. Magnetic Structures of the Triphylite $LiFePO_4$ and of Its Delithiated Form $FePO_4$. *Chemistry of Materials*. Vol. 15, pages 4082–4090 (2003).

238. D. Morgan, A. V. der Ven and G. Ceder. Li Conductivity in Li_xMPO_4 (M = Mn , Fe , Co , Ni) Olivine Materials. *Electrochemical and Solid-State Letters*. Vol. 7, pages A30–A32 (2004).

239. M. Armand, M. Gauthier, J. F. Magnan and N. Ravet. Procédé de synthèse de matériau à base de $Li_xM_{1-y}M'_y(XO_4)n$. Patent WO 2002027824A1. Issued April 4, 2002.

240. N. Ravet, J. B. Goodenough, S. Besner, M. Simoneau, P. Hovington and M. Armand. Improved Iron Based Cathode Material. *196th meeting of the Electrochemical Society, Oct. 1999, Honolulu, Hawaii - Abstract n°127*. (1999).

241. N. Ravet, Y. Chouinard, J. F. Magnan, S. Besner, M. Gauthier and M. Armand. Electroactivity of natural and synthetic triphylite. *Journal of Power Sources*. Vol. 97–98, pages 503–507 (2001).

242. H. Huang, S.-C. Yin and L. F. Nazar. Approaching Theoretical Capacity of $LiFePO_4$ at Room Temperature at High Rates. *Electrochemical and Solid-State Letters*. Vol. 4, pages A170–A172 (2001).

243. A. Yamada, S. C. Chung and K. Hinokuma. Optimized $LiFePO_4$ for Lithium Battery Cathodes. *Journal of The Electrochemical Society*. Vol. 148, pages A224–A229 (2001).

244. S. Yang, Y. Song, K. Ngala, P. Y. Zavalij and M. Stanley Whittingham. Performance of $LiFePO_4$ as lithium battery cathode and comparison with manganese and vanadium oxides. *Journal of Power Sources*. Vol. 119–121, pages 239–246 (2003).

245. M. S. Islam, D. J. Driscoll, C. A. J. Fisher and P. R. Slater. Atomic-Scale Investigation of Defects, Dopants, and Lithium Transport in the $LiFePO_4$ Olivine-Type Battery Material. *Chemistry of Materials*. Vol. 17, pages 5085–5092 (2005).

246. A. Yamada, M. Hosoya, S.-C. Chung, Y. Kudo, K. Hinokuma, K.-Y. Liu and Y. Nishi. Olivine-type cathodes: Achievements and problems. *Journal of Power Sources*. Vol. 119–121, pages 232–238 (2003).

247. M. S. Whittingham, Y. Song, S. Lutta, P. Y. Zavalij and N. A. Chernova. Some transition metal (oxy)phosphates and vanadium oxides for lithium batteries. *Journal of Materials Chemistry*. Vol. 15, pages 3362–3379 (2005).

248. Z. Li, D. Zhang and F. Yang. Developments of lithium-ion batteries and challenges of $LiFePO_4$ as one promising cathode material. *Journal of Materials Science*. Vol. 44, pages 2435–2443 (2009).

249. W.-J. Zhang. Comparison of the Rate Capacities of $LiFePO_4$ Cathode Materials. *Journal of The Electrochemical Society*. Vol. 157, pages A1040–A1046 (2010).

250. J. W. Fergus. Recent developments in cathode materials for lithium ion batteries. *Journal of Power Sources*. Vol. 195, pages 939–954 (2010).

251. Y. Wang, P. He and H. Zhou. Olivine $LiFePO_4$: development and future. *Energy & Environmental Science*. Vol. 4, pages 805–817 (2011).

252. K. Amine, H. Yasuda and M. Yamachi. Olivine $LiCoPO_4$ as 4.8 V Electrode Material for Lithium Batteries. *Electrochemical and Solid-State Letters*. Vol. 3, pages 178–179 (2000).

253. A. Yamada and S.-C. Chung. Crystal Chemistry of the Olivine-Type $Li(Mn_yFe_{1-y})PO_4$ and ($Mn_yFe_{1-y})PO_4$ as Possible 4 V Cathode Materials for Lithium Batteries. *Journal of The Electrochemical Society*. Vol. 148, pages A960–A967 (2001).

254. S. Okada, S. Sawa, M. Egashira, J. Yamaki, M. Tabuchi, H. Kageyama, T. Konishi and A. Yoshino. Cathode properties of phospho-olivine $LiMPO_4$ for lithium secondary batteries. *Journal of Power Sources*. Vol. 97–98, pages 430–432 (2001).

255. F. Zhou, M. Cococcioni, K. Kang and G. Ceder. The Li intercalation potential of $LiMPO_4$ and $LiMSiO_4$ olivines with M = Fe, Mn, Co, Ni. *Electrochemistry Communications*. Vol. 6, pages 1144–1148 (2004).

256. C. Delacourt, L. Laffont, R. Bouchet, C. Wurm, J.-B. Leriche, M. Morcrette, J.-M. Tarascon and C. Masquelier. Toward Understanding of Electrical Limitations (Electronic, Ionic) in $LiMPO_4$ (M = Fe, Mn) Electrode Materials. *Journal of The Electrochemical Society*. Vol. 152, pages A913–A921 (2005).

257. C. Delacourt. Apport de la chimie des solutions à la préparation de phosphates de métaux de transition: Influence de la structure et de la morphologie sur le comportement électrochimique dans les accumulateurs au lithium. Ph.D. dissertation, Amiens (France), November 4, 2005 Available at http://charles.delacourt.free.fr.

258. Y. Le Page and G. Donnay. The crystal structure of the new mineral maricite, $NaFePO_4$. *The Canadian Mineralogist*. Vol. 15, pages 518–521 (1977).

259. P. R. Tremaine and C. Xiao. Enthalpies of formation and heat capacity functions for maricite,$NaFePO_4(cr)$, and sodium iron(III) hydroxy phosphate,$Na_3Fe(PO_4)_2 \cdot (Na_{4/3}H_{2/3}O)(cr)$. *The Journal of Chemical Thermodynamics*. Vol. 31, pages 1307–1320 (1999).

260. B. L. Ellis, W. R. M. Makahnouk, Y. Makimura, K. Toghill and L. F. Nazar. A multifunctional 3.5 V iron-based phosphate cathode for rechargeable batteries. *Nature Materials*. Vol. 6, pages 749–753 (2007).

261. P. Moreau, D. Guyomard, J. Gaubicher and F. Boucher. Structure and Stability of Sodium Intercalated Phases in Olivine $FePO_4$. *Chem. Mater.* Vol. 22, pages 4126–4128 (2010).

262. M. Casas-Cabanas, V. V. Roddatis, D. Saurel, P. Kubiak, J. Carretero-González, V. Palomares, P. Serras and T. Rojo. Crystal chemistry of Na insertion/deinsertion in $FePO_4$–$NaFePO_4$. *Journal of Materials Chemistry*. Vol. 22, pages 17421–17423 (2012).

263. S.-M. Oh, S.-T. Myung, J. Hassoun, B. Scrosati and Y.-K. Sun. Reversible $NaFePO_4$ electrode for sodium secondary batteries. *Electrochemistry Communications*. Vol. 22, pages 149–152 (2012).

264. M. Armand, P. Hovington, C. Michot, N. Ravet and M. Simoneau. Lithium insertion electrode materials based on orthosilicate derivatives. Patent US 6085015. Issued July 4, 2000.

265. M. Armand, P. Hovington, C. Michot, N. Ravet and M. Simoneau. New lithium insertion electrode materials based on orthosilicate derivatives. Patent EP 1134826. Issued September 19, 2001.

266. A. Abouimrane, N. Ravet, M. Armand, A. Nytén and J. Thomas. Lithium Iron Silicate and Gemanate as New Cathode Materials. *12th International Meeting on Lithium Batteries, Nara, Japan - Abstract n°350*. (2004) Available at http://www.electrochem.org/meetings/satellite/imlb/12/abstracts/symposia/pil1.htm#abs0350.

267. A. Nytén, A. Abouimrane, M. Armand, T. Gustafsson and J. O. Thomas. Electrochemical performance of Li_2FeSiO_4 as a new Li-battery cathode material. *Electrochemistry Communications*. Vol. 7, pages 156–160 (2005).

268. M. S. Islam, R. Dominko, C. Masquelier, C. Sirisopanaporn, A. R. Armstrong and P. G. Bruce. Silicate cathodes for lithium batteries: alternatives to phosphates? *Journal of Materials Chemistry*. Vol. 21, pages 9811–9818 (2011).

269. A. Nytén, S. Kamali, L. Häggström, T. Gustafsson and J. O. Thomas. The lithium extraction/insertion mechanism in Li_2FeSiO_4. *Journal of Materials Chemistry*. Vol. 16, pages 2266–2272 (2006).

270. R. Dominko, M. Bele, M. Gaberšček, A. Meden, M. Remškar and J. Jamnik. Structure and electrochemical performance of Li_2MnSiO_4 and Li_2FeSiO_4 as potential Li-battery cathode materials. *Electrochemistry Communications*. Vol. 8, pages 217–222 (2006).

271. Z. L. Gong, Y. X. Li and Y. Yang. Synthesis and electrochemical performance of Li_2CoSiO_4 as cathode material for lithium ion batteries. *Journal of Power Sources*. Vol. 174, pages 524–527 (2007).

272. G. Quoirin, F. Taulelle, L. Dupont and C. Masquelier. Crystal Chemistry and Electrochemical Delithiation of Li_2FeSiO_4. *Meeting Abstracts*. Vol. MA2007-01, pages 98–98 (2007).

273. G. Quoirin. Apport de la résonance magnétique nucléaire à la description structurale et électrochimique de matériaux paramagnétiques. Synthèse, Etudes Structurales et électrochimiques du silicate de fer Li_2FeSiO_4. Ph.D. dissertation, Amiens (France), 2007.

274. Z. L. Gong, Y. X. Li, G. N. He, J. Li and Y. Yang. Nanostructured Li_2FeSiO_4 Electrode Material Synthesized through Hydrothermal-Assisted Sol-Gel Process. *Electrochemical and Solid-State Letters*. Vol. 11, pages A60–A63 (2008).

275. S. Nishimura, S. Hayase, R. Kanno, M. Yashima, N. Nakayama and A. Yamada. Structure of Li_2FeSiO_4. *J. Am. Chem. Soc.* Vol. 130, pages 13212–13213 (2008).

276. A. R. Armstrong, C. Lyness, M. Ménétrier and P. G. Bruce. Structural Polymorphism in Li_2CoSiO_4 Intercalation Electrodes: A Combined Diffraction and NMR Study. *Chemistry of Materials*. Vol. 22, pages 1892–1900 (2010).

277. A. Boulineau, C. Sirisopanaporn, R. Dominko, A. R. Armstrong, P. G. Bruce and C. Masquelier. Polymorphism and structural defects in Li_2FeSiO_4. *Dalton Transactions*. Vol. 39, pages 6310–6316 (2010).

278. C. Sirisopanaporn, C. Masquelier, P. G. Bruce, A. R. Armstrong and R. Dominko. Dependence of Li_2FeSiO_4 Electrochemistry on Structure. *J. Am. Chem. Soc.* Vol. 133, pages 1263–1265 (2010).

279. C. Sirisopanaporn. Structural and electrochemical properties of Li_2MSiO_4 cathode materials for Li batteries. Ph.D. thesis, Amiens (France), 2011.

280. M. E. Arroyo-de Dompablo, M. Armand, J.-M. Tarascon and U. Amador. On-demand design of polyoxianionic cathode materials based on electronegativity correlations: An exploration of the Li_2MSiO_4 system (M = Fe, Mn, Co, Ni). *Electrochemistry Communications*. Vol. 8, pages 1292–1298 (2006).

281. A. Saracibar, A. Van der Ven and M. E. Arroyo-de Dompablo. Crystal Structure, Energetics, And Electrochemistry of Li_2FeSiO_4 Polymorphs from First Principles Calculations. *Chemistry of Materials*. Vol. 24, pages 495–503 (2012).

282. A. R. Armstrong, N. Kuganathan, M. S. Islam and P. G. Bruce. Structure and Lithium Transport Pathways in Li_2FeSiO_4 Cathodes for Lithium Batteries. *Journal of the American Chemical Society*. Vol. 133, pages 13031–13035 (2011).

283. R. Dominko. Li_2MSiO_4 (M = Fe and/or Mn) cathode materials. *Journal of Power Sources*. Vol. 184, pages 462–468 (2008).

284. R. Dominko, D. E. Conte, D. Hanzel, M. Gaberscek and J. Jamnik. Impact of synthesis conditions on the structure and performance of Li_2FeSiO_4. *Journal of Power Sources*. Vol. 178, pages 842–847 (2008).

285. Z. L. Gong, Y. X. Li and Y. Yang. Synthesis and Characterization of $Li_2Mn_xFe_{1-x}SiO_4$ as a Cathode Material for Lithium-Ion Batteries. *Electrochemical and Solid-State Letters*. Vol. 9, pages A542–A544 (2006).

286. R. Dominko, C. Sirisopanaporn, C. Masquelier, D. Hanzel, I. Arcon and M. Gaberscek. On the Origin of the Electrochemical Capacity of $Li_2Fe_{0.8}Mn_{0.2}SiO_4$. *Journal of The Electrochemical Society*. Vol. 157, pages A1309–A1316 (2010).

287. V. Legagneur, Y. An, A. Mosbah, R. Portal, A. Le Gal La Salle, A. Verbaere, D. Guyomard and Y. Piffard. $LiMBO_3$ (M=Mn, Fe, Co): synthesis, crystal structure and lithium deinsertion/insertion properties. *Solid State Ionics*. Vol. 139, pages 37–46 (2001).

References

288. J. C. Kim, C. J. Moore, B. Kang, G. Hautier, A. Jain and G. Ceder. Synthesis and Electrochemical Properties of Monoclinic $LiMnBO_3$ as a Li Intercalation Material. *Journal of The Electrochemical Society*. Vol. 158, pages A309–A315 (2011).

289. A. Yamada, N. Iwane, Y. Harada, S. Nishimura, Y. Koyama and I. Tanaka. Lithium Iron Borates as High-Capacity Battery Electrodes. *Advanced Materials*. Vol. 22, pages 3583–3587 (2010).

290. Y. Janssen, D. S. Middlemiss, S.-H. Bo, C. P. Grey and P. G. Khalifah. Structural Modulation in the High Capacity Battery Cathode Material $LiFeBO_3$. *Journal of the American Chemical Society*. Vol. 134, pages 12516–12527 (2012).

291. L. Tao. New Transition Metal Borates and Borophosphates as Cathode Materials for Li/Na Batteries. Ph.D. dissertation, Amiens (France), 2013.

292. D.-H. Seo, Y.-U. Park, S.-W. Kim, I. Park, R. A. Shakoor and K. Kang. First-principles study on lithium metal borate cathodes for lithium rechargeable batteries. *Physical Review B*. Vol. 83, page 205127 (2011).

293. A. Yamada, N. Iwane, S. Nishimura, Y. Koyama and I. Tanaka. Synthesis and electrochemistry of monoclinic $Li(Mn_xFe_{1-x})BO_3$: a combined experimental and computational study. *Journal of Materials Chemistry*. Vol. 21, pages 10690–10696 (2011).

294. Y. Yamashita, P. Barpanda, Y. Yamada and A. Yamada. Demonstration of Co^{3+}/Co^{2+} Electrochemical Activity in $LiCoBO_3$ Cathode at 4.0 V. *ECS Electrochemistry Letters*. Vol. 2, pages A75–A77 (2013).

295. J. Barker, M. Y. Saidi and J. L. Swoyer. Lithium metal fluorophosphate materials and preparation thereof. Patent WO 2001/084655. Issued November 8, 2001.

296. J. L. Pizarro-Sanz, J. M. Dance, G. Villeneuve and M. I. Arriortua-Marcaida. The natural and synthetic tavorite minerals: Crystal chemistry and magnetic properties. *Materials Letters*. Vol. 18, pages 327–330 (1994).

297. L. A. Groat, M. Raudsepp, F. C. Hawthorne, T. S. Ercit, B. L. Sherriff and J. S. Hartman. The amblygonite-montebrasite series; characterization by single-crystal structure refinement, infared spectroscopy, and multinuclear MAS-NMR spectroscopy. *American Mineralogist*. Vol. 75, pages 992–1008 (1990).

298. J. Barker, M. Y. Saidi and J. L. Swoyer. Electrochemical Insertion Properties of the Novel Lithium Vanadium Fluorophosphate, $LiVPO_4F$. *Journal of The Electrochemical Society*. Vol. 150, pages A1394–A1398 (2003).

299. J. Barker, M. Y. Saidi and J. Swoyer. Novel Battery Systems based on Advanced Fluorophosphate Active Materials - Abstract 232. (2003).

300. J. Barker, M. Y. Saidi and J. L. Swoyer. A Comparative Investigation of the Li Insertion Properties of the Novel Fluorophosphate Phases, $NaVPO_4F$ and $LiVPO_4F$. *Journal of The Electrochemical Society*. Vol. 151, pages A1670–A1677 (2004).

301. J. Barker, R. K. B. Gover, P. Burns, A. Bryan, M. Y. Saidi and J. L. Swoyer. Performance Evaluation of Lithium Vanadium Fluorophosphate in Lithium Metal and Lithium-Ion Cells. *Journal of The Electrochemical Society*. Vol. 152, pages A1776–A1779 (2005).

302. J. Barker, R. K. B. Gover, P. Burns and A. Bryan. A Symmetrical Lithium-Ion Cell Based on Lithium Vanadium Fluorophosphate, LiVPO$_4$F. *Electrochemical and Solid-State Letters*. Vol. 8, pages A285–A287 (2005).

303. J. Barker, R. K. B. Gover, P. Burns, A. Bryan, M. Y. Saidi and J. L. Swoyer. Structural and electrochemical properties of lithium vanadium fluorophosphate, LiVPO$_4$F. *Journal of Power Sources*. Vol. 146, pages 516–520 (2005).

304. R. K. B. Gover, P. Burns, A. Bryan, M. Y. Saidi, J. L. Swoyer and J. Barker. LiVPO$_4$F: A new active material for safe lithium-ion batteries. *Solid State Ionics*. Vol. 177, pages 2635–2638 (2006).

305. J. Barker, M. Y. Saidi, R. K. B. Gover, P. Burns and A. Bryan. The effect of Al substitution on the lithium insertion properties of lithium vanadium fluorophosphate, LiVPO$_4$F. *Journal of Power Sources*. Vol. 174, pages 927–931 (2007).

306. J.-M. Tarascon, N. Recham and M. Armand. Method for producing inorganic compounds. Patent WO 2010046608. Issued April 29, 2010.

307. N. Recham, J.-N. Chotard, J.-C. Jumas, L. Laffont, M. Armand and J.-M. Tarascon. Ionothermal Synthesis of Li-Based Fluorophosphates Electrodes. *Chemistry of Materials*. Vol. 22, pages 1142–1148 (2010).

308. J.-M. Tarascon, N. Recham, M. Armand, J. N. Chotard, P. Barpanda, W. Walker and L. Dupont. Hunting for Better Li-Based Electrode Materials via Low Temperature Inorganic Synthesis. *Chemistry of Materials*. Vol. 22, pages 724–739 (2010).

309. T. N. Ramesh, K. T. Lee, B. L. Ellis and L. F. Nazar. Tavorite Lithium Iron Fluorophosphate Cathode Materials: Phase Transition and Electrochemistry of LiFePO$_4$F-Li$_2$FePO$_4$F. *Electrochemical and Solid-State Letters*. Vol. 13, pages A43–A47 (2010).

310. B. L. Ellis, T. N. Ramesh, W. N. Rowan-Weetaluktuk, D. H. Ryan and L. F. Nazar. Solvothermal synthesis of electroactive lithium iron tavorites and structure of Li$_2$FePO$_4$F. *Journal of Materials Chemistry*. Vol. 22, page 4759 (2012).

311. C. Masquelier, A. K. Padhi, K. S. Nanjundaswamy and J. B. Goodenough. New Cathode Materials for Rechargeable Lithium Batteries: The 3-D Framework Structures Li$_3$Fe$_2$(XO$_4$)$_3$ (X=P, As). *Journal of Solid State Chemistry*. Vol. 135, pages 228–234 (1998).

312. N. Marx, L. Croguennec, D. Carlier, A. Wattiaux, F. L. Cras, E. Suard and C. Delmas. The structure of tavorite LiFePO$_4$(OH) from diffraction and GGA + U studies and its preliminary electrochemical characterization. *Dalton Transactions*. Vol. 39, pages 5108–5116 (2010).

313. S. Yang, P. Y. Zavalij and M. Stanley Whittingham. Hydrothermal synthesis of lithium iron phosphate cathodes. *Electrochemistry Communications*. Vol. 3, pages 505–508 (2001).

314. B. L. Ellis and L. F. Nazar. Anion-Induced Solid Solution Electrochemical Behavior in Iron Tavorite Phosphates. *Chem. Mater.* Vol. 24, pages 966–968 (2012).

315. Y. Yang, M. Hirayama, M. Yonemura and R. Kanno. Synthesis, crystal structure, and electrode characteristics of LiMnPO$_4$(OH) cathode for lithium batteries. *Journal of Solid State Chemistry*. Vol. 187, pages 124–129 (2012).

316. Y. Yang, M. Hirayama, K. Kubota and R. Kanno. Synthesis and electrode characteristics of solid solution $LiMn_{1-x}Fe_xPO_4(OH)$ ($0 \leq x \leq 0.3$) with tavorite structure for lithium batteries. *Journal of Power Sources*. Vol. 205, pages 394–401 (2012).

317. N. Recham, J.-N. Chotard, L. Dupont, K. Djellab, M. Armand and J.-M. Tarascon. Ionothermal Synthesis of Sodium-Based Fluorophosphate Cathode Materials. *Journal of The Electrochemical Society*. Vol. 156, pages A993–A999 (2009).

318. N. Recham. Synthèse, structure et propriétés électrochimiques de nouveaux matériaux d'électrodes pour batteries à ions lithium. Ph.D. dissertation, Amiens (France), February 19, 2010.

319. L. Sebastian, J. Gopalakrishnan and Y. Piffard. Synthesis, crystal structure and lithium ion conductivity of $LiMgFSO_4$. *Journal of Materials Chemistry*. Vol. 12, pages 374–377 (2002).

320. J.-M. Tarascon, N. Recham and M. Armand. Fluorosulphates useful as electrode materials. Patent WO 2010046610. Issued April 29, 2010.

321. N. Recham, J.-N. Chotard, L. Dupont, C. Delacourt, W. Walker, M. Armand and J.-M. Tarascon. A 3.6 V lithium-based fluorosulphate insertion positive electrode for lithium-ion batteries. *Nature Materials*. Vol. 9, pages 68–74 (2010).

322. M. Wildner and G. Giester. The crystal structures of kieserite-type compounds. I, Crystal structures of $Me(II)SO_4.H_2O$ (Me=Mn,Fe,Co,Ni,Zn). *Neues Jahrbuch für Mineralogie Monatshefte*. pages 296–306 (1991).

323. G. Rousse and J.-M. Tarascon. Sulfate-based Polyanionic Compounds for Li-ion Batteries: Synthesis, Crystal Chemistry and Electrochemistry Aspects. *Chemistry of Materials*. (2013) doi:10.1021/cm4022358.

324. M. Ati, M. T. Sougrati, N. Recham, P. Barpanda, J.-B. Leriche, M. Courty, M. Armand, J.-C. Jumas and J.-M. Tarascon. Fluorosulfate Positive Electrodes for Li-Ion Batteries Made via a Solid-State Dry Process. *Journal of The Electrochemical Society*. Vol. 157, pages A1007–A1015 (2010).

325. J.-M. Tarascon, M. Ati, M. Armand and N. Recham. Method for preparing alkali metal and transition metal fluorosulfates. Patent WO 2011144838. Issued November 24, 2011. Available at http://www.wipo.int/patentscope/search/en/WO2011144838.

326. M. Ati, W. T. Walker, K. Djellab, M. Armand, N. Recham and J.-M. Tarascon. Fluorosulfate Positive Electrode Materials Made with Polymers as Reacting Media. *Electrochemical and Solid-State Letters*. Vol. 13, pages A150–A153 (2010).

327. R. Tripathi, T. N. Ramesh, B. L. Ellis and L. F. Nazar. Scalable Synthesis of Tavorite $LiFeSO_4F$ and $NaFeSO_4F$ Cathode Materials. *Angewandte Chemie*. Vol. 122, pages 8920–8924 (2010).

328. A. Sobkowiak, M. R. Roberts, R. Younesi, T. Ericsson, L. Häggström, C.-W. Tai, A. M. Andersson, K. Edström, T. Gustafsson and F. Björefors. Understanding and Controlling the Surface Chemistry of $LiFeSO_4F$ for an Enhanced Cathode Functionality. *Chemistry of Materials*. (2013) doi:10.1021/cm401063s.

329. P. Barpanda, N. Recham, J.-N. Chotard, K. Djellab, W. Walker, M. Armand and J.-M. Tarascon. Structure and electrochemical properties of novel mixed $Li(Fe_{1-x}M_x)SO_4F$ (M = Co, Ni, Mn)

phases fabricated by low temperature ionothermal synthesis. *Journal of Materials Chemistry*. Vol. 20, pages 1659–1668 (2010).

330. P. Barpanda, M. Ati, B. C. Melot, G. Rousse, J.-N. Chotard, M.-L. Doublet, M. T. Sougrati, S. A. Corr, J.-C. Jumas and J.-M. Tarascon. A 3.90 V iron-based fluorosulphate material for lithium-ion batteries crystallizing in the triplite structure. *Nature Materials*. Vol. 10, pages 772–779 (2011).

331. P. Barpanda, J.-N. Chotard, N. Recham, C. Delacourt, M. Ati, L. Dupont, M. Armand and J.-M. Tarascon. Structural, Transport, and Electrochemical Investigation of Novel $AMSO_4F$ (A = Na, Li; M = Fe, Co, Ni, Mn) Metal Fluorosulphates Prepared Using Low Temperature Synthesis Routes. *Inorganic Chemistry*. Vol. 49, pages 7401–7413 (2010).

332. M. Ati, B. C. Melot, G. Rousse, J.-N. Chotard, P. Barpanda and J.-M. Tarascon. Structural and Electrochemical Diversity in $LiFe_{1-\delta}Zn_\delta SO_4F$ Solid Solution: A Fe-Based 3.9 V Positive-Electrode Material. *Angewandte Chemie International Edition*. Vol. 50, pages 10574–10577 (2011).

333. R. Tripathi, G. Popov, B. L. Ellis, A. Huq and L. F. Nazar. Lithium metal fluorosulfate polymorphs as positive electrodes for Li-ion batteries: synthetic strategies and effect of cation ordering. *Energy & Environmental Science*. Vol. 5, page 6238 (2012).

334. J.-M. Tarascon, P. Barpanda, M. Ati, J.-N. Chotard and M. Armand. Novel Fluorinated Material Usable as an Active Electrode Material. Patent WO 2012/146842. Issued November 2, 2012. Available at http://patentscope.wipo.int/search/en/WO2012146842.

335. M. Ati, B. C. Melot, J.-N. Chotard, G. Rousse, M. Reynaud and J.-M. Tarascon. Synthesis and electrochemical properties of pure $LiFeSO_4F$ in the triplite structure. *Electrochemistry Communications*. Vol. 13, pages 1280–1283 (2011).

336. L. Liu, B. Zhang and X. Huang. A 3.9 V polyanion-type cathode material for Li-ion batteries. *Progress in Natural Science: Materials International*. Vol. 21, pages 211–215 (2011).

337. M. Ati, M. Sathiya, S. Boulineau, M. Reynaud, A. M. Abakumov, G. Rousse, B. C. Melot, G. Van Tendeloo and J.-M. Tarascon. Understanding and Promoting the Rapid Preparation of the triplite-phase of $LiFeSO_4F$ for Use as a Large-Potential Fe Cathode. *Journal of the American Chemical Society*. Vol. 134, pages 18380–18387 (2012).

338. L. Nazar, R. Tripathi, G. Popov and X. Sun. Ultra-Rapid Microwave Synthesis of Triplite $LiFeSO_4F$. *Journal of Materials Chemistry A*. Vol. 1, pages 2990–2994 (2012).

339. A. V. Radha, J. D. Furman, M. Ati, B. C. Melot, J.-M. Tarascon and A. Navrotsky. Understanding the Stability of Fluorosulfate Li-ion Battery Cathode Materials: A Thermochemical Study of $LiFe_{1-x}Mn_xSO_4F$ ($0 \leq x \leq 1$) Polymorphs. *Journal of Materials Chemistry*. Vol. 22, pages 24446–24452 (2012).

340. M. Anji Reddy, V. Pralong, V. Caignaert, U. V. Varadaraju and B. Raveau. Monoclinic iron hydroxy sulphate: A new route to electrode materials. *Electrochemistry Communications*. Vol. 11, pages 1807–1810 (2009).

341. M. Ati, M.-T. Sougrati, G. Rousse, N. Recham, M.-L. Doublet, J.-C. Jumas and J.-M. Tarascon. Single-Step Synthesis of $FeSO_4F_{1-y}OH_y$ ($0 \leq y \leq 1$) Positive Electrodes for Li-Based Batteries. *Chem. Mater.* Vol. 24, pages 1472–1485 (2012).

342. C. V. Subban, M. Ati, G. Rousse, A. M. Abakumov, G. Van Tendeloo, R. Janot and J.-M. Tarascon. Preparation, Structure, and Electrochemistry of Layered Polyanionic Hydroxysulfates: LiMSO$_4$OH (M=Fe, Co, Mn) Electrodes for Li-ion Batteries. *Journal of the American Chemical Society*. Vol. 135, pages 3653–3661 (2013).

343. P. Barpanda, M. Ati, N. Recham, J.-N. Chotard, W. Walker, M. Armand and J.-M. Tarascon. Crystal Structure and Electrochemical Study of A(Fe$_{1-x}$M$_x$)SO$_4$F (A = Li/Na; M = Co/Ni/Mn) Fluorosulphates Prepared by Low Temperature Synthesis. *ECS Transactions*. Vol. 28, pages 1–9 (2010).

344. R. Tripathi, G. R. Gardiner, M. S. Islam and L. F. Nazar. Alkali-ion Conduction Paths in LiFeSO$_4$F and NaFeSO$_4$F Tavorite-Type Cathode Materials. *Chemistry of Materials*. Vol. 23, pages 2278–2284 (2011).

345. M. Ati, L. Dupont, N. Recham, J.-N. Chotard, W. Walker, C. Davoisne, P. Barpanda, V. Sarou-Kanian, M. Armand and J.-M. Tarascon. Synthesis, structural, and transport properties of novel bihydrated fluorosulphates NaMSO$_4$F.2H$_2$O (M=Fe, Co, and Ni). *Chemistry of Materials*. Vol. 22, pages 4062–4068 (2010).

346. M. Reynaud. Synthèse et caractérisation de nouveaux fluorosulfates de lithium et de sodium. Master thesis, Amiens (France), September 2010.

347. M. Reynaud, P. Barpanda, G. Rousse, J.-N. Chotard, B. C. Melot, N. Recham and J.-M. Tarascon. Synthesis and crystal chemistry of the NaMSO$_4$F family (M = Mg, Fe, Co, Cu, Zn). *Solid State Sciences*. Vol. 14, pages 15–20 (2012).

348. B. C. Melot and J.-M. Tarascon. Design and Preparation of Materials for Advanced Electrochemical Storage. *Accounts of Chemical Research*. Vol. 46, pages 1226–1238 (2013).

349. A. Gutierrez, N. A. Benedek and A. Manthiram. Crystal-Chemical Guide for Understanding Redox Energy Variations of M^{2+}/$^{3+}$ Couples in Polyanion Cathodes for Lithium-Ion Batteries. *Chemistry of Materials*. Vol. 25, pages 4010–4016 (2013).

350. B. C. Melot, D. O. Scanlon, M. Reynaud, G. Rousse, J.-N. Chotard, M. Henry and J.-M. Tarascon. Chemical and Structural Indicators for Large Redox Potentials in Fe-Based Positive Electrode Materials. *ACS Applied Materials & Interfaces*. (2014) doi:10.1021/am405579h.

351. G. Ceder. High throughput computational methods towards new materials. (2011) Available at http://www.college-de-france.fr/site/jean-marie-tarascon/.

352. A. Jain, G. Hautier, C. J. Moore, S. P. Ong, C. C. Fischer, T. Mueller, K. A. Persson and G. Ceder. A high-throughput infrastructure for density functional theory calculations. *Computational Materials Science*. Vol. 50, pages 2295–2310 (2011).

353. S. P. Ong, A. Jain, G. Hautier, M. Kocher, S. Cholia, D. Gunter, D. Bailey, D. Skinner, K. Persson and G. Ceder. The Materials Project. Available at http://materialsproject.org/.

354. G. Hautier, A. Jain and S. Ong. From the computer to the laboratory: materials discovery and design using first-principles calculations. *Journal of Materials Science*. Vol. 47, pages 7317–7340 (2012).

355. G. Hautier, A. Jain, H. Chen, C. Moore, S. P. Ong and G. Ceder. Novel mixed polyanions lithium-ion battery cathode materials predicted by high-throughput ab initio computations. *Journal of Materials Chemistry*. Vol. 21, pages 17147–17153 (2011).

356. A. Jain, G. Hautier, C. Moore, B. Kang, J. Lee, H. Chen, N. Twu and G. Ceder. A Computational Investigation of $Li_9M_3(P_2O_7)_3(PO_4)_2$ (M = V, Mo) as Cathodes for Li Ion Batteries. *Journal of The Electrochemical Society*. Vol. 159, pages A622–A633 (2012).

357. H. Chen, G. Hautier, A. Jain, C. Moore, B. Kang, R. Doe, L. Wu, Y. Zhu, Y. Tang and G. Ceder. Carbonophosphates: A New Family of Cathode Materials for Li-Ion Batteries Identified Computationally. *Chemistry of Materials*. Vol. 24, pages 2009–2016 (2012).

358. F. C. Hawthorne, S. V. Krivovichev and P. C. Burns. The Crystal Chemistry of Sulfate Minerals. *Reviews in Mineralogy and Geochemistry*. Vol. 40, pages 1–112 (2000).

359. H. Strunz and E. H. Nickel. Nickel-Strunz Mineralogical Tables (10th edition). *Pending publication* . .

360. D. Barthelmy. Nickel-Strunz Classification. *webmineral.com*. Available at http://webmineral.com/strunz.shtml#.UjoClX8UWdw.

361. J. Ralph and I. Chau. Nickel-Strunz Classification - Primary Groups 10th edition. *mindat.org*. Available at http://www.mindat.org/strunz.php.

362. A. E. Tutton. A Comparative Crystallographical Study of the Double Selenates of the Series $R_2M(SeO_4)_2.6H_2O$ salts in Which M is Zinc. *Proceedings of the Royal Society of London*. Vol. 67, pages 58–84 (1900).

363. M. Reynaud, M. Ati, S. Boulineau, M. T. Sougrati, B. C. Melot, G. Rousse, J.-N. Chotard and J.-M. Tarascon. Bimetallic Sulfates $A_2M(SO_4)_2.nH_2O$ (A = Li, Na and M = Transition Metal): as New Attractive Electrode Materials for Li- and Na-Ion Batteries. *ECS Transactions*. Vol. 50, pages 11–19 (2013).

364. M. Reynaud, G. Rousse, A. M. Abakumov, M. T. Sougrati, G. Van Tendeloo, J.-N. Chotard and J.-M. Tarascon. Design of new electrode materials for Li-ion and Na-ion batteries from the Bloedite mineral $Na_2Mg(SO_4)_2 \bullet 4H_2O$. *Journal of Materials Chemistry A*. Vol. 2, pages 2671–2680 (2014).

365. C. Lauro. Ricerche röntgenografiche sulla bloedite. *Periodico di Mineralogia*. Vol. 11, pages 89–94 (1940).

366. I. M. Rumanova and G. I. Malitskaya. *Kristallografiya*. (1959) Available at http://scholar.google.com/scholar?q=rumanova+malitskaya+.

367. M. Giglio. Die Kristallstruktur von $Na_2Zn(SO_4)_2.4H_2O$ (Zn-Blödit). *Acta Crystallographica*. Vol. 11, pages 789–794 (1958).

368. V. I. Bukin and Y. Z. Nozik. A neutronographic investigation of hydrogen bonding in zinc astrakanite $Na_2Zn(SO_4)_2 \cdot 4H_2O$. *Journal of Structural Chemistry*. Vol. 15, pages 616–619 (1974).

369. V. I. Bukin and Y. Z. Nozik. $Na_2Co(SO_4)_2.4H_2O$. *Kristallografiya*. Vol. 20, page 293 (1975).

370. F. C. Hawthorne. Refinement of the crystal structure of bloedite; structural similarities in the [^{VI}M(^{IV}TPhi$_4$)$_2$Phi$_n$) finite-cluster minerals. *The Canadian Mineralogist*. Vol. 23, pages 669–674 (1985).

371. C. Vizcayno and M. T. Garcia-Gonzalez. Na$_2$Mg(SO$_4$)$_2$.4H$_2$O, the Mg end-member of the bloedite-type of mineral. *Acta Crystallographica Section C: Crystal Structure Communications*. Vol. C55, pages 8–11 (1999).

372. D. Stoilova and M. Wildner. Blödite-type compounds Na$_2$Me(SO$_4$)$_2$·4H$_2$O (Me=Mg, Co, Ni, Zn): crystal structures and hydrogen bonding systems. *Journal of Molecular Structure*. Vol. 706, pages 57–63 (2004).

373. M. E. Díaz de Vivar, S. Baggio, M. T. Garland and R. Baggio. Disodium nickel bis(sulfate) tetrahydrate: a nickel astrakanite. *Acta Crystallographica Section E Structure Reports Online*. Vol. 62, pages i196–i198 (2006).

374. M. E. Díaz de Vivar, S. Baggio, A. Ibáñez and R. Baggio. Disodium zinc bis(sulfate) tetrahydrate (zinc astrakanite) revisited. *Acta Crystallographica Section E*. Vol. E64, pages i30–i31 (2008).

375. M. Hudák, J. G. Díaz and J. Kožíšek. Disodium tetraaquabis(sulfato)iron(II). *Acta Crystallographica Section E Structure Reports Online*. Vol. 64, pages i10–i10 (2008).

376. L. Cot and P. Conquet. Sur le sulfate double Na$_2$Co(SO$_4$)$_2$ et sur ses hydrates. *Comptes Rendus des Séances de l'Académie des Sciences*. Vol. 264, pages 1294–1297 (1967).

377. L. Cot. Sur le sel double Na$_2$Ni(SO$_4$)$_2$ anhydre et sur ses hydrates. *Comptes Rendus des Séances de l'Académie des Sciences*. Vol. 264, pages 1955–1957 (1967).

378. L. Cot. Thermolyse du sel double Na$_2$Fe(SO$_2$)$_2$.4H$_2$O. Existence d'une espèce cristalline de formule Na$_2$Fe$_x^{3+}$Fe$_{1-x}^{2+}$(SO$_4$)$_2$(OH)$_x$. *Comptes Rendus des Séances de l'Académie des Sciences*. Vol. 266, pages 921–923 (1968).

379. L. Cot and M. Tiesi. Sur le sel double Na$_2$Zn(SO$_4$)$_2$: variétés cristallines et hydrates. *Comptes Rendus des Séances de l'Académie des Sciences*. Vol. 266, pages 1159–1161 (1968).

380. L. Cot and S. Peytavin. Relations structurales dans la série des sulfates doubles isotypes de formule Na$_2$M^{II}(SO$_4$)$_2$.4H$_2$O avec M^{II} = Fe, Co, Ni ou Zn. *Comptes Rendus des Séances de l'Académie des Sciences*. Vol. 268, pages 64–65 (1969).

381. L. Cot. Analogies et différences dans le comportement thermique et la cristallographie des sels doubles de la série Na$_2$M(SO$_4$)$_2$.4H$_2$O avec M = Fe^{2+}, Co^{2+}, Ni^{2+} ou Zn^{2+}. *Revue de Chimie Minérale*. Vol. 6, pages 1041–1070 (1969).

382. R. W. Berg and N. Thorup. The Reaction between ZnO and Molten Na$_2$S$_2$O$_7$ or K$_2$S$_2$O$_7$ Forming Na$_2$Zn(SO$_4$)$_2$ or K$_2$Zn(SO$_4$)$_2$, Studied by Raman Spectroscopy and X-ray Diffraction. *Inorganic Chemistry*. Vol. 44, pages 3485–3493 (2005).

383. J. Rodríguez-Carvajal. *FullProf Suite*. Available at http://www.ill.eu/sites/fullprof/index.html.

384. J. Rodríguez-Carvajal. Recent advances in magnetic structure determination by neutron powder diffraction. *Physica B: Condensed Matter*. Vol. 192, pages 55–69 (1993).

385. H. M. Rietveld. A profile refinement method for nuclear and magnetic structures. *Journal of Applied Crystallography*. Vol. 2, pages 65–71 (1969).

386. S. P. Ong, V. L. Chevrier, G. Hautier, A. Jain, C. Moore, S. Kim, X. Ma and G. Ceder. Voltage, stability and diffusion barrier differences between sodium-ion and lithium-ion intercalation materials. *Energy & Environmental Science*. Vol. 4, pages 3680–3688 (2011).

387. N. Recham, G. Rousse, M. T. Sougrati, J.-N. Chotard, C. Frayret, M. Sathiya, B. C. Melot, J.-C. Jumas and J.-M. Tarascon. Preparation and Characterization of a Stable $FeSO_4F$-based Framework for Alkali Ion Insertion Electrodes. *Chemistry of Materials*. Vol. 24, pages 4363–4370 (2012).

388. R. E. Stoiber and W. I. J. Rose. Recent volcanic and fumarolic activity at Santiaguito volcano, Guatemala. *Bulletin Volcanologique*. Vol. 33, pages 475–502 (1969).

389. T. Balic-Zunic, A. Garavelli, P. Acquafredda, E. Leonardsen and S. P. Jakobsson. Eldfellite, $NaFe(SO_4)_2$, a new fumarolic mineral from Eldfell volcano, Iceland. *Mineral Mag*. Vol. 73, pages 51–57 (2009).

390. P. C. Piilonen and G. Poirier. New Mineral Names. *American Mineralogist*. Vol. 95, pages 204–208 (2010).

391. C. Osborne Hutton. Yavapaiite, an anhydrous potassium ferric sulfate from Jerome, Arizona. *American Mineralogist*. Vol. 44, pages 1105–1114 (1959).

392. E. J. Graeber and A. Rosenzweig. The crystal structures of yavapaiite $KFe(SO_4)_2$, and goldichite, $KFe(SO_4)_2.4H_2O$. *American Mineralogist*. Vol. 56, pages 1917–1933 (1971).

393. J. W. Anthony, W. J. McLean and R. B. Laughon. The crystal structure of yavapaiite: A discussion. *American Mineralogist*. Vol. 57, pages 1546–1549 (1972).

394. *Formation of alkali iron sulfates ans other compounds causing corrosion in boilers and gas turbines*. (1966) Available at http://stinet.dtic.mil/oai/oai?&verb=getRecord&metadataPrefix=html&identifier=AD0647777.

395. R. Viswanathan, J. F. Henry, J. Tanzosh, G. Stanko, J. Shingledecker, B. Vitalis and R. Purgert. U.S. program on materials technology for ultra-supercritical coal power plants. *Journal of Materials Engineering and Performance*. Vol. 14, pages 281–292 (2005).

396. R. C. Corey and S. S. Sidhu. X-Ray Diffraction Studies of Anhydrous Sodium and Potassium Ferric Sulfates. I. The Disulfates and Trisulfates. *Journal of the American Chemical Society*. Vol. 67, pages 1490–1491 (1945).

397. J. Bernard, P. Couchot and F. Théobald. Préparation et étude radiocristallographique de quelques sulfates doubles de formule $M^I_3M^{III}(SO_4)_3$. *Comptes Rendus des Séances de l'Académie des Sciences*. Vol. 270, pages 1119–1122 (1970).

398. R. Perret and P. Couchot. Préparation et caractérisation de quelques "aluns anhydres" de sodium. *Comptes Rendus des Séances de l'Académie des Sciences*. Vol. 274, pages 366–369 (1972).

399. F. L. Forray, C. Drouet and A. Navrotsky. Thermochemistry of yavapaiite $KFe(SO_4)_2$: Formation and decomposition. *Geochimica et Cosmochimica Acta*. Vol. 69, pages 2133–2140 (2005).

400. F. Scordari, G. Ventruti, A. F. Gualtieri and A. Lausi. Crystal structure of $Na_3Fe(SO_4)_3$, a high temperature product of thermal decomposition of sideronatrite, $Na_2Fe(SO_4)_2(OH)3H_2O$. *American Mineralogist*. Vol. 96, pages 1107–1111 (2011).

401. J. Barker. Lithium-containing sulfates, method of preparation and uses thereof. Patent US 5908716. Issued June 1, 1999. Available at http://www.google.fr/patents?id=_-QYAAAAEBAJ.

402. I. D. Brown and D. Altermatt. Bond-valence parameters obtained from a systematic analysis of the Inorganic Crystal Structure Database. *Acta Crystallographica Section B Structural Science*. Vol. 41, pages 244–247 (1985).

403. R. Zboril, M. Mashlan and D. Krausova. The mecanism of beta-Fe_2O_3 formation by solid-state reaction between NaCl and $Fe_2(SO_4)_3$. *Mössbauer Spectroscopy in Materials Science*. pages 49–56 (1999).

404. M. Touboul, P. Edern, F. Broszniowski and E. Bétourné. Li_2SO_4-MSO_4 (M=Co, Ni) phase diagrams and considerations about α-$Li_{2-2x}M_xSO_4$ solid solutions and $Li_2M_y(SO_4)_{1+y}$ compounds (M: divalent ions). *Solid State Ionics*. Vol. 50, pages 323–328 (1992).

405. M. Touboul, E. Le Samedi, N. Sephar, F. Broszniowski, P. Edern and E. Bétourné. Binary systems with Li_2SO_4 as one of the components. *Journal of Thermal Analysis*. Vol. 40, pages 1151–1156 (1993).

406. P. G. Bruce and A. R. West. Phase diagram of the LISICON, solid electrolyte system, Li_4GeO_4-Zn_2GeO_4. *Materials Research Bulletin*. Vol. 15, pages 379–385 (1980).

407. P. G. Bruce and A. R. West. Ionic conductivity of LISICON solid solutions, $Li_{2+2x}Zn_{1-x}GeO_4$. *Journal of Solid State Chemistry*. Vol. 44, pages 354–365 (1982).

408. A. Benrath and K. Drekopf. *Zeitschrift für Physikalische Chemie*. Vol. 99, page 57 (1921).

409. A. Kvist and A. Lundén. Electrical Conductivity of Solid and Molten Lithium Sulfate. *Zeitschrift Naturforschung Teil A*. Vol. 20, page 235 (1965).

410. B. Heed, A. Lundén and K. Schroeder. Sulphate-based solid electrolytes: properties and applications. *Electrochimica Acta*. Vol. 22, pages 705–707 (1977).

411. L. Nilsson, J. O. Thomas and B. C. Tofield. The structure of the high-temperature solid electrolyte lithium sulphate at 908K. *Journal of Physics C: Solid State Physics*. Vol. 13, pages 6441–6451 (1980).

412. V. K. Deshpande and K. Singh. Electrical conductivity of lithium sulphate in its monoclinic phase. *Solid State Ionics*. Vol. 6, pages 151–154 (1982).

413. K. Singh and V. K. Deshpande. Effect of preparative parameters on the electrical conductivity of Li_2SO_4 in its monoclinic phase. *Solid State Ionics*. Vol. 7, pages 295–299 (1982).

414. A. Lundén, A. Bengtzelius, R. Kaber, L. Nilsson, K. Schroeder and R. Tärneberg. Phase diagram, electrical conductivity, and cation diffusion of the system lithium sulphate - zinc sulphate. *Solid State Ionics*. Vol. 9-10, pages 89–94 (1983).

415. K. Singh and V. K. Deshpande. Electrical conductivity of binary sulphates of lithium sulphate. *Solid State Ionics*. Vol. 13, pages 157–164 (1984).

416. K. Singh, S. S. Bhoga and F. C. Raghuwanshi. Aliovalent substitution in β-Li$_2$SO$_4$ towards conductivity enhancement. *Bulletin of Materials Science*. Vol. 9, pages 263–267 (1987).

417. A. Lundén, K. Schroeder and H. Ljungmark. Phase diagrams of binary Li$_2$SO$_4$–MeSO$_4$(Me=Be, Mg, Ca, Sr, Ba, Zn, Cd, Mn). *Solid State Ionics*. Vol. 28-30, pages 262–266 (1988).

418. A. Lundén. Enhancement of cation mobility in some sulphate phases due to a paddle-wheel mechanism. *Solid State Ionics*. Vol. 28–30, pages 163–167 (1988).

419. A. Lundén. Evidence for and against the paddle-wheel mechanism of ion transport in superionic sulphate phases. *Solid State Communications*. Vol. 65, pages 1237–1240 (1988).

420. M. Touboul, M. Quarton, J. Lokaj and V. Kettmann. Structure of dilithium dimagnesium trisulfate. *Acta Crystallographica Section C Crystal Structure Communications*. Vol. 44, pages 1887–1889 (1988).

421. M. Touboul, E. Le Samedi and M. Quarton. Caracterisation thermique et cristallographique de Li$_2$Mg$_2$(SO$_4$)$_3$ dans le systeme Li$_2$SO$_4$-MgSO$_4$. *Journal of the Less Common Metals*. Vol. 146, pages 67–73 (1989).

422. P. P. Fedorov. Concerning the incorporation of divalent cations into the high-temperature modification of Li$_2$SO$_4$. *Solid State Ionics*. Vol. 84, pages 113–115 (1996).

423. R. Tärneberg and B.-E. Mellander. Ion transport in high temperature rotator phase solid electrolytes. *Solid State Ionics*. Vol. 98, pages 175–183 (1997).

424. A. Elfakir, J.-P. Souron, G. Wallez, M. Quarton and M. Touboul. Tl$_2$SO$_4$–Li$_2$SO$_4$ phase diagram and properties of TlLiSO$_4$. *Solid State Ionics*. Vol. 110, pages 145–151 (1998).

425. J. Isasi, S. Jaulmes, A. Elfakir and M. Quarton. Crystal structure of dilithium nickel disulfate, Li$_2$Ni(SO$_4$)$_2$. *Zeitschrift für Kristallographie - New crystal structures*. Vol. 216, pages 331–332 (2001).

426. M. Reynaud, M. Ati, B. C. Melot, M. T. Sougrati, G. Rousse, J.-N. Chotard and J.-M. Tarascon. Li$_2$Fe(SO$_4$)$_2$ as a 3.83 V positive electrode material. *Electrochemistry Communications*. Vol. 21, pages 77–80 (2012).

427. M. Ati. Synthèse, structures et propriétés des composés LiMSO$_4$F (M = métal 3d) en tant que matériaux d'électrode positive pour batteries à ions Li. Ph.D. dissertation, Amiens (France), January 29, 2013.

428. M. Reynaud, M. Ati, J.-N. Chotard and J.-M. Tarascon. Sulfates utiles comme matériaux d'électrode. Patent FR 12 51854.

429. A. Boultif and D. Louër. Indexing of powder diffraction patterns for low-symmetry lattices by the successive dichotomy method. *Journal of Applied Crystallography*. Vol. 24, pages 987–993 (1991).

430. A. Boultif and D. Louër. Powder pattern indexing with the dichotomy method. *Journal of Applied Crystallography*. Vol. 37, pages 724–731 (2004).

431. V. Favre-Nicolin and R. Černý. *FOX, Free Objects for Crystallography*. Available at http://objcryst.sourceforge.net.

432. V. Favre-Nicolin and R. Černý. FOX, Free Objects for Crystallography: a modular approach to ab initio structure determination from powder diffraction. *Journal of Applied Crystallography*. Vol. 35, pages 734–743 (2002).

433. A. Altomare, M.-C. Burla, M. Camalli, B. Carrozzini, G. L. Cascarano, C. Giacovazzo, A. Guagliardi, A.-G. Moliterni, G. Polidori and R. Rizzi. EXPO: a program for full powder pattern decomposition and crystal structure solution. *Journal of Applied Crystallography*. Vol. 32, pages 339–340 (1999).

434. A. Altomare, R. Caliandro, M. Camalli, C. Cuocci, C. Giacovazzo, A.-G. Moliterni and R. Rizzi. Automatic structure determination from powder data with EXPO2004. *Journal of Applied Crystallography*. Vol. 37, pages 1025–1028 (2004).

435. A. Altomare, M. Camalli, C. Cuocci, C. Giacovazzo, A. Moliterni and R. Rizzi. EXPO2009: structure solution by powder data in direct and reciprocal space. *Journal of Applied Crystallography*. Vol. 42, pages 1197–1202 (2009).

436. L. M. Gelato and E. Parthé. STRUCTURE TIDY – a computer program to standardize crystal structure data. *Journal of Applied Crystallography*. Vol. 20, pages 139–143 (1987).

437. M. A. Simonov, S. I. Troyanov, E. Kemnitz, D. Haas and M. Kammler. Crystal structure of $Mg(HSO_4)_2$. *Kristallografiya*. Vol. 31, pages 1220–1221 (1986).

438. S. I. Troyanov and M. A. Simonov. Crystal structure of $Zn(HSO_4)_2$. *Kristallografiya*. Vol. 34, pages 233–234 (1989).

439. J. Clark, C. Eames, M. Reynaud, G. Rousse, J.-N. Chotard, J.-M. Tarascon and M. S. Islam. High-Voltage Sulphate Cathodes $Li_2M(SO_4)_2$ (M = Fe, Mn, Co): Atomic-Scale Studies of Structures, Lithium Diffusion and Voltage Trends. *Journal of Materials Chemistry A*. (submitted).

440. C. Frayret, A. Villesuzanne, N. Spaldin, E. Bousquet, J.-N. Chotard, N. Recham and J.-M. Tarascon. $LiMSO_4F$ (M = Fe, Co and Ni): promising new positive electrode materials through the DFT microscope. *Phys. Chem. Chem. Phys.* Vol. 12, pages 15512–15522 (2010).

441. J.-M. Ateba Mba, C. Masquelier, E. Suard and L. Croguennec. Synthesis and Crystallographic Study of Homeotypic $LiVPO_4F$ and $LiVPO_4O$. *Chem. Mater.* Vol. 24, pages 1223–1234 (2012).

442. M. Reynaud, G. Rousse, J.-N. Chotard, J. Rodríguez-Carvajal and J.-M. Tarascon. Marinite $Li_2M(SO_4)_2$ (M = Co, Fe, Mn) and $Li_1Fe(SO_4)_2$: model compounds for super–super exchange magnetic interactions. *Inorganic Chemistry*. Vol. 52, pages 10456–10466 (2013).

443. J. Rodríguez-Carvajal and J. González Platas. *Fourier Program*. Available at http://www.ill.eu/sites/fullprof/index.html.

444. K. Mereiter. Die Kristallstruktur von Rhomboklas, $H_5O_2^+\{Fe[SO_4]_2\cdot 2H_2O\}^-$. *Tschermaks mineralogische und petrographische Mitteilungen*. Vol. 21, pages 216–232 (1974).

445. J. Majzlan, A. Navrotsky, R. B. McCleskey and C. N. Alpers. Thermodynamic properties and crystal structure refinement of ferricopiapite, coquimbite, rhomboclase, and $Fe_2(SO_4)_3(H_2O)_5$. *European Journal of Mineralogy*. Vol. 18, pages 175–186 (2006).

446. R. C. Peterson, E. Valyashko and R. Wang. The atomic structure of $(H_3O)Fe^{3+}(SO_4)_2$ and rhomboclase, $(H_5O_2)Fe^{3+}(SO_4)_2 \cdot 2H_2O$. *The Canadian Mineralogist*. Vol. 47, pages 625–634 (2009).

447. A. Ponrouch and M. R. Palacín. Patent EU 12380045.0.

448. A. Ponrouch, A. R. Goñi and M. R. Palacín. A New Room Temperature and Solvent FREE Carbon Coating Process - Abstract #987. (2013) Available at https://ecs.confex.com/ecs/224/webprogram/Paper24069.html.

449. A. Ponrouch, A. R. Goñi, M. T. Sougrati, M. Ati, J.-M. Tarascon, J. Nava-Avendaño and M. R. Palacín. A new room temperature and solvent free carbon coating procedure for battery electrode materials. *Energy & Environmental Science*. Vol. 6, pages 3363–3371 (2013).

450. L. Lander, M. Reynaud, M. T. Sougrati, R. Messinger, G. Rousse and J.-M. Tarascon. (submitted).

451. A. Perea, M. T. Sougrati, C. M. Ionica-Bousquet, B. Fraisse, C. Tessier, L. Aldon and J.-C. Jumas. Operando ^{57}Fe Mössbauer and XRD investigation of $Li_xMn_yFe_{1-y}PO_4/C$ composites (y = 0; 0.25). *RSC Advances*. Vol. 2, pages 2080–2086 (2012).

452. S. C. Tarantino, P. Ghigna, C. McCammon, R. Amantea and M. A. Carpenter. Local structural properties of $(Mn,Fe)Nb_2O_6$ from Mössbauer and X-ray absorption spectroscopy. *Acta Crystallographica Section B Structural Science*. Vol. 61, pages 250–257 (2005).

453. H. Zhou, S. Upreti, N. A. Chernova, G. Hautier, G. Ceder and M. S. Whittingham. Iron and Manganese Pyrophosphates as Cathodes for Lithium-Ion Batteries. *Chemistry of Materials*. Vol. 23, pages 293–300 (2011).

454. A. Castets, D. Carlier, Y. Zhang, F. Boucher, N. Marx, L. Croguennec and M. Ménétrier. Multinuclear NMR and DFT Calculations on the $LiFePO_4 \cdot OH$ and $FePO_4 \cdot H_2O$ Homeotypic Phases. *The Journal of Physical Chemistry C*. Vol. 115, pages 16234–16241 (2011).

455. G. Ceder, Y.-M. Chiang, D. R. Sadoway, M. K. Aydinol, Y.-I. Jang and B. Huang. Identification of cathode materials for lithium batteries guided by first-principles calculations. *Nature*. Vol. 392, pages 694–696 (1998).

456. M. Ben Yahia, F. Lemoigno, G. Rousse, F. Boucher, J.-M. Tarascon and M.-L. Doublet. Origin of the 3.6 V to 3.9 V voltage increase in the $LiFeSO_4F$ cathodes for Li-ion batteries. *Energy & Environmental Science*. Vol. 5, pages 9584–9594 (2012).

457. C. Combelles, M. Ben Yahia, L. Pedesseau and M.-L. Doublet. Design of Electrode Materials for Lithium-Ion Batteries: The Example of Metal–Organic Frameworks. *The Journal of Physical Chemistry C*. Vol. 114, pages 9518–9527 (2010).

458. Y. S. Meng and M. E. Arroyo-de Dompablo. First principles computational materials design for energy storage materials in lithium ion batteries. *Energy & Environmental Science*. Vol. 2, pages 589–609 (2009).

459. J. B. Goodenough. Theory of the Role of Covalence in the Perovskite-Type Manganites $[La,M(II)]MnO_3$. *Physical Review*. Vol. 100, pages 564–573 (1955).

460. J. B. Goodenough. An interpretation of the magnetic properties of the perovskite-type mixed crystals $La_{1-x}Sr_xCoO_{3-\lambda}$. *Journal of Physics and Chemistry of Solids*. Vol. 6, pages 287–297 (1958).

461. J. Kanamori. Superexchange interaction and symmetry properties of electron orbitals. *Journal of Physics and Chemistry of Solids*. Vol. 10, pages 87–98 (1959).

462. P. W. Anderson. New Approach to the Theory of Superexchange Interactions. *Physical Review*. Vol. 115, pages 2–13 (1959).

463. J. B. Goodenough, A. Wold, R. J. Arnott and N. Menyuk. Relationship Between Crystal Symmetry and Magnetic Properties of Ionic Compounds Containing Mn^{3+}. *Physical Review*. Vol. 124, pages 373–384 (1961).

464. J. B. Goodenough. *Magnetism And The Chemical Bond*. (John Wiley And Sons, 1963) Available at http://archive.org/details/magnetismandthec031326mbp.

465. B. C. Frazer and P. J. Brown. Antiferromagnetic Structure of $CrVO_4$ and the Anhydrous Sulfates of Divalent Fe, Ni, and Co. *Physical Review*. Vol. 125, pages 1283–1291 (1962).

466. B. C. Melot, G. Rousse, J.-N. Chotard, M. Ati, J. Rodríguez-Carvajal, M. C. Kemei and J.-M. Tarascon. Magnetic Structure and Properties of the Li-Ion Battery Materials $FeSO_4F$ and $LiFeSO_4F$. *Chemistry of Materials*. Vol. 23, pages 2922–2930 (2011).

467. B. C. Melot, G. Rousse, J.-N. Chotard, M. C. Kemei, J. Rodríguez-Carvajal and J.-M. Tarascon. Magnetic structure and properties of $NaFeSO_4F$ and $NaCoSO_4F$. *Physical Review B*. Vol. 85, page 094415 (2012).

468. B. C. Melot, J.-N. Chotard, G. Rousse, M. Ati, M. Reynaud and J.-M. Tarascon. Synthesis, Structure, and Magnetic Properties of the $NaCoXO_4F \cdot 2H_2O$ Phases Where X = S and Se. *Inorganic Chemistry*. Vol. 50, pages 7662–7668 (2011).

469. S. Vilminot, M. Richard-Plouet, G. André, D. Swierczynski, F. Bourée-Vigneron and M. Kurmoo. Hydrothermal Synthesis in the System $Ni(OH)_2$–$NiSO_4$: Nuclear and Magnetic Structures and Magnetic Properties of $Ni_3OH)_2(SO_4)_2(H_2O)_2$. *Inorganic Chemistry*. Vol. 42, pages 6859–6867 (2003).

470. M. Ben Salah, S. Vilminot, G. André, M. Richard-Plouet, F. Bourée-Vigneron, T. Mhiri and M. Kurmoo. Synthesis, Nuclear, and Magnetic Structures and Magnetic Properties of $[Mn_3(OH)_2(SO_4)_2(H_2O)_2]$. *Chemistry – A European Journal*. Vol. 10, pages 2048–2057 (2004).

471. M. Ben Salah, S. Vilminot, G. André, F. Bourée-Vigneron, M. Richard-Plouet, T. Mhiri and M. Kurmoo. Nuclear and Magnetic Structures and Magnetic Properties of $Co_3(OH)_2(SO_4)_2(H_2O)_2$. Comparison to the Mn and Ni Analogues. *Chemistry of Materials*. Vol. 17, pages 2612–2621 (2005).

472. A. S. Wills and A. Harrison. Structure and magnetism of hydronium jarosite, a model Kagomé antiferromagnet. *Journal of the Chemical Society, Faraday Transactions*. Vol. 92, pages 2161–2166 (1996).

473. A. S. Wills. Conventional and unconventional orderings in the jarosites. *Canadian Journal of Physics*. Vol. 79, pages 1501–1510 (2001).

474. D. G. Nocera, B. M. Bartlett, D. Grohol, D. Papoutsakis and M. P. Shores. Spin Frustration in 2D Kagomé Lattices: A Problem for Inorganic Synthetic Chemistry. *Chemistry – A European Journal*. Vol. 10, pages 3850–3859 (2004).

475. P. D. Battle, A. K. Cheetham, C. Gleitzer, W. T. A. Harrison, G. J. Long and G. Longworth. A novel magnetic phase transition in anhydrous iron (III) phosphate, $FePO_4$. *Journal of Physics C: Solid State Physics*. Vol. 15, pages L919–L924 (1982).

476. G. J. Long, G. Longworth, P. Battle, A. K. Cheetham, R. V. Thundathil and D. Beveridge. A study of anhydrous iron(III) sulfate by magnetic susceptibility, Moessbauer, and neutron diffraction techniques. *Inorg. Chem.* Vol. 18, pages 624–632 (1979).

477. J. W. Culvahouse. Anhydrous iron sulfate: An example of weak ferrimagnetism. *Journal of Magnetism and Magnetic Materials*. Vol. 21, pages 133–136 (1980).

478. P. D. Battle, A. K. Cheetham, G. J. Long and G. Longworth. Study of the magnetic properties of iron(III) molybdate, by susceptibility, Moessbauer, and neutron diffraction techniques. *Inorganic Chemistry*. Vol. 21, pages 4223–4228 (1982).

479. G. Rousse, J. Rodríguez-Carvajal, C. Wurm and C. Masquelier. Magnetic Structural Studies of the Two Polymorphs of $Li_3Fe_2(PO_4)_3$: Analysis of the Magnetic Ground State from Super-Super Exchange Interactions. *Chemistry of Materials*. Vol. 13, pages 4527–4536 (2001).

480. G. Rousse, J. Rodríguez-Carvajal, C. Wurm and C. Masquelier. Magnetic structure of two lithium iron phosphates: A- and B-$Li_3Fe_2(PO_4)_3$. *Applied Physics A*. Vol. 74, pages s704–s706 (2002).

481. G. Rousse, J. Rodríguez-Carvajal, C. Wurm and C. Masquelier. A neutron diffraction study of the antiferromagnetic diphosphate $LiFeP_2O_7$. *Solid State Sciences*. Vol. 4, pages 973–978 (2002).

482. H. Serrano-González, S. T. Bramwell, K. D. M. Harris, B. M. Kariuki, L. Nixon, I. P. Parkin and C. Ritter. Magnetic structures of the triangular lattice magnets $AFe(SO_4)_2$ (A=K, Rb, Cs). *Journal of Applied Physics*. Vol. 83, pages 6314–6316 (1998).

483. H. Serrano-González, S. T. Bramwell, K. D. M. Harris, B. M. Kariuki, L. Nixon, I. P. Parkin and C. Ritter. Structural and magnetic characterization of the frustrated triangular-lattice antiferromagnets $CsFe(SO_4)_2$ and $RbFe(SO_4)_2$. *Physical Review B*. Vol. 59, pages 14451–14460 (1999).

484. M. Reynaud, J. Rodríguez-Carvajal, J.-N. Chotard, J.-M. Tarascon and G. Rousse. Magnetic structure and properties of orthorhombic $Li_2Ni(SO_4)_2$: a possible magnetoelectric material. *Physical Review B*. Vol. 89, page 104419 (2014).

485. A. P. Ramirez. Strongly Geometrically Frustrated Magnets. *Annual Review of Materials Science*. Vol. 24, pages 453–480 (1994).

486. B. M. Bartlett and D. G. Nocera. Long-Range Magnetic Ordering in Iron Jarosites Prepared by Redox-Based Hydrothermal Methods. *Journal of the American Chemical Society*. Vol. 127, pages 8985–8993 (2005).

487. E. F. Bertaut. Magnetic structure analysis and group theory. *Journal de Physique Colloques*. Vol. 32, pages C1–462–C1–470 (1971).

488. J. Rodríguez-Carvajal. *SIMBO, ENERMAG and PHASE_DIAGRAM programs, available within the examples of the CrysFML repository*. Available at http://forge.ill.eu/projects/crysfml/repository.

489. N. El Khayati, R. Cherkaoui El Moursli, J. Rodríguez-Carvajal, G. André, N. Blanchard, F. Bourée, G. Collin and T. Roisnel. Crystal and magnetic structures of the oxyphosphates MFePO5 (M = Fe,

Co, Ni, Cu). Analysis of the magnetic ground state in terms of superexchange interactions. *The European Physical Journal B - Condensed Matter and Complex Systems*. Vol. 22, pages 429–442 (2001).

490. *International Tables for Crystallography*. Vol. A-G, (2007).

491. M. L. Medarde. Structural, magnetic and electronic properties of $RNiO_3$ perovskites (R = rare earth). *Journal of Physics: Condensed Matter*. Vol. 9, pages 1679–1707 (1997).

492. J. L. García-Muñoz, J. Rodríguez-Carvajal and P. Lacorre. Sudden Appearance of an Unusual Spin Density Wave At the Metal-Insulator Transition in the Perovskites $RNiO_3$ (R = Pr, Nd). *EPL (Europhysics Letters)*. Vol. 20, pages 241–247 (1992).

493. J. Rodríguez-Carvajal, S. Rosenkranz, M. Medarde, P. Lacorre, M. T. Fernandez-Díaz, F. Fauth and V. Trounov. Neutron-diffraction study of the magnetic and orbital ordering in $^{154}SmNiO_3$ and $^{153}EuNiO_3$. *Physical Review B*. Vol. 57, pages 456–464 (1998).

494. G. Rousse. Cristallochimie et structures magnétiques de nouveaux matériaux pour le stockage de l'énergie. H.D.R. dissertation, Paris (France), December 7, 2012.

495. P. Barpanda, M. Ati, B. C. Melot, G. Rousse, J.-N. Chotard, M.-L. Doublet, M. T. Sougrati, S. A. Corr, J.-C. Jumas and J.-M. Tarascon. A 3.90 V iron-based fluorosulphate material for lithium-ion batteries crystallizing in the triplite structure. *Nature Materials*. Vol. 10, pages 772–779 (2011).

496. J. Etourneau, J. Portier and F. Ménil. The role of the inductive effect in solid state chemistry: how the chemist can use it to modify both the structural and the physical properties of the materials. *Journal of Alloys and Compounds*. Vol. 188, pages 1–7 (1992).

497. G. F. Taylor. Apparatus for making hard metal compositions. Patent US 1896854. Issued February 7, 1933. Available at http://www.google.com/patents?id=LkZHAAAAEBAJ.

498. Z. A. Munir, U. Anselmi-Tamburini and M. Ohyanagi. The effect of electric field and pressure on the synthesis and consolidation of materials: A review of the spark plasma sintering method. *Journal of Materials Science*. Vol. 41, pages 763–777 (2006).

499. M. Morcrette, Y. Chabre, G. Vaughan, G. Amatucci, J.-B. Leriche, S. Patoux, C. Masquelier and J.-M. Tarascon. In situ X-ray diffraction techniques as a powerful tool to study battery electrode materials. *Electrochimica Acta*. Vol. 47, pages 3137–3149 (2002).

500. A. S. Prakash, D. Larcher, M. Morcrette, M. S. Hegde, J.-B. Leriche and C. Masquelier. Synthesis, Phase Stability, and Electrochemically Driven Transformations in the $LiCuO_2–Li_2CuO_2$ System. *Chem. Mater.* Vol. 17, pages 4406–4415 (2005).

501. W. Weppner and R. A. Huggins. Determination of the Kinetic Parameters of Mixed-Conducting Electrodes and Application to the System Li_3Sb. *Journal of The Electrochemical Society*. Vol. 124, pages 1569–1578 (1977).

502. C. J. Wen, B. A. Boukamp, R. A. Huggins and W. Weppner. Thermodynamic and Mass Transport Properties of "LiAl."*Journal of The Electrochemical Society*. Vol. 126, pages 2258–2266 (1979).

503. K. Momma and F. Izumi. VESTA 3 for three-dimensional visualization of crystal, volumetric and morphology data. *Journal of Applied Crystallography*. Vol. 44, pages 1272–1276 (2011).

504. C. Janot. Effet Mössbauer et applications à la physique du solide. Vol. 48, pages 53–64 (1976).

505. R. G. Burns. Mineral Mössbauer spectroscopy: Correlations between chemical shift and quadrupole splitting parameters - Springer. *Hyperfine Interactions*. Vol. 91, pages 739–745 (1994).